DECEMBER 1960 VOLUME 9 (1960) No. 3

GREGG M. SINCLAIR LIBRARY
UNIVERSITY OF HAWAII
8-7-63

NUCLEAR INSTRUMENTS & METHODS

A JOURNAL ON ACCELERATORS, INSTRUMENTATION AND TECHNIQUES IN NUCLEAR PHYSICS

EDITOR: K. SIEGBAHN – UPPSALA

LAST NUMBER OF THIS VOLUME

CONTENTS

R. L. GRAHAM, G. T. EWAN and J. S. GEIGER, A one-meter-radius iron-free double-focusing $\pi\sqrt{2}$ spectrometer for β-ray spectroscopy with a precision of $1:10^5$. 245

H. P. HERNANDEZ, J. M. PETERSON, B. H. SMITH and C. J. TAYLOR, The Livermore variable-energy 90-inch cyclotron 287

C. CERNIGOI, I. GABRIELLI and G. IERNETTI, Behaviour of photomultipliers against short light-pulses 303

J. E. LYNN, Computational methods for analysis of resonance transmission data for S-wave neutrons 315

P. GRIVET et H. HAHN, La stabilisation du champ magnétique par un maser à résonance magnétique nucleaire (II) 328

E. MALISZEWSKI, The optical properties of slow chopper and time-of-flight device 341

W. WEIDEMANN, On the design of quadrupole focusing systems 347

L. BERTANZA, P. FRANZINI, I. MANNELLI and G. V. SILVESTRINI, A rapid cycling bubble chamber 354

Letters to the Editor

TORBJÖRN WESTERMARK, BJÖRN GRAPENGIESSER, HANS LINDROTH and NADIM GHANEM, Note on the determination of tritium by means of liquid scintillators and DC-measurements of photomultiplier currents 357

TORBJÖRN WESTERMARK, On the possibility of a radiation chemical nuclear track chamber 360

AUTHOR INDEX 361

SUBJECT INDEX 363

NORTH-HOLLAND PUBLISHING COMPANY — AMSTERDAM

NUCLEAR INSTRUMENTS AND METHODS

A journal on accelerators, instrumentation and techniques in nuclear physics

EDITOR: K. SIEGBAHN, UPPSALA

EDITORIAL BOARD:

J. B. ADAMS (CERN)
F. A. ALSINA (Buenos Aires)
E. AMALDI (Rome)
H. L. ANDERSON (Chicago)
K. T. BAINBRIDGE (Cambridge, Mass.)
P. R. BELL (Oak Ridge)
R. E. BELL (Montreal)
A. BERTHELOT (Saclay)
H. BRINKMAN (Groningen)
E. H. COOKE-YARBOROUGH (Harwell)
S. DE BENEDETTI (Pittsburgh)
M. DE HEMPTINNE (Louvain)
A. DE-SHALIT (Rehovoth)
M. DEUTSCH (Cambridge, Mass.)
S. DU TOIT (Pretoria)
B. S. DŽELEPOV (Leningrad)
W. GENTNER (Heidelberg)
P. C. GUGELOT (Amsterdam)
H. HALBAN (Paris)
O. HAXEL (Heidelberg)
P. HUBER (Basel)
S. KIKUCHI (Tokyo)
J. KOCH (Copenhagen)
M. S. KOZODAEV (Moscow)
S. LIVINGSTON (Cambridge, Mass.)
E. M. MCMILLAN (Berkeley)
M. G. MEŠČERJAKOW (Moscow)
P. B. MOON (Birmingham)
M. L. OLIPHANT (Canberra)
W. PAUL (Bonn)
A. S. RAO (Bombay)
G. SALVANI (Rome)
P. SAVIĆ (Belgrade)
P. SCHERRER (Zürich)
CH. SCHMELZER (CERN)
R. TANGEN (Oslo)
D. TAYLOR (Northampton)
V. I. VEKSLER (Moscow)
G. VON DARDEL (CERN)
O. WERNHOLM (Stockholm)
R. R. WILSON (Cornell)
S. D. WINTER (Saclay)

INSTRUCTIONS FOR CONTRIBUTORS

Contributions may be sent to the Editor, Professor K. Siegbahn, Institute of Physics, University of Uppsala, Sweden, either directly or through the intermediation of one of the members of the Editorial Board. Contributions may be written in English, French or German but should always, except for very short papers, be supplied with a brief abstract in English. Figures should be in inked original drawings or glossy prints and they should be sufficiently large. Contributors should make sure that important details in drawings and photographs will show up clearly in the diminished copy used by the publisher.

Books for review should be sent to Professor Siegbahn.

Objective and descriptive material on endeavours and product developments from the industry for the section "Spotlight on Industry" should be sent directly to the publishers, North-Holland Publishing Company, P.O. Box 103, Amsterdam.

Nuclear Instruments and Methods is published monthly. The subscription price of a volume of 360 pages is $ 17.00 (130 s), postage free.

Subscriptions should be sent to the publishers, North-Holland Publishing Company, P.O. Box 103, Amsterdam, or to any subscription-agent.

No part of this issue may be reproduced in any form, by print, photoprint, microfilm or any other means without written permission from the publisher.

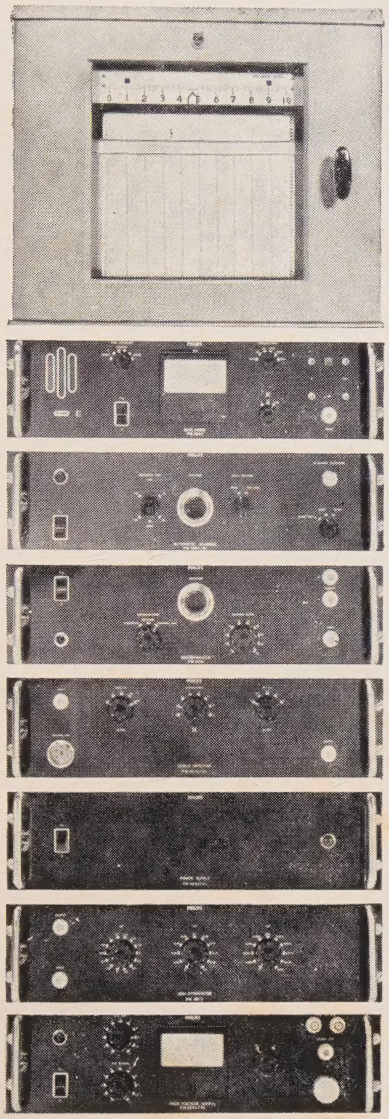

Automatic Single-Channel Gamma Spectrometer

for the qualitative analysis of radiation patterns produced by separate radio-active isotopes or by isotope mixtures. The instrument is also used for quantitative measurements of radiation, for the determination of the purity of isotopes, to study scattering and absorption effects.
The instrument is equipped to produce differential as well as integral spectra.
Both manual and automatic operation provided.
Four scanning times; chart speed adjustable to obtain uniform curve length.

HALF-VALUE WIDTH guaranteed better than 9½% (for the 662 KeV photopeak of Cs 137) with scintillation detector PW 4119 and preamplifier PW 4071 - **HIGH VOLTAGE RANGE** 300-2500 V in steps of 22 V - **REGULATION AND DRIFT** H.V. variations less than 0.005% per 1% mains fluctuation. Drift less than 0.05% in 24 hours - **LOG. ATTENUATION** 1-660 x, in steps of $10^{0.002}$ - **AMPLIFIER RESOLUTION** 1 μsec (5 μsec for 100 x overload) - **CHANNEL HEIGHT** 4-100 V (10-turn helical potentiometer) - **CHANNEL WIDTH** 1-2-4-8-12-16-20-24-28-32 V - **SCANNING TIMES** 3.5-14-24-100 min - **MEASURING RANGES** 300-1000-3000-10 000-30 000 c.p.m. - **TIME CONSTANT** 0.1-1-3-10-30-100 sec.

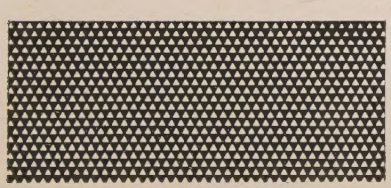

PHILIPS
nuclear equipment

N.V. PHILIPS' GLOEILAMPENFABRIEKEN - EINDHOVEN - HOLLAND
Particle accelerators - Reactor control instrumentation - Health protection and monitoring equipment - Radiation measuring and detection equipment - Geiger-Müller counters - Photomultipliers - Radio-active isotopes.

a new approach to time interval measurement

0.25 milli microsecond measurements

WITH THE

Eldorado

MODEL TH-300

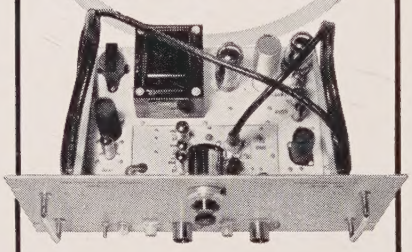

TIME-TO-PULSE HEIGHT CONVERTER

applications

* *Neutron time-of-flight measurements*
* *Half-life determinations of short lived isotopes*
* *Determination of short-time decay in isomeric states*
* *Fast coincidence studies*
* *Delay line calibration*
* *Energy determinations*
* *Transient time studies*

An analog-to-analog converter which transforms time to amplitude over the time range of 1 to 3000 milli microseconds, the TH-300 provides an output pulse whose amplitude is proportional to time. The output can be measured with a pulse height analyzer or scope.

KEY SPECIFICATIONS Three time ranges – 300, 1000, and 3000 milli microsecond full scale. Input, pulse start channel, amplitude of 2 – 100 v negative, duration of 0.01 – 0.10 microseconds; stop channel, amplitude 15 – 150 v negative, duration of 0.01 – 1.00 microseconds. Output, negative ramp, 8 v full scale. Domestic price $795. Immediate delivery.

For complete technical and sales information, call your nearest Eldorado Engineering Representative or write directly to Dept. 79

Eldorado Electronics

2821 Tenth Street
Phone THornwall 1-4613
Berkeley 10, California

TMC AIRS NEW SERVICE POLICY . . .

A sound service policy — and fast service — are important to anyone making such a substantial investment as an instrument like our CN-110. And in spite of all the advanced designing and "technological breakthroughs" currently in the news, things can go kaput. Our units are no exceptions — but one nice thing about them is the fact that almost all circuitry is confined to small, uncluttered, inexpensive boards. If you call in the problem, we can have a new board flying first-class jet almost as soon as you hang up. On the slight chance that factory assistance is needed, we can dispatch one of our top dogs* in a plane we keep for that purpose. Service is by no means the least of your worries and rates some thought when you make a purchase.

We also use the plane to ferry demonstrators hither and yon when prospects want to see it "live" in their own facilities and under their specific working conditions. This we can do easily — just a phone call (collect) from you will set it up.

new logic . . . We now have several new plug-in logic units for the CN-110 that bring the total of standards up to six: 2 Pulse Height, Time-of-flight, Pulsed Neutron, Mass Spectrometer, Pair Spectrometer (16 x 16). And we think we can concoct just about any other program that might be needed. The first four listed here are described in the 6-page folder that gives details of the complete system and its various methods of readout.

The transistorized CN-110 bench-top 256-channel analysis system, its interchangeable plug logic units, and sundry types of readout are all described in a new 6-page bulletin, available on request.

growing . . . Our brand new building is now complete. We're hoping to fill part of the space with bright young men interested in transistor circuit design work in a congenial company. The confusion is about average, but no one is really frantic — yet. If you're interested, write to the attention of our Director of Engineering.

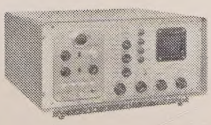

TMC TECHNICAL MEASUREMENT CORPORATION
441 Washington Avenue, North Haven, Connecticut

SCINTILLATION SPECTROMETRY

NON-OVERLOADING LINEAR PULSE AMPLIFIER NE 5202:

with 5 microsecond recovery for 100 times overload. Designed for scintillation spectrometry and pulse height analysis studies, this amplifier features high gain (50,000), high gain stability (better than 0.25% per week), good linearity, low noise (less than 40 microvolts at input), excellent overload characteristics, and operation at high duty cycles. Rise time 0.2 microseconds and integral linearity 0.15%. Preamplifier NE 5202A also available. Based on the double delay line differentiated Fairstein system, it consits of three high gain feedback groups, and a White cathode follower output.

SINGLE CHANNEL PULSE HEIGHT SELECTOR NE 5102

Resolving time 1.2 microsecs; 3–140 volts operating range with energy zero drift less than 0.05 volts per day; 0 to 10 volt gate width with less than 0.01 volts per day drift; maximum counting rate, 2×10^5 c.p.s.; Larger gate widths and automatic scanning facilities available.

E.H.T. SUPPLY UNIT NE 5302

Output stability 0.01%; low noise and ripple—less than 3 mV; output voltage continuously variable from 500–1,500 V; output current 5 mA.

E.H.T. SUPPLY UNIT NE 5303:

As NE 5302, but with output voltage range from 1,000–5,000 V.

SHIELDED SCINTILLATION HEAD UNITS NE 5501–3:

containing White cathode follower preamplifiers with noise level of 25 microvolts; photomultipliers of 1″ or 2″ can be accomodated; for general use or for C14 and H3 investigations with special rotary light locking device.

OTHER UNITS AVAILABLE:

Precision Ratemeter NE 5401.

Scanning scintillation spectrometer Ne 8601. Complete human body monitors and low level counting facilities.

Multi-channel scintillation spectrometer NE 8201 for industrial tracer investigations. Scintillometers for geophysical exploration, including transistorised airborne and carborne equipment.

C14 and H3 counting unit HE 8301.

Exclusive concessionaire for C.D.C./ Bendix 100-channel Transistorised Kicksorter in Great Britain.

Sole agent for Harshaw Sodium Iodide Crystals in the United Kingdom.

Visit our stand No. 61 at the physical society exhibition

Write for new catalogue and price list

For full details of the above and of our SCINTILLATION PHOSPHOR PRODUCTS (plastic, liquids, loaded liquids, crystals, gels, neutron detectors, and chemiclas) write to:

Nuclear Enterprises (G.B.) Ltd.

BANKHEAD MEDWAY, SIGHTHILL, EDINBURGH 11, SCOTLAND. (TEL. CRA 5262)

Associate Company: Nuclear Enterprises Ltd., 550, Berry Street, Winnipeg 12, Canada.

(ndh) 1406

CDC's PROVEN PERFORMANCE

100-CHANNEL PULSE HEIGHT ANALYZER

CHALK RIVER KICKSORTER

Manufactured by Computing Devices of Canada, Limited, from specifications prepared by Atomic Energy of Canada, Limited.

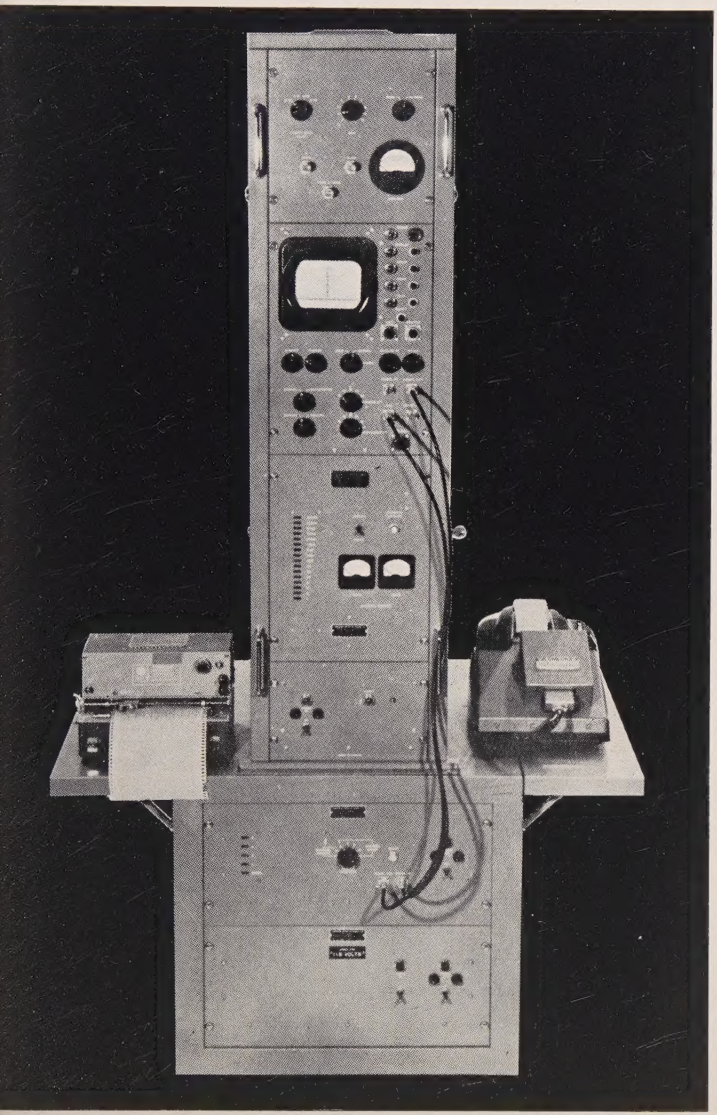

ne convenience and speed of automatic printout can be obtained by adding a Decimal aler, a Print Control Unit, and an Electric Printer as accessories, shown with the Kick- rter. Provision is also made in the circuitry for the addition of a Pen Recorder for more accurate analog output.

88% TRANSISTORIZED

- Printed Circuitry
- Low Maintenance—High Reliability
- Low Power Consumption—120 Watts
- No Ventilation or Cooling Problems

VERSATILE DATA PRESENTATION

- Oscilloscope Display
- Binary Manual count readout allows the count on any channel to be displayed in digital form.
- Magnetic Core Memory—65,535 counts can be stored per channel.
- Permanent Count Storage—sixteen magnetic cores for each of the 100 channels.
- Highly Versatile—can be modified to accommodate most applications which require additional features.

The Chalk River "Kicksorter" is designed to span random pulses of various amplitudes and shapes, sort them according to amplitude into 100 channels, and store a record of the counted pulses in a magnetic core memory. This computer, with its magnetic core memory and versatile data display system, makes it possible to observe the pulse amplitude spectrum as it accumulates or after it has accumulated.

In addition to its wide use in gamma spectroscopy, the "kicksorter" has many applications in medical research, neutron time-of-flight studies, radioactive fallout studies, shielding studies, oil well and uranium logging, neutron activation analyses, measuring of radioactivity in humans, and other areas.

The analyzer is designed so that information accumulated may be displayed or read out in various ways. Data may be observed on the oscilloscope, or information already accumulated in the memory core may be displayed on the screen, plotted on a strip chart recorder, or printed out in decimal form on an automatic printer.

For additional information, wire or write to:

Bendix International

DIVISION OF THE BENDIX CORPORATION
205 East 42nd Street
New York 17, N. Y., U.S.A.
Cable Address: "Bendixint"

Sales Representative for Great Britain

NUCLEAR ENTERPRISES (G.B.) LTD.

BANKHEAD MEDWAY, SIGHTHILL,
EDINBURGH 11, SCOTLAND

SALES AND SERVICE AVAILABLE THROUGHOUT THE WORLD

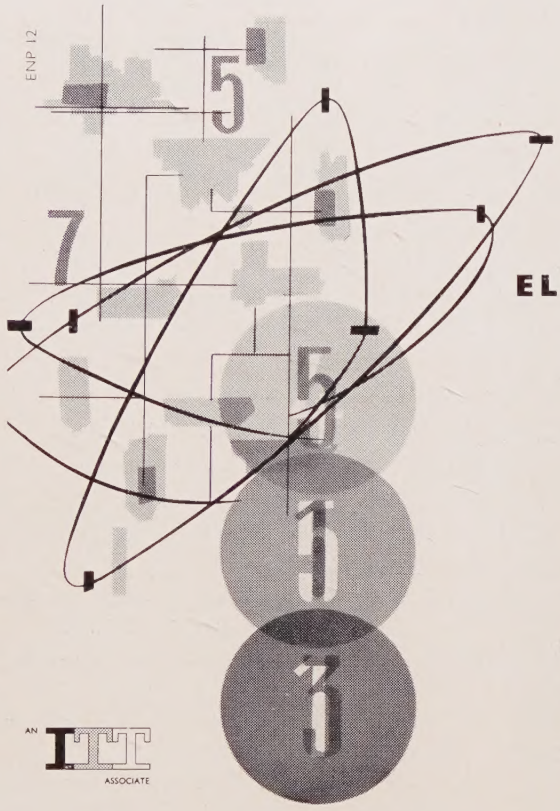

ELECTRONICS FOR NUCLEONICS

SCALER CHRONOSCOPE

Bell Telephone scaler chronoscope gives you top quality reproduction of automatic counting and printing.
It is so constructed that from a small stock of basic modules a wide scope of performances can be covered. This type normally supplied in a metal case is also available for rack mounting

- preset time
- preset count
- result printing facilities
- interchangeable modules
- in line read out
- fully transistorized

Our staff is always available to answer your inquiries.

Bell Telephone Mfg Co

"Nuclear Energy division"
33, Berkenrodelei
HOBOKEN-Antwerp-BELGIUM

NANOSECOND PULSES? MICROSECOND PULSES?

MODEL 414 CALIBRATION PULSER

Decay Times	*Ranges*
0.003 microseconds	0 - 1 millivolts
0.01 microseconds	0 - 5 millivolts
0.03 microseconds	0 - 10 millivolts
0.1 microseconds	0 - 50 millivolts
0.3 microseconds	0 - 100 millivolts
1. microseconds	0 - 500 millivolts
3. microseconds	0 - 5 Volts
10. microseconds	0 - 10 Volts
100. microseconds	0 - 50 Volts
	0 - 100 Volts

Dual purpose- manual or motor driven slider.
Dual 50 ohm output permits coincidence circuit applications.
Internal standard cell calibration.

Polarity switch for positive or negative pulses.
0.1% helical potentiometer.
High pressure hermetically sealed mercury relay.

Write for details.

$ 785 f.o.b. factory

RADIATION INSTRUMENT CO. — P.O. BOX 733 — SILVER SPRING, MARYLAND, U.S.A.

maximum accessibility for servicing...
maximum flexibility of data presentation...

AEI PULSE HEIGHT ANALYSER

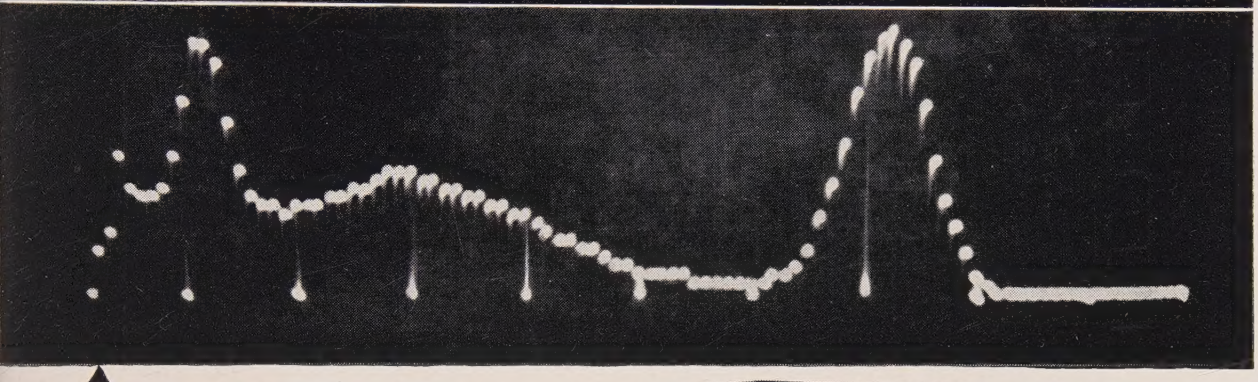

Typical presentation of analogue count on the CRT. This is the gamma spectrum of gold foil irradiated for 30 minutes at a neutron flux of 2×10^5 n/cm²/S. The curve and two significant peaks are due to ^{198}Au.

* Unit construction for easy servicing
* Analogue presentation on cathode ray tube or chart recorder
* Decimal presentation on Dekatrons or 3″ paper tape
* Ferrite memory prevents loss of count if mains fail
* Circuitry largely transistorised for reliability
* 100 Channels, capacity 65,535 pulses per channel
* Console or rack-mounted versions.

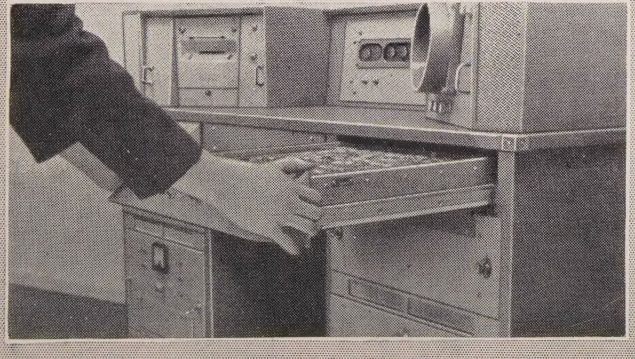

All units draw out on runners so that servicing and setting up can be accomplished without switching off power or removing inter-connecting cables.

A full technical specification of the P.H.A. is given in publications 2451-70 available from:

AEI

Instrumentation Division
Associated Electrical Industries Limited
P.O. BOX 1 - Harlow - Essex - ENGLAND

sc/108

-how to sell your nuclear products internationally-

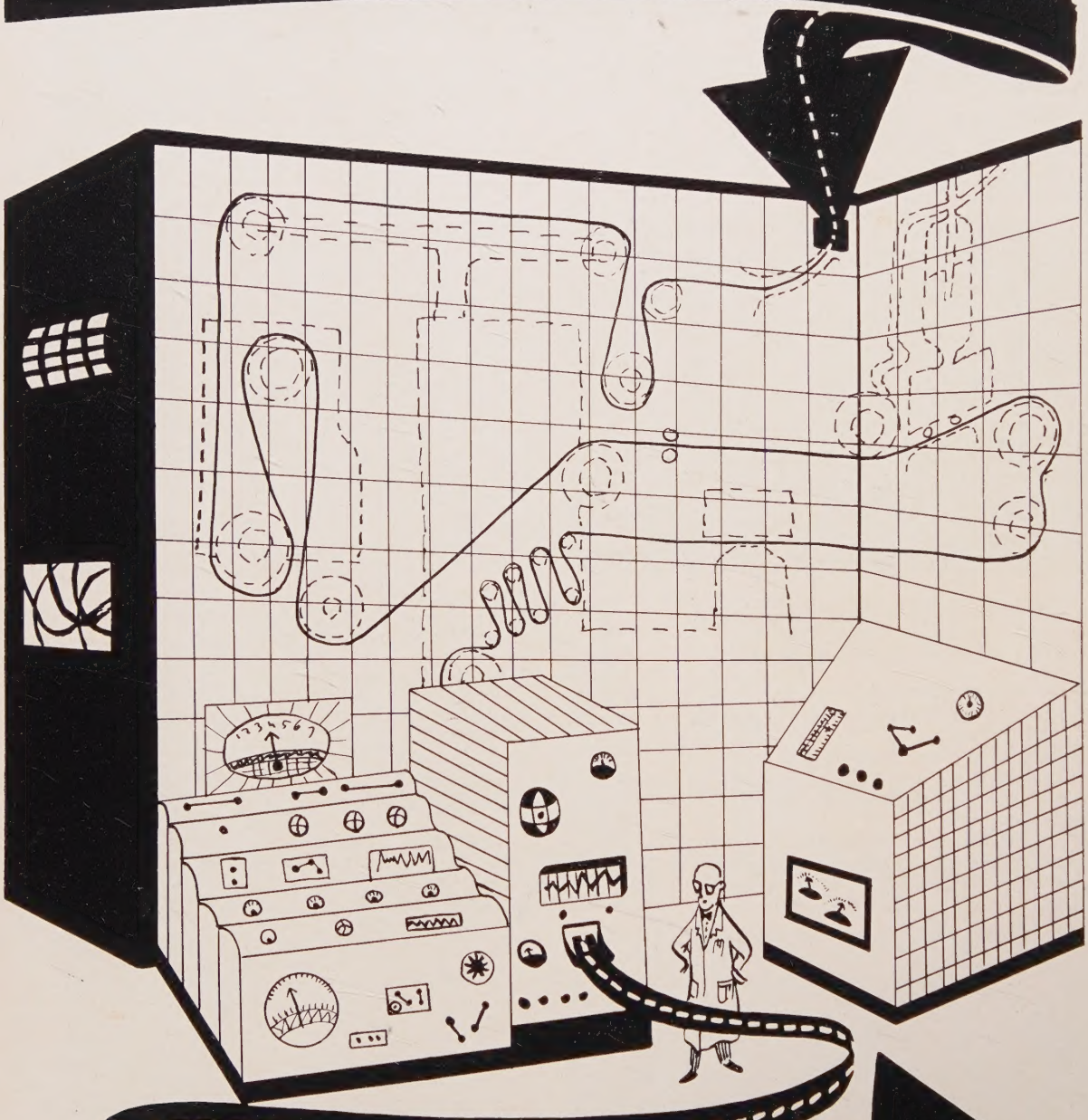

-advertise in nuclear instruments & methods

Go International with your Sales Program today-Write

William F. Baars-Advertising Manager, North-Holland Publishing Company

P.O. Box 103, Amsterdam, The Netherlands

Fewer components . . . greater reliability

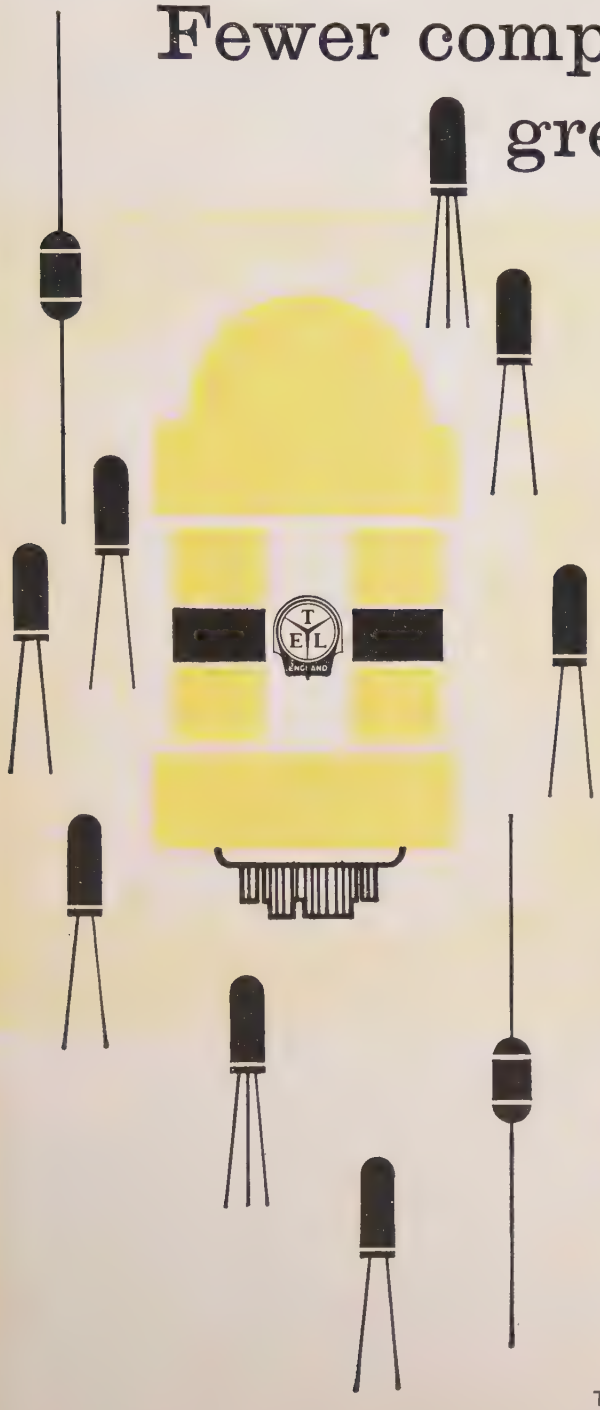

Reliability is not the easiest of terms to define—someone else's definition inevitably takes no account of your own requirements. Yet on one thing all agree, there are only two ways to get greater circuit reliability, one is to choose only the best components and the other to reduce the numbers used. Here difficulties arise for although there are many excellent component alternatives it is only rarely that there becomes available a device which will, without sacrificing performance, allow big component saving.
Trochotron Beam Switching Tubes are such devices.
With the 28V VS.10.K, the Ericsson range has been further extended to give Trochotron reliability at low voltage working and here again component saving is remarkable. For instance, in conventional transistorized decade counters with visual readout, transistors and diodes may number about 90, whereas using the VS.10.K Trochotron this total is reduced by about *ninety percent.*
If, therefore you are concerned with counting, frequency dividing, timing, programming, gating etc., make sure you get greater reliability with fewer components by using Etelco Trochotron Beam Switching Tubes.

28V TROCHOTRON

Heater.....6.3 or 28.0 V
Max. spade to cathode voltage.....30 V
Min. spade to cathode voltage.....24 V
Target current.....2.0 mA nom.
Counting speed.....1 Mc/s

The whole range of Trochotrons is being colour coded for ease of identification. VS.10.G-Red. VS.10.H-Yellow. VS.10.K-Green.

For booklet and leaflets please write to:-

TUBE DIVISION
BEESTON NOTTINGHAM

ETELCO

ETELCO LIMITED · HEAD OFFICE · 22 LINCOLN'S INN FIELDS LONDON W.C.2

DIRECT INSTRUMENTAL ANALYSIS

with *Van de Graaff*® NEUTRON SOURCES

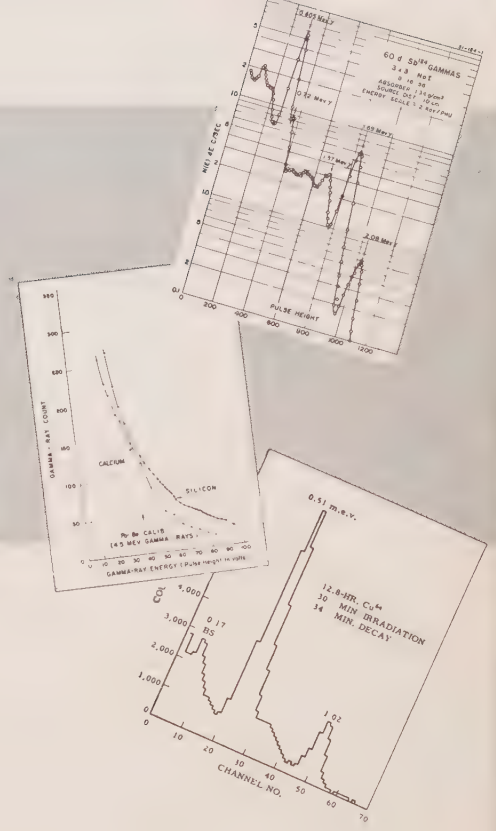

- RAPID
- NON-DESTRUCTIVE
- EASY SAMPLE PREPARATION
- NO REAGENT CONTAMINATION

Sensitive, non-destructive analysis of many elements can be accomplished with great rapidity using a purely instrumental method involving neutron activation. The method requires little sample preparation with complete freedom from reagent contamination. It is useful not only for measurement of trace concentrations, but also for analyses of a number of elements at macro concentrations. Activation plus counting or spectroscopic measurement frequently totals minutes compared with hours using other means.

Intense, controllable neutron fluxes from Van de Graaff accelerators using D-T and D-Be reactions provide the ready means for sample activation.

Standard Neutron Sources	Fast Neutron Flux n/sec-cm²	Reaction	Thermal Neutron Flux n/sec-cm²	Reaction
AN-400	2×10^8	D-T	2×10^7	D-T
AN-1300N	2×10^8	D-T	3×10^8	D-Be
AN-2000N	1.5×10^8	D-T	1×10^9	D-Be
KN-500	2×10^9	D-T	2×10^8	D-T

Model AN-2000 is also suitable for charged particle activation analysis, wear and corrosion studies, and other research programs. For neutron fluxes greater than 10^9 n/sec-cm², other, more powerful neutron sources are also available. Standard neutron sources are priced from $19,000 to $70,000.

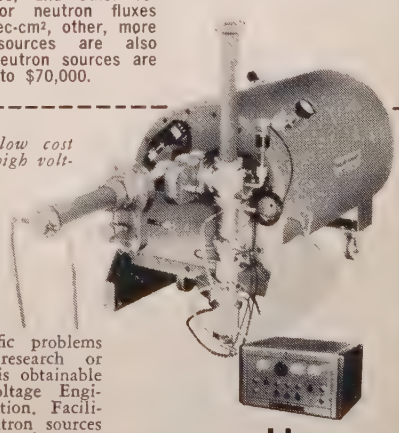

MODEL AN-400 low cost neutron source — high voltage fully insulated.

Help on specific problems in analytical research or process control is obtainable from High Voltage Engineering Corporation. Facilities include neutron sources for experimental work. Write Technical Sales.

High Voltage Servicing Company, Ltd.
London, England

High Voltage Engineering (Europa) N.V.
Amersfoort, The Netherlands

HIGH VOLTAGE ENGINEERING CORPORATION
BURLINGTON, MASSACHUSETTS • U. S. A.
APPLIED RADIATION CORPORATION — HIGH VOLTAGE ENGINEERING (EUROPA) N.V.

NUCLEAR INSTRUMENTS AND METHODS 9 (1960) 245–286; NORTH-HOLLAND PUBLISHING CO.

A ONE-METER-RADIUS IRON-FREE DOUBLE-FOCUSING $\pi\sqrt{2}$ SPECTROMETER FOR β-RAY SPECTROSCOPY WITH A PRECISION OF 1: 10^5

R. L. GRAHAM, G. T. EWAN and J. S. GEIGER

Physics Division, Atomic Energy of Canada Limited, Chalk River, Ontario

Received 28 August 1960

This high resolving power, high luminosity $\pi\sqrt{2}$ spectrometer employs a novel coil geometry which leaves ample room for large, accessible source and detector assemblies. The exact coil diameters and spacings used to achieve axial focusing up to the fourth order were specified by Lee-Whiting after a detailed theoretical study of the electron optical focusing properties of the coil arrangement. Four pairs of precisely manufactured coils generate the cylindrically symmetrical field whose shape closely approximates a $1/\sqrt{r}$ form near the optic circle, $r_0 = 100$ cm. The largest pair has 560 turns per coil and a mean diameter of 395.1 cm. The temperature control arrangements for this all-aluminum spectrometer ensure a constancy in the calibration ratio, gauss cm per ampere, of better than 1 part in 10^5 for electron energies up to 4 MeV. At resolution settings of 0.01%, 0.1%, and 1.0%, transmission values of 0.08%, 0.26%, and 1.1% respectively, can be used. At resolution settings of 0.1%, or better, the luminosity (source area times transmission) is larger than the luminosities of other precision spectrometers. The degaussing system, iron-free building, source, baffle and detector arrangements, current-regulating and measuring systems, automatic controls, and readout system are discussed briefly. Several examples of the performance at resolution settings in the range 0.1% to 0.01% are given which illustrate this instrument's luminosity, ultimate resolution in momentum of 1 part in 10^4, and inherent precision of 1 part in 10^5.

CONTENTS

1. Introduction 246

2. Concept 247

3. Coils 249
   3.1. Theory 249
   3.2. Construction and assembly. 252
   3.3. Experimental field form 255
   3.4. Cooling system 256

4. Baffles and vacuum system 257
   4.1. Baffle calculations 257
   4.2. Construction of baffles. 259
   4.3. Baffle tests 259
   4.4. Vacuum chamber and pumping system 261

5. Degaussing coils and building 261

6. Luminosity calculations 263

7. Sources and detectors 267
7.1. Sources 267
7.2. Counters. 268
7.3. Photographic tests 269

8. Electronic equipment 270
8.1. Regulation and measurement of the spectrometer current 270
8.2. Regulation of degaussing currents. 273
8.3. Counter circuitry 274
8.4. Automatic controls and read-out 275

9. Performance 276
9.1. At 0.1% resolution 276
9.2. Natural line widths 278
9.3. Precision measurements 279
9.4. Limiting resolution 282
9.5. Comparison with other spectrometers 282

10. Acknowledgements. 284

Appendix I. Aberrations 285

Appendix II. Temperature coefficients 286

1. Introduction

In the years since World War II there have been great improvements in the techniques for resolving and accurately measuring nuclear γ-ray and conversion-line energies. To a large extent the improved techniques have stemmed from two groups. One of these, at Pasadena, under the guidance of Professor J. W. M. DuMond, has pioneered the use of crystal-diffraction techniques for measuring the wavelengths of nuclear γ-rays[1]; from applications of this technique have come some of the most accurately determined γ-ray energy values that are currently used as standards[1,2]). The other, in Sweden, associated with Professor Kai Siegbahn, has made important contributions to the technique of conversion line energy measurement by magnetic deflection. The double-focusing $\pi\sqrt{2}$ beta-ray spectrometer was first proposed by Svartholm and Siegbahn[3]) and the air-cored version of this type of instrument described by Siegbahn and Edvardson[4]) has shown a capability for the high precision previously attainable only with uniform-field single-focusing flat spectrometers. Work with this spectrometer has yielded a number of new momentum standards for β-ray spectroscopy[4]) as well as improved values of electron binding energies[5]).

The need for high resolution in nuclear spectroscopy becomes apparent when one realizes that some nuclides give rise to as many as 30 or more gamma transitions.The internal (or external) conversion process, in turn, gives rise to many monoenergetic electron groups for each transition, due to conversion in the K, L_I, L_{II}, L_{III}, M_I etc. shells as well as the Auger lines, some of which are very closely spaced or may overlap electron groups of other transitions. Interpretation of conversion line spectra therefore is often quite

[1]) D. E. Muller, H. C. Hoyt, D. J. Klein and J. W. DuMond, Phys. Rev. **88** (1952) 775.
[2]) P. Bergvall, Arkiv f. Fysik **17** (1960) 125.
[3]) N. Svartholm and K. Siegbahn, Arkiv, f. Mat. Astr. Fys. A **33** (1946) No. 21.
[4]) K. Siegbahn and K. Edvarson, Nucl. Phys. **1** (1956) 137.
[5]) E. Sokolowski, Ark. f. Fys. **15** (1959) 1;
C. Nordling, Ark. f. Fys. **15** (1959) 357;
C. Nordling and S. Hagstrom, Ark. f. Fys. **15** (1959) 431.

ambiguous without adequate resolution. Coupled with this need for good resolution is the need for high precision (i.e., relative accuracy). High resolving power and high precision together can often provide sufficient information for the unravelling and interpreting of nuclear disintegration schemes. These two capabilities make it possible to identify nuclear energy levels using the Ritz combination principle to find the simplest unique set of levels that accounts for the observed lines. High resolving power, also, often enables one to identify uniquely the multipolarity of a given transition from a comparison of the experimental internal conversion line intensity ratios $K:L_I:L_{II}:L_{III}$ etc. with the theoretically predicted ratios[6,7]) for various multipolarities. A third need, which can only be realized after those of high resolution and high precision have been achieved, is that for high absolute accuracy. This is much more difficult since self consistency in precision does not, in general, reveal the presence of systematic errors. These become apparent only when intercomparing a wide variety of measurements by different techniques, preferably in different laboratories. The difficulties that workers in any one laboratory have in making a true assessment of the errors in their measurements are made abundantly apparent in the excellent review of Cohen, Crowe and DuMond[8]). The achievement of high absolute accuracy ultimately becomes essential if one is to be able to compare, meaningfully, the precise measurements by one technique with those by another.

In this paper we report on the design, construction and performance of a large new $\pi\sqrt{2}$ spectrometer. The aim was to realize good intrinsic spectrometer resolution, i.e. $\sim 0.01\%$ in momentum, so that the usable resolution in practice would depend chiefly on other factors. One such factor is natural line width; another is energy degradation due to finite source thickness, which depends upon the specific activity of the source material. Coupled with our desire for good resolution was an equally strong desire for high precision. Brief descriptions of this new type of double focusing spectrometer have already appeared elsewhere[9–12]). The detailed description that follows will reveal some of the precautions that were taken to ensure that the resulting instrument would have the highest inherent capability for precision that it seemed possible to achieve in a double focusing $\pi\sqrt{2}$ spectrometer. The performance to date has shown that these efforts were worth while. As yet, this capability for high precision has not been fully exploited.

2. Concept

The performance requirements aimed for, in designing this precision double focusing beta spectrometer, were an ultimate resolution of $\sim 0.01\%$ coupled with as high a luminosity (i.e. source area times transmission) as possible. We limited our consideration to spectrometers of air-cored design; the magnetic-field strength, and hence the momentum of the focused electrons, in such instruments is directly proportional to the excitation current in the coils, which can be measured with high precision using standard methods. Another equally important reason for an air-cored construction is that the form of the magnetic field generated by an array of current loops is calculable to any desired accuracy; hence, so are the electron orbits. Consequently, the performance of the resulting β-ray spectrometer can be accurately predicted. The desire for high transmission at high resolution led to the choice of double

[6]) M. E. Rose, Internal Conversion Coefficients (North-Holland Publishing Company, Amsterdam, 1958).

[7]) L. A. Sliv and I. M. Band, Coefficients of Internal Conversion of γ-Radiation (1957). The K-conversion coefficients have been issued as Report 57 I.C.C.K.1, University of Illinois; the L-conversion coefficients circulated privately.

[8]) E. R. Cohen, K. M. Crowe and J. W. DuMond, The Fundamental Constants of Physics (Interscience Publishers Inc., New York, 1957).

[9]) R. L. Graham, J. S. Geiger and G. T. Ewan, Bull. Am. Phys. Soc. Series II, **4** (1959) 64; also Bull. C.A.P. **1** (1959)

[10]) R. L. Graham, G. T. Ewan and J. S. Geiger (reported by D. A. Bromley), Proc. Rehovoth Conf. on Nuclear Structure, ed. H. J. Lipkin (North-Holland Publishing Company, Amsterdam, 1958).

[11]) G. T. Ewan, J. S. Geiger, R. L. Graham and D. R. MacKenzie, Can. J. Phys. **37** (1959) 174.

[12]) J. S. Geiger, R. L. Graham and G. T. Ewan, Nucl. Phys. **16** (1960) 1.

focusing, first proposed by Svartholm and Siegbahn[3]), with as large a radius as seemed practicable in order to maximize the usable source area for a given resolution setting. In principle, the usable source area goes up as the square of the design radius, r_0, but so does counter area. Hence this gain may be nullified to some extent by an increase of the counter background. There are, however, certain practical difficulties encountered in preparing narrow, thin sources from pile-produced β-emitters and the fact that the "geometrical resolution" attainable for a source of given width improves linearly with linear dimensions is in itself a compelling reason for a large radius instrument. To quote Rosenblum: "Faites-le grand! J'ai toujours fait des grands spectros et j'ai toujours regretté de ne pas les avoir fait encore plus grands!"[13]). The limiting factors of cost and of magnetic interference from outside sources such as magnetic storms, power lines, laboratory magnets, etc., seemed to place a practical upper limit on the radius of the optic circle of ~ 1 meter, so the convenient "figure" of 100 cm, was chosen as the design value of the optic-circle radius r_0.

There are, undoubtedly, many different configurations of current carrying conductors that will generate, in a given region, a magnetic field whose shape closely approximates a particular desired shape. Siegbahn and Edvarson[4]) have constructed a 30 cm radius precision $\pi\sqrt{2}$ spectrometer which utilizes two concentric solenoids to create between them a field form approximating

$$B_z(r) = B(r_0) \times (r/r_0)^{-\frac{1}{2}}. \qquad (1)$$

This design has the merit of constructional simplicity but it restricts easy access to the source and counter region, an important point to consider if one wishes to measure angular correlations between γ quanta and conversion electrons.

The initial approach used for the instrument described here was to try to create the desired field form with several pairs of current loops of different diameters, spacings, and current strengths. The strength of the axial field component, B_z, in the plane of symmetry for a pair of loops of radius, a cm, and half separations, z cm, were evaluated using the text book formula[14]) or taken from the tabulation of Martin *et al.*[15]). We are indebted to Dr. J. L. Wolfson for the initial computations on suitable coil arrangements. Subsequently other combinations of current loops were examined using large-scale graphical plots of log B_z versus log r on transparent sheets of graph paper for a series of z/a ratios. The plots for two or more z/a ratios were then superimposed and the resultant field obtained by addition. Coil combinations were sought whose combined fields had the $1/\sqrt{r}$ form of equation (1) over an appreciable radial range. In particular, we sought to find an arrangement that did not have coils on or near the plane of symmetry outside the optic circle, so that there would be ready access to both counter and source. Such a design would, also, permit one to swing a scintillation counter assembly about an axis passing through the line source so that γ-ray-conversion-line angular-correlation experiments would be feasible.

This rough graphical analysis for suitable field forms revealed two general arrays of coil combinations that would create a field of approximately the desired form. One array consisted of three pairs of coils whose magnetic fields all reinforced each other on the optic circle. This combination was subsequently treated analytically by Lee-Whiting whose results are briefly summarized in section 3, and was adopted for the spectrometer described in this paper. It resembles to some extent the coil system employed by Moussa and Bellicard[16]).

The other array of coil pairs that would generate a field of the form desired, did so by

[13]) M. S. Mladjenović, Bull. of the Institute of Nuclear Sciences "Boris Kidrich" **6**, No. 95 (1956) 53.

[14]) W. R. Smythe, Static and Dynamic Electricity (McGraw-Hill Book Co. Inc., 1953).

[15]) D. F. Martin, M. M. Hill and M. Harris, U.C.R.L. No. 4531 (1955).

[16]) A. Moussa and J. B. Bellicard, J. Phys. et Rad. **15** (1954) 85A. A more recent spectrometer using the Moussa and Bellicard geometry is described by Q. Baird, J. C. Nall and S. K. Haynes, Bull. Am. Phys. Soc. Series II, **3** (1958) 306.

partial cancellation of the individual contributions to the field strength. A rough calculation showed that the mass of the windings and hence also the power required for this type of coil combination would be about three times as large as for the chosen arrangement. It is possible that this approach might have led to a spectrometer having slightly better electron optical properties; for economic reasons it was not further explored.

As the concept of the spectrometer took shape, a number of factors that could limit the ultimate performance became apparent. In order to utilize a resolution of 0.01%, one needs a precision of 0.001% or better, which means that the current-regulating and -measuring system must have a reproducibility of $\sim$ 10 p.p.m. (parts per million). A low-current, high-voltage regulating system was chosen so that conventional current-control methods (tubes) and measuring methods (standard resistances near 1 ohm with potential differences of $\sim$ 1 volt) could be used. Designing for low currents results in each coil having a fairly large number of turns and hence the ratios of the current strengths in each coil, i.e., turn ratios (all coils connected in series) are available as design parameters which can be adjusted in suitably small increments. The achievement of a precision of $\sim$ 10 p.p.m. also requires dimensional and hence temperature stability of $\sim$ 1°C or better. Thus to take advantage of the inherent proportionality between field strength and coil current it is essential that the coils have good heat transfer and that a constant coolant temperature be maintained. In addition, a large radius r_0 means relatively low magnetic strengths ($\sim$ 10 gauss for 100 keV electrons) and hence the spectrometer calibration is particularly sensitive to small variations of the earth's field. Great care must therefore be taken to cancel or "degauss" this field adequately.

The following sections describe how these various problems in design and control were solved and how this type of double-focusing spectrometer performs in its present state of development.

3. Coils

3.1. THEORY

The design of the spectrometer coils was based on the theoretical calculations of Lee-Whiting and Taylor. These are discussed in detail in their papers[17,18]) and only a brief outline of the theory will be given in this section.

For the circularly symmetric field of a $\pi\sqrt{2}$ double focusing spectrometer the magnetic field strength B_z on the plane of symmetry can be expressed in the form of a Taylor expansion.

$$B_z(r,0) = B_0 \sum_{n=0}^{\infty} a_n \eta^n \qquad (2)$$

where B_0 is the axial component of the field on the optic circle $r = r_0$, $z = 0$, and η is the dimensionless parameter, $(r - r_0)/r_0$, that gives a measure of the radial distance from the optic circle. The coefficient $a_1 = -\frac{1}{2}$ gives first-order focusing for both radial and axial departures of the electron orbits from the optic circle. The coefficient a_2 may be chosen to be $\frac{1}{8}$ which gives second-order radial focusing for orbits having large radial departures from the optic circle, or to be $\frac{3}{8}$ which gives second-order radial focusing for orbits having large axial departures from the optic circle. We have chosen $a_2 = \frac{3}{8}$ for the reasons discussed by Lee-Whiting[17,18]). Briefly these are (a) $a_2 = \frac{3}{8}$ gives zero second-order axial as well as radial focusing for large axial orbit departures (b) the parabolic bending of the image (see section 6) is smaller and (c) the field form is more suitable for photographic recording because of its similarity to a $1/\sqrt{r}$ field form. The reader is referred to Lee-Whiting and Taylor's paper[18]) for a full discussion of the solutions for higher-order coefficients, $a_3, \cdots, a_6$, which are chosen to make zero, successively, higher-order coefficients in the expansion expression for radial aberration due to large axial orbit departures. The values for a_1 to a_6 are summarized in table 1. Equation (2) with these

[17]) G. E. Lee-Whiting and E. A. Taylor, Can. J. Phys. **35** (1957) 1.

[18]) G. E. Lee-Whiting and E. A. Taylor, On the Design of an Iron-Free $\sqrt{2}\,\pi$ β-Spectrometer (Chalk River Report CRT-668, Oct. 1956).

TABLE 1
Values of magnetic field expansion coefficients, a_n

n	a_n Optimum field form	a_n $1\sqrt{\bar{r}}$ field form	Tolerance Δa_n		a_n Original proposal [b]	a_n Present coils [c]
			$T = 0.3$ [a]	$T = 0.15$ [a]		
0	1.0000	1.0000	—	—	+ 1.0000	+ 1.0000
1	— 0.5000	— 0.5000	— 0.0013	— 0.0013	— 0.4998	— 0.50006
2	+ 0.3750	+ 0.3750	+ 0.0004	+ 0.0017	+ 0.3748	+ 0.37517
3	— 0.2986	— 0.3125	+ 0.0063	+ 0.025	— 0.2994	— 0.2983
4	+ 0.2400	+ 0.2734	— 0.0046 [d]	— 0.074	+ 0.2411	+ 0.2392
5	— 0.2017	— 0.2461	— 0.050	— 0.80	— 1.8491	— 1.889
6	+ 0.1768	+ 0.2256	+ 0.075	+ 4.80	+ 0.9888	+ 1.024
7	—	—	—	—	+ 2.813	+ 2.805
8	—	—	—	—	— 8.152	— 7.861

[a]) Deviations from optimum values that cause an increase of $1 \cdot 10^{-4}$ in the radial intercept at the image plane for an orbit having source-departure-angle parameters of $H = 0.025$ and the value of T indicated.

[b]) Coil dimensions are given in table 3.1.

[c]) Coil dimensions are given in table 3.2.

[d]) The value for Δa_4 quoted in reference 17 is in error.

coefficients defines the "optimum" field form for the purposes of this paper although we are aware that the true optimum field form should include seventh- and higher-order terms which have yet to be evaluated theoretically. It is useful to know how accurately these coefficients must be matched in order to keep the aberrations acceptably small. Tolerances, Δa_n, are summarized in table 1 for two cases typical of operation at a resolution near 0.01% in momentum. Their significance is discussed in the footnote.

In his discussion of the field form generated by an array of current loops, Lee-Whiting has found it more convenient to describe the magnetic field in terms of an expansion of the vector potential A near the optic circle

$$[rA(r,\tau)]_{r\ r_0} = r_0 A_0 + B_0 r_0^2 \sum_{\text{even } m=2,4}^{\infty} k_m \frac{\tau^m}{m!} \qquad (3)$$

together with a radial derivative expansion of the form

$$\left[\frac{\partial}{\partial r} rA(r,\tau)\right]_{r=r_0} = B_0 r_0 \sum_{\text{odd } m=1,3}^{\infty} k_m \frac{\tau^m}{(m-1)!} \qquad (4)$$

where $\tau = z/r_0$ is the axial departure from the plane of symmetry and A_0 is the vector potential at the optic circle ($\eta = 0$, $\tau = 0$). The new expansion coefficients k_m ($m = 1,2,\cdots$) have been derived directly from the equivalent set a_n, and are listed in table 2. For convenience the representation of equations (3) and (4) will be used in discussing the coil parameters.

In our spectrometer as originally conceived three pairs of coils were to be used to generate the required field form. Such an array has 7 degrees of freedom or parameters that can be varied independently in attempting to fit the k_m coefficients of the vector potential. These parameters are r_1/r_2, r_1/r_3, I_1/I_2, I_1/I_3 and z_1/r_1, z_2/r_2, z_3/r_3 where r is the radius of the coil, I is the current in the coil, and z the axial half-separation of the coil. Practical limitations, on the positioning of the coils, in order to have accessibility to the spectrometer, and on sizes of coils for economic reasons, made it impossible for Lee-Whiting to fit more than four vector potential coefficients, $k_2, \cdots, k_5$ with k_1 defined as unity. The mathematical procedure used to match coil parameters has been fully described[18]). He first assumed that the coils are current loops and calculated the coil parameters needed to match $k_1, \ldots, k_5$ exactly. He then considered the effect of the finite size of the current-carrying elements of the actual coils as they would be manufactured. This gives a new set of coefficients $k_1, \ldots, k_5$ which are slightly different than the

TABLE 2
Values of vector-potential expansion coefficients k_m

m	k_m Optimum field form	Δk_m Tolerance [a] $T = 0.15$	k_m Original [b] proposal	k_m Present [c] coils
1	+ 1.0000	—	+ 1.000	+ 1.000
2	+ 0.5000	+ 0.0013	+ 0.49987	+ 0.50006
3	— 0.2500	— 0.0033	— 0.2497	— 0.2503
4	— 0.5417	+ 0.15	— 0.5470	— 0.5394
5	+ 0.927	— 2.2	+ 0.9438	+ 0.9111
6	+ 3.56	+ 97.	+ 194.2	+ 206.0
7	— 15.4	— 3500.	— 7.0	— 18.4

[a]) Defined in note [a]), table 1. [b]) See table 3.1. [c]) See table 3.2.

optimum values. He then readjusted the coil parameters to again match the optimum parameters. In all practical cases considered so far, the corrections for finite size turn out to be quite small. As a final step in optimizing coil parameters he took the measurements of the actual radii and finite size, after the coils were manufactured, and recalculated the half-separations to give the best match to $k_1, \ldots, k_5$.

The question of manufacturing tolerances on the coil parameters has also been approached analytically[18,19]). As a first step Lee-Whiting computed tolerances Δk_m which would give rise to a specified degree of image broadening if the k_m term only were mismatched. The Δk_m values in table 2 correspond to a departure that would cause a basal broadening of about one-quarter line width at a resolution setting of $\sim 0.01\%$. He assumed that the maximum axial departure angle at the source, between the orbits and a tangent to the optic circle, would be $\varphi_z \simeq 8.5°$. For convenience in his mathematical treatment, he defines the departure-angle parameter $T = \sqrt{2} \tan \varphi_z$; the limit chosen thus corresponds to $T_0 = \sqrt{2} \tan \varphi_z = 0.15$. As will be seen below, we can use a slightly larger value of T ($T_0 \simeq 0.2$) for the maximum axial-departure parameter but not as large an axial-departure parameter as would be permitted had we matched the optimum field form; larger values of T_0 are precluded because of the mismatch of k_6 and higher terms. This appears to be a limitation inherent in the present current-loop approach. Knowing the permissible ranges of k_m ($m = 1$ to 5) the effects of five possible manufacturing or assembly errors were considered: (i) radial dilatation or expansion of one member of a coil pair, (ii) vertical displacement of one member, (iii) asymmetrical displacement of one member with respect to the

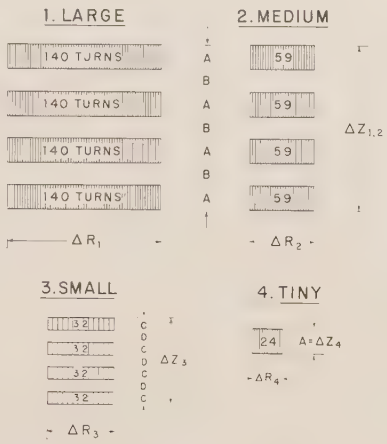

Fig. 1. This figure shows in cross section the arrangement of the current-carrying elements of the coils used in this spectrometer. All coils were wound with aluminum ribbon with the number of turns shown in the figure. The ribbon used in making coils numbers 1, 2, and 4, was 1.200 in. wide by 0.060 in. thick and that used in making coils number 3 was 0.600 in. wide by 0.120 in. thick. The other dimensions in the figure are $A = 3.048$ cm, $B = 2.652$ cm, $C = 1.524$ cm, $D = 1.382$ cm, $\Delta R_1 = 19.792$ cm, $\Delta R_2 = 8.334$ cm, $\Delta R_3 = 8.545$ cm, and $\Delta R_4 = 3.393$ cm. These dimensions were used in making the finite-size corrections discussed in section 3.1. The spaces B and D are occupied by the cooling-water channels which are not shown here.

[19]) G. E. Lee-Whiting, private communications 1955 to 1957.

axis, (iv) tilt of one member and (v) elliptical distortion. These represent the most important coil imperfections likely to occur in the construction process and serve to give a fairly clear idea of the tolerances required for achieving 0.01% resolution.

The β-ray spectrometer, as conceived initially, was to have had only three pairs of coils. The coils were each to have been constructed in four sections using 1.000 in. by 0.040 in. copper ribbon in large and intermediate coils and using 0.500 in. by 0.080 in. copper ribbon in the small coils. The conductor cross-section showing spaces left for cooling-water channels is similar to those shown in fig. 1. The manufacturing specifications for this coil arrangement are summarized in table 3.1. The properties of such a spectrometer have been considered theoretically in great detail[18]) and served as the basis for the design of the baffle system (section 4).

The coil arrangement finally adopted is a slight variation of the original choice. It consists of four pairs of coils rather than three and uses larger conductor cross-sections. The specifications for this arrangement are summarized in table 3.2. The changes were made for two reasons, neither of which reflect on the electron optical properties predicted for the first arrangement. The tiny pair of coils was added to create a small zero-field region at the centre of the spectrometer where a magnetometer could be placed to monitor the earth's field. The parameters of these small coils were chosen to make zero the second-order derivatives of the spectrometer field at the centre, $r = 0$, $z = 0$, and simultaneously the parameters of the other three pairs were recomputed to match again the vector potential expansion parameters k_1 to k_5 at the optic circle $r_0 = 100$ cm. The larger conductor cross-section resulted from a desire on the part of the manufacturer, Canadair Limited (Montreal, Canada), to use aluminum which has a higher specific resistance than copper. The cross-section of the entire spectrometer is shown in fig. 2. Only the outline of each coil assembly, including the cooling water channels, is shown here.

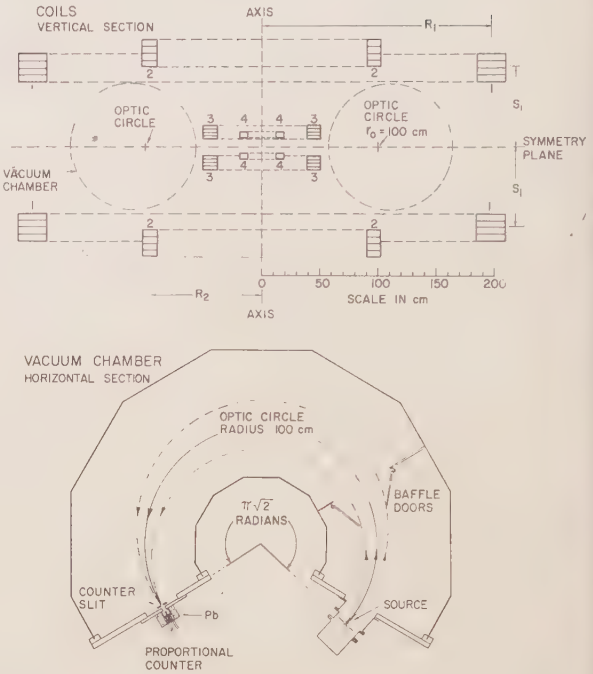

Fig. 2. The upper part of the figure shows a vertical section of the spectrometer coils and vacuum chamber in the east-west direction. The diagram is to scale. The current flow in coils 3 and 4 is opposite to that in coils 1 and 2 so that all field components add on the optic circle. The coil parameters are listed in table 3.2. The lower part shows a plan section of the vacuum chamber. The defining baffles which limit the radial aperture are hinged on shafts which extend up through vacuum seals. Each shaft is equipped with a long lever arm and calibrated scale for external adjustment. The defining slit in front of the counter is also externally adjustable by means of a calibrated dial. Not shown are vacuum lock doors in front of both source and counter assemblies. These make it possible to change the source or detector assembly in a matter of minutes. A 30-foot-long, 20-inch-diameter pumping line connects the chamber to an Edwards F903 diffusion pump and a Kinney DH130 roughing pump.

3.2. CONSTRUCTION AND ASSEMBLY

The detailed mechanical design and construction of the coils, to the fine tolerances required, and of the support structure, was carried out by the Nuclear Division of Canadair Ltd., Montreal. The final physical arrangement of the spectrometer is shown in fig. 3.

As indicated in section 2 above, it was decided to use relatively small coil currents (< 40 amperes) and relatively large voltage drops across the windings. For the coil parameters of table 3.2 a current of 40 amperes at about 500 volts is

TABLE 3.1
Original proposal for coil dimensions [a])

	(1) Large pair	(2) Medium pair	(3) Small pair
Number of sections	4	4	4
Turns per section	140	59	— 32[f])
Mean[b]) radii of windings (cm)	196.971 ± 0.200	96.601 ± 0.100	45.060 ± 0.076
Maximum difference between mean radii of assembled coils (cm)	0.076	0.038	0.038
Maximum radial deviation Δr from circularity (e.g., elliptical distortion) (cm)	0.038	0.025	0.025
Mean[b]) half separation, i.e., axial distance z from symmetry plane (cm)	66.450	79.220	12.560
Maximum deviation Δz from mean (cm)	0.038	0.025	0.025
Radial depth of windings [c]) (cm)	16.51	6.96	7.54
Axial length of windings [c]) (cm)	17.8	17.8	8.9

TABLE 3.2
Coil dimensions in cm for present instrument [d])

		(1) Large pair	(2) Medium pair	(3) Small pair	(4) Tiny pair
Number of sections		4	4	4	1
Turns per section		140	59	— 32[f])	— 24[f])
Mean[b]) radii of windings (cm)	Requested	197.560 ± 0.200	96.690 ± 0.100	45.060 ± 0.076	15.460 ± 0.076
	Achieved	197.552	96.670	45.061	15.467
Difference in mean coil radii (cm)	Requested	< 0.076	< 0.038	< 0.038	< 0.019
	Achieved	$\lesssim$ 0.032	$\lesssim$ 0.022	$\lesssim$ 0.008	$\lesssim$ 0.007
Deviation from circularity Δr (cm)	Requested	< 0.038	<0.025	< 0.025	< 0.013
	Achieved	$\lesssim$ 0.027	$\lesssim$ 0.023	$\lesssim$ 0.008	$\lesssim$ 0.008
Mean[b]) halfseparation z from symmetry plane (cm)	Requested[e])	66.770 ± 0.076	79.740 ± 0.051	12.780 ± 0.051	8.869 ± 0.025
	Achieved[g])	66.838	79.771	12.794	8.887
Maximum deviation Δz from mean (cm)	Requested	< 0.038	< 0.025	< 0.025	< 0.025
	Achieved	$\lesssim$ 0.038	$\lesssim$ 0.035	$\lesssim$ 0.028	$\lesssim$ 0.030
Radial depth of windings[c]) (cm)		19.792	8.334	8.545	3.393
Axial length of windings[c]) (cm)		20.148	20.148	10.242	3.048

[a]) Using copper conductors of cross-section 0.258 cm² (0.040 sq. in.).
[b]) Arithmetic mean.
[c]) For arrangement of conductors and details of dimensions, see fig. 1.
[d]) Using aluminum conductor of cross-section 0.389 cm² (0.060 sq. in.).
[e]) These z values are appropriate to the requested mean radii and not to those achieved during manufacture of the coils.
[f]) Minus sign indicates that the current flow direction is opposite to coils 1 and 2.
[g]) These mean z values were adjusted to match those requested after the coils were wound and the achieved mean radii were known.

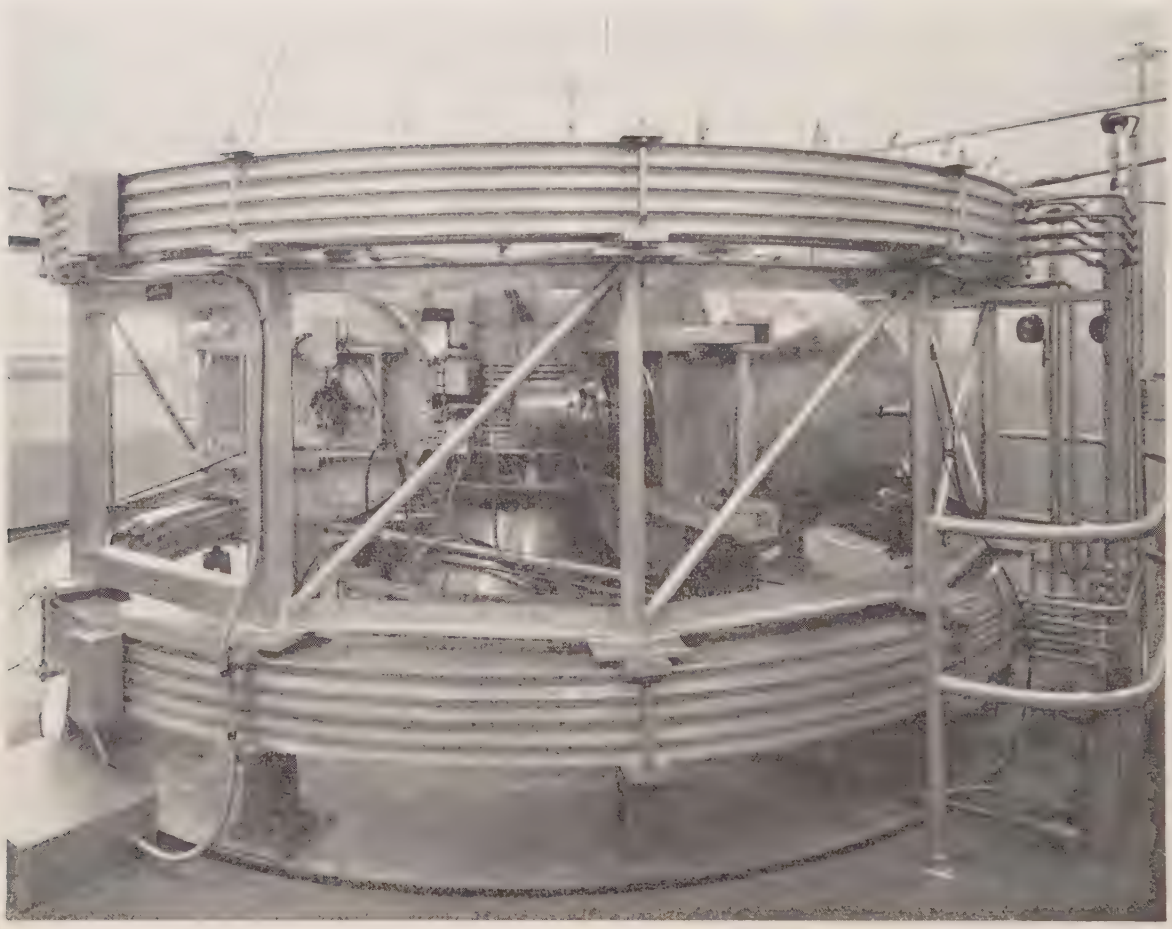

Fig. 3. A photograph of the completed spectrometer. In the foreground are seen the largest coils which have a mean diameter of 3.951 meters and a mean separation of 1.337 meters. The instrument is housed in a frame building (see also fig. 9) which was specially constructed for this purpose. The earth's magnetic field is cancelled to $< 10^{-3}$ gauss in the region of the electron orbits by an array of large degaussing coils, some of which are visible in the background.

required to focus 4 MeV β-rays. In order to meet the simultaneous demand for good electrical insulation ($> 10^7$ ohms) and good heat transfer (max. temp. rise in windings $< 6°$C), a design study was carried out by Canadair Limited. This yielded a practical method of bonding 0.005 in. layers of Mylar tape, as the electrical insulation, to the aluminum conductors and cooling channels. A prototype intermediate-coil section was manufactured and tested to assess the soundness of the proposed method. At a steady current of 40 amperes the measured mean rise in the winding temperature was found to be 3.4°C. The insulation resistivity at $\lesssim 50\%$ humidity was found to exceed 10^9 ohms.

The individual coil sections (see fig. 1) consist of a single-layer winding of aluminum ribbon conductor interleaved with 0.005 in. etched Mylar tape as insulation. The formers on which the large, intermediate, and small coils are wound were made by casting a 0.75 in. thick ring of epoxy-resin insulation around a machined aluminum ring. When set, the epoxy-resin ring was machined to the desired inside winding diameter on the 10 ft. boring mill on which the coils were subsequently wound. The aluminum ribbon was interleaved with etched Mylar tape, 0.005 in. thick, which had been sprayed on both sides with quick-setting epoxy-resin cement. The outer radius of the winding was monitored continuously during the winding process with a dial-gauge micrometer; the readings were recorded every

60°. Deviations from the desired radial depth were corrected during the winding process by changing the winding tension and, where necessary, by adding an extra thickness of the Mylar interturn insulation. The mean diameter of the conductors in each coil section was determined in this way with an accuracy of ~ 0.010 in. Upon completion, each section was tested for turn-to-turn shorts, and mounted on to its cooling water channel. Two 0.005 in. thick layers of etched Mylar sheet bonded with epoxy resin cement serve as the electrically insulating heat-transfer medium. After heat-transfer and insulation tests, the coils were assembled in groups of four sections selected so as to match the mean winding diameters of the two coil assemblies in each pair as closely as possible. The resulting dimensions are summarized in table 3.2. The construction of the tiny coils is similar to that of the other coils, the chief difference being that each has only one section. The former for these tiny coils is an integral part of the water channel.

The installation, testing, assembly and alignment of the coils was carried out under the supervision of Canadair Limited. The alignment was a painstaking, tedious, but nevertheless purely mechanical procedure involving the use of a temporary overhead crane, plumb bobs, dumpy levels, stick micrometers etc. After the installation was completed an independent check on the measurements was made to show that all specified tolerances had been achieved. Fig. 3 shows a view of the assembled spectrometer in the specially constructed building (see section 5) after removal of the installation equipment and completion of the floor and end wall of this part of the building.

3.3. EXPERIMENTAL FIELD FORM

To demonstrate the manner in which the required field form is generated, fig. 4 shows the calculated contribution of each pair of coils to the total field strength on the plane of symmetry as a function of radial distance from the symmetry axis. For convenience in computing the individual contributions of the four pairs of coils it was assumed that each coil was a current loop, i.e., finite size corrections were neglected. These corrections are small and not detectable on the plot.

The field form has been measured experimentally using a Serson flux-gate magnetometer[23]). The compensating currents needed to produce a null magnetometer signal were measured to a precision of about 1 in 10^3 using a Weston Laboratory standard milliammeter; a variety of spectrometer currents were used in order to keep the magnetometer currents near the maximum of this meter. These readings were normalized to the computed field strength at 100 cm radius and are plotted in fig. 4. No readings could be taken for $r < 60$ cm since the 4 in. long magnetometer head was too large to pass between the two small coils (see fig. 2). We note that the field has the desired shape from approximately $r = 60$ cm to 140 cm. The slight departure of experimental points from the predicted line is not considered to be significant since (a) finite winding-size corrections are neglected and (b) the magnetometer head is not a point detector but gives (in some sense) a measure of the average field intensity over its 10 cm long axis.

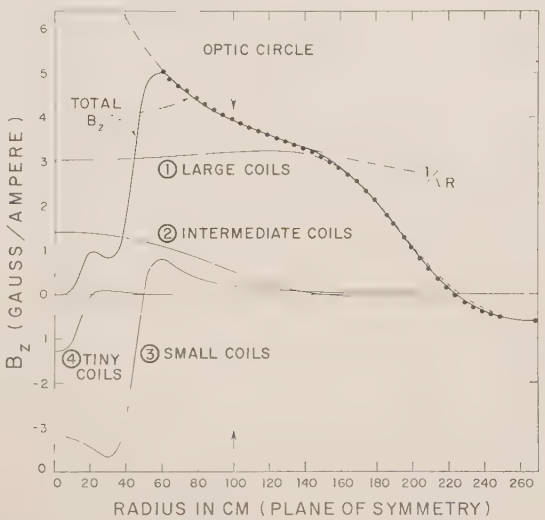

Fig. 4. This displays the computed spectrometer magnetic-field form along the plane of symmetry, and shows the contributions due to individual pairs of coils. The experimental points are magnetometer readings normalized to the total B_z curve near the optic circle. The tiny coils (4) were incorporated to make the field zero at the central symmetry point so that a magnetometer could be placed at this location to monitor the earth's field correction and also sense possible drifts in coil parameters which would result in a non-zero field at this point (e.g., shorted turns, overheating, etc.)

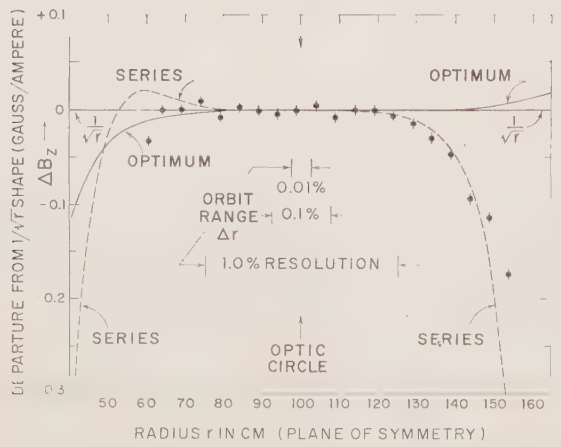

Fig. 5. Various spectrometer field forms discussed in the text are compared by subtracting a $1/\sqrt{r}$ form, normalized at $r = 100$ cm, from each before plotting on the expanded B_z scale. The curve labelled "optimum" is the 6th-order series expansion deduced by Lee-Whiting for the $\beta = a_2 = \frac{3}{8}$ case. The dashed line labelled "series" is that appropriate to the spectrometer described in this paper and was calculated from the series expansion using the coefficients a_n up to the 8th order listed in the last column of table 1. The error bars on the experimental points indicate the estimated relative accuracy in the magnetometer measurements.

Fig. 5 shows a more detailed comparison of the measured field with the theoretically desired field in the region of the electron orbits. In order to expand the ordinate scale a field of the form $1/\sqrt{r}$, normalized at $r = 100$ cm, has been subtracted from the field shapes being considered. This convenient method for expanding the scale was adopted since the difference between the $1/\sqrt{r}$ field form and the shapes being considered is very small. The experimentally observed field is here compared (1) with the sixth-order optimum field form calculated by Lee-Whiting[17]) and (2) the field form predicted by a series expansion to the eight order for the coils used (column 7, table 1). Over the region of orbits giving rise to image breadths of 0.01%–1% in momentum the fit of the measured field to the "optimum" field is good. While the accuracy of these measurements is not sufficiently good to establish all the coefficients of the expansion, the absence of detectable slope on this plot indicates $a_1 = -0.500 \pm 0.008$.

3.4. COOLING SYSTEM

A closed circuit cooling water system was designed to keep the coil temperatures essentially constant during normal use. Since the expansion coefficient of aluminum is 2.4×10^{-5} per °C and a calibration reproducibility of $\sim 1 \times 10^{-5}$ was desired, a temperature stability of $\lesssim 1$°C seemed necessary. A detailed theoretical analysis of the temperature dependence of the various spectrometer components is summarized in table 4. (See Appendix II for calculation.) It should be noted that if all coil temperatures rise 1°C simultaneously the predicted calibration shift is very small since the individual contributions

Table 4
Analysis of the temperature dependence of the calibration constant.
Fractional change in $B\rho$ per ampere per °C multiplied by 10^6 [a])

Effect	Coil Pair	1	2	3	4	All
Expansion of coils	Radial: $\Delta B/B_0$	— 10.45	+ 8.86	+ 2.85	+ 0.04	+ 1.30
	Axial separation: $\Delta B/B_0$	— 10.63	— 2.52	— 0.26	— 0.002	— 13.41
Expansion of optic circle (vacuum chamber)	Decrease in field: $\Delta B/B_0$	—	—	—	—	— 12.0
	Increase in radius: $\Delta r/r_0$	—	—	—	—	+ 24.0
Expanding scale of entire instrument: $\Delta B\rho/B_0\rho_0$ = Sum =						— 0.11[b])

[a]) Since the entire instrument is made of aluminum and its alloys, it is assumed that the expansion coefficient of $+ 24 \times 10^{-6}$ per °C applies to all elements.

[b]) This should theoretically be zero under assumption [a]). The reason for the small discrepancy is discussed in the text. The sum would not be zero if the different elements had different expansion coefficients.

almost cancel. An experimental test in which the temperature of all coils was raised about 7 °C above normal operating temperature has shown that the shift in calibration is less than 1 part in 10^5 in agreement with the predictions. However, the temperature increases due to resistive heating in the various coil sections are not exactly the same. With the full flow of cooling water, tests have shown that the mean temperature rise in the windings with 40 amperes current is for (1) large coils, $\sim 3.2°$C, (2) intermediate coils, $\sim 2.3°$C, (3) small coils, $\sim 1.7°$C, and (4) tiny coils, $\sim 3.0°$C. If we assume that the expansions of the windings are not restrained by the mechanical bonds to the cooling channels, these rises, together with the radial expansion coefficients for the coils shown in table 4, suggest that the calibration constant, (expressed in gauss cm per ampere) at 4 MeV would change by -8.1×10^{-6}. However, there is a mechanical restraint of perhaps a factor of two. Moreover in most experiments, which involve β-ray energies less than 2 MeV, the resistive heating, due to the smaller coil currents $I < 25$ amperes, is less than half that at 4 MeV where $I \approx 40$ amperes. Thus in normal practice we do not expect the calibration constant to vary more than ~ 3 parts in 10^6.

The cooling system consists of a circulating pump (75 gallons per minute), a heat exchanger, and an aluminum pipe distribution system to the various coils. The latter has been designed to give roughly equal water velocities in each cooling channel (turbulence is required for good heat transfer) and roughly equal increases in water temperature in the various cooling channel branches. The initially pure water used in the closed circuit is continuously purified by an ion-exchange unit in order to minimize corrosion. The heat exchanger is servo-regulated to maintain the closed-circuit water temperature within $\pm$ 0.6°C of any desired pre-set value in the range 18–28°C. The temperature is monitored continually by a chart recorder which also provides the servo system correction signal.

[20]) G. E. Lee-Whiting, private communication May 1960.

4. Baffles and Vacuum System

4.1. BAFFLE CALCULATIONS

Perhaps the most important advantage of an aircored spectrometer is that the field form is calculable and hence so are the electron trajectories. In discussing theoretical orbits we use the notation of Lee-Whiting, who uses the optic circle as the reference basis. The trajectories leave the source at angles defined by the parameters $H = \sqrt{2} \tan \varphi_r$ and $T = \sqrt{2} \tan \varphi_z$ where φ_r and φ_z are the radial and axial departure angles in radians measured with respect to the tangent to the optic circle at the source position. The radial and axial distances between the trajectory and the optic circle at any value of the parameter $\psi = \theta/\sqrt{2}$ (θ in radians) are expressed by the dimensionless parameters $\eta(\psi) = (r - r_0)/r_0$ and $\tau(\psi) = (z - z_0)/z_0$. In a perfect double-focusing instrument the orbits leaving a point source on the optic circle at $\eta(0) = \tau(0) = 0$ should come to a focus on the optic circle at the point $\eta(\pi) = \tau(\pi) = 0$, i.e., at the angle $\theta = \pi\sqrt{2}$ radians where $\psi = \pi$. Non-zero values of $\eta(\pi)$ or $\tau(\pi)$ are the radial and axial aberrations respectively. Theoretical expressions for $\eta(\pi)$ and $\tau(\pi)$, which are valid for small departure angles, H and T, and the coil system of table 3.1, are given in Appendix I. More accurate orbit computations for the actual coil system used (table 3.2) have recently been carried out[20]). The differences between these new aberration values and those predicted by the expressions in Appendix I are small and have yet to be assessed in detail. The following discussion is in terms of the aberration formulae that were used in the original design.

The baffle apertures which can be used with the air-cored spectrometer of table 3.1 are displayed in fig. 6. To a good first approximation the quantities H and T defining the source departure angles also represent the maximum distances of departure of the electron orbits from the optic circle in units of r_0, i.e., $H \simeq \eta(\pi/2)$ and $T \simeq \tau(\pi/2)$. The permissible departure-angle parameters shown in fig. 6 were calculated from the theoretical expression for radial aberrations $\eta(\pi)$ given in Appendix I for monoenergetic electrons

leaving a point source on the optic circle. The effects of axial aberrations and source dimensions are neglected here since they are of secondary importance in the baffle calculations. They are discussed below in section 6. The permitted ranges of departure angles are those that give rise to negative radial aberrations. For example, the combinations of H and T that give a constant aberration of $\eta(\pi) = -4 \times 10^{-4}$ are the two contour lines labelled 0.01%. Since the instrumental dispersion factor is four i.e., the images of electron groups having momenta p and $p + \Delta p$ have a radial separation of $4(\Delta p/p) \times r_0$, the aberration $\eta(\pi) = -4 \times 10^{-4}$ is that which gives an apparent shift in momentum of $\Delta p/p = 0.01\%$. The double cross-hatching shows those departure angles that give $\eta(\pi) > 0$. Since $\eta(\pi)$ goes positive quite rapidly in these regions it is not practical to attempt to make any use of these orbits. These "forbidden" regions appear to be a consequence of failing to match the optimum values for the k_6 and higher-order coefficients in the vector-potential expansion, equations (3) and (4), and would recede as the spectrometer field approached the optimum field form.

The solid angle subtended at the source, Ω (steradians), that can be used at a given resolution is proportional to the area between the appropriate contours in fig. 6. From this one can deduce the transmission, $T \simeq \Omega/4\pi \approx$ area$/8\pi$, where the area is measured in the units shown on the abscissa and ordinate scales. From this relation and fig. 6, we deduce that the usable transmissions at 0.01%, 0.1%, and 1.0% resolution are $\sim$ 0.08%, 0.26%, and 1.1%, respectively. These are considerably smaller than would be permitted for an "optimum" field form; in a plot corresponding to fig. 6 the contours for the optimum field form would have essentially the same spacings as shown at $T = 0$, but would extend to higher values of T before bending. The imperfections in our practical field form limit the usable solid angle very considerably at good-resolution settings and to a lesser degree at poorer-resolution settings.

Fig. 6 was not expected, originally, to give accurate predictions for the spectrometer described in this paper for two reasons. First, the field form for which the computations were made (Appendix I) is for a coil array having slightly different parameters (see table 3). Secondly, the computations did not take into account eighth- and higher-order terms in the expansions for the vector potential [equations (3) and (4)]. The newer and much more accurate orbit calculations show that the shapes of the iso-aberration

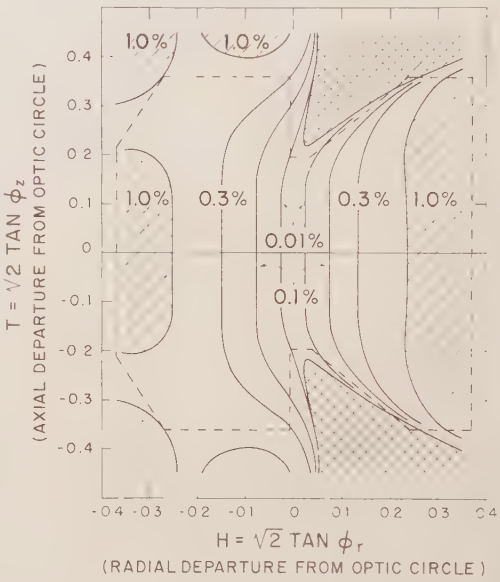

Fig. 6. This graph gives the permissible range of source-departure angles, ϕ_r and ϕ_z, permitted for various radial-aberration values in the image plane. The plot here is in terms of the parameters, defined by Lee-Whiting $H = \sqrt{2}$ tan ϕ_r and $T = \sqrt{2}$ tan ϕ_z, and is intended to show the baffle apertures that can be used with this type of $\pi\sqrt{2}$ spectrometer. The constant-aberration contour lines labelled 0.01% correspond to orbits which intercept the image plane at a radial distance r_0 $(1 - 0.0004)$, when the $H = T = 0$ orbit intercept it at r_0 (optic-circle radius); this is the definition of a radial aberration, $\eta(\pi) = 4 \times 10^{-4}$, and corresponds to an image broadening of 0.01% in momentum (see Appendix I). The doubly cross-hatched regions indicate orbits for which the intercept on the image plane exceeds r_0, i.e., $\eta(\pi)$ is positive. The transmission is roughly proportional to area A on this plot, $\Omega/4\pi \simeq (8\pi)^{-1} A$, where A is measured in the units shown on the abscissa and ordinate. The distortion of the contours and the prominence of the forbidden doubly cross-hatched regions illustrate the fundamental limitation of this type of air-cored spectrometer. The dashed lines show the approximate limits allowed by the fixed baffle in the present spectrometer. The edge of the inner baffle door is shaped to approximate the 0.3% contour. The outer door has a straight edge. While this plot is not applicable in detail to the present instrument (table 3.2) the differences are small.

contours shown in fig. 6 are qualitatively correct and that this figure gives a good idea of the performance to be expected at high resolving power. Since no better theoretical information was available at the time of construction it was used as a guide in the design of the present baffle system.

4.2. CONSTRUCTION OF BAFFLES

In the instrument described here we have incorporated a fixed baffle plate at $\theta \simeq 72°$ from the source plane (see fig. 2) which limits the maximum source-departure parameters, H and T, to approximately the limits shown by the dashed lines in fig. 6. On this plate are mounted adjustable baffle doors on vertical hinges for setting the radial (H) limits. The doors have parallel straight edges which touch each other and the optic circle, $H = 0$, when closed. To the inner door is fastened a shaped countour plate which extends the upper and lower parts of the door edge where $T \gtrsim 0.2$ so that it overlaps the outer door when both are closed. The shape was chosen to match the 0.1% and 0.3% contours approximately when the inner door is opened to the appropriate angles. A more complex method of adjusting the baffle aperture to match all the theoretical contours might be worth considering when the new set of more accurate orbit computations is completed and analysed and the conclusions are tested by experimental measurements of aberrations as a function of H and T. An improved baffle system should permit the use of somewhat larger solid angles for a given resolution than is now possible, particularly at resolution settings of $> 0.1\%$.

4.3. BAFFLE TESTS

In fig. 7 are shown the results of a series of experiments designed to test the suitability of the present baffle-door system and to give some idea of the validity of the theoretical computations that led to fig. 6. Ideally, the tests should be made with an infinitely narrow source and detector. In order to obtain acceptable counting rates the source used was a sublimed deposit of Cs^{137}, 0.4 mm wide by 2 cm high on 0.8 mg/cm² Al foil The counter slit was adjusted to a width of 2 mm. The K-conversion line of the 661.6 keV transition in Ba^{137} was used for these tests. The data in the upper part of fig. 7 show conversion-line profiles at various outer baffle-angle settings. This is equivalent to having all orbits between the dashed lines in fig. 6, with $H \leq 0$, masked off and allowing only orbits with different positive H_0 limits to be focused. The data in the lower half of fig. 7 show the corresponding behaviour when only the inner baffle door is opened allowing orbits having negative H values to be transmitted. The dependence of line shape upon baffle door angles is qualitatively what one would predict. Increasing either H_0 limit adds to the low momentum side of the line profile without affecting its shape near the peak.

The line profiles in fig. 7 differ predictably from those calculated by assuming that only the leading term $-\frac{2}{3} H^2$ in the expression for $\eta(\pi)$ (Appendix I) is important, i.e., assuming that the field form had the "optimum" shape. If this were true, the "low-energy" edge of each profile would drop quite sharply from the solid line (door open) to zero in ~ 0.0005 volts, i.e., the change in current corresponding to a radial image shift equal to the counter slit width of 2 mm. The more gradual nature of the drop-off observed experimentally, particularly for larger baffle angles, shows that the door edges do not define, accurately, a constant-aberration cut-off. Thus, we have shown that the constant-aberration contours at the baffle plane are not the vertical straight lines expected for the optimum field form but must be curved, which is predicted in fig. 6.

Let us now compare the intensity of the door-open profiles with that predicted using fig. 6. To simplify slightly, let us ignore the source width. The counter-slit aperture, which is 2 mm wide, will accept orbits having a range of radial aberration equal to 2×10^{-3}. Thus, at a particular current setting, with one door open, those orbits that pass through the baffle plane between the two iso-aberration contour lines $\eta(\pi) = y$ and $\eta(\pi) = y + 2 \times 10^{-3}$ will be detected. We note that the contour lines for positive H in fig. 6 are

crowded together as T increases and those at negative H values are more widely spaced. Since the transmission for the detected orbits is to first order proportional to the area on fig. 6 between near $H \simeq -0.2$ and $T \simeq \pm 0.25$. One therefore expects to see a secondary peak at a current setting of $\sim 0.6\%$ below that of the main peak; this is observed experimentally

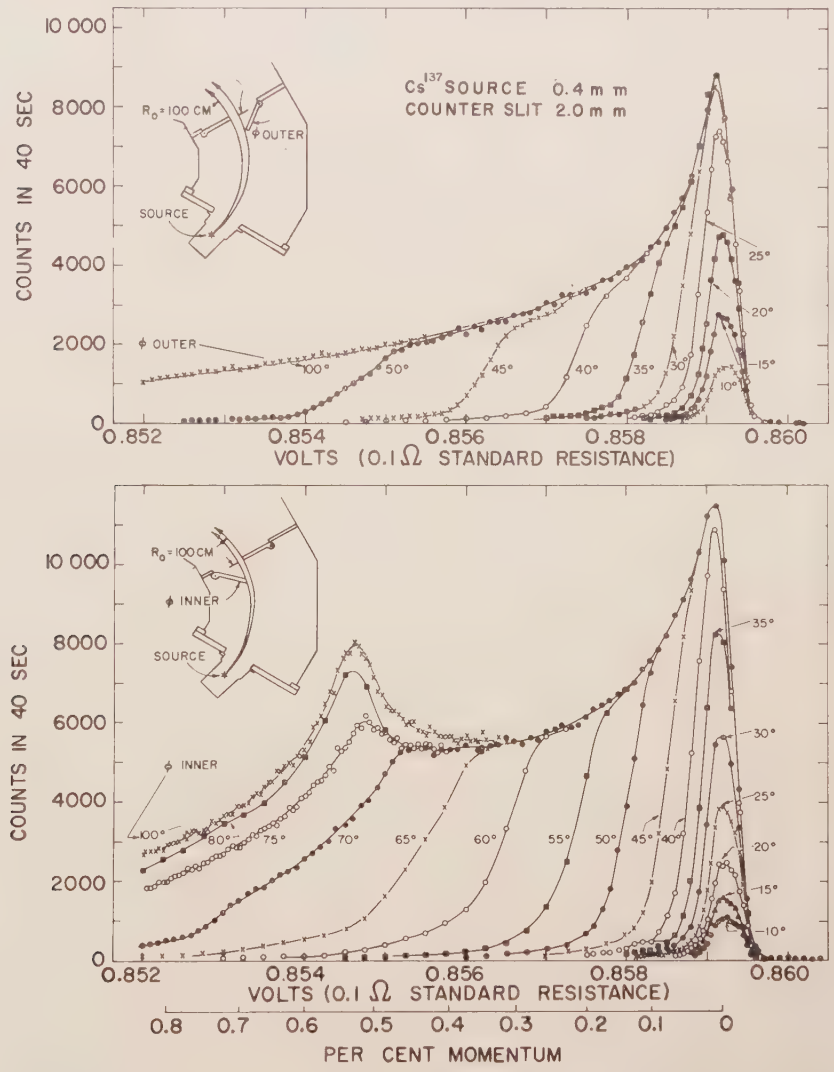

Fig. 7. The spectrometer image profiles presented here were obtained using the K-conversion line of the 661.6 keV transition in Ba^{137} at various angular settings of the baffle doors. The significance of these results and their interpretation in terms of the baffle apertures (fig. 6) is discussed in the text.

the two contour lines y and $y + 2 \times 10^{-3}$ we expect to observe much higher counting rates for the inner door open than for the outer door open, which is verified qualitatively by the experimental results. Note that there is a large area between contours in fig. 6 in the regions (see fig. 7) when the inner door is wide open. These tests demonstrate that the shape of the iso-aberration contours in fig. 6 is qualitatively correct and show us how to adjust the present baffle doors for any desired resolution setting.

4.4. VACUUM CHAMBER AND PUMPING SYSTEM

An important consideration in the design of the vacuum chamber was that the source and counter should be readily accessible for conversion-electron-gamma coincidence measurements.

The design used was a $\frac{2}{3}$ doughnut, as shown in fig. 2. The assembly must be rigid so that when evacuated it does not flex with changing atmospheric pressure as does, for example, the Bourdon pressure gauge. Mechanical stability is achieved by having a circular cross-section, walls of $\frac{3}{8}$ in. aluminum, and two braces joining the ends of the chamber. The cross-section diameter of 106 cm provides adequate clearance for all focused electron orbits. This large diameter reduces the possibility of detecting electrons scattered from the walls. The ends of the vacuum chamber consist of thick hinged doors which are positioned precisely on the end flanges by means of dowels. The doors may be opened to allow access to the baffles. Each door has a 12 in. diameter aperture for mounting the source and detector assemblies discussed below in section 6.

The main pumping system comprises a 30 ft. long, 20 in. diameter pumping line, an Edwards F903 diffusion pump (1500 litres/sec), and a Kinney DH-130 single-stage mechanical forepump (60 litres/sec). The long pumping line is required to minimize magnetic interference due to the ferrous casings of the diffusion and forepumps. The measured pumping speed at the vacuum chamber is $\sim 10^3$ litres/sec at a pressure of $\sim 10^{-5}$ mm Hg; the ultimate vacuum is $\sim 5 \times 10^{-7}$ mm Hg. A liquid-air thimble in the pumping line near the diffusion pump is used to freeze out condensable vapours.

Vacuum lock doors (not shown in fig. 2) are mounted on the inside of each end door so that the source or detector assemblies can be isolated from the main system. These permit the source or counter assembly to be changed, pumped down independently and opened again to the vacuum chamber in about 10 minutes without destroying the vacuum in the main pumping system.

5. Degaussing Coils and Building

In order to make measurements of electron momentum ratios with a precision of 1 part in 10^5, it is important that stray magnetic fields in the region of the spectrometer be kept extremely small. For example, in the present spectrometer ($r_0 = 100$ cm) an unrecognized uniform stray axial field of 10^{-4} gauss would give rise to an error of 10^{-2} gauss cm in a momentum value deduced from the coil current value alone. For electrons of energy ~ 80 keV (~ 1000 gauss cm) this corresponds to an error of 1 part in 10^5 in the relationship between coil current and the momentum of the focused electrons. In choosing the location of the building, and in the design of the degaussing system, we have aimed at controlling the earth's magnetic field and man-made fields to $\sim 10^{-4}$ gauss in the axial or vertical direction and $\sim 10^{-3}$ gauss in the horizontal direction.

With these limits in mind a magnetic survey was made of the vacant land available to us near the existing Physics buildings at this Project. Initially, the absolute values of the three components of the earth's field were measured for us by Dr. P. H. Serson (of the Department of Geomagnetism, Dominion Observatory, Ottawa) at three possible locations simultaneously. One of these was near enough to the bus platform and car parking lot (< 200 feet) to show changes of $\sim 10^{-3}$ gauss during vehicle movements. Subsequently, the vertical component was mapped at 40-foot intervals in the region of the other two locations and an isomagnetic contour map constructed. Because of the rocky terrain, which has significant amounts of ferrous ores, the field gradients are appreciable, typically 3×10^{-4} gauss per meter. This survey revealed two maxima around each of which the nearby isomagnetic contour lines had approximately circular symmetry. One of these was chosen as the location of the spectrometer axis; not until the excavation for the building was almost complete was it realized that our contour map had, in fact, located a large subterranean boulder some 8 feet below ground level. The upper portion of this boulder was removed by blasting

to provide a firm base for the concrete support pad for the spectrometer. An a.c. magnetic survey, made before construction started, showed that stray 60 cycle magnetic fields from power lines and nearby laboratories was acceptably small, i.e., $\lesssim 10^{-3}$ gauss.

spacings, and no. of terms) to make the 8th-order term also vanish. An attempt to solve for this condition proved unsuccessful[21]). The free parameter thus provides a family of 6th-order solutions. The parameters for the vertical and north-south coil systems are two such solutions

Table 5
Degaussing coils

I	Vertical:	Pair A	Pair B
	Diameter	27.50 feet	14.65 feet
	Separation	9.22 feet	19.49 feet
	Turns per coil	66	22
	Current (coils in series)	2.85 amperes[a])	
II	North-South:	Pair A	Pair B
	Diameter	27.50 feet	27.50 feet
	Separation	25.85 feet	6.68 feet
	Turns per coil	52	23
	Current (coils in series)	1.07 amperes[b])	
III	East-West	One pair of coils	
	Size	26.40 feet square	
	Separation	14.39 feet	
	Turns per coil	52	
	Current (coils in series)	$<$ 0.1 amperes[c])	

[a]) For vertical field component of 0.57 gauss.
[b]) For horizontal field component of 0.13 gauss.
[c]) For a possible east-west component of 0.015 gauss.

The parameters of the degaussing coil arrangement used to cancel out the earth's field in the region of the spectrometer electron orbits are summarized in table 5. The assumption was made that the earth's field is uniform over the region of interest and the coil arrangement is designed to create a uniform opposing field equal in magnitude to $\lesssim 10^{-4}$ gauss over this region. The parameters were computed for us by Lee-Whiting[21,22]). Those of the vertical and north-south compensating coils are chosen so as to make zero the second-, fourth-, and sixth-order terms in the Taylor expansion series expression for the field strength about the central point of symmetry of each four-coil (two pair) array. The odd order terms vanish because of symmetry. In principle, there are sufficient (four) independent parameters (i.e., ratios of diameters, which were chosen to be compatible with the architectural design of the building (listed in table 5). The pair of square coils, which are included for east-west compensation, satisfy the Helmholtz condition, i.e., a zero second-order term in the Taylor series expansion. The ratio of separation to side of square that satisfies this condition is 0.544 506.

In the two upper parts of fig. 8 we compare the field form predicted theoretically for the vertical degaussing-coil system with that measured using a Serson magnetometer[23]). The experimental

[21]) G. E. Lee-Whiting, Uniform Magnetic Fields (Chalk River Report CRT-673, Feb. 1957).

[22]) G. E. Lee-Whiting, private communication (Dec. 1956).

[23]) P. H. Serson, Can. J. Phys. **35** (1957) 1387; and private communications. We are also indebted to Dr. Serson for the loan of a Schmidt balance used in the initial field survey.

results are the differences between the measurements with degaussing-coil current on and off. At the time of writing, the field pattern with current on is not uniformly zero over the entire vacuum-chamber region within the desired limits of $\sim 10^{-4}$ gauss; the maximum variation of about 5×10^{-4} gauss around the optic circle, shown in the lower part of fig. 8, is typical of the field gradients found during the initial magnetic survey and suggests that the excavation for the building has upset, slightly, the initial field pattern. This source of calibration uncertainty has not been a serious limiting factor in the investigations carried out so far and no difficulty is envisaged in the ultimate elimination of this small gradient, e.g., by altering the degaussing-coil spacings.

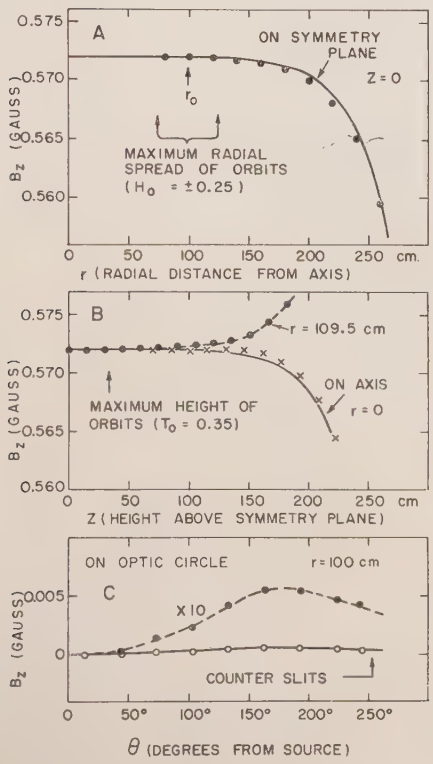

Fig. 8. The upper graph shows the uniformity of the field created by the vertical degaussing coil system. The solid line shows the calculated field intensity on the plane of symmetry as a function of the radial distance from the symmetry axis. The points show the measured field strength along a N E radial line. The solid line in the middle graph shows the theoretical field intensity for axial departures from the symmetry plane at the axis ($r = 0$). Measurements at $r = 0$ and $r = 109.5$ cm are shown by the points. The lower part shows the net vertical component of the earth's field along the optic-circle circumference with the vertical and north-south degaussing systems operating. As yet no steps have been taken to correct the small non-uniformity in field of $\sim 5 \times 10^{-4}$ gauss shown here.

The design specifications for the building were based on a series of magnetic tests on possible construction materials. No iron has been used in the basic structure itself. The foundation walls are 20-inch-thick, non-reinforced concrete. The remainder of the building has been constructed of wood, asbestos shingles, and other non-ferrous materials. Brass or aluminum fittings have been used throughout. Some ferrous electrical and air-conditioning fittings were subsequently permitted in the control room at distances of > 25 feet from the spectrometer axis following tests to determine that they would not give rise to unacceptable field gradients near the optic circle. The building is air-conditioned in order to maintain constant temperature and low humidity. The latter is also helpful in preventing electrical surface leakages in the coil insulation which become detectable at > 70% relative humidity. Fig. 9 shows an artist's cutaway sketch of the building which was drawn before construction. It shows where the degaussing coils and some of the other equipment are located within the building.

6. Luminosity Calculations

The utility of a β-ray spectrometer operating at any specified resolution is often assessed by its luminosity L, defined as the product of the transmission, $\Omega/4\pi$, multiplied by the area A of source deposit. Luminosity, so defined, gives a direct measure of the conversion-line peak counting rate if the detector area is sufficiently large to receive all focused monoenergetic electrons simultaneously, i.e., if the counter has an acceptance factor of unity. This is seldom true in practice and we must include an acceptance factor F, i.e., determine the product LF, in assessing the effective luminosity. The significance of LF as a criterion of excellence is appreciated when one realizes that the specific activity of source material is frequently the limiting factor in achieving good resolution. The

sources must be made sufficiently thin to keep the mean fractional energy loss $\Delta E/E$ smaller than the desired resolution $\Delta p/p$. The maximum source activity that can be utilized for a given energy loss is proportional to source area which can be used which in turn depends on the size and electron optical properties of the instrument. In this section we consider the geometrical factors that should give the maximum luminosity, at a given resolution, for the present instrument.

The geometrical factors that determine the conversion-line profile (counting rate vs. coil

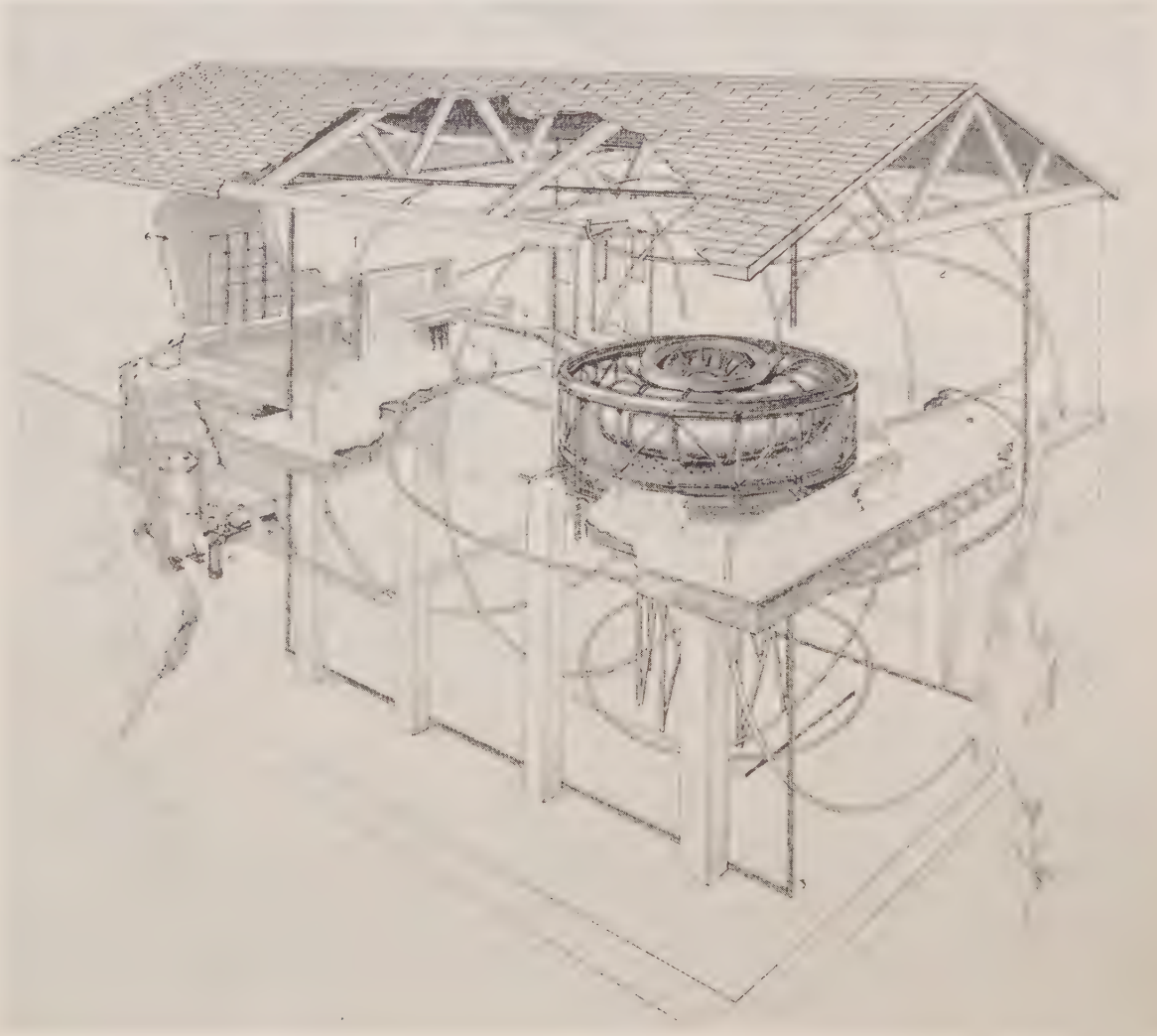

Fig. 9. This cutaway sketch of the spectrometer building shows the location of the important elements. The spectrometer and degaussing coil system are arranged symmetrically in the main room which is 28 feet square, inside dimensions. No. 1 is one of the four north-south degaussing coils. No. 2 is one of the four vertical axis coils and No. 3 is one of the two east-west square degaussing coils. A long pumping line, No. 4, leads to the north end of the basement which contains the diffusion pump, mechanical pump, electrical supply panels, water pump, and heat exchanger (at No. 5). An auxiliary building to the north (not shown) houses the compressor for the air-conditioning units. The building is oriented accurately along the magnetic meridian in order to minimize the east-west degaussing correction. Most of the electronic equipment is located in a separate control room 28 ft. by 13.5 ft. at the left (No. 6) which is the north end of the building. The building was constructed without the use of iron; where necessary, brass or aluminum fittings were used. Those units which by their very nature contain ferrous components, e.g., motors, pumps, meters, etc., are far enough away from the spectrometer to have negligible effect on the spectrometer field form. Where practical, large ferrous objects, e.g., generators, mains- supply transformers, compressor, etc., were located in remote buildings.

current) are: (a) the height $2t_0$ and width $2h_0$ of the source which we assume to be a uniform deposit (b) the source departure-angle parameters H and T permitted by the baffle aperture and (c) the width of the counter slit aperture which we assume is longer than the focused image of the source, i.e., $> 2t_0$. Expressions are given in Appendix I for the radial and axial image coordinates $\eta(\pi)$ and $\tau(\pi)$ for a trajectory leaving a point in the source plane $\eta(0)$, $\tau(0)$ with departure-angle parameters H and T. η and τ are measured from the optic circle in units of the optic-circle radius r_0. Inspection shows that for central orbits, $H \simeq 0$ and $T \simeq 0$, the image of a line source, $\eta(0) = h$, $|\tau(0)| < t_0$ is not a straight line but is parabolic in form with $\eta(\pi) = -\eta(0) - \frac{1}{2}\tau^2(0)$. Parabolically shaped detector slits are thus required to match the images from tall sources, $t_0 \gg h_0$. When using a constant width slit aperture shaped to match the parabolic curvature of the image, we must take into account the axial as well as the radial focusing aberrations in estimating the spectrometer resolution. The effect of axial aberrations introduced by the finite range of departure-angle parameters H and T is important only when using tall sources. For example, at a resolution setting of 0.01% where $H < 0.025$ and $T < 0.2$ (see fig. 6) the predicted axial aberration (Appendix I) is $\Delta \sim 2 \times 10^{-3}$ (2 mm). At height $\tau(\pi)$ in the image plane, orbits from the source region $\tau(0) = -[\tau(\pi) \pm \Delta]$ will contribute giving rise to a radial image spread of $\sim \frac{1}{2}[\tau(\pi) + \Delta]^2 - \frac{1}{2}[\tau(\pi) - \Delta]^2 = 2\tau(\pi)\Delta$. For the $R = 0.01\%$ example ($\Delta = 2 \times 10^{-3}$) the image from a line source is broadened by 4×10^{-4} (0.04 cm) at a height $\tau(\pi) = 0.10$ (10 cm). Thus the combined effects of parabolic bending and axial aberrations set a theoretical limit to the source area that can be employed at a given resolution if finite baffle apertures are employed. The inaccuracies inherent in the aberrations do not allow us to estimate the maximum permissible source area with any precision. One can, however, set a rough upper limit as follows: let us restrict the width of the source deposit at height $\tau(0) \sim \tau(\pi)$ so that the total image breadth at $\tau(\pi)$, i.e., the "effective" radial blurring plus the source width at height $\tau(0) \simeq \tau(\pi)$, is constant and equal to the maximum source width $2h_0$ at $\tau(0) = 0$. This will give rise to an image whose width is $\simeq 2h_0$ at all heights ignoring the effect of radial aberrations which will be discussed later. The source shape permitted under these restrictions is approximately diamond-shaped, tapering linearly from a width $2h_0$ at $\tau(0) = 0$ on the symmetry plane to zero width at height $\tau(0) = h_0/\Delta$ and having an area of $2h_0^2/\Delta$.

If linear rather than parabolically shaped slit edges are used to define the detector aperture one must either produce parabolically shaped sources or restrict the height of linear source deposits in order to maintain constant resolution. For the latter case one can set as a rough height limit, $t_0 = \pm (2h_0)^{\frac{1}{2}}$ which is the height that gives rise to an image bending of one-half the source width $2h_0$. In this case the image does not match the counter slit exactly and the slight broadening of the conversion-line profile should be taken into account when assessing effective luminosity at a given resolution. We have chosen to ignore this height dependence in the radial image-intensity distribution in order to simplify the line-image and luminosity calculations.

Let us next consider the radial aberration of the image given in Appendix I. Fig. 6 shows the permitted ranges of source departure-angle parameters H and T for a point source at $\eta(0) = \tau(0) = 0$, for aberration values appropriate to several typical resolution settings. For $T \lesssim 0.2$ the following simplified argument is sufficiently accurate for a first estimate of the luminosity. The image intensity from a line source will be a maximum for central, $H \doteq 0$, orbits, i.e., along the "perfect-image" line $\eta(\pi) = -\eta(0) - \frac{1}{2}\tau^2(0)$. The next leading term in the radial-aberration expression, $-\frac{2}{3}H^2$, expresses the lack of second-order radial focusing. Since the transmission increases linearly with H the intensity of the image at a distance $x =$

$$x = -[\eta(\pi) + \eta(0) + \tfrac{1}{2}\tau^2(0)] = \tfrac{2}{3}H^2$$

from the "perfect-image" line decreases with increasing H, $I(x)\,\mathrm{d}(x) \sim (\frac{3}{8}x)^{\frac{1}{2}}\,\mathrm{d}x$. This term

gives the image what appears to be a sharp high-energy edge and an intensity distribution that falls off in the low-energy direction as $x^{-\frac{1}{2}}$ until it reaches a sharp low-energy edge at $x = \frac{2}{3}H_0^2$, H_0 being the radial limit of the baffle aperture. For uniform source deposits having a the maximum counting rate observed divided by the total electron intensity in the image at the focal plane. The spectrometer resolution, R, is defined as the fractional full width in momentum of the conversion-line profile at half-maximum height.

Table 6
Parameters for optimum luminosity when using a counter[a])

Resolution R (%)	0.01	0.1	1.0
Source width $s = 2h_0$ (cm)	0.034	0.34	3.4
Source height $2t_0$ (cm)	3.7	11.6	37
Source area A (cm²)	0.126	3.94	126
Transmission[b]) $\Omega/4\pi$	0.06	0.20	0.80
Luminosity $L = A\,\Omega/4\pi$ (cm²)	7.6×10^{-5}	7.9×10^{-3}	10.1×10^{-1}
Counter slit width (cm)	0.034	0.34	3.4
Counter acceptance factor F	0.83	0.83	0.83
Effective luminosity LF (cm²)	6.3×10^{-5}	6.6×10^{-3}	8.4×10^{-1}

[a]) Based on 6 coil (3 pair) design with coil dimensions given in table 3.1 and assuming straight-edged sources and counter slits.

[b]) These solid angles are slightly smaller than those indicated in fig. 6. As discussed in section 6 the optimum luminosity is obtained with a radial aberration $a = 2.3R$. The contours in fig. 6 correspond to $a = 4R$, i.e., a radial aberration broadening equal to the desired resolution R. Thus the aperture in fig. 6 between the 0.1% contour lines is appropriate for optimum-luminosity operation at a resolution of $R = (4/2.3) \times 0.1\% = 0.174\%$.

radial width $-h_0 \leqq \eta(0) \leqq +h_0$ the radial image-intensity distribution $I(x)\,\mathrm{d}x$ in the focal plane is obtained by the folding of a rectangular source-intensity distribution

$$I[\eta(0)]\,\mathrm{d}\eta(0) = N_0(2h_0)^{-1}\,\mathrm{d}\eta(0), \quad |\,\eta(0)\,| \leqslant h_0\,,$$

with the radial aberration intensity factor $I(x)\,\mathrm{d}x = Ax^{-\frac{1}{2}}\,\mathrm{d}x$, $0 \leqq x \leqq \frac{2}{3}H_0^2$. The integrated intensity of the resultant image is the source strength N_0 multiplied by the transmission value permitted by the baffle aperture.

To obtain the conversion-line profile, under these simplifying assumptions, one must again fold the image-intensity distribution with a rectangular factor having a width equal to the assumed width, $2w$, of the slit defining the counter aperture. Unless $2w \geqq 2h_0 + \frac{2}{3}H_0^2$ the counter will not accept the entire image. For convenience, we define the maximum fraction of the image intensity that can pass through the counter slit as the counter acceptance factor F. Assuming that the counter aperture is taller than the image this factor F then gives the ratio of

Conversion-line profiles have been computed for a variety of ratios of the three factors affecting the widths, i.e., source width $2h_0$, radial aberration $a = \frac{2}{3}H_0^2$, and counter slit widths $2w$. The luminosity at resolution settings of 0.01%, 0.1%, and 1.0% were then deduced by scaling the widths of these profiles to the desired R values. This gives the true source width $2h_0$ and the radial width $2H_0$ of the baffle aperture. The counter acceptance factor F depends only on the ratios $h_0 : a : w$ and not on the scaling factor. These results combined with the source-height limit $t_0 = \pm\,(2h_0)^{\frac{1}{2}}$ and the appropriate baffle-aperture heights T_0 shown in fig. 6, enable one to estimate the luminosity $L =$ (source area) $\times$ (transmission, $\Omega/4\pi$) which might be realized when using straight-edged counter slits. These computations show that the maximum product LF is realized with $2h_0 = 2w \simeq 3.4R$ and $a = \frac{2}{3}H_0^2 \simeq 2.3R$. The factor F is $\simeq 0.83$. The results are summarized in table 6. It should be noted that the luminosity figures deduced in this simple way are considerably smaller than those

theoretically possible using parabolically shaped counter slits. They are, however, appropriate to the instrument as now operated.

The penalty for achieving good resolution becomes evident from these computations. The source area is proportional to $R^{\frac{3}{2}}$ and the transmission is proportional to $R^{\frac{1}{2}}$ ignoring the variation in T_0. To a rough approximation the maximum source thickness that can be tolerated because of energy degradation is also proportional to R. Thus the penalty for attempting to achieve high resolving power is a reduction in line counting rate proportional to R^3.

The criteria for optimum performance using photographic recording are somewhat different. First, there is no point in employing a source much higher than the desired image height since the blackening on the film or plate at a height $\tau(\pi)$ comes from the source region $\tau(0) \pm 2$ mm (if $T_0 \sim 0.2$). For a given luminosity, ($2h_0\sqrt{a} =$ constant) the narrowest image and hence "blackest" peak occurs with $2h_0 = a \simeq 1.07\,R$. The penalty for sharpening the resolution R is a $\frac{3}{2}$ power reduction in blackening or a $\frac{5}{2}$ power reduction in blackening if one allows for reduced source thickness. The time required to record a given momentum region photographically depends only on the luminosity since all momentum settings in a given range are recorded simultaneously. Thus the overall penalty factor when scanning a given momentum region photographically is $R^{2.5}$. On the other hand, when a counter is used as the recording mechanism the momentum steps must be decreased in size as the resolution is narrowed, which raises the penalty factor to R^4. Lee-Whiting has calculated[19]) that a momentum range of $\Delta p/p \simeq 8\%$ can be recorded on 32 cm long photographic plates at $R \simeq 0.01\%$ with only slight image broadening at the ends of the plate, i.e., to $\lesssim 0.015\%$. These arguments favour the photographic techniques only at high resolving power, i.e., $R \sim 0.01\%$. At poorer resolution the counting technique rapidly becomes preferable particularly as the data can be interpreted quantitatively. Recently, we, in collaboration with Dr. J. M. McKenzie, of this laboratory, have tested, successfully, a small silicon p-n junction detector using focused electrons (50 keV–2 MeV) from the spectrometer. Should it become practical to construct an array of, say, 100 such narrow β counters side by side, full advantage of the simultaneity of the photographic technique could be realized without sacrifice. In this event the counts could be accumulated in a core memory and the 100-channel momentum spectrum could be displayed and read out in the manner now used for multichannel pulse-height analysers.

7. Sources and Detectors

7.1. SOURCES

The source holder in current use is shown schematically to scale in fig. 2, and is visible in the center of the photograph, fig. 3. It is designed for sources up to ~ 12 cm high which are mounted on rings up to 15 cm dia. Dowels determine the precise positions of the main components of this assembly. The entire unit has been designed so that the source position can be reproduced precisely after disassembly and reassembly. There is provision for adjusting the source plane ± 1 cm along a tangent to the optic circle. Vernier screw adjustments with calibrated dials enable the radial position (± 1 cm) and vertical alignment ($\pm 5°$) of the framework on which the source is mounted to be varied externally. There is also an up-down adjustment (± 5 mm) to locate the source deposit symmetrically with respect to the plane of symmetry of the instrument. All four mechanical adjustments are independent. The cylindrical chamber behind the source is designed to minimize back-scattering. This part can be removed without affecting source location and replaced by a NaI scintillation spectrometer assembly for $\gamma - e^-$ coincidence investigations. A vacuum-lock door (noted above in section 4) makes it possible to change sources in a few minutes without disturbing the main vacuum system.

Uniform deposition of the source material is essential when attempting to use high resolving power. Sources are customarily prepared by

subliming the source material in vacuo from a shaped tungsten or tantalum boat onto a thin supporting foil of aluminum. The foil is mounted on the supporting ring of about 5 cm dia. The source width is determined by the width of a machined slot in a mask between the boat and the foil. The lengths of sources used to date have ranged from 1 to 2 cm. A much larger sublimation apparatus is nearing completion which will make it possible to prepare sublimed sources of up to 5 cm or more in length using up to 10 cm dia. rings. Since good sources are almost invisible deposits it is not practical to align them in the source holder by visual techniques and a mechanical method is now used. The location of the source mount ring and the mask in the sublimation apparatus is determined by two small dowels in line with the machined mask slot. The source mount ring is positioned in the source holder on an identical pair of dowels, thus assuring reproducible alignment from one source to the next.

7.2. COUNTERS

In almost all investigations to date, we have employed a proportional counter as detector. The first detector used was a continuous flow proportional counter having a 25 mm dia, end-window of 0.9 mg/cm² Mylar film. It is a standard A.E.C.L. type-FB-2, designed by I.L. Fowler, of the Counter Development group, who kindly adapted it for use with the spectrometer. The counter operates with an atmospheric-pressure filling of methane and has excellent characteristics. The plateau with focused monoenergetic electrons is typically $\sim$ 500 volts long with a slope of $\lesssim$ 0.4% per 100 volts. The window of Mylar plastic film is coated on its inner surface with a thin conducting layer of "Aquadag" colloidal graphite to prevent charging. A simple grid of four stiff wires helps support the window against the atmospheric pressure of the methane filling. The width of the acceptance aperture in front of the counter is defined by two 3 mm thick brass plates having parallel edges. The edges are slightly rounded to minimize electron penetration through the sharp corners. The width of the aperture can be adjusted from 0 to 20 mm by a vernier screw mechanism having an external calibrated dial and control knob. The counter is partially shielded with 5 cm of lead. A two-tube preamplifier is mounted on the lead shielding and is used to raise the pulse amplitude to $\sim$ 0.1 volts before transmission to the main amplifier and scalers some 8 meters away. The counter window has a low-energy cut-off of $\sim$ 20 keV. The reader is referred to earlier publications[11,12]) for a detailed discussion of the transmission efficiency of this window as a function of impinging electron energy.

Two additional proportional counters have been designed by I. L. Fowler, specifically for use with the spectrometer. One of these is a large cylindrical counter 6.75 in. long by 2.5 in. dia. for use with large sources at poor resolution. The focused electrons enter through a side window 38 mm by 127 mm. Because of its size and the difficulty of shielding it in our present arrangement, the background rate is high, typically 200 c.p.m. under operating conditions. Little use has been made of this counter since there appears to be no simple cure for the high background rate. Some form of anti-coincidence shielding would, perhaps, be helpful. The alternative of a large-area scintillation detector may prove more satisfactory but has yet to be tried.

The second special-purpose counter was designed to minimize the background rate for high-resolution studies. It has an active volume of 12 mm dia. by 57 mm long and a typical background rate of 20 c.p.m. The side-window aperture is defined by a removable brass plate having seven square openings, 6.3 mm by 6.2 mm in a row with 1.6 mm-wide supports between successive holes. This basic aperture will transmit 80% of a focused image 54 mm high and 6 mm wide. The "O"-ring vacuum seal for the counter window is in the body of the counter. The desired window material is mounted on one of a number of identical plates and screwed to the counter. This makes it possible to prepare a variety of windows and interchange as desired. With a graphite-coated Mylar window

($\sim$ 1 mg/ cm^2) the unit may be operated as a flow-type proportional counter with an atmospheric-pressure methane filling.The plateau under these conditions is about 800 volts long with a slope of $\lesssim 0.5\%$ per 100 volts. In some recent investigations we have used much thinner windows with lower filling pressures. Plastic windows having surface densities of ~ 100 μg/cm^2 were prepared by superimposing 10 to 20 layers of VYNS plastic films[24]) each of thickness ~ 5 μg/cm^2. This laminated film is supported by a fine-mesh metallic grid of $\sim 90\%$ open area[25]) which in turn is mounted on one of the brass plates. A Cartesian manostat[26]) is used to maintain a constant filling pressure of a few cm Hg pressure. The counter characteristics when used as a methane-filled flow-type proportional counter at this reduced pressure are not as good as at atmospheric pressure and become progressively poorer at lower pressures. Typical performance at 7 cm Hg pressure shows a voltage plateau $\sim$ 200 volts long with a slope of $\sim 2\%$ per 100 volts. The transmission-vs.-energy behaviour of the thin-window films is found to be very similar to that measured by Lane and Zaffarano[27]) for low-energy (< 50 keV) electrons normally incident upon thin films of comparable thicknesses. This thin-window technique has made it possible to measure the relative intensities of conversion lines down to energies of ~ 3 keV. The reduced stopping power of the low-pressure gas filling does, however, reduce the efficiency for energetic β electrons, some of which can traverse the counter without creating one ion pair. When comparing the intensities of low- and high-energy lines we have found it advisable to use more than one counter arrangement.

[24]) VYNS is a copolymer, consisting of $\sim 90\%$ polyvinyl chloride and $\sim 10\%$ polyvinyl acetate made by the Bakelite Co., N.Y., and obtained by us from Canadian Resins and Chemicals Ltd., Montreal. The properties of this VYNS film are described by B.D. Pate and L. Yaffe, Can. J. Chemistry **33** (1955) 15.

[25]) Obtained from the Buckbee Mears Co., St. Paul, Minnesota.

[26]) Made by the Emil Greimer Co., N.Y., and supplied to us by Edwards High Vacuum (Canada) Ltd., Burlington, Ontario, after being equipped with vacuum fittings.

[27]) R. O. Lane and D. J. Zaffarano, Iowa State Report I.S.C.-439, (1953) and Phys. Rev. **94** (1954) 959.

Scintillation counters are not normally used in precision investigations since the magnetic shielding required for the photomultiplier tubes disturbs the field form. The magnitude of the disturbance could be reduced by using a long light pipe so that the phototube could be located in the null field region at $r \approx 220$ cm (see fig. 4). At resolution settings of $\sim 0.10\%$ it is found that the disturbance caused by 2 in. photomultiplier assemblies located on the optic circle does not seriously disturb the focusing properties although it does affect the calibration by ~ 1 part in 800. It is practical therefore to use scintillation detectors for fast-slow β–γ coincidence studies where the instrument calibration is not of primary concern. With the slight modification to the source holder mentioned above, a 2 in. $\times$ 2 in. dia. NaI γ-detector can be brought to within < 1 cm of the source. The proportional β counter is replaced by a plastic or organic phosphor mounted on the end of a two-inch-dia. photomultiplier tube. While this spectrometer is not ideally suited for general coincidence studies because of the relatively low transmission (3×10^{-3} at 0.1 % resolution) the technique can be profitably employed when one of the detectors must have good resolution in order to resolve closely spaced γ-transitions. Some conversion-line-γ-ray coincidence experiments have been carried out using this arrangement and will be reported elsewhere.

7.3. PHOTOGRAPHIC TESTS

Theoretical predictions by Lee-Whiting[22]) suggest that photograph films could be used to advantage for the simultaneous recording of a range of electron momenta at good resolution. The estimated image widths for monoenergetic electrons of momentum $p = p_0 \pm 4\%$ are about 0.01 % in momentum broader than for those of momentum p_0 which follow the optic circle of radius 100 cm. Since the theoretical instrumental dispersion factor is 4 the corresponding 8 % momentum range is spread radially over 32 cm of film in the image plane $\pi\sqrt{2}$ radians from the source.

The suitability of photographic techniques for

recording conversion electrons was tested using a 0.5 mm by 2 cm long source of Cs^{137} having a strength of $\sim 30\,\mu c$. The K-661 line was recorded at various radial positions on the film by varying the current setting of the spectrometer; each image corresponded to $\sim 5 \times 10^5$ electrons (16 minute exposure). The baffle aperture was set for $\sim 0.03\%$ resolution. The central image ($r = 100$ cm) had the expected width of ~ 1.2 mm ($\Delta p/p \simeq 0.03\%$) and height of ~ 2 cm. The observed broadening at other positions was somewhat larger than expected for $r < 100$ cm but was less pronounced for $r > 100$ cm, i.e., was asymmetrical. These tests demonstrate that the photographic technique may prove useful in survey work at good resolution. Under the conditions of these tests, the estimated threshold for detecting a conversion line is $\sim 50\,000$ electrons. For survey work at resolutions of $> 0.05\%$ the present automatic counting and recording techniques using a single proportional counter as detector seem more profitable.

The measured spacings between the images agreed with those predicted theoretically within the estimated limits of experimental accuracy of $\sim 0.2\%$ and confirmed that the dispersion factor is 4.00 ± 0.01. The images were a few mm longer than the source deposit as expected from the calculated axial aberration of $\Delta = \pm 2$ mm for the small baffle aperture used in these tests.

8. Electronic Equipment

8.1. REGULATION AND MEASUREMENT OF THE SPECTROMETER CURRENT

The precision with which momentum of focused monoenergetic electron lines can be measured using this air-cored spectrometer depends primarily on the precision with which the current through the coils can be controlled and measured. As described above in section 3, great care has been taken in the design and construction of the coils to ensure that the proportionality between the momentum of the focused electrons and the current in the coils is constant over the useful momentum range to better than 1 part in 10^5. We assume for the moment that the earth's field is cancelled perfectly. We describe briefly in this section the electrical circuits used to achieve a precision of 1 part in 10^5 or better in the control and measurement of the coil current.

The eight spectrometer coils in series have a total resistance of ~ 13 ohms and generate a magnetic field of approximately 3.94 gauss per ampere on the optic circle. The coil design is conservative for currents up to 40 amperes, i.e., for electron momenta up to ~ 16000 gauss cm or energies up to ~ 4.3 MeV. The current source is a 600 volt 50 ampere d.c. generator located in a remote building about 300 feet away. A block diagram of the regulating system is shown in fig. 10. It is designed for completely automatic

TABLE 7
Standard resistance unit

Position	Specified resistance (ohms)	Maximum current (amp)	Calibration[a]) May 1958 (ohms)	Calibration[a]) Feb. 1960 (ohms)
1	$0.025 \pm 0.001\%$	50	$0.024\,999_8 \pm 0.002\%$	$0.024\,998_2 \pm 0.002\%$
2	$0.05 \pm 0.001\%$	30	$0.050\,000 \pm 0.002\%$	$0.049\,998 \pm 0.002\%$
3	$0.1 \pm 0.001\%$	20	$0.100\,000 \pm 0.001\%$	$0.099\,998 \pm 0.001\%$
4	$0.2 \pm 0.001\%$	10	$0.200\,002 \pm 0.001\%$	$0.200\,002 \pm 0.001\%$
5	$0.4 \pm 0.001\%$	5	$0.400\,00_3 \pm 0.001\%$	$0.400\,00_2 \pm 0.001\%$

[a]) These calibrations were carried out at the National Research Council of Canada, Ottawa, by the Electrical Standards group in the Division of Applied Physics. A test current of 0.5 amperes was passed through the current terminals in all cases and the resistance values were measured between the potential terminals.

operation. Some of the pertinent characteristics of the circuit are described in the caption to fig. 10. The loop gain is sufficient to maintain the voltage drop across the standard resistance equal to the reference potential within a few microvolts over a wide range of reference potentials. Since the voltage drop across the standard resistance is our measure of the current in the coil system, great was taken to obtain a set of standard resistances that have accurately known resistance ratios and low temperature coefficients. A standard resistance unit was specially designed and built to meet our requirements by Tinsley Instruments (Canada). The specified resistance values of the five resistors and the results of two subsequent calibrations are summarized in table 7. The resistors are made from annealed manganin wire all taken from the same batch. They are suspended in a bath of mineral oil which is circulated by a 1/60 h.p. impeller pump and regulated at 30.0°C with a stability of about $\pm$ 0.02°C. This temperature is about 0.5°C below the "peaking" temperature for this particular batch of manganin wire and ensures that the change in resistance due to resistive heating is kept to within 1 part in 10^5 of the zero-current resistance value for currents up to the maximum specified for each element. The resistance element desired is selected manually by a heavy-duty 4-pole 5-position rotary switch located in the oil bath; there are separate current and potential terminals. The two absolute calibrations reveal a small, long-term drift of a few parts in 10^5 in the lower-value resistances; this is attributed to aging of the manganin and is of the magnitude expected during the first year or so after manufacture. No tests have been performed to measure accurately the coefficient of resistance with current. The ratings are believed to be quite conservative and tests show no evidence of such non-linearities as large as 1 part in 10^5 when passing typical operating currents.

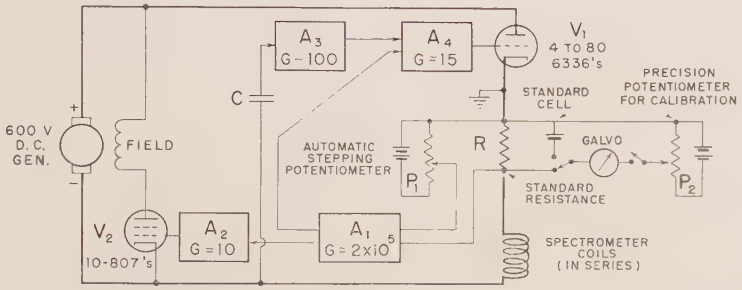

Fig. 10. The basic elements of the spectrometer-current control system are shown in this simplified schematic diagram. The power is derived from a 600 volt 50 ampere D.C. generator. The current passes through a bank of up to eighty double triodes V_1 (Chatham type-6336), a standard resistance, and the spectrometer coils (13Ω) which are all connected in series. The system seeks to make the RI potential difference across the standard resistance (choice of 0.4, 0.2, 0.1, 0.05 or 0.025Ω) equal to the reference potential from P_1. The difference between these two potentials is amplified by the chopper-modulated D.C. amplifier A_1 and applied through A_2 and V_2 to the generator field as well as through A_4 to the series triodes V_1. Because the frequency response of the chopper-modulated d.c. amplifier A_1 is limited (< 20 cycles per sec.) the control at higher frequencies, for ripple and phase angle, is derived through the condenser C and the wideband chopper-stabilized amplifier A_3. The overall loop gain is $\gtrsim 10^5$ at 0 cycles (D.C.) falling to $\sim 10^3$ at 70 c.p.s. and to unity at $\sim$ 80 kc/s. The long- and short-term drifts are normally $\lesssim 10\ \mu$V on the standard resistance RI potential difference which is usually operated within the range 0.5 to 1.0 volts. For measurements requiring higher precision the RI potential differences during automatic runs have been monitored manually using the precision potentiometer P_2. In this way the mean potential across the precision standard resistance during each counting interval can be determined with a precision of $\sim 2\ \mu$V, i.e., current ratios can be measured with a precision of < 1 part in 10^5.

The reference potentiometer P_1 (fig. 10) was designed so that it could be programmed automatically. Up to 1000 equally spaced voltages can be generated sequentially starting at any desired zero-position voltage, V_0, in the range 0 to 1 volt. The magnitude of the primary voltage increments, ΔV, are independent of V_0 and can be set to any of a variety of values in the range 5 to 1000 microvolts. The maximum combined

reference voltage generated at position 999, $V_0 + 999\,\Delta V$, is therefore ~ 2.0 volts. This unit may be programmed to restart the sequence of voltage steps after having scanned from the zero position up to any pre-set decade of primary voltage in increments, i.e., at position 10, 20, 30, etc. Provision is made for jumping increments, if desired, by skip programming, i.e., the unit can be pre-set to stop at every second, fifth, tenth, twentieth, fiftieth, or hundredth position. Thus a smaller number of effective increments > 1000 microvolts are also available for the coarse scanning of β spectra. This unit advances from one voltage setting to the next upon receiving an electrical impulse from the main timing and control unit. Suitable circuitry has been incorporated in the stepping potentiometer unit so that the index position (000 to 999) can be recorded by the readout mechanism associated with the timing and control units. This potentiometer was constructed mainly from high-quality commercial resistances (0.05% General Radio type-500) and stepping switches as well as miscellaneous wire-wound potentiometers, switches and connectors of the usual commercial varieties. The reference potential is generated across a high-quality 10000 Ω wire-wound resistor by adding the pre-set currents from the coarse and fine V_0 units and the scanning currents from the three ΔV stepping-switch units. Both the V_0 and ΔV units are supplied from the same regulated supply of — 105.0 volts which is referred to a saturated standard cell located in a constant-temperature ($\pm$ 0.05°C) oil bath at $\sim$ 28°C. A high-gain d.c. chopper amplifier, of the same type as used for the current regulator (fig. 10), is incorporated in the feed-back network. The d.c. loop gain is $> 10^5$. The resistance-dividing network (105 volts to 1.018 volts) is made from high-quality Karma wire-wound resistors also located in the same oil bath as the standard cell. All the other resistances in the reference stepping potentiometer circuit are located in one chassis, in air, and are used conservatively in order to minimize drifts caused by resistive heating. This unit has in no sense been designed as a high-accuracy potentiometer. The design has inherent limitations on the equality of successive voltage increments because of the current-adding feature. Compensation networks have been included that can be adjusted to bring increment equality to $< 1\%$. The prime requirement was reproducibility, i.e., both short- and long-term freedom from drift. Operating experience over some 22 months has shown that the overal stability of the current-regulating system including this stepping potentiometer is $\lesssim 5\mu$V short term at RI drops of $\lesssim 1$ volt and $\lesssim 20\ \mu$V long term, i.e., over periods of days. When very precise information is desired the RI voltage may be monitored manually during each successive current setting using the precision potentiometer discussed below. It has been found that potential differences can be estimated in this way to the nearest 1 μV setting of P_2. While the present stepping potentiometer has proved quite satisfactory for the bulk of the experimental work to date at spectrometer resolution settings of $\sim 0.1\%$ it is not ideally suited for precision work at better resolution. Consideration is being given to obtaining an automatic potentiometer of improved linearity and high absolute accuracy which can be programmed in a more flexible manner.

The current settings are calibrated using a precision potentiometer, P_2 (Tinsley type-6343D) of high accuracy, to measure the voltage drop across the standard resistance R, see fig. 10. It is standardized against one of a pair of saturated standard cells in a constant-temperature enclosure ($\pm$ 0.02°C at 25.0°C). Since saturated standard cells have a temperature coefficient of $\sim 50 \times 10^{-6}$ per °C, the uncertainty in voltage reproducibility due to temperature fluctuations alone is smaller than the typical long-term stability of $\sim 2\ \mu$V or more found for such cells[28]). The manufacturer claims

[28]) Dr. A. F. Dunn, of the Electrical Standards Group, National Research Council of Canada, Ottawa, informs us that it is not unusual for one of a group of such cells, in the same enclosure, to show excursions of two or three microvolts for no accountable reason. For long-term accuracy approaching one microvolt it will be necessary to intercompare between three or more standard cells in the same constant-temperature enclosure. We are indebted to Dr. Dunn for several helpful discussions regarding precision voltage-and current-measuring techniques.

the 6343D potentiometer is linear to within 3 parts per million. An independent examination of this potentiometer by the Electrical Standards group of the National Research Council of Canada showed that, at the time of calibration, its accuracy was better than 10 μV and their measurements indicate that, when comparing two potential differences corresponding, say, to two conversion-line settings which in practice are often within a factor of 2, the ratio of these voltages can be measured meaningfully to ~ 3 parts per million. Since all manganin resistance elements tend to drift slightly with age, periodic calibrations of this potentiometer as well as the standard resistance unit will be necessary for experiments requiring a precision of 1 part on 10^5 or better. In a typical experiment one sets up the desired starting voltage on P_2 (fig. 10) and adjusts the zero-position voltage setting in P_1 with the current regulator running to obtain a null galvanometer reading. The voltage increment size and number are selected and the *RI* voltages at several stepping-potentiometer positions in the scan range are also measured. Except when the highest precision is desired, the voltage settings are not measured again until the end of the scan. As noted above, the drift in calibration is usually small, i.e., < 20 μV.

8.2. REGULATION OF DEGAUSSING CURRENTS

Because of the large optic-circle radius and low field strengths needed to focus electrons, small fluctuations in the earth's magnetic field appear as serious perturbations. For example, the field strength on the optic circle needed to focus 80 keV electrons is only 10 gauss. The vertical component of the earth's field at the spectrometer is about 0.57 gauss. Thus an error of 1 part in 10^3 in cancelling the latter gives rise to a spectrometer calibration error of ~ 6 parts in 10^5 since we take the spectrometer-coil current as a direct measure of the focused-electron momentum. The diurnal variation of the earth's field is $\sim 5 \times 10^{-4}$ gauss; during magnetic storms the earth's field strength shows large random fluctuations of many times this amount, sometimes changing by 10^{-2} gauss in a matter of minutes. In addition to this occasional solar disturbance, one also has to contend with man-made disturbances, e.g., passing cars, trucks, etc. The problem of cancelling the earth's field at all times with sufficient accuracy that one can keep the spectrometer calibration constant to ~ 1 part in 10^5, is a formidable one. Fortunately magnetic storms are not frequent and last only a day or so. The remote location of the spectrometer was chosen specifically to minimize man-made disturbances. Thus for a large fraction of the time the only important source of disturbance is the diurnal variation which is fortunately small enough to be neglected in all but the highest-precision studies.

Two fixed-current regulating systems are now in use, one for the vertical coil system and one for the north-south coil system. Because the spectrometer building is oriented accurately along the north-south magnetic meridian, no east-west correction is yet needed. The regulators are identical and similar in principle to that used for the spectrometer current (fig. 10) except that the 220 volt generator supply is common to both systems and is not controlled by either feed-back system. A fraction of the *RI* voltage drop across a manganin resistor is kept equal to the voltage from a standard cell; both elements are in a constant-temperature oil bath. The fraction is determined by a helipot which may be adjusted to give the desired degaussing-coil current. The long-term stability of both regulators is ~ 1 part in 10^4. No attempt is made to determine the absolute value of the current; the currents are periodically set to give null magnetometer[23]) readings, i.e., $\lesssim 10^{-4}$ gauss, in the region of the optic circle with the spectrometer turned off.

The accuracy, with which the vertical component of the earth's field is cancelled, is monitored during operation by a magnetometer located at the centre of symmetry of the spectrometer (see fig. 2) where the field from the coils is theoretically zero (see fig. 5). A pen recorder with a calibrated time chart is used to record this signal; it has a fullscale sensitivity of 2×10^{-3} gauss. It was found that there is a small field

from the spectrometer coils at this central point which is now cancelled by a small coil system wound around the magnetometer head; the current needed for a zero magnetometer reading is proportional to the spectrometer current and is derived by connecting these compensating coils in series with appropriate resistances across the spectrometer coil and standard resistance element in fig. 10. The readings are usually quite steady during the counting intervals when the spectrometer current is constant. Temporary fluctuations are observed when the current is altered; this effect is attributed to eddy-current generation in the coil-support system which temporarily upsets the field cancellation at this central point. Fluctuations during the counting periods can arise from several causes, e.g., malfunctioning of the current-regulating system as well as variations in the earth's field strength. Occasionally gradual small drifts have been observed that did not seem to be correlated with earth's field fluctuations as monitored elsewhere. These may have arisen from a number of causes, e.g., very slight changes in coil parameters due to temperature variations, and do not necessarily imply a proportionate error in spectrometer calibration; see table 4.

For some time it has been planned to have the degaussing currents adjusted automatically so that they follow the fluctuations in the earth's field. In principle it should be possible to keep the cancellation continuously correct to $\lesssim 10^{-4}$ gauss. It was originally hoped that the central symmetry point would be a suitable location for the sensing magnetometers; direct feed-back could then be used. Practical experience with the monitor magnetometer shows that this location is not desirable for the reasons noted above. We now propose to use signals from a remote three-component magnetometer station[23]) to provide the reference signal variation needed for continuous cancellation. This is a less direct approach and has yet to be put into operation. It requires very stable magnetometer circuitry in which the ratio of output signal voltage to magnetic field strength being measured is known to be constant to better than 1 part in 10^4. Some difficulty has been experienced in adapting the Serson magnetometers[23]) we have been using for this purpose. It is hoped that this innovation can be put into operation in the near future.

8.3. COUNTER CIRCUITRY

Most of the circuits employed with the proportional counter are of conventional design. The high voltage (up to 3000 volts) is derived from an adjustable electronically regulated supply. A two-tube preamplifier is mounted directly on the outside of the counter shielding. This was found to be necessary; with adequate preamplification, $G \gtrsim 20$, the signal level being transmitted to the remote amplifier, through a 10-meter-long co-axial cable, can be kept above the random disturbance level caused by sporadic interference from other electrical circuits. The electronic amplifier now in use is a double-delay-line amplifier similar to that described by Kelley[29]). It is followed by a transistorized scaler of A.E.C.L. design[30]). The system dead-time is ~ 2.5 μsec. The scaler (capacity 10^9 digits) has been supplied as a part of a comprehensive data-handling system devised especially for use with the spectrometer[31]). This system is discussed in more detail below.

Large fluctuations in the β counter background rate occur quite frequently due to atmospheric contamination by A^{41}. This nuclide has a 1.82 hour activity with a penetrating γ-ray of 1.29 MeV. A^{41} is created by neutron activation of the natural argon in the air used for cooling parts of the NRX and NRU reactors. This air is ventilated to the atmosphere through a tall stack about 1 km north-west of the spectrometer building.

[29]) A.E.C.L. type-AEP 1439. These units, due to Mr. C. E. Gingell, of this laboratory, combine the double-delay-line amplifier of G. G. Kelley, Oak Ridge National Laboratory Progress Report (Sept. 10, 1956), the differential-integral pulse-height selector described by E. Fairstein, Rev. Sci. Instr. **27** (1956) 549, and a suitable stabilized power supply, all in one chassis.

[30]) This scaler is similar to that described by F. S. Goulding, in Chalk River Report CREL-772 (1958).

[31]) The automatic counting system developed for the spectrometer by W. D. Howell, is similar to an earlier system described by L. B. Robinson and W. D. Howell, in Chalk River Report CREL-774 (1959) but employs a revised read-out system.

The amount of A^{41} present in the air near the spectrometer building changes with atmospheric conditions and varies in an unpredictable manner. It is impractical to shield the β detector completely since there must be an aperture to admit the focused electrons. In most experiments to date, the background rate has been monitored with an unshielded Geiger counter located near the β detector. The signal from its counting-rate meter is fed to a pen recorder having a time-calibrated chart. This makes it possible to correlate the A^{41} background contribution with the β detector counting rates so that unreliable data may be rejected. A separate scaler has been incorporated into the new comprehensive data-handling system specifically to record background counts registered by such a separate counter. The counting periods for this scaler are identical with those of the β detector; simultaneous recording makes it possible to correct for a fluctuating background when processing the data.

In addition to the two scalers already mentioned, a third scaler of capacity 10^4 counts has been included in the comprehensive system for recording coincidences. This system also includes a hundred-channel transistorized pulse-height analyser (kicksorter) of Chalk River design[32]). As noted earlier, fast-slow coincidence circuitry is also available for use with scintillation counters, and has been used to record γ pulse-height spectra that are coincident with selected conversion electron groups. It is proposed to modify these circuits so that they may also be used as time sorters in the manner described by Green and Bell[33]); this will make possible the investigation of nuclear lifetimes using the spectrometer as one of the energy selectors.

8.4. AUTOMATIC CONTROLS AND READ-OUT

Except for the initial testing period of about three months, the spectrometer has been operated automatically. All the circuits associated with it were designed with a view to 24-hour day, seven-day week operation without manual assistance. The first automatic control system was relatively simple; it utilized a solenoid-operated electric typewriter as the readout mechanism. The method of automatic current control is discussed above in sub-section 8.2.

Recently, a new and more flexible system has been installed. This system has been tailored to the needs of the spectrometer program by W. D. Howell, of the A.E.C.L. Electronics Branch, and includes the transistorized scalers and multi-channel pulse-height analyser mentioned above[31]). It has been designed so that almost any conceivable experiment involving the spectrometer can be programmed automatically. This system can read out a total of 50 digits of information from scalers, stepping potentiometer, etc., plus the contents of the 100-channel kicksorter store at the end of any pre-selected counting interval of 10, 20, 40... 10000 seconds. The timing system is basically a 1000 cycle tuning-fork oscillator feeding transistorized scalers. Both the counting interval (up to 10^4 sec) and time elapsed from the start of any experiment are read out to the nearest second; the precision on the time gates is $\sim 10^{-3}$ sec, i.e., one cycle. In addition to this time information, which is useful in computing decay corrections, a parallel system records the time of day in hours and minutes, day of month, and year. After reading out the data, the stepping potentiometer is advanced to the next setting, the scalers are reset and counting at the new current setting is started. The current stabilizer normally settles down to the new value in < 1 second except after large changes, e.g., after returning from the end to the beginning of a current sequence. The time needed to read out these data is about 6 seconds for the 50-digits from the scalers etc. and about 2 minutes for that from the kicksorter.

The entire read-out cycle is frequently not required, so provision is made for several shorter read-out cycles. For example, when scanning a simple β-ray spectrum only twenty digits are

[32]) F. S. Goulding, Chalk River Report CREL-768 (1958); F. S. Goulding, G. Jones and R. A. McNaught, Chalk River Report CREL-770 (1958).

[33]) R. E. Green and R. E. Bell, Nucl. Instr. **3** (1958) 127.

recorded; the others are ignored. All digits are arranged in groups of ten which is the "word" length for the chalk river electronic computer (Datatron). As now wired, the first word of the two-word cycle consists of 3 digits for the index positions of the stepping potentiometer (P_1 in fig. 10), four digits for the four-decade scaler used for background counts plus three blanks, and the second word contains nine digits from the accumulated count scaler plus one blank. This shortened cycle takes only about 2 seconds. The impulse to advance the stepping-switch potentiometer is given after the index positions are recorded. If desired, the additional 30 digits (3 words) of information can be read out on an intermittent basis, say, after 10 positions or 100 positions or upon restarting the current scan. The kicksorter spectrum can also be read out on this intermittent basis if it is needed.

The read-out facilities consists of a solenoid-operated IBM electric typewriter, an IBM 8-hole tape punch, and an automatic plotter. The typewriter and punch operate in parallel at a rate of 10 digits per second and are the basic limiting factors determining the total read-out time. The automatic plotter attached to this system was developed for the special purpose of plotting the β spectrum as the data are being taken. It consists of a small relay matrix which stores the accumulated β-scaler counts (up to 10^6 only) and the stepping-potentiometer index numbers as they are being processed by the read-out system. A set of precision resistors associated with the relay matrix generates six analogue voltage signals. These are plotted as six different coloured points on the 12 in. wide chart of a Brown recorder equipped as a six-position point plotter. After plotting the chart is advanced one position so that it is ready for plotting the next set of data. One plotting signal is zero, one is proportional to the number of the stepping-potentiometer index position, and the four remaining give fullscale deflections for 10^3, 10^4, 10^5, and 10^6 counts. The plotting accuracy is $\lesssim 0.2\%$ which is quite adequate for rough analysis. The numbers are, of course, also available from the typewritten or punched records for more elaborate analysis. The plotting cycle typically takes $\sim$ 10 sec, so that rapid scanning, i.e., with 10-second counting intervals is practicable. There are several other features associated with this sytem which add to its flexibility. For example, the punched-tape record can be written in either IBM or Datatron code. Clock pulses can be deleted from those words that one does not want read into the computer memory. A variety of interlocks are included as safeguards. At the time of writing, not all features have yet been exploited.

9. Performance

9.1. AT 0.1% RESOLUTION

For almost all the experimental investigations carried out to date, resolution settings of $\sim 0.10\%$ have proved to be the most profitable. This is better resolution than has been used in the previous investigations of most nuclides and is easily realized in our spectrometer. The sources required, of width $\sim$ 2 mm and typical length 20 mm, can be prepared with high efficiency using the sublimation technique (section 7). This resolution is usually adequate to resolve the L sub-shell conversion lines of most transitions in medium and heavy nuclides. Comparison of the experimental L sub-shell ratios with the theoretical conversion-coefficient ratios often makes it possible to assign multipolarities unambiguously. For M1 transitions it is frequently possible to establish the E2/M1 mixing ratio with high accuracy, particularly for the lower-energy transitions. As has been noted in section 6 above, there is a strong penalty factor of $\sim R^4$ in attempting to use sharper resolution, R, when the specific activity of the source material is the main limiting factor. Occasionally, better resolution is needed to resolve closely spaced line groups if there is ambiguity.

A representative sample of the results obtained at $\sim 0.1\%$ resolution is shown in fig. 11. The radioactive material was obtained by irradiating Tb_3O_4 for about two months in the NRX reactor at a neutron flux of 6×10^{13} sec^{-1} cm^{-2}. The source was prepared by subliming in vacuo the active material from a boat-

shaped tantalum filament at ~ 2000°C through a defining slit ~ 1.6 mm wide onto backing foil of surface density 800 $\mu g/cm^2$. The source was about 12 mm long. This plot shows the conversion lines of two of the transitions which deexcite the $K = 2$ vibrational band in the Dy^{160} nucleus. The doublet nature of this line group was first proposed by Nathan[34]) and is clearly demonstrated here. The small inset shows, on an expanded momentum scale, two of the lines at 0.05 % resolution. A brief summary of our investigation of the Tb^{160} decay scheme has been reported[35]) and a complete account is now in preparation.

[34]) O. Nathan, Nucl. Phys. **4** (1957) 125.

[35]) G. T. Ewan, R. L. Graham and J. S. Geiger, Bull. Am. Phys. Soc. Series II, **4** (1959) 292.

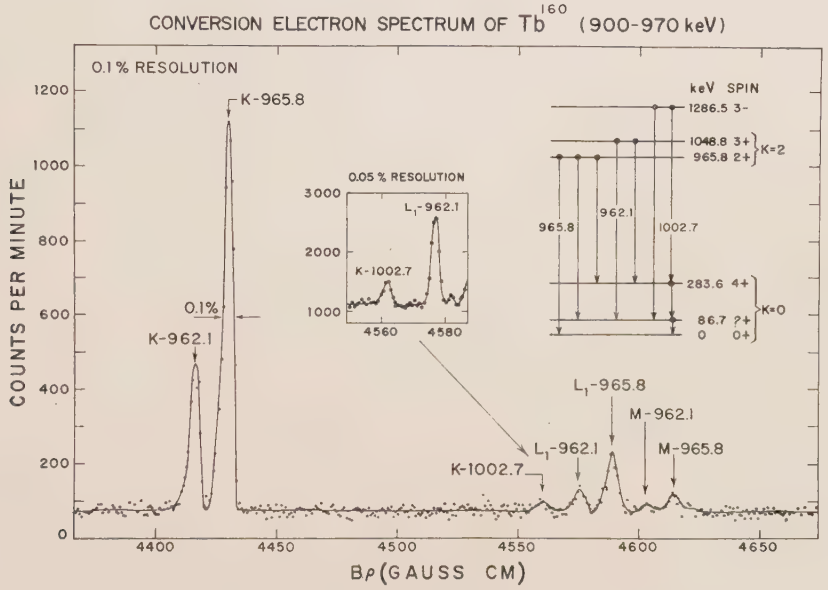

Fig. 11. A portion of the conversion electron spectrum observed with a Tb^{160} source. Except when higher resolving power is needed spectra are usually scanned at resolution setting of ~ 0.1 %. The inset shows a detailed scan at a narrower resolution setting.

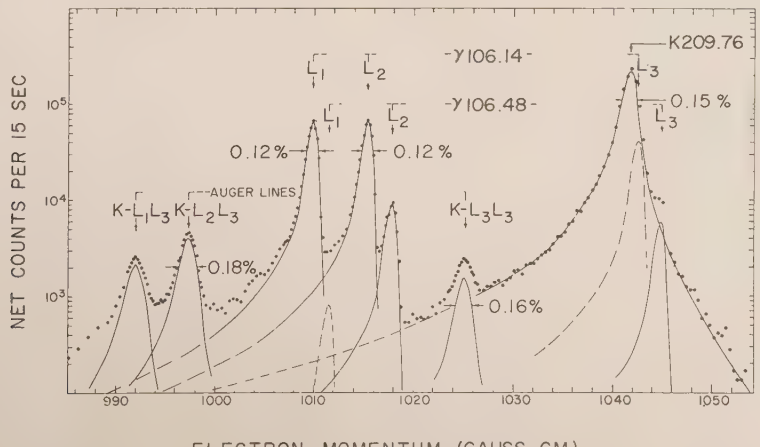

Fig. 12. A portion of the conversion-line spectrum obtained with a 2 mm × 20 mm Np^{239} source at a resolution setting of ~ 0.1 % in momentum. The original data were corrected for counter dead-time, background, and decay prior to subtracting the β-continuum contribution. This type of plot is often convenient for interpreting complex conversion-line groups since all lines in such a group should have essentially the same shape apart from broadening due to natural widths.

9.2. NATURAL LINE WIDTHS

The natural width of an electron-shell vacancy becomes increasingly observable at higher Z. For example, Mladjenović[36]) has shown that for $Z = 83$ the K-shell vacancy has a width of $\Gamma_K \sim 60$ eV and the L_I, L_{II} and L_{III} shell vacancy widths are respectively ~ 10.5, ~ 4.5, and ~ 5.4 eV. The widths for $Z \geqq 30$ appear to vary as $Z^{3.4}$ [37]). The natural-width phenomenon thus becomes an important limiting factor in determining what is a usable spectrometer resolution for transitions in high Z nuclei.

The effect of natural widths on conversion-line shapes at $Z = 94$ is displayed in figs. 12 and 13. In fig. 12 is shown a portion of the conversion-line spectrum in Pu^{239} following Np^{239} decay, taken with a spectrometer resolution setting of 0.1% in momentum. The reader is referred to an earlier publication[38]) for a complete account of this investigation. The data plotted in both figures are the net counting rates, due to conversion lines only, after subtracting the counter background and β continuum rates. It is often easier to interpret the net conversion-line spectrum on a semi-log plot such as this where all lines have similar shapes. The shapes would be identical for truly monoenergetic lines apart from the momentum scale factor. One can see here evidence for the two additional factors that affect line shapes. One is energy degradation within the finite thickness of the source deposit. The source used for the spectrum in fig. 12 was a barely visible (interference colours) deposit on the aluminum foil backing, yet an asymmetrical low-energy tail is prominent on all lines. The other factor is the contribution of the natural line width. It is a symmetrical broadening effect (Lorentz factor) and is most prominent for the K conversion line. The high-energy flare to the K-209.76 line is a characteristic feature of the natural-width factor. Line broadening from instrumental-aberration and source-thickness effects give rise only to low energy tails and one expects to see a sharp high energy edge. This is evident for the prominent L_1 and L_2 106.14 lines which are expected to have a much smaller natural-width contribution. The K–LL Auger

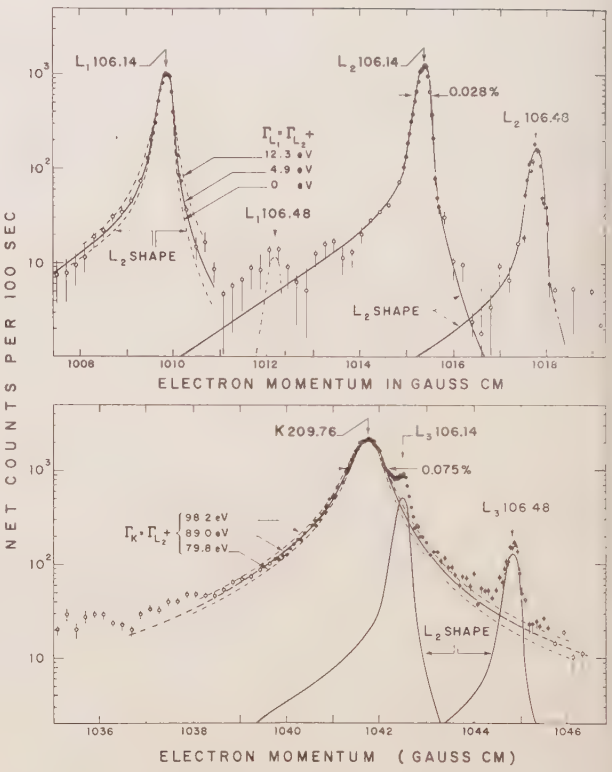

Fig. 13. Some of the lines of fig. 11 taken with a 0.15 mm × 20 mm Np^{239} source at a resolution setting of ~ 0.02 % are shown. The counter background and β-continuum rates were subtracted before plotting the data. The solid line shown for the K-209 peak was computed by folding the shape observed for the L_2 106.14 line (upper part) with a Lorentz factor of width $\Gamma = 89$ eV. Calculated shapes for two other Γ values are also shown. This analysis shows that the difference in natural widths for the K and L_2 shell at $Z = 94$ is ~ 90 eV.

lines are expected to be slightly broader than K conversion lines since the natural widths from three shell vacancies will contribute. This is consistent with the increased line widths observed for the Auger lines in fig. 12.

An estimate of the natural width of the K-shell vacancy for $Z = 94$ has been obtained from the results of fig. 12. The line shape used to fit the L_1 and L_2 106.14 lines has been folded with Lorentz factors of $\Gamma = 75$, 100, and 125 eV by

[36]) M. Mladjenović, Ark. f. Fys. **8** (1954) 27.

[37]) B. G. Gokhale, Annales de Physique **7** (1952) 852. Gokhale shows that his data fit a Z^3 law better than Z^4. On an expanded plot we find that his data for $Z > 40$ is best fitted by a $Z^{3.4}$ law.

[38]) G. T. Ewan, J. S. Geiger, R. L. Graham and D. R. MacKenzie, Phys. Rev. **116** (1959) 950.

numerical integration. The line shape obtained with $\Gamma = 100$ eV closely matches the K-209.76 shape while the $\Gamma = 75$ eV and $\Gamma = 125$ eV shapes are too narrow and too wide respectively. This result is not the true value for the K-shell natural width since (a) the folded shapes are appropriate to a slightly lower momentum line, (b) the L-106.14 shape has a slightly more prominent energy-degradation tail than is appropriate to the higher-energy K-209.76 line and (c) the line shape used to fit the L_1 and L_2 106.14 peaks already includes the mean value of the L_1 and L_2 natural widths. The difference of ~ 100 eV. is, however, consistent with the value of $\Gamma_K \simeq 100$ eV predicted for a $Z = 94$ K-shell vacancy by extrapolating the results of Ghokale[37]) assuming a $Z^{3.4}$ dependence.

Fig. 13 shows even more dramatically how good resolution can be used, in some cases, to assign the atomic shell responsible for a conversion line without corroborative information from other lines. This figure displays on an expanded momentum scale some of the lines in fig. 12 taken with a resolution setting of $\sim 0.02\%$. Both L_3 conversion lines now appear as sharp clean lines, whereas in fig. 12 they were masked by the intense K-209.76 line. There is no question here that the intense line must originate in the atomic K shell as evidenced by its broad shape and pronounced high-energy tail. A folding procedure to simulate the shape of the K-209.76 line starting with that of the L_2 106.14 line has also been carried out for these results for a variety of assumed Γ values. Three of the resulting line shapes are shown in fig. 13. The curve for $\Gamma = 89$ eV gives the best fit and is consistent with a total natural width of $\Gamma_K \simeq 100$ eV for the K shell at $Z = 94$. It is clear that this type of experimental and analytical procedure can be used to obtain good estimates for natural widths at high Z.

9.3. PRECISION MEASUREMENTS

Great care was taken in the design and construction of this instrument to ensure that it would be capable of making measurements with a precision of ~ 1 part in 10^5 over the entire range of energies normally encountered in β spectroscopic studies. For several reasons this aspect of the instrument's capabilities has not as yet been exploited to any extent. It did not seem worthwhile to attempt an extensive program of precision work at good resolution until the earth's field degaussing system was automatically compensated. Also the yield of interesting data per day, when used as a probe for nuclear-level information at resolutions of $\sim 0.1\%$, has matched the original high expectations. Some tests of the instrument's suitability for precision studies at high resolving power have been made with a view to future improvements in associated equipment and techniques. The only serious limiting factors at present seem to be (a) continuous precise cancellation of the earth's field and (b) the obtaining of source materials of high enough specific activity. As has been noted above, improvement in the former is anticipated; the acquisition, in the near future, of a mass separator[39]) for this establishment should help with the latter difficulty. It is perhaps worth noting that this spectrometer came into operation during the most intense period of solar activity observed for over 100 years. When the solar minimum arrives, a few years hence, magnetic conditions may be expected to be much steadier.

A typical example of performance at good resolution is shown in fig. 14. The Au^{198} source was prepared by irradiating gold leaf for two days in a neutron flux of $\sim 6 \times 10^{13}$ cm^2 sec^{-2}. It was subsequently dissolved in HCl and the active solution was placed in the boat-shaped filament and heated to dryness. The AuCl was sublimed in vacuo at $\sim 1000°$C through a defining slit 0.1 mm wide onto 800 μg/cm^2 Al foil. The resulting deposit was a thin but clearly visible black deposit ~ 12 mm long having an estimated surface density of $\lesssim 50$ μg/cm^2.

The data shown in fig. 14 are typical sweeps selected from a series of scans at a resolution

[39]) This mass separator is being constructed for us by Komanditbolaget C. Mileikowsky and Co., Västerås, Sweden, and is similar to that described by K. I. Nielsen, Nucl. Instr. 1 (1957) 289, and D. Almen and I. O. Nielsen, Nucl. Instr. 1 (1957) 302.

setting of 0.015% in momentum. The differences in line widths are consistent with those expected for atomic-shell vacancies in Hg which range from ~ 4.5 eV in the L_2 shell up to ~ 60 eV in the K shell. The data were recorded automatically

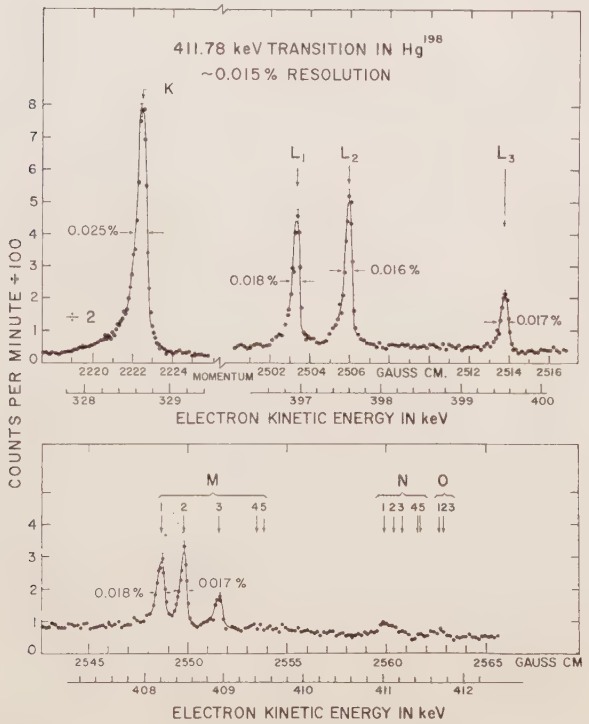

Fig. 14. The conversion lines due to the 411.77 keV transition in Hg^{198} taken with a 0.2 mm × 20 mm source of Au^{198} at a resolution setting of ~ 0.015 %. The extra width of the K line is largely attributable to the greater natural width of the atomic state having a K shell vacancy, $\Gamma_K \sim 50$ eV, although some of the breadth may also be caused by the thickness, ~ 50 $\mu g/cm^2$, of the source deposit. A precision comparison of these data with the K-661.6 line from a similar Cs^{137} source is discussed in the text and table 8.

and the voltage settings checked before and after each run. The drifts were small; the estimated precision in evaluating current ratios is $\lesssim 5$ parts per million. The degaussing currents were checked between successive sweeps to ensure that the earth's field cancellation was kept constant to $\lesssim 3 \times 10^{-4}$ gauss. During two of the runs small magnetic disturbances occurred causing short-term fluctuations of a few $\times 10^{-3}$ gauss. These caused clearly observable shifts in line positions from one sweep to the next which were not diagnosed immediately; the recording magnetometer had not been installed at that time. The data were subsequently time correlated with the magnetometer records of Mr. J. F. Steljes, at Deep River. In this way it was possible to reject the unreliable data. Another test of the theoretical properties of the instrument was made unwittingly during these runs. The temperature regulation of the cooling system failed, causing the cooling-water temperature to drop about 5°C over a period of several hours. There was no detectable shift in line position that could be correlated with this change in mean coil temperature. This is consistent with the small predicted effect, see table 4.

For comparison the K line of the 661.60 keV transition in Ba^{137} was scanned with identical spectrometer settings, using a Cs^{137} source of similar dimensions. For simplicity in analysing the Au^{198} source data we assumed initially that the Cs^{137} source line gives us the spectrometer calibration constant. In table 8 are summarized the resulting momentum and energy values of the seven Hg^{198} conversion lines. The r.m.s. scatter from the mean transition energy indicates a standard deviation of ~ 9 eV which corresponds to a consistency of ~ 14 parts per million in momentum. The absolute value so deduced has an inherent calibration uncertainty of ~ 90 eV. It is more meaningful to reverse the procedure. Taking the crystal diffraction result [40,2]) of 411.770 ± 0.036 keV for the transition energy in Hg^{198} we deduce that the K-line momentum from Ba^{137} is 3381.08 ± 0.30 gauss cm and the transition energy is 661.595 ± 0.076 keV. This comparison of the two transition energies is in excellent agreement with the two crystal-diffraction values of Muller *et al.*[40]). The value obtained here for the Ba^{137} transition is more accurate; the error quoted includes an allowance for possible systematic errors.

In an attempt to evaluate the electron optical resolving power achievable with the spectrometer, the L_2 conversion line of the 411.77 keV transition in Hg^{198} was scanned repeatedly using

[40]) D. E. Muller, H. C. Hoyt, D. J. Klein and J. W. M. DuMond, Phys. Rev. **88** (1952) 775.

TABLE 8
411.77 keV transition in Hg^{198}

Conversion line	$B\rho$ [a] (Gauss cm)	Energy (keV)	B.E. [b] (keV)	γ energy (keV)	
K	2222.45	328.67_7	83.106	411.78_3	Calibration uncertainty ± 0.092 keV
L_1	2503.30	396.93_5	14.84_1	411.77_6	
L_2	2505.89	397.57_7	14.21_2	411.78_9	
L_3	2513.61	399.49_0	12.28_5 [c]	411.77_5	
M_1	2548.62	408.19_6	3.56_3	411.75_9	
M_2	2549.82	408.49_5	3.28_1	411.77_6	
M_3	2551.57	408.93_2	2.84_8	411.78_0	
			MEAN	411.777	
			σ(r.m.s.)	± 0.009	
Crystal Diffraction Results	Muller, Hoyt and DuMond[40]			411.770 ± 0.036	
	Bergvall[2]			411.770 ±0.033	

[a] Assuming Cs^{137} K-661.660 = 3381.11 (± 0.5) gauss cm. If one uses the Hg^{198} transition as the standard these results give a Ba^{137} transition energy of 661.595 ± 0.076 keV and a K-661.595 momentum value of 3381.08 ± 0.30 gauss cm (see text).

[b] Y. Cauchois, J. de Physique et le Radium **13**, 113 (1952).

[c] B.E. L_{III} = 12.2846 ± 0.0003, E. Sokolowski, Ark. Fys. **15** (1959) 1.

a variety of baffle-angle and counter-slit-width settings. The source used was the same as that for fig. 14. The limiting width was found to be ~ 0.010%. This width may be due in part to the visible thickness of the black source deposit and to the expected natural line width for this shell of ~ 4.5 eV. Another possibility is that there are small electron optical imperfections due, perhaps, to a slight misalignment of the coils. This has yet to be explored; the coil-spacing parameters have not been altered from the initial alignment based on Lee-Whiting's theoretical calculations.

The possibility of making an absolute calibration by accelerating electrons from an electron gun through an accurately measured potential of 50 to 100 keV is being considered. This method has already been used by Meyer and Schmidt to obtain a precise measure of the momentum of the F line of thorium-B[41]) with an estimated accuracy of ~ 150 parts per million. Siegbahn and Edvarson[4]) report a more accurate (~ 70 parts per million) measurement of the same line momentum which makes use of the accurately measured X-ray wavelengths. As DuMond has pointed out[42]) the present knowledge of the physical constants indicates an uncertainty of ~ 20 parts per million in transferring from the X-ray or Siegbahn scale (X units) to the c.g.s. scale (milliangstroms). This is therefore the inherent limit at present for refinements of the Siegbahn technique. The electron-gun method avoids this particular limitations but it poses practical problems. If it proves possible to build a really good voltage-dividing network so that the accelerating voltages can be compared accurately with calibrated standard cells, an overall absolute accuracy of ~ 10 parts per million might possibly be realized. An independent technique such as this would make it possible to check the precision quoted for the current nuclear-energy standards and to search for possible systematic errors arising from the use of X-ray wavelengths as standards.

[41]) D. I. Meyer and F. H. Schmidt, Phys. Rev. **94** (1954) 927.

[42]) J. W. DuMond, Proc. National Academy of Sciences (U.S.) **45** (1959) 1052.

9.4. LIMITING RESOLUTION

Another attempt has been made to establish the limiting resolution obtainable with the spectrometer in its present form. The source was a narrow (0.1 mm by 20 mm) sublimed deposit of Np^{239}. The Np^{239} was kindly prepared for us in carrier-free from by Mrs. Janet S. Merritt, of this laboratory. The resolution tests were made using the L_1 and L_2 lines of the 228.2 keV transition in Pu^{239}. One of the scans is shown in the lower part of fig. 15. The expected L_1 and L_2 natural widths for $Z = 94$ are ~ 7 eV and ~ 17 eV which should give momentum broadenings of $\sim 0.002\%$ and $\sim 0.005\%$ respectively. No combination of baffle settings and counter-slit adjustments was found which would give a line profile narrower than 0.010% at half-maximum for either of these lines. The source deposit was extremely thin, being invisible to the naked eye; the line shapes did not have the pronounced low-energy tail characteristic of energy degradation within the source material. Under the conditions of these tests we had expected to see experimental line widths as narrow, perhaps, as $\sim 0.006\%$. This discrepancy between expected and observed line widths again suggests the possibility of small electron-optical imperfections in the spectrometer.

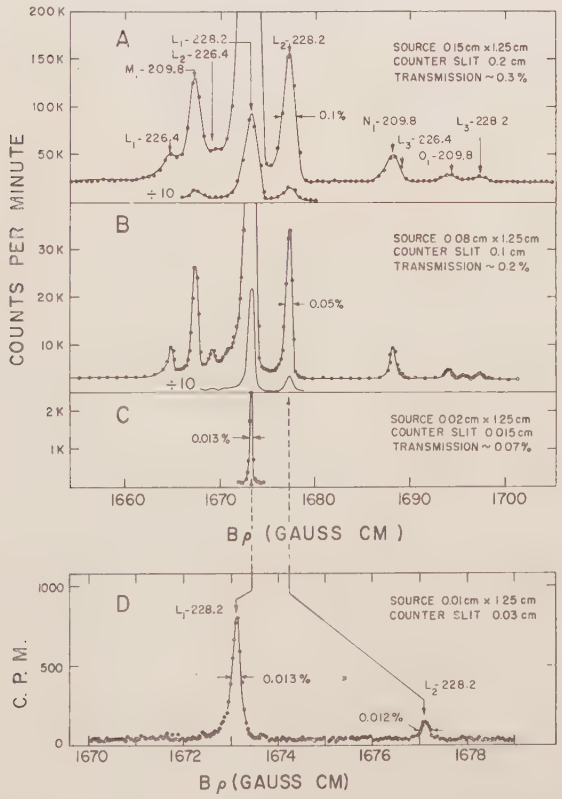

Fig. 15. A portion of the Np^{239} conversion-electron spectrum taken at different resolution settings. The results in the lowest part are results taken during an unsuccessful attempt to achieve an experimental resolution of better than 0.01 %. The width a half-maximum of 0.012 % for the L_2 228.2 line shown here is close to the limiting resolution value of $\sim 0.010\%$ with the instrument as presently operated.

Slight re-alignment of the coils might be needed to improve the resolution. Since great care and effort went into the initial alignment and since there is no provision for the usual empirical "cut-and-try" method, no changes have yet been made in the original adjustments. The results so far have borne out the theoretical predictions in a satisfactory manner and, except for what appears to be a limit on line width, there is no real evidence that the spectrometer is not performing as it should. It is quite possible, for example, that an improvement in baffle-aperture control would help. It is proposed to measure the radial and axial aberrations using an electron gun to test their dependence on the departure angles H and T. In addition, Lee-Whiting's new and more accurate electron-orbit computations help in providing a more detailed understanding of the inherent theoretical limitations. This new knowledge both experimental and theoretical should make it possible to establish the important factors that limit the ultimate resolution.

9.5. COMPARISON WITH OTHER SPECTROMETERS

In fig. 16 we compare the performance of the present instrument with a few recent spectrometers, in other laboratories, which are designed for precision β-ray spectroscopy. The design aim was to achieve an ultimate resolution near 0.01 % with as high a luminosity as possible. The solid line at the upper right in fig. 16, is the theoretical limit for the present instrument when using straight-edged sources and counter slits (see section 6, and table 6). The experimental points for the Chalk River instrument correspond

to the parameters shown for the upper three parts of fig. 15. The transmission values are experimental quantities deduced from the measured ($\pm$ 20%) source strengths and known line intensities per disintegration[38]). The luminosities are smaller than shown by the theoretical limit curve partly because it was not possible to prepare longer sources at the time (1958) in the small sublimation apparatus then being used, and partly because the ratios of the other geometric parameters (source width, counter-slit width, and baffle aperture) did not match the optimum ratios discussed in section 6 for the resolution values obtained.

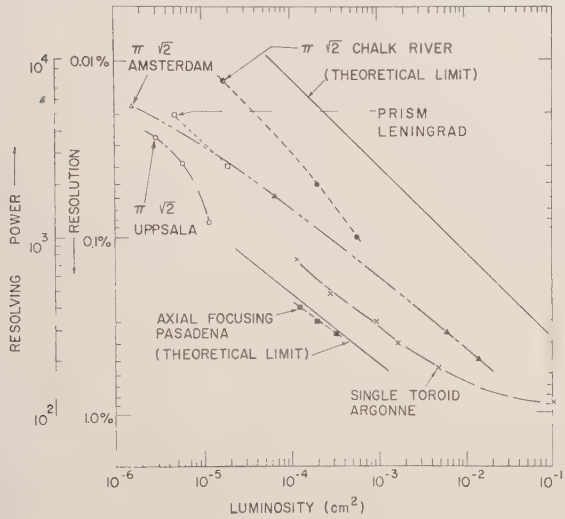

Fig. 16. We compare here the theoretical and experimental luminosities of some recent precision β-ray spectrometers. The upper theoretical line shows the theoretical limit for luminosity for the Chalk River instrument when using straight-edged sources and slits. As noted in the text, the use of parabolically curved counter-slit edges should permit luminosity values that exceed the plotted luminosity limit by more than a factor of two at narrow resolution settings. The theoretical line for the Pasadena machine[44,45]) is not extended past 0.1 % resolution since this appears to be its limiting resolution. Typical experimental values obtained with the various machines are shown by the points. The Amsterdam spectrometer[43]) is essentially identical to the Uppsala instrument[4]) in its electron optical properties but has a larger vacuum chamber and better arrangements for cooling the coils. The Argonne instrument[46]) has very high transmission (up to 19 % per section) and has been designed primarily for coincidence work rather than high resolving power investigations. The Leningrad spectrometer, as developed by Kelman[47]), is suited primarily for investigations requiring high resolving power; it has the smallest transmission ($T \lesssim 0.02$ %) of those compared here and is the only one employing iron (prism magnet).

The points for the other spectrometers shown in fig. 16 were taken, or deduced, from published results. The luminosity figures for the Uppsala double-focusing instrument come from table 2 of Siegbahn and Edvarson's paper[4]) and probably do not represent the true capabilities of their spectrometer. The data for the Amsterdam spectrometer come from the thesis of deVries[43]); the electron optical design is essentially that of the Uppsala instrument but a large vacuum chamber permits the use of larger sources and transmission values. De Vries' data would appear to represent something like the true capabilities of the Siegbahn-Edvarson design of double-focusing spectrometer which has an optic-circle radius of 30 cm. To compare the intrinsic electron optical qualities of these two iron-free double-focusing spectrometers with those of the Chalk River spectrometer, one should multiply the Uppsala and Amsterdam luminosity figures by the square of the inverse ratio of the optic-circle radii, i.e., $(100/30)^2 \simeq 11$. This makes the luminosity values independent of the scales of the two types of instrument. The intrinsic performance figures would then be similar; even after making such a scaled comparison the Chalk River instrument appears to have somewhat superior luminosity at the highest resolving powers and of course has a marked advantage in accessibility to both the source and counter which is essential in coincidence studies using scintillation detectors. The theoretical performance limit for the Pasadena spectrometer has been worked out in detail by DuMond[44]). The luminosity values shown by the closed squares in fig. 16, were deduced from the only two publications[45]) which quote both experimental resolution values and source dimensions. Since transmission values were not quoted, it was assumed, perhaps optimistically, that the actual trans-

[43]) C. de Vries, doctoral thesis (Amsterdam, Feb. 1960); C. de Vries and A. H. Wapstra, Nucl. Instr. and Meth. **8** (1960) 121.

[44]) J. W. M. DuMond, Annals of Physics **2** (1957) 283.

[45]) L. L. Baggerly, P. Marmier, F. Boehm and J. W. M. DuMond, Phys. Rev. **100** (1955) 1364; E. N. Hatch, F. Boehm, P. Marmier and J. W. M. DuMond, Phys. Rev. **104** (1956) 745.

mission values achieved were as large as those predicted theoretically[44]). A survey of the experiments carried out with this instrument (bibliography of reference[44])) suggests that it has a limiting resolution of $\sim 0.1\%$. The performance data for the first half of the newly constructed iron-free toroidal "orange" beta spectrometer at Argonne, were taken from the privately circulated announcement of Freedman *et al.*[46]). This latter instrument has been designed specifically for high transmission rather than high luminosity. The measured transmission values, of up to 19% for the first toroid, show that this machine will have no equal for electron-electron coincidence studies when the second "orange" toroid is completed. The prism spectrometer, described by Kelman[47]) is adapted to work at high resolving powers. Of these high performance instruments it is the only one employing iron and is least suited to coincidence studies because of its very low transmission, $T \lesssim 0.02\%$.

At the time of writing, two smaller double-focusing spectrometers based on the Chalk River design, are under construction[48,49]). Both are scaled down in size to an optic-circle radius of $r_0 = 35$ cm. The corrections to the field form for the finite size of the current-carrying elements in the coils become more important since the number of ampere turns required in each coil to focus electrons of a given momentum is independent of the scale of the instrument. Nevertheless, Lee-Whiting has shown that there is no difficulty in making the finite-size corrections for this scale of instrument[50]), and no deterioration in electron optical performance is expected.

10. Acknowledgements

We are indebted to Dr. L. G. Elliott for suggesting the construction of a large precision beta-ray spectrometer, and for his continuing advice and interest in its development. We would like to thank Dr. J. L. Wolfson for his contributions to the concept of this spectrometer and for many computations in the initial design phase. We are most indebted to Professor J. M. Robson (now at the University of Ottawa) for guidance and help throughout the construction period, particularly with the many administrative details. We would like to thank Messrs. C. A. Crawford, J. A. Cooke, and W. O. Findlay, of the Engineering Design Division, and Drs. R. Edis, A. R. Johnson, J. T. Rogers, Messrs A. Harris, W. R. Cuff, and J. Pritchard, formerly of Canadair Limited, for their various contributions to the mechanical design of the coil system, vacuum chamber, and building. We are particularly grateful to Mr. J. M. Putnam, of A.E.C.L.'s Building Maintenance and Construction Branch, who meticulously supervised the construction of the building and the installation of the spectrometer in a most capable fashion. In addition to those mentioned at various points in the text, we would like to thank Mr. W. McAlpin for designing and installing the vacuum locks, the liquid air-thimble, and the diffusion-pump manifold. As has been indicated frequently throughout the text, we have benefited from many pleasant and fruitful discussions with Dr. G. E. Lee-Whiting. We would like to thank Dr. H. Carmichael for critically reviewing this manuscript.

Messrs. R. B. Walker, H. Niemann, and W. Perry have constructed much of the electronic and electrical equipment, prepared many of the sources, and assisted in the operation and maintenance of the spectrometer. Their cooperation and assistance in these aspects of the spectrometer program is gratefully acknowledged.

[46]) M. S. Freedman, F. Wagner Jr., F. T. Porter, J. Terandy and P. P. Day, privately circulated announcement. Argonne National Laboratory, March 14, 1960; and Bull. Am. Phys. Soc. Series II, **5** (1960) 356.

[47]) V. M. Kelman, Vestnik Akad. Nauk SSSR, No. 7 (1958) 75. For an analysis of this instrument's performances as well as those of other recent β-ray spectrometers see M. Mladjenović, Nucl. Instr. and Meth. **7** (1960) 11.

[48]) J. L. Wolfson, private communications (1958 and 1959).

[49]) J. W. M. DuMond, private communications (1959).

[50]) G. E. Lee-Whiting, private communication (Nov. 1959).

APPENDIX I

Aberrations

We summarize here the theoretical information now available on the electron optical aberrations for a point source of monoenergetic electrons located at a height $t = \tau(0) = z/r_0$ above the optic circle. It is assumed that the field strength has been adjusted so that electrons leaving the source from the point $\eta(0) = 0$, $\tau(0) = 0$, in a direction tangential to the optic circle ($H = 0$, $T = 0$) will follow the optic circle that intersects the image plane $\psi = \pi$ (i.e., $\theta = \pi\sqrt{2}$ radians) at the point $\eta(\pi) = 0$ and $\tau(\pi) = 0$. For other departure angles, H and T, the intercepts $\eta(\pi)$ and $\tau(\pi)$ are not in general general zero and are called aberrations, i.e., measures of imperfect focusing.

One can derive theoretical expressions for aberrations with any desired degree of accuracy since the magnetic-field form from an array of air-cored coils is calculable. Le-Whiting has derived analytical expressions for aberrations to be expected for the original proposal of three pairs of coils described in table 3.1. These are in the form of a polynomial expansion of the departure-angle parameters $H = \sqrt{2}\tan\phi_r$ and $T = \sqrt{2}\tan\phi_z$ up to sixth order only. As a check he also obtained trajectory shapes by numerical integration using the University of Toronto electronic computer for a field form valid up to the eight order (assuming higher-order terms are zero). The resulting aberrations confirm the analytical expressions for small H and T values but differ appreciably for large angles. From these results, Lee-Whiting has estimated the magnitude of a few higher-order terms and these are included in brackets in the following expressions for the point on the image plane at which a trajectory, leaving the point $\eta(0)$, $\tau(0)$ in the source plane, intersects it:

$$\begin{aligned}\eta(\pi) = &-\eta(0) - \tfrac{1}{2}\tau^2(0) + \cdots \\ &- 0.00063\,H - \tfrac{2}{3}H^2 - 0.0065\,HT^2 \\ &+ 0.0023\,H^3 + 0.00093\,T^4 + 0.173\,H^2T^2 \\ &+ 0.296\,H^4 + 16.16\,HT^4 - 5.29\,T^6 \\ &+ \{\,71\,H^2T^4 - 36\,H^3T^2 + 1.55\mid T^7\mid + \cdots\}\,,\end{aligned}$$

$$\begin{aligned}\tau(\pi) = &-\tau(0) + \cdots \\ &+ 0.00063\,T - 0.1288\,T^3 - 0.0065\,H^2T \\ &+ 0.00372\,HT^3 - 0.107\,H^3T - 3.214\,T^5 \\ &+ \{\,33\,H^2T^3 - 21\,HT^5 + \ldots\}\,.\end{aligned}$$

The first expression has been used to compute the permissible baffle apertures shown in fig. 6. The iso-aberration contours, $\eta(\pi) + \eta(0) =$ constant, deduced from this expression are not expected to be valid for values of H and T approaching unity since ninth- and higher-order terms, in the magnetic-field-form expansion, have been neglected. The recent more accurate electron-orbit computations for the coils of table 3.2 give aberration values in qualitative agreement with the above expressions and confirm the general validity of fig. 6 for this type of spectrometer.

APPENDIX II

Temperature Coefficients

It is useful to know quantitatively how the spectrometer calibration figure, (expressed in gauss cm per ampere) depends upon the temperatures of the coils, support system, and vacuum chamber. It is easy to see that, if the expansion coefficients for all components of the spectrometer are the same, then the calibration figure is independent of overall temperature changes. In our system this should be true since it is made exclusively of aluminum. The temperatures of the coil windings are determined primarily by the closed-circuit cooling water system while the mean temperatures of the vacuum chamber and the support system (which determine the coil separations) will be closer to the ambient temperature. Since the two temperature-regulating systems are independent the individual factors affecting the calibration must be considered. To simplify this analysis slightly, let us consider that the field strength B_0 on the optic circle multiplied by the optic-circle radius r_0 defines the momentum of the focused electrons. The field strength on the optic circle is the sum of four contributions of the form $I^iK_1{}^i$, one for each pair of coils ($i = 1,2,3,4$); I^i is the number of ampere turns in each member of the i–th pair and $K_1{}^i$ is equal to the integral $C_1{}^i$ defined by Lee-Whiting and Taylor[18]). It is not difficult to show that $\partial K_1{}^i/\partial\alpha_i = D_2{}^i$ and $\partial K_1{}^i/\partial\beta_i = -C_2{}^i$ where α_i and β_i are the mean radius and mean half-separation of the i–th pair of coils in units of r_0 and the integrals C_1, C_2, and D_2 are defined and tabulated[18]) for current loops having parameters α_i,β_i. The tabulated values do not include finite-size corrections but are nevertheless sufficiently accurate for present purposes.

Consider a small fractional change δ in any of the eight parameters α_i,β_i ($i = 1$ to 4). The fractional change in the field strength B_0 on the optic circle due to an increase of $\delta\alpha_i$ in the radius of the i–th pair of coils can be shown to be

$$B_0{}^{-1}\,[\partial B_0/\partial\alpha_i]\,\delta\alpha_i = \delta\alpha_i\, I^iD_2{}^i/\{\,\Sigma_i\, I^iC_1{}^i\,\}$$

and similarly the fractional increase in B_0 due to an increase in the half-separation $\delta\beta_i$ of the i–th pair of coils can be shown to be

$$B_0{}^{-1}\,[\partial B_0/\partial\beta_i]\,\delta\beta_i = -\delta\beta_i\, I^iC_2{}^i/\{\,\Sigma_i\, I^iC_1{}^i\,\}\,.$$

If the vacuum chamber alone undergoes a small symmetrical expansion of δ in all dimensions we note that the optic-circle radius becomes $r_0(1+\delta)$ while the field strength on this larger optic circle is reduced by

$$[\partial B_0/\partial r_0]\,\delta r_0 = B_0a_1\delta = -\tfrac{1}{2}B_0\delta\,.$$

Thus the momentum calibration for electrons following the enlarged optic circle is

$$\begin{aligned} B_\delta r_\delta &= B_0(1-\tfrac{1}{2}\delta)\times r_0(1+\delta) \\ &\simeq B_0r_0(1+\tfrac{1}{2}\delta)\,. \end{aligned}$$

These expressions were used in evaluating the temperature coefficients listed in table 4.

NUCLEAR INSTRUMENTS AND METHODS 9 (1960) 287–302; NORTH-HOLLAND PUBLISHING CO.

THE LIVERMORE VARIABLE-ENERGY 90-INCH CYCLOTRON†

H. P. HERNANDEZ, J. M. PETERSON, B. H. SMITH and C. J. TAYLOR

Lawrence Radiation Laboratory, University of California, Livermore, California

Received 1 September 1960

A variable-energy cyclotron is described which accelerates protons from 2.6 to 15 MeV, deuterons from 5.2 to 12.5 MeV, and alpha particles from 10.4 to 25 MeV. The 90-in.-diameter magnet incorporates a special fringing field to reduce the angular divergence of the emerging beam. The single dee is driven by a crystal-controlled power amplifier, variable in steps of 55 kc/s from 4.0 to 9.5 Mc/s. The internal beam is limited to 200 μA to avoid septum damage, and 15 to 25% of this beam can be extracted. The external beam has a 2% total spread in energy, and an individual pulse in the beam has a time spread of 2% of the radiofrequency period. Most of the external beam is contained in an elliptical cone with half angles of 0.30° and 0.15°.

1. Introduction

This accelerator was built as a facility for neutron research in the energy region below 30 MeV. The design was based on the use of the d-d, d-t, and p-t reactions for obtaining reasonably mono-energetic neutrons. Proton energies variable from a few MeV up to 15 MeV and deuteron energies up to 12.5 MeV were required. A steady, high-intensity, mono-energetic beam was needed at external targets some thirty feet from the accelerator. The cyclotron was selected as the accelerator that best fitted these requirements. To get a reasonable amount of beam on a distant target, it was felt necessary to keep the angular divergence of the external beam in the median plane smaller than that obtained in the conventional fringing field. A special fringing field was incorporated to provide this feature.

The 90-inch cyclotron was constructed at Livermore for the University of California Radiation Laboratory (UCRL) at Livermore under AEC Contract W-7405-eng-48. The mechanical and electrical design work was carried out at UCRL, Berkeley. The cyclotron design was started in August, 1952, and construction started in the spring of 1953. The first internal beam was obtained in February, 1955.

† Work was performed under the auspices of the U.S. Atomic Energy Commission.

2. Variable Energy Parameters

The energy range was determined primarily by the desire to produce neutron energies up to 14 MeV using the p-t reaction. Protons of 15 MeV are required to produce 14-MeV neutrons in the forward direction. Lower energy neutrons can then be produced in the forward direction by using protons of energies less than 15 MeV. The design was also influenced by the desire to do charged-particle experiments utilizing the range of proton energies available, and by the desirability of producing deuterons in the same energy range. Then, in addition, the d-d reaction can be used to produce neutrons with energies up to 14 MeV if the deuterons have a maximum energy of 12 MeV, and the d-t reaction can be used to make neutrons with energies from 14 to 30 MeV.

The cyclotron parameters were fixed primarily by the large variation of magnetic field required to obtain a large change in energy, and the resulting desire to avoid complications that would be introduced by operating the magnet in the saturation region. An upper limit of 8 200 G was selected as reasonably below saturation. The maximum radius of acceleration was then fixed at 35 in., the radius of curvature of a 12.5-MeV deuteron in this magnetic field. The maximum frequency, 9.5 Mc/s, was that needed to accelerate protons to 15 MeV at a radius of 35 in. The

maximum frequency required for 12.5-MeV deuterons is much smaller-namely, 6.2 Mc/s. The minimum frequency was set at 4.0 Mc/s in order to simplify the design of the radio-frequency (rf) system. The magnetic field for proton acceleration corresponding to this minimum frequency is 2600 G.

In order to provide a high-quality external beam, an extraction system was chosen which consisted of a large electrostatic deflector and a special shape of pole face, which will be described later. A two-dee accelerating system was incompatible with this extraction system because of clearance requirements. Although it is common for single-dee cyclotrons to employ dummy dees, it was felt that, in this case, the complications so introduced were not warranted.

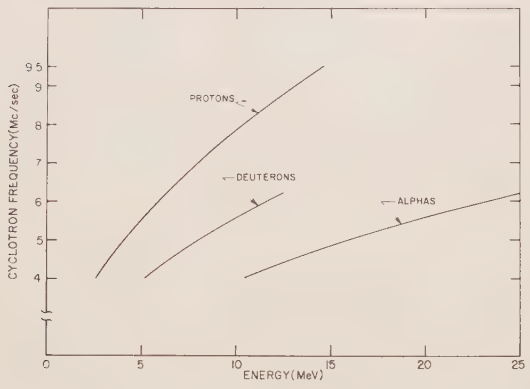

Fig. 1. Operating range. The upper energy limit of deuterons and alpha particles is determined by the maximum magnetic field of 8200 G.

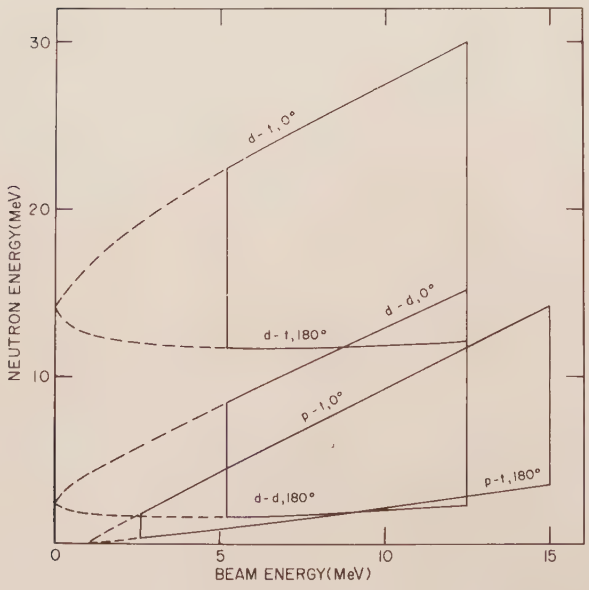

Fig. 2. Range of neutron energies available using hydrogen isotope reactions. The neutron energies corresponding to the areas enclosed within the solid lines are available by varying the cyclotron energy or the angle of emission of the neutrons. Third-harmonic acceleration can be used to obtain some of the energies corresponding to points enclosed within the dashed lines.

The design energy operating range of the cyclotron is shown in fig. 1. The ranges of neutron energies obtainable using the hydrogen isotope reactions are shown in fig. 2.

3. Magnet

3.1. DESIGN CONSIDERATIONS

The radial dependence of magnetic field which was chosen was a compromise between the conflicting demands for low threshold dee voltage and for adequate axial focusing. A linear fall-off of 1 % at full radius was used. The corresponding n value of this field shape increases linearly to a maximum of 0.01 at full radius. The relatively low fall-off of field makes the system particularly sensitive to small magnetic bumps. In particular it was necessary that saturation effects not cause a radial increase in magnetic field at low excitation when the magnet was shimmed for the required fall-off at high excitation.

This low value of n restricts the tolerable values of azimuthal variation in the magnetic field if radial oscillations are to be kept low. Hough[1]) has given a method for determining the displacement of the orbit center caused by harmonics in the magnetic field. Field measurements obtained from a one-ninth scale model of the magnet indicated that the amplitude of the first harmonic would most probably increase linearly with radius, and that the maxima of the first harmonic at different radii would all be located along one radial line, since the most probable source of first harmonic content would be misalignment of the pole faces. Application of Hough's method[2]) indicated that such a first

[1]) P. V. C. Hough, Rev. Sci. Instr. **24** (1953) 42.

[2]) Summarized in unpublished LRL, Livermore, P-Division Report NuPh-122, by C. J. Taylor.

harmonic with an amplitude of 0.1% at 35 in. would cause a 2-in. displacement of the orbit center when the ion reached the extraction radius of 35 in. Since such a displacement was considered to be within the range of adjustment of the deflector system, and since it was expected that pole face windings could be used to shift the orbit centers, this amount of linearly increasing first harmonic was used as an upper acceptable limit.

3.2. DESCRIPTION

The magnetic gap is 12 in. at the center, and increases linearly to 12.140 in. at the 35-in. radius. In the 180° sector not containing the cam the gap continues to increase at the same linear rate out to 39 in., and then reduces to 12 in. for the remaining distance to the maximum radius of 45 in. In the cam region this slope is continued to within 7 in. of the edge of the pole face. The desired magnetic field was achieved by careful alignment and precision machining of the pole faces, including machining to remove the first harmonic produced inside the extraction radius by the iron of the cam, and by the addition of a few edge shims and pole face windings.

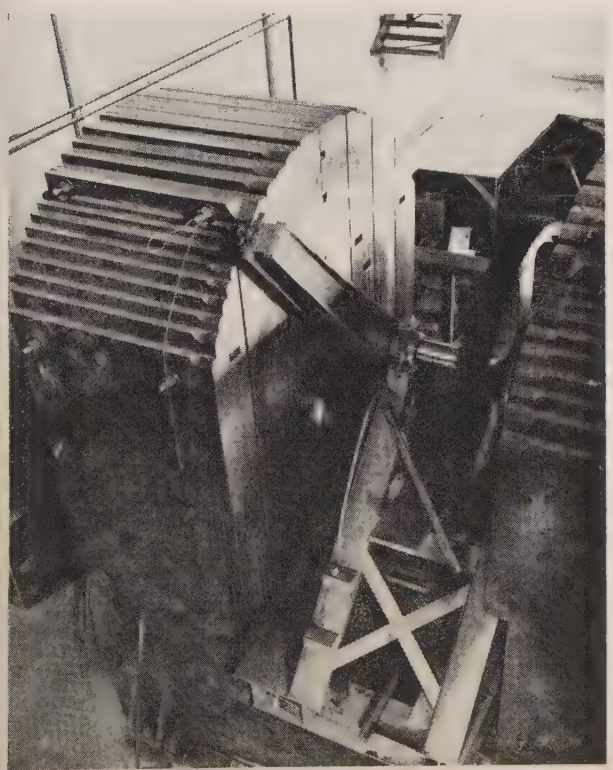

Fig. 3. Magnet yoke being machined prior to installation of pole pieces.

A C-shaped magnet yoke was chosen to provide maximum access to the accelerating region. This magnet was constructed of 2-in. laminations, and was erected with the accelerating plane vertical so that the mechanical support of dee and liners would be simplified. Cylindrical pole pieces were added to form a 300-ton C-shaped magnet. Accurate machining of the two faces of the magnet yoke to which the pole pieces were attached and of the component parts of the pole pieces was essential in obtaining the desired magnetic field shape. Fig. 3 shows the yoke being machined. Alignment of the centers of the two pole faces was obtained by positioning all pole pieces by locking rings placed in grooves machined in mating surfaces. Deflection of the yoke by magnetic forces was prevented by a nonmagnetic steel stanchion wedged in the magnet gap at the top of the magnet.

Each magnet coil was constructed of 720 turns of $\frac{1}{8}$-in. by 1-in. oil-cooled copper strap. There are 8.5 tons of copper in the two coils. A 150-kW generator furnishes 100 to 600 A to the series-connected coils. The current is regulated to 0.01% by a magnet regulator of the two feedback-loop type. The low-frequency loop receives its signal from a 2-V water-cooled shunt which meters the magnet current. The high-frequency loop receives its signal from the voltage across the magnet winding. The transfer functions of the two loops were measured and complementary equalizers were designed to provide stability with a loop gain of 10000. The current reference consists of a specially developed regulated power supply which has a loop gain of 15000 and uses mercury cells as a standard.

3.3. POLE FACE WINDINGS

An array of pole face windings on the pole tips (fig. 4) permit small alterations in the magnetic field shape. The central windings were designed to aid in improving the axial focusing near the

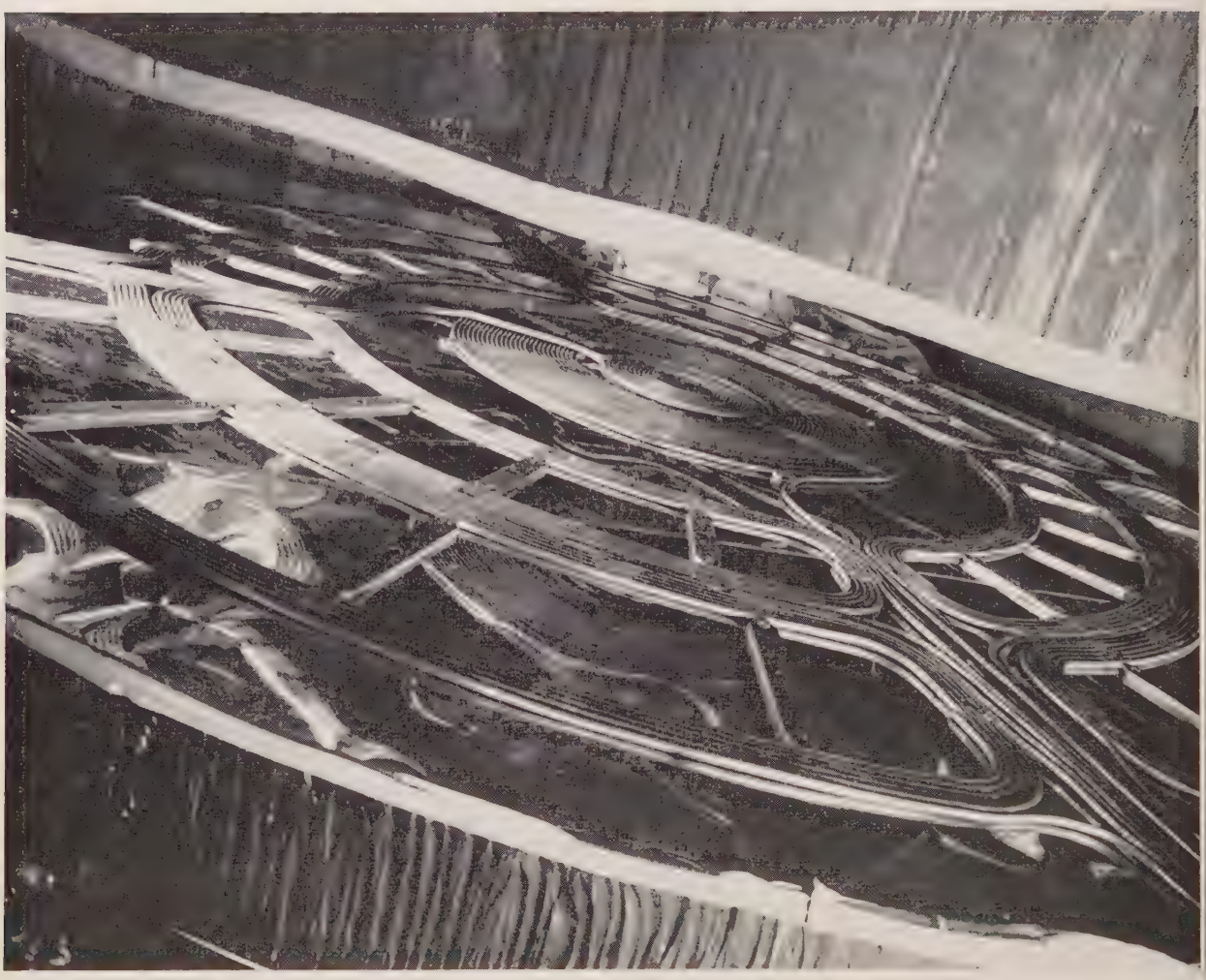

Fig. 4. Photograph of magnet gap showing pole face windings attached to one pole. A similar set is attached to the other pole. When opposite pairs of windings are fully energized so as to add their effects, the central windings can produce a change of 40 G at the orbit plane, and the quadrant coils a change of 16 G.

center of the magnet. The quadrant coils centered at extraction radius and 0.7 of extraction radius were provided to control the first harmonic in the magnetic field. These coils consist of flat windings of five turns of mineral-insulated, copper-sheathed wire fastened to the pole faces and water-cooled at the edge of the coil. They are supplied with currents up to 60 A from selenium-rectifier power supplies. They can be used to modify the radial gain per turn, to steer the beam into the deflector, and to make substantial changes in the energy without changing the cyclotron frequency.

3.4. EXTRACTION REGION

Emergent cyclotron beams usually suffer from large angular divergences in the median plane, since the beam is badly defocused radially in crossing the fringing field contours at a small angle. Professor Lawrence suggested that this condition could be avoided by adding a magnetic cam to the 90-in.-diameter magnet in such a manner that the beam is extracted by the deflector in a high-field region and then is brought through the fringing field perpendicular to the field contours.

Professor McMillan pointed out the interesting possibility of using the cam to produce focusing

in the external beam. The focal properties depend both on the angle α of the cam edge with respect to the radius and on the angular distance ϕ of the source from the cam, as shown in the insert to fig. 5. For example, the cam acts as a stigmatic lens with focus at a distance of one radius from the cam exit point when α is 45° and ϕ is 148° the focus is at infinity for an α of 26° and a ϕ of 116°. For these examples we have assumed a uniform field within the magnet and ignored the slight complication due to the electrostatic field of the deflector.

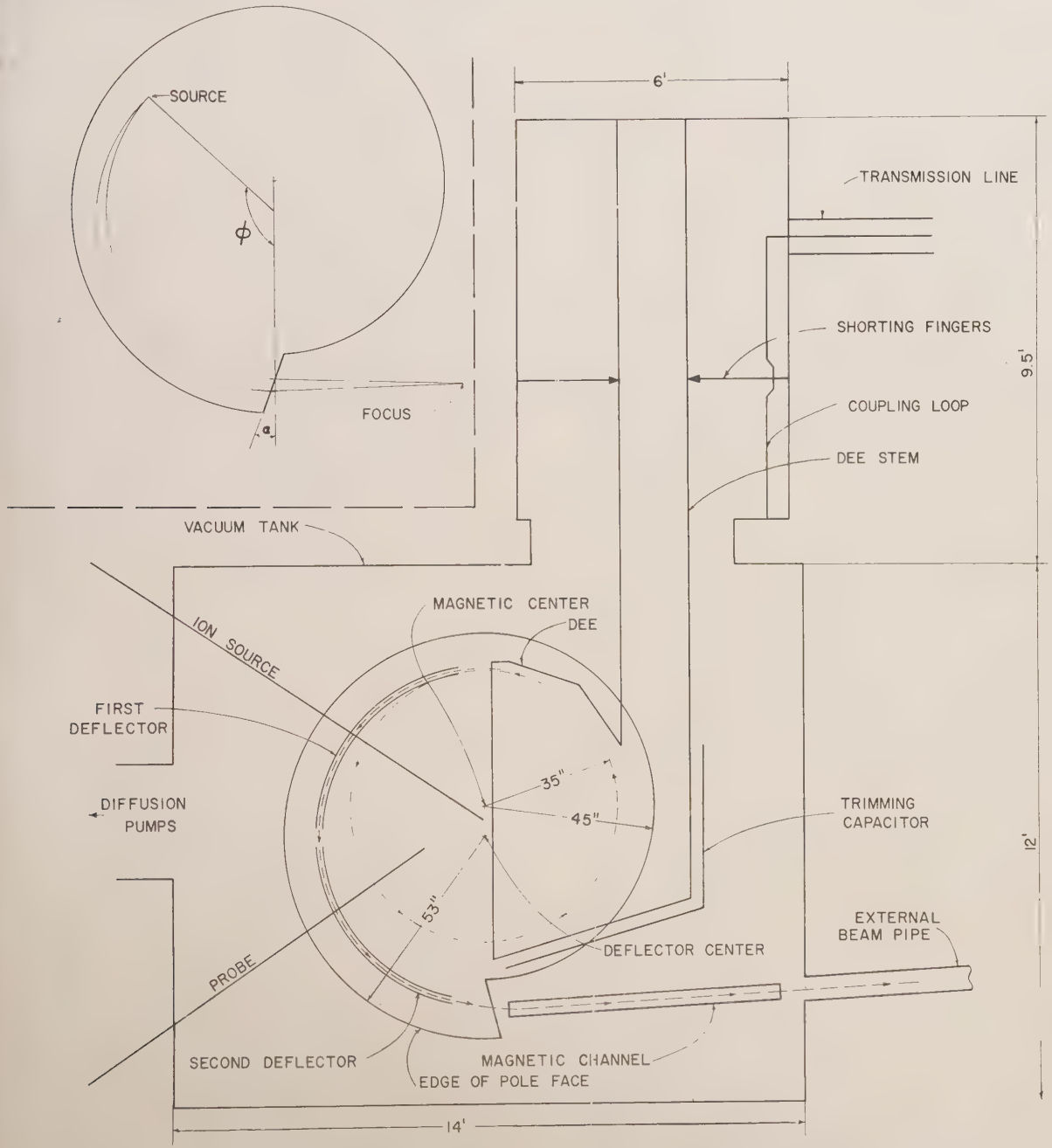

Fig. 5. Simplified elevation view of cyclotron. The insert in the upper left illustrates the possible focusing effect of the cam end, as discussed in the text.

These focusing properties could be used to advantage if there were a virtual source of particles at some known or controllable point within the cyclotron. However, we felt during the design stage that there would probably be a continuum of such sources, in which case a cam lens would focus some of the particles and defocus others. Even if there should be a unique virtual source, it was not known at the design stage where it would be or to what extent it could be controlled. For these reasons it was thought best to make the cam lens neutral for both the radial and the axial components of motion. This condition is simply that the *average* angle between the beam trajectory and the magnetic gradient vector be zero in the fringing field where the beam leaves the magnet. (The word "average" is emphasized because the magnetic contour lines flare outward in the vicinity of the edge of the cam, so that the angle between the beam and the magnetic gradient cannot be a constant here.) Incidentally, the magnetic contours are at quite an angle to the straight edge of the cam; in order to have the average contour line radial near the cam edge, the cam edge itself had to be made 15° beyond radial, as shown in fig. 5. The magnetic field is 98% of the central field value at the exit end of the second deflector and falls rapidly as the beam crosses the edge of the cam.

Within a few inches after crossing the cam edge, the beam enters an iron magnetic channel which shields it from the remaining fringing field of the magnet. Without the channel, the magnetic field along the beam line falls rather slowly because for several feet the beam is still inside the magnet coils, and because the magnetic gap here is 2.9 ft instead of being infinite. The iron channel reduces the field as seen by the beam to a negligible value within a few inches of the cam, so that the magnetic optics are both better and more easily understood. Furthermore, it allows the beam to leave the magnet at an angle which is both convenient (about 3° above horizontal) and controllable. Without the channel the beam would slowly bend upward another 25° or so and would have objectionable flaring in the radial component of motion. The channel can be moved several inches along the line of the beam, which serves to vary the angle of the beam. One inch of motion of the channel produces approximately one degree change in the angle of the external beam. The channel is remotely controlled at the console and can be moved with the magnet energized. The magnetic force on the channel, as determined from model measurements, amounts to about 2 tons at full field.

The iron in the channel throws an appreciable bump into the magnetic field in the accelerating region of the cyclotron. This effect was measured for various positions of the channel and nullified, on the average, by shimming.

All surfaces of the magnetic channel which could conceivably be struck by the direct beam of the cyclotron are covered with a layer of carbon sufficiently thick to stop the most energetic particles. The opening of the channel is 1.5 in. wide in the radial direction at the entrance and flares to 3 in. at the exit; in the axial direction, the opening is $3\frac{3}{4}$ in. and constant over the 72-in. length. The thickness of the iron walls is 2.0 in. in the flux-carrying walls and 1.0 in. in the other walls over the first of the channel, where the magnetic field is the strongest. Over the last 36 in., all four channel walls are 1.0 in. thick.

3.5. MAGNETIC FIELD MEASUREMENTS

The magnetic field in the midgap plane was explored with a bismuth resistor probe[3]) that was 0.2 in. in diameter and 0.2 in. long. This probe operates on the principle that a change in strength of the magnetic field will produce a corresponding change in the electrical resistance of the probe. Thus measurements of the probe resistance can be used to determine magnetic field strength. The bismuth resistor probe used here had a resistance that increased from 70 Ω at zero magnetic field to over 100 Ω at a field

[3]) H. B. Keller, UCRL-2249, unpublished, C. G. Dols, UCRL Engineering Note 4310-17, MT-1, unpublished. The resistance wire was Analc insulated No. 36 AWG bismuth, 0.005 in. diam.

strength of 8 200 G. (The temperature of the resistor was kept at a constant — 30°C by immersion in boiling Freon 12, to preclude any change in resistance due to temperature variation.)

The resistor was calibrated to proton resonance frequencies measured with a General Radio 620 A Heterodyne Frequency Meter. During calibration, the nuclear magnetic resonance probe and the bismuth probe were positioned in the magnet gap near each other at equal radii.

The bismuth resistor probe could be moved continuously either azimuthally or radially, and the position recorded by converting shaft rotations to digital numbers A regulated 300-V power supply produced a current of approximately 4 mA through a limiting resistor in series with the bismuth resistor. Since the bismuth resistor's potential drop was of the order of 0.5 V, the current was relatively independent of changes in probe resistance. The probe's potential drop was measured to a resolution of 10^{-5} V. This equipment produced hour-to-hour reproducibility of about $\pm$ 4 G with a probe response of 0.01 V per 0.4 G. Azimuthal field plots were obtained accurate to $\pm$ 0.5 G.

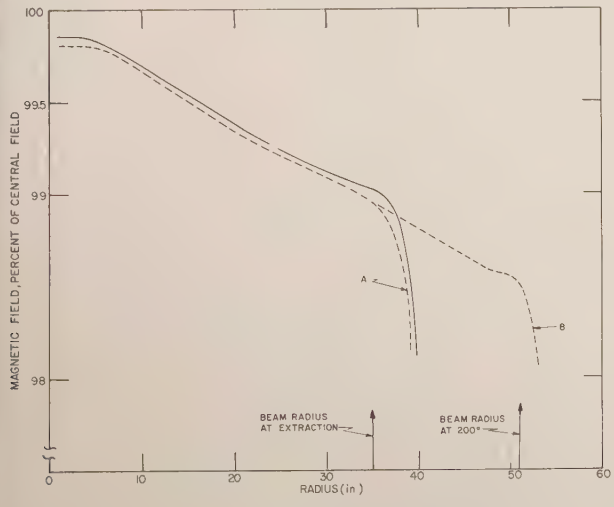

Fig. 6. Radial dependence of magnetic field. Magnetic field is expressed in percent of the central field given by extrapolation of the linear dependence back to zero radius. The solid curve and dashed curve A are for central fields of 3275 and 8468 G respectively at an azimuthal position of 45° (see fig. 8). Dashed curve B is for the higher field at an azimuthal position of 200° (across the cam).

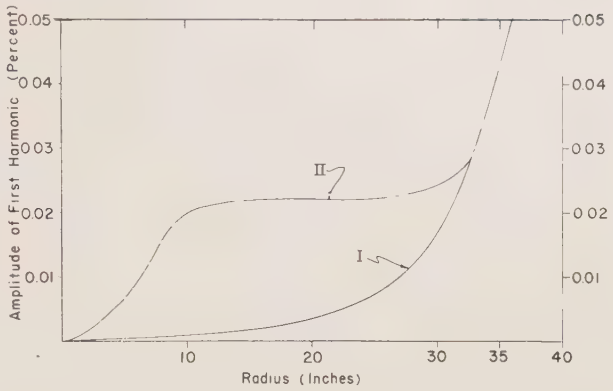

Fig. 7. Variation of amplitude of first harmonic in magnetic field with radius. The two curves labeled "I" and "II" indicate the limit of accuracy of the determination.

An IBM Card-Programmed Calculator was used to convert the nonlinear bismuth resistance data into flux density and to compute the difference between the measured and desired magnetic fields, the value of n as a function of radius for various azimuthal positions, and the first-harmonic content of the magnetic field at various radii.

The radial shape of the magnetic field obtained is shown in fig. 6 for two different field excitations. The azimuthal variation is best represented by the amplitude of the first harmonic in the magnetic field, and is shown in fig. 7 as a function of radius for a field excitation of 8 000 G. The variation of n with radius, averaged over seven different azimuthal positions, is shown in fig. 8. Hough's method[2]), using the experimentally determined values of first harmonic and n, indicates that the displacement of the maximum-radius orbit center from the geometrical center does not exceed $\frac{1}{2}$ in.

The well-known current-carrying-wire technique was used to determine the displacement of the beam from the geometric plane of the magnet[4]). This method provides a close analogy to the motion of ions in a magnetic field. However, where a radially decreasing magnetic field will provide axial focusing for a circulating beam,

[4]) Glen R. Lambertson, "Use of the Wire Loop in Locating the Orbital Surface of a Cyclotron Field", UCRL-3366, unpublished, C. G. Dols, UCRL Engineering Note 4910-04, MT-2, unpublished.

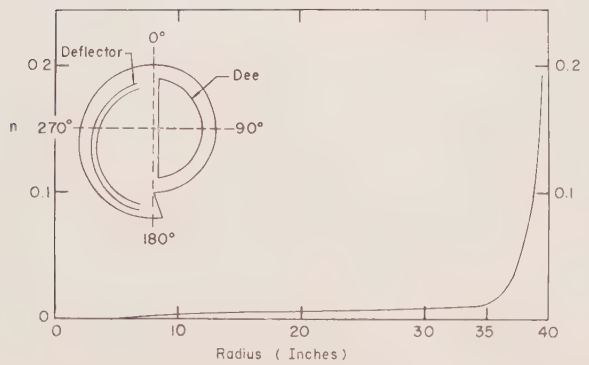

Fig. 8. Variation of n with radius. This curve represents an average of measurements made at 15, 30, 60, 90, 120, 150, and 315 degrees.

it will provide only a position of unstable equilibrium for a current-carrying wire and will in practice deflect the wire to one pole face. This difficulty has often been overcome in cyclotron median-plane measurements, where the loop was horizontal, by supplying supports at points along the wire. The fact that the accelerating plane in this cyclotron is vertical allowed the inherent instability of an isolated current loop to be circumvented by hanging the loop as the bob of a pendulum. The stability provided by the pendulum effect could be changed by adding weight at the top of the loop. The pendulum support permitted free movement in the horizontal plane, and a counterbalanced support permitted vertical motion. The equilibrium position of the loop was determined by moving the point of support until the loop did not move

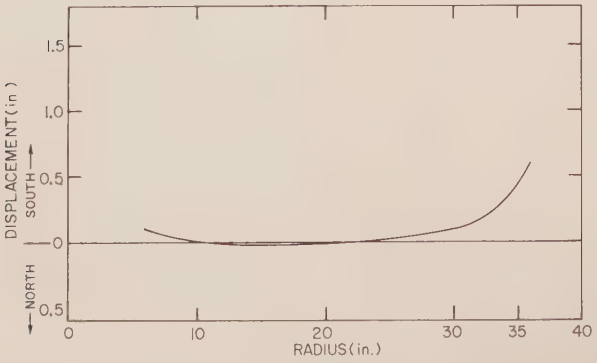

Fig. 9. Wire-loop median plane measurement. The azimuthally averaged displacement of the loop from the center of the magnet gap is shown as a function of radius for a magnet excitation of 8400 G.

when the current in the loop was increased to 2 A from its normal value of 1.5 A. Equilibrium positions were determined for a number of loop radii, and at maximum and near-minimum field excitations of 8400 and 3400 G. The observed positions of the wire loop shown in fig. 9 indicate that the median surface is displaced from the midgap plane a maximum of $\frac{1}{2}$ in. at the extraction radius.

4. Radiofrequency System

4.1. RESONATOR

Electrically the dee forms part of a resonant, high-Q system. The stem, from which the dee hangs, forms the center conductor of a large quarter-wave coaxial resonator foreshortened by the capacity of the dee to its ground planes, which are in the form of movable liners. This resonator is driven by a power amplifier through a nominally half-wave coaxial transmission line tightly coupled to the resonator by a large loop.

The cyclotron may be tuned from 4 to 9.5 Mc/s in two bands. To shift from the low to the high-frequency band, the electrical length of the coaxial resonator is decreased by shorting out its upper half by a switch consisting of four sets of shorting fingers which are hinged on the outer wall (see fig. 5). The rf contact on each of the four shorting arms is made by a 32-in. section of fingers each $\frac{1}{8}$ in. wide. The maximum current occurs at 9.5 Mc/s and is 9280 amp for a dee voltage of 180 kV. This implies a current density at the fingers of 72 A per linear in. Within each band the resonant frequency may be varied continuously by adjustment of the dee-to-liner spacing so as to match the 100 operating crystal-controlled frequencies spaced 55 kc/s apart from 4.0 to 9.5 Mc/s. The division frequency between the two bands, 6.2 Mc/s, was selected to permit maximum dee-to-liner spacing at the top of the deuteron range, where the threshold dee voltage is relatively high.

Each dee liner is suspended by two phosphor-bronze ball bearings, which carry the vertical load, and is driven by four lead screws. The bearings are mounted behind the liners out of

the rf field and are further protected from its currents by spring fingers which make contact across them. The four lead screws are connected mechanically by a motor-driven chain. The distance between dee and liners can be changed from $2\frac{5}{8}$ in. to $\frac{3}{4}$ in.

The area of the resonator coupling loop required for the low-frequency range is greater than for the high range. This difference in effective area is achieved by making the loop above the shorting fingers in the form of a 50-Ω, parallel-plane transmission line. The rest of the loop passes through an open corner between the shorting mechanisms and thus couples to the high-frequency resonant system. In the high-frequency range, the upper part of the loop forms an extension of the 50-Ω transmission line and the coupling is small because there are negligible fields in this part of the resonator; the coupling is due almost entirely to the lower part of the loop.

The trimming condenser, which is varied to keep the rf system in resonance, is located at the rear and bottom of the dee. It is mounted on ball bearings which are protected in the same way as those of the liners. The rf currents are carried from the trimmer by flexible straps connected along its length. The trimmer is designed to compensate for change in resonant frequency caused by thermal expansion and magnetic strain. Experience indicates that these effects can vary the resonant frequency as much as 1%. The geometry is such that the trimmer provides approximately the same percentage change of frequency throughout the range of the machine.

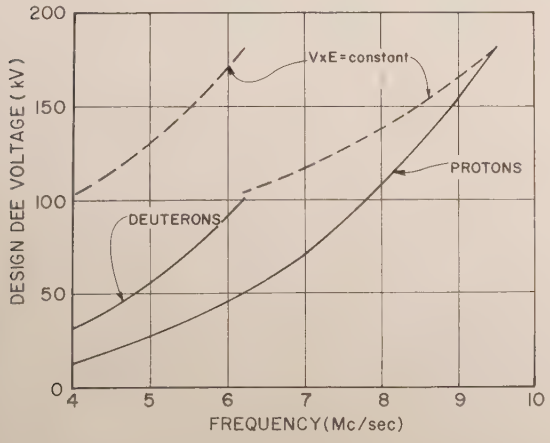

Fig. 10. Design operating dee voltage as a function of frequency. This voltage is twice the calculated threshold voltage. Also shown is a curve of the maximum dee voltage possible (based on voltage times voltage gradient being a constant) normalized to the design voltage at 9.5 Mc/sec.

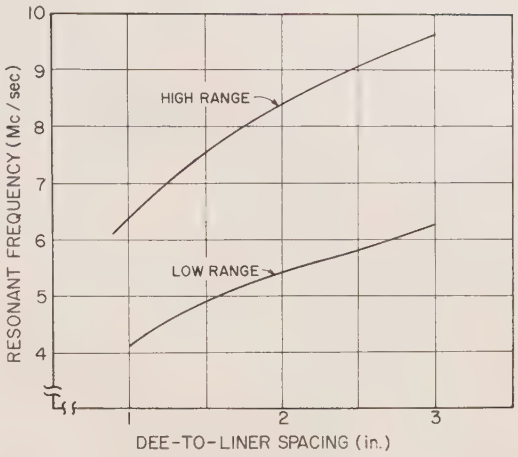

Fig. 11. Resonant frequency vs dee-to-liner spacing.

The ability to hold dee voltage within a cyclotron is determined by the materials of the high-voltage surfaces, particularly contaminants such as dust and oil, and the product of voltage and gradient. By comparison of figs. 10 and 11 this product can be determined for any frequency, and it is apparent that the most severe sparking condition occurs at 9.5 Mc/s. As the frequency is lowered by decreasing the dee-to-liner spacing, the threshold dee voltage decreases more rapidly than the sparking voltage. The machine was designed to operate at twice threshold, which for 9.5 Mc/s is 180 kV. With sufficient bake-in time 180 kV might be held, but under ordinary conditions the maximum voltage is 150 kV. The usual operating voltage of 120 kV is sufficient to produce a good stable beam.

The rf skin power of the resonator, transmission line, and final amplifier is about 150 kW. The final amplifier was designed to deliver 300 kW, leaving 150 kW for stray ion and beam losses. The rf power is delivered to the resonator by a half-wave-length, 50-Ω transmission line, which permits location of the final amplifier outside the concrete shielding. A longer line is required for the low range than for the high range

because of the increased wave length. The extra line is added by means of a transmission-line switch. The increased length of line also shifts the frequency of a transmission-line mode in the vicinity of 12 Mc/s so that it does not line up with the second harmonic at the upper end of the low range.

A driven type of rf system was chosen for the 90-in. cyclotron because this type is basically more stable and less difficult to develop than the self-excited type for a variable-energy machine. Parasitic oscillations are much more easily avoided in the driven case because the grid circuit is coupled to the anode only through the grid-plate capacitance of the final amplifier. This is an almost pure capacitance and free of modes up to at least 100 Mc/s and therefore it is easily neutralized over a wide range of frequencies. Also the grid circuit is physically smaller than in the self-excited case and has fewer modes within the range of frequencies in which parasitic oscillations are possible. In addition, a driven system is simpler because it has no grid-circuit transmission line and no grid-circuit vacuum insulator.

The rf modes were studied on a full-scale model. The most important problems occur when a resonator mode is excited by a harmonic. There are two unfortunate conditions which can occur: (a) The harmonic voltage may build up along the transmission line in such a phase that a voltage maximum occurs at the anode of the final amplifier, reducing the efficiency and the available power. (b) The voltage maximum may be displaced from the final-amplifier anode in such a way that a step-up ratio exists between the anode and the vacuum insulator and produces excessive voltage at the insulator.

Fortunately, most of the higher-order modes are foreshortened by the anode capacitance of the final amplifier and the other lumped capacitances and inductances throughout the resonator, so that the higher modes are not harmonically related to the fundamental. The frequency spectrum was searched for the two undesired conditions described above. Through slight adjustment of the length of the transmission line, a favorable mode distribution was found which did not appreciably disturb the curve of dee voltage vs frequency.

A second rf problem arose which was associated with the voltage taper along the dee edge. This condition results from the necessity, in this particular case, of attaching the dee stem to the dee from one side rather than symmetrically. A quarter-scale model resonator was built in which a wood dee was painted with conducting paint and then copper plated. This construction lends itself well to experimental modification. Initially the voltage of the lower tip of the dee was higher than that of the upper tip. A notch was then cut at the upper rear of the dee (fig. 5) so that the current flowing to the top of the dee edge would travel a longer path, thus raising the voltage at that point. The dee voltage taper was reduced to about 1.5%. The remainder of the modeling program consisted of routinely checking the theoretical rf analysis and adjusting the resonator lengths to precisely the right values.

4.2. FINAL AMPLIFIER

An RCA A2332 shielded-grid triode is used as the final amplifier. The maximum operating conditions as determined from the constant-current characteristic are:

plate voltage	20 kV dc
plate current	25 A dc
grid current	0.5 A dc
transconductance	87 000 micromhos
grid resistor	1400 Ω
grid driving power	1500 W
efficiency	79%
rf power output	380 kW

The type A2332 tube is capable of considerably more power than is indicated above. In the present application, the power is limited by the 500-kW power supply. The thorough shielding of the massive control grid from the anode and the high power sensitivity make the tube well suited to accelerator applications.

A modified form of broad-band grid neutralization is employed and does not require adjustment over the range of frequencies to which the cyclotron tunes, i.e., 4.0. to 9.5 Mc/s. The

grid circuit consists of a foreshortened parallel-conductor line, and is tuned by a shorting plane which is mounted on motor-driven lead screws within the conductors of the line.

4.3. EFFICIENCY SERVO SYSTEM

The cyclotron trimmer is controlled by a servo system to keep the resonator in tune with the crystal oscillator. The phase angle between grid and anode voltages of the final amplifier is measured and the trimmer position adjusted to keep the phase angle constant. The servo electronics consist of four chassis: two frequency converters (one installed in the final amplifier cabinet near the grid and the other near a pickup loop at the resonator), the phase detector in the control room, and the servo amplifier located with the other power equipment.

The frequency converter, which preserves phase angle, was developed for this application. It employs diodes in such a way that the output signal is exactly equal in amplitude to the smaller of the two input signals. Because the amplitude of the local oscillator signal is independent of cyclotron operation, it is made the smaller of the two signals, and thus no adjustment of the phase-control equipment is required as the operating conditions of the cyclotron are varied. The output frequency of the frequency converter is 55 kc/s, which is suitable for transmission to the phase detector in the control room. The latter produces a dc output signal which controls the servo amplifier and thus drives the cyclotron trimming capacitor.

4.4. DRIVER

The driver employs three tubes, a 2E26, a 4-250, and a 6166, the last of which drives the grid of the A2332. The tuned circuits in the driver chassis are ganged and driven by a servo system which is controlled by a potentiometer on the shaft of the crystal switch in the master oscillator. Thus, tuning the master oscillator automatically tunes the driver amplifier. A similar servo automatically tunes the final amplifier grid circuit.

4.5. MASTER AND LOCAL OSCILLATORS

In order to break through the multipactoring region, dee voltage is built up as rapidly as possible. This is accomplished by keying the amplifier chain at the screen of the 4-250 tube with a relay after all other voltages have been applied. In order to establish dee voltage, however, the resonator must first be tuned to the signal frequency. This is accomplished by connecting a small variable-frequency oscillator directly to the transmission lines by an appropriately interlocked motor-driven switch. The oscillator provides only a few volts on the dee, which is not sufficient to cause a discharge but may be measured by means of a sensitive voltmeter. Thus the resonant frequency is measured and adjusted to that of the master oscillator. As an aid to quick, precise adjustment, the beat note is presented on a loudspeaker. After the resonator is tuned, the tune-up oscillator is disengaged and normal voltages are applied to the amplifier chain, which excites the dee.

4.6. FINAL-AMPLIFIER ANODE POWER SUPPLY

Two 10-kV, 25-Amp power supplies are series-connected to supply the final amplifier. Each rectifier contains six 857B rectifier tubes connected in a three-phase bridge circuit. One power tranformer is connected delta-delta, whereas the other is connected delta-wye; thus the ripple from the combined power supply is 12-phase the ripple frequency is 720 cps. The input voltage of the rectifier transformers is adjusted by means of an induction regulator.

The power supply includes a type GL5779 ignitron crowbar for protection of the final amplifier tube. The crowbar removes the power supply from the power line rapidly by interrupting the firing of the ignitrons in the ignitron contactor. The ignitron contactor is used also to limit the inrush currents of the plate transformer and induction regulator by retarding the igniter firing pulses and allowing the phase to advance to full conduction over a 10-sec period. The induction regulator is protected from the snap-out currents of the ignitrons by a resistance-capacitance surge network. This is a rather large

unit mounted on the transformer pad. Further protection of the transformer equipment is accomplished by means of Westinghouse Autogaps and Thyrite.

The power supply includes a recycling system to re-establish anode power following a fault. When a fault occurs, the crowbar fires within 10 microseconds and within the next 8 milliseconds the ignitron contactor removes the power supply from the line. Five seconds later the recycler reactivates the power supply.

The ignitron crowbar is fired only in the case of extreme over-currents of 150 A or more. It is intended to provide protection against power arcs within the final amplifier tube and insulation breakdown in the anode circuit. Minor faults activate only the excitation crowbar which simply removes grid excitation from the final amplifier. This is described in the following section.

4.7. SPARKING AND TRANSIENTS

An important consideration in the design of cyclotron rf equipment is the transient nature of the load. When the dee sparks, the energy stored in the resonator changes suddenly and a high-voltage transient propagates through the resonator and transmission line. The transmission-line insulators, the final amplifier, and the vacuum insulator are the components most easily damaged by the transients. Transmission-line insulators are protected by corona shields and spark gaps. But the problems associated with the final amplifier and the vacuum insulator are more subtle. The danger at the final amplifier is that the transient will initiate a power arc within the tube. When this occurs the crowbar removes plate power within 10 μsec, which is sufficiently rapid to avoid damage. The danger at the vacuum insulator is that it might be broken by the heat from a spark-initiated discharge. A discharge detector is employed which consists of a copper ring located on the vacuum side of the insulator and charged to approximately 1500 V. In the event of a discharge, ions flow to the ring and produce a pulse which opens the ignitron contactor.

The power-supply equipment is protected by Thyrite and spark gaps from transients produced by the crowbars. The techniques are the same as those used in the electrical power industry.

5. Deflector System

The deflector is located in the cam region of the magnetic field, as shown in fig. 5. The two major requirements of the deflector were to deflect the beam in a magnetic field roughly equal to the central field, and to steer the beam into the magnetic channel. The first requirement necessitated electric fields of as much as 53 kV/cm, or 140 kV across a deflector gap of 1 in. The magnetic channel can be moved remotely only along the beam direction, a motion useful for small angular corrections of the beam in the median plane. This arrangement requires extraction of the beam from a fixed 35-in. radius and accurate steering into the channel throughout the range of magnet excitation from 2600 to 8200 G. Since it was not known in the design stage how easily this could be done, the deflector was made in two 75° sections which have independent high-voltage supplies and can be independently moved from the control desk. Each end of the ground and high-voltage electrode of each section can be moved radially over a range of 6 in. Thus the position and the separation of electrodes, as well as the high voltage applied to each section, can be independently changed.

The high-voltage electrodes were made of Inconel. Operation was started using graphite septums, but they have now been replaced by tantalum septums which normally last from one to two months when operating five 24-hour days per week.

The deflector power supplies were manufactured by the Beta Electronic Company to our specifications. They deliver a maximum of 140 kV at 15 mA and have an internal impedance of 1.5 MΩ. The supplies are connected to the 220-V line by a thyratron contactor which may be opened within 8 msec in the event of a deflector supply over-current. The contactor contains a recycler which re-establishes deflector voltage automatically. A motor-driven variac controlled by a servo amplifier provides deflector-voltage regulation.

6. Vacuum System

The vacuum tank is welded, rectangular aluminum-alloy box[5]). It is 10 ft square and 2 ft deep and is mounted in the magnet gap so that the pole pieces form the sides of the vacuum barrier. One side of the tank has a diaphragm $\frac{5}{8}$ in. thick that permits misalignment or deflection of the magnet gap by $\pm\frac{1}{16}$ in. and prevents the transfer of loads to the vacuum tank. Initial tests of this tank showed that the best pressure obtained on a liquid-nitrogen-trapped ion gauge was 1.0×10^{-6} mm Hg, and that the total leak rate was 0.23 μl/sec.

The rf cavity is a vacuum vessel made of copper-clad steel $\frac{1}{2}$ in. thick which eliminated the need for a separate copper liner and reduced the overall size and cost. Two 32-in. mercury diffusion pumps and cold baffles were used originally. The baffle temperature of 161°K was maintained by a cascade refrigerator using Freon 22 and Freon 13. The refrigerator was used successfully the first 17 months of cyclotron operation and accounted for only 4.3% of the maintenance down time. However, during the 20th month, after three months of refrigerator troubles, the refrigerator was severely damaged and had to be taken out of operation and rebuilt. Vacuum is now maintained using one pump and one baffle converted to liquid nitrogen use.

Mercury pumps were chosen to keep organic materials out of the vacuum system and thus aid in obtaining the required high rf voltage gradients. As a further aid, dry lubricants were tried initially. These have now been replaced by Rulon or Nylotron bearings[6]), which have performed more satisfactorily.

7. Ion Source and Probe

A hooded ion source of the Oak Ridge type is used, consisting of a hot filament and a tantalum tube to contain the plasma. A small slit is cut in the side of the tube through which ions are extracted. For easy and fast maintenance, both the filament and the ion source can be extracted from the vacuum system through air locks without disturbing the tank vacuum. The ion source is mounted on the end of a long rod and several degrees of freedom are provided for positioning. The source can be rotated about the axis of the rod to align the hood with the magnetic field. The filament can be moved for proper alignment with the source hood. In addition, the entire ion source may be moved both radially and azimuthally with respect to the magnet center. All of these motions have remote control and indication at the console.

An internal probe provided with several probe heads can be used to detect the beam turn-to-turn spacing, radial oscillations, and axial oscillations. Other probe heads have quick-change features for bombarding various materials and targets. The probe can be inserted and rotated remotely from the console, where its radial position is indicated to within 0.1 in.

8. Physical Arrangement of Accelerator

The building available for the cyclotron was a wooden, arch-roofed, former navy drill hall, 312 ft long, 116 ft wide, and 42 ft high. A 15-ton, semi-gantry crane travels down the length of the building and over the cyclotron.

The cyclotron arrangement is shown in fig. 12. The cyclotron is located in a pit 29 ft long, 25 ft wide, and 18 ft deep. Adjacent to the cyclotron pit is an experimental 40-ft cubical pit. Considerations of cost and the height of the rf system determined the fraction of cyclotron and experimental space that should be built above ground level, as concrete-block wall, and that which should be built below.

Surrounding both pits is a concrete-block, radiation-shield wall 12 ft high and 5 ft thick. The two pits are separated by a 5-ft-thick concrete block wall with openings for the beam tube. The concrete shielding blocks are reinforced regular concrete (150 lb/ft^3 density) 5 ft long, 4 ft high, and 5 ft wide, with tongue-and-groove joints 6 in. high and 30 in. wide all around.

[5]) Aluminum alloy 6061-T6 satisfied the magnetic requirements, appeared to cost the least, and offered some new experience in welding heavy aluminum plate. Welding procedures and tests are reported in UCRL Engineering Note 7202–04, M1 and M2.

[6]) Rulon was obtained from the Dixon Corporation, Bristol, R. I., and Nylatron from the Polymer Corporation of Pennsylvania, Reading, Pa.

The cyclotron pit has a 3-ft-thick roof made of concrete beams weighing 15 tons each. A wood roof 3 ft thick was added to the adjacent experimental pit after it was found that the neutron flux level outside the pit could exceed the tolerance level when neutrons were produced. This shielding roof reduced the exterior level by factors of 10 to 100.

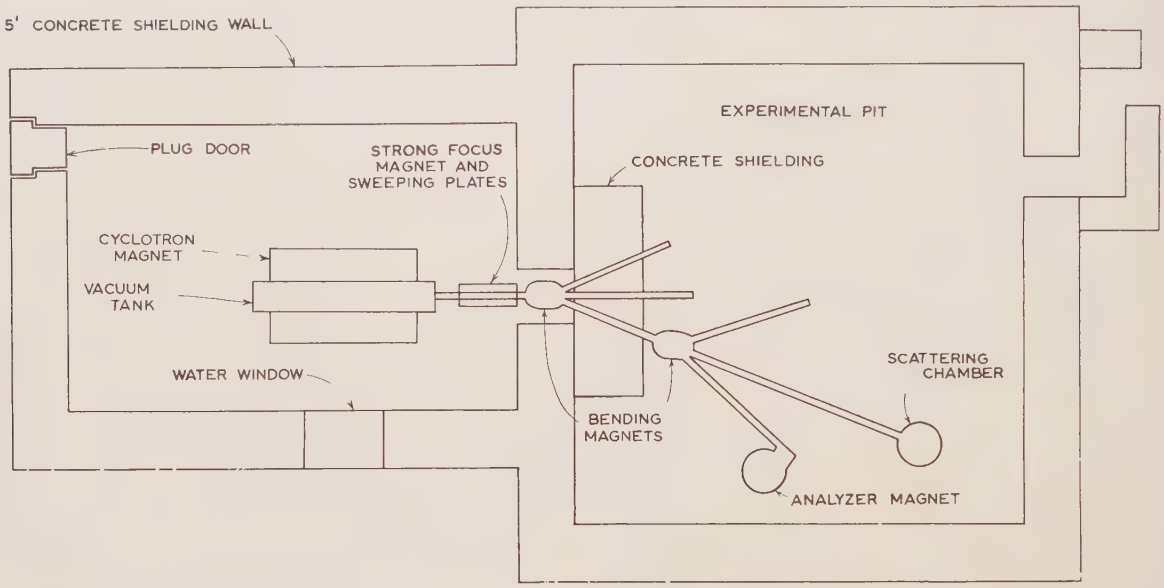

Fig. 12. Plan view showing the cyclotron and experimental pits, and the external beam pipes available.

The entrance to the cyclotron pit is closed by a power-operated concrete door 5 ft thick. The cyclotron pit has a water window 5 ft thick through which a telescope is sighted to view the operating conditions of the ion source, the deflector septum, and other components.

9. Results

9.1. INITIAL OPERATION

The first attempt to accelerate a beam was made on 18 February 1955. (The rf system had already been tested for a time of 16 running hours.) After 12 hours of acceleration time, a beam of 800 μA was obtained at full radius. The machine has now operated for five years with proton, deuteron, and alpha beams readily available.

9.2. BEAM CHARACTERISTICS

The dynamics of the internal beam have been explored with various measuring probes. Radial dependence of the internal beam is shown in fig. 13. A probe consisting of a fine needle parallel to the magnetic field was used to locate the individual turns of the internal beam; the results are shown in fig. 14. A segmented probe was used to examine the axial oscillations occurring during beam acceleration, and typical results are shown in fig. 15.

9.3. EXTERNAL BEAM

Operating experience has shown that from 30 to 75% of the internal beam can be extracted through the first deflector, and from 15 to 25% of the internal beam through both deflectors. Since the position of the deflectors is fixed by the external beam plumbing and since the final orbit centers vary over the energy range of the cyclotron, it is necessary in general to steer the beam into the deflector properly by means of the first harmonics produced by the pole face windings. Experience has shown that this system works well.

The optical properties of the external beam after it leaves the magnetic channel have been measured by passing it through a carbon slab having a matrix of $\frac{1}{8}$-in.-diameter holes on $\frac{1}{4}$-in. centers. This serves to break up the beam into many small rays the direction of each of which is

detected by the darkening it produces on ozalid paper put about three feet beyond the carbon. Tracing each ray from its spot on the ozalid paper through its corresponding hole in the carbon shows that all of the beam appears to diverge from a single point source located inside the lower electrostatic deflector about two ft from the cam edge. This experiment has been performed with protons at seven different energies ranging from 2.8 to 14 MeV, always giving the same position of the virtual source, within experimental uncertainty ($\pm$ 1 ft). The beam profile is roughly elliptical; most of the beam is within an elliptical cone whose half angle is 0.30° in the radial direction and 0.15° in the direction parallel to the magnetic axis. The beam produces a spot approximately 1 in. high and $\frac{1}{2}$ in. wide near the exit end of the magnetic channel, about 6.5 ft from the cam edge.

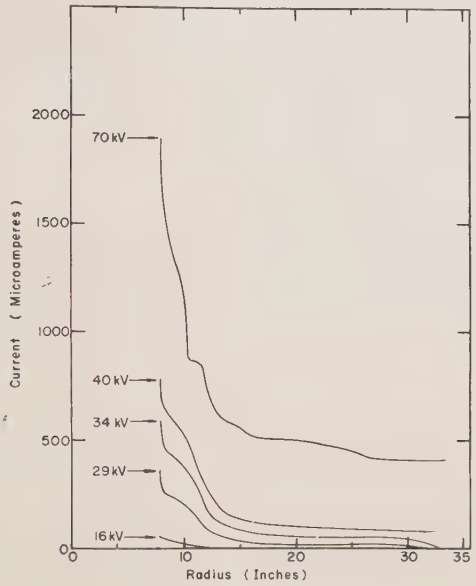

Fig. 13. Radial dependence of internal beam. Protons were accelerated to 5.36 MeV, with a cyclotron frequency of 5.760 Mc/s. The measurement was made for a number of dee voltages to verify the theoretical threshold voltage of 20 kV.

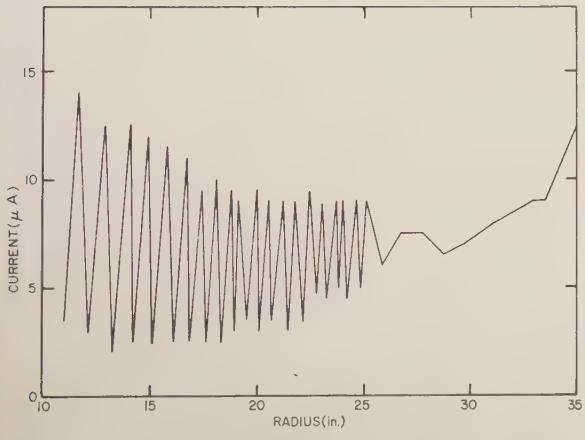

Fig. 14. Spacing between turns observed while accelerating deuterons to 11.8 MeV at a dee voltage of 100 kV. The current was collected on a $\frac{1}{16}$-in.-diam needle placed perpendicular to the median plane. The curve does not show actual beam profile. No attempt was made to obtain more than the radial position of the maxima and minima.

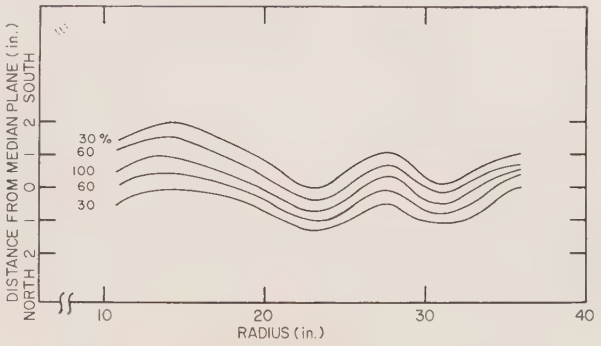

Fig. 15. Axial oscillations observed using a four-element segmented probe (each element $\frac{1}{2}$ in. wide) while accelerating protons to 5.5 MeV with a cyclotron frequency of 5.760 Mc/s and 80 kV dee voltage. The observed currents were used to construct contours of peak, 0.6 of peak, and 0.3 of peak beam intensity versus radius. The results of a number of such investigations at widely different frequencies agreed well with the expression $\omega_z = \omega n^{\frac{1}{2}}$, where ω_z and ω are the axial oscillation and cyclotron frequencies.

Sample portions of the external beam have been found to have an energy spread of less than 1% using a differential range type detector; and practically all of this measured spread can be accounted for by instrumental effects produced by the range-measuring equipment. However, when the beam is explored vertically and horizontally for spread in energy, it is found that there is a 2% difference in energy from top to bottom of the beam but no measurable change in the horizontal direction. It has been found at times that modulations of both 120 and 720 cps are present in the beam. The time spread of an individual beam pulse has been measured to be typically 3 mμsec at 7 Mc/s cyclotron frequency, or 2% of the rf cycle.

9.4. THIRD HARMONIC ACCELERATION

In normal cyclotron operation the particle orbital frequency and the accelerating rf are equal. However, it has long been recognized that other acceleration modes are possible in which the two frequencies are harmonically related. In particular, acceleration is possible with 180° dees if the rf is three times the orbital frequency. We have used this principle in order to obtain energies less than those possible with normal operation. For example, in one experiment in which a deuteron beam of 3 MeV was required, this method was used to produce an external beam of normal intensity.

9.5. BEAM SWEEPING

Electrostatic displacement of the beam in phase with submultiples of the cyclotron frequency has been employed to extend the low-energy limit of time-of-flight experiments. Deflection plates 18 in. long and 4 in. apart are placed astride the beam path near the cyclotron. A maximum peak-to-peak voltage of 40 kV at an rf equal to one-fourth of the cyclotron frequency can be applied to the deflection plates and used in conjunction with appropriate steering and phasing equipment to permit only every second or every fourth beam burst to pass through a slit, and deflect the unwanted bursts. For instance, with an acceleration frequency of 9 Mc/s and a neutron flight path of 500 cm, the lowest-energy neutron which can be observed by the time-of-flight equipment is about 8.5 MeV before overlap with the gamma rays from the next burst occurs. But when the sweeper is operated to accept every fourth burst, the minimum energy observable is reduced to 0.66 MeV. This system has performed very satisfactorily.

9.6. EXPERIMENTAL FACILITIES

At present the beam can be focused by a quadripole lens and directed by means of two bending magnets to five different regions within the experimental pit. Three of these beam pipes lead to semi-permanent installations near the pit walls where there are located a radioisotope production facility, a 40-in. scattering chamber, and a charged-particle magnetic analyzer. The other two beam pipes bring the beam to the central region of the pit and have been used normally to study mono-energetic neutron interactions and reactions in which neutrons are produced.

Acknowledgments

The design, construction, and successful operation of the cyclotron depended upon the efforts of a large number of people at Berkeley and Livermore, and only a few of these can be listed here. The late Professor E. O. Lawrence, Professors E. M. McMillan, K. R. MacKenzie, J. R. Richardson, and R. L. Thornton, and Dr. E. J. Lofgren and Enos Kane contributed much to the initial planning of the accelerator.

J. W. Kelso, P. E. Frazier, and O. M. Barlow were involved in the design of the rf system, and Frazier has also contributed many improvements since the machine was finished. W. L. Dexter, M. Harris, and J. R. Mitchell designed and supervised the installation of the electrical and control systems. The Berkeley mechanical engineering group included (among many others) D. H. Vorkoeper, W. F. Eaton, and R. Marker, who were responsible for the mechanical design and the supervision of construction of the components, which was done both in Berkeley shops and by outside fabricators. The magnetic field measurements and shimming corrections were done by the Berkeley magnetic field measuring group, under the direction of H. B. Keller and including C. G. Dols and J. H. Dorst. Edna Vienop handled the reduction of the magnetic field data. The refrigeration system was designed by H. R. Smith and P. B. Kennedy.

Installation of components at Livermore was supervised by I. W. Snyder. Mechanical design work at Livermore was under the direction of first J. D. Fahey and then H. E. Brooks. The operation of the cyclotron was first the responsibility of R. K. Mullins, J. A. Galvin, and O. A. Tvietmoe, and now, of L. M. Erickson and D. R. Rawles. Construction of many of the features added to the accelerator has been supervised by L. Talbot and J. A. Gray. A. Bratenahl, R. Stahl, R. Booth, V. J. Ashby, and J. M. Le Blanc were involved in studies of the quality of the internal and external beam.

NUCLEAR INSTRUMENTS AND METHODS 9 (1960) 303–314; NORTH-HOLLAND PUBLISHING CO.

BEHAVIOUR OF PHOTOMULTIPLIERS AGAINST SHORT LIGHT-PULSES

C. CERNIGOI, I. GABRIELLI and G. IERNETTI

Istituto di Fisica dell' Universita, Trieste

Istituto Nazionale di Fisica Nucleare, Sottosezione di Trieste

Received 5 August 1960

The response of some photomultiplier to very short light-pulses is considered. Three light sources have been used: hydrogen discharge, plastic scintillator and Čerenkov light. The hydrogen discharge lamp is used for tests where a fixed time reference is required. The comparison among the responses to the three kinds of light pulses and the single electron pulses gives some characteristic features of the photomultipliers.

1. Introduction

In a preceding paper[1]) we studied the response of some high gain photomultipliers to high-frequency modulated light. The purpose of this article is to present the responses of the same photomultipliers against very short light-pulses, in order to give also some explanations of the failure of the high-frequency response under certain conditions.

Three kinds of light sources have been used: flashes from a hydrogen discharge lamp[2]), light pulses from plastic scintillators and light pulses from Čerenkov radiation.

With the light pulses from the hydrogen lamp several investigations can be made; among these we considered the variations of the electron transit-time mean value resulting from the displacement of the starting point of the photoelectrons on the photocathode area, the dependence of the rise and decay time of the pulse on the cathode illumination conditions, the broadening of the output pulse with increasing light level, the degree of linearity of the photomultiplier output and the resolving power against two light pulses separated by a variable time interval.

The results obtainable with H_2 light pulses can be extended, to a certain degree, in the case of Čerenkov light pulses or pulses from scintillators, taking into account the pulse shape given by the photomultiplier in these cases.

2. Experimental Procedure

In all cases the procedure of investigation was based on the observation of the output pulses on

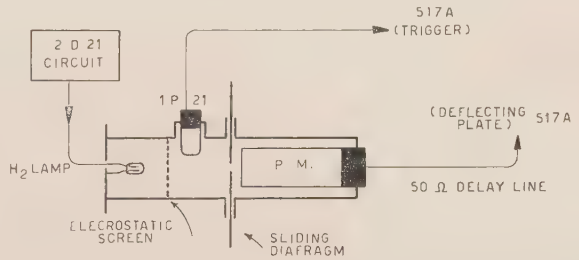

Fig. 1. Experimental setup.

the screen of a 517-A Tektronix scope, the vertical plates of which were directly connected, through a suitable 52-ohm delay cable, to the photomultiplier anode. Damping resistances (total value 180 ohm) were connected in series to the vertical plates pins.

In the case of hydrogen lamp light pulses, the triggering of the time axis was obtained by the output of an auxiliary 1P21 photomultiplier viewing the same light as the photomultiplier under test.

The trigger stability is very good (see fig. 9), due to the fact that the 1P21 is working in its saturation region.

The schematic arrangement is shown in fig. 1.

[1]) a) C. Cernigoi, I. Gabrielli and G. Iernetti, Nucl. Instr. & Meth. 6 (1960) 193.
b) Supplemento Nuovo Cimento 16 (1960) 256.

[2]) J. H. Malmberg, Rev. Sci. Instr. 28 (1957) 1027.

With plastic scintillator and Čerenkov light, the triggering signal was taken through a "takeoff system", as suggested by C. N. Winningstad[3]); in this case the length of the delay cable required was greater than in the first system.

For the plastic scintillator pulses, a piece of 5 mm in thickness and 1 cm^2 of scintillating material, was placed on the photocathode area; some sheets of absorbing and diffusing paper were placed between the hydrogen lamp and the photocathode.

The resolving time of the photomultipliers was measured by collecting simultaneously the light from the hydrogen lamp and the light through curved plexiglass light pipes of lengths realizing the required delay between the two light pulses.

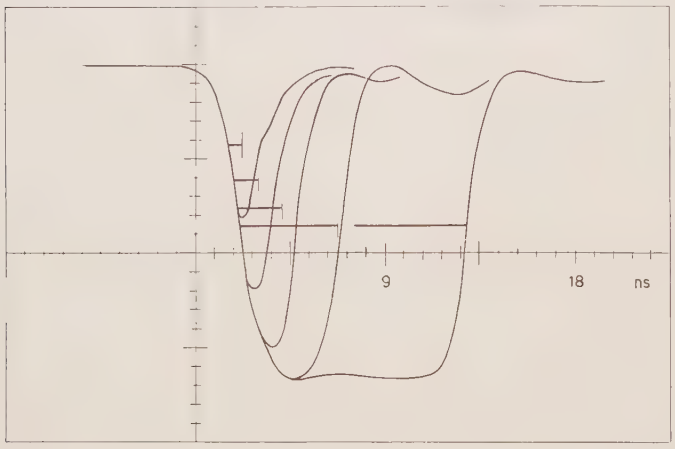

Fig. 2a. Response of the display equipment, 52 ohm line and vertical plates circuit, to mercury switch pulses of increasing duration. True widths are indicated.

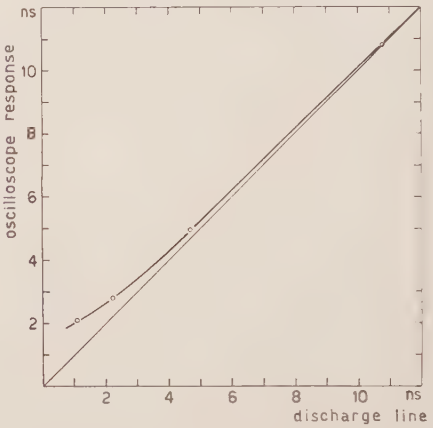

Fig. 2b. Width at half amplitude of the displayed pulse against length of the discharge line.

β rays of 2.34 MeV were used to obtain scintillations.

The Čerenkov light was given by cosmic ray muons in a plexiglass cylinder, 10 cm in height, with the base equal to the photocathode area and optically connected to it.

For studying the variations of the mean value of electron transit-times, a movable "pointlike light illumination" was obtained by means of a sliding and turnable diaphragm, located close to the photocathode of the photomultiplier under test. The diaphragm itself has a series of calibrated holes, in order to vary the light flux according to well defined ratios.

The rise and decay of the output pulse, its broadening and the linearity of the response versus increasing light flux, were investigated either with "pointlike" cathode illumination or with spread illumination; in the latter case, The two light pulses were separately equalized in intensity and the delay was measured on the time axis.

The rise and decay time of the system, delay cable plus vertical plate circuit, was evaluated by means of a S.K.L. mercury switch pulse generator.

In fig. 2 are shown the responses of the oscilloscopic system to the S.K.L. pulses of different lengths and intrinsic rise and decay time of 0.5 ns (from 10 to 90 per cent). The oscilloscopic rise and decay times for rectangular pulses longer than 5 ns are of 2.3 ± 0.1 ns. For rectangular pulses shorter than 5 ns the rise time is less than the above value and is dependent on the pulse length; correspondingly the amplitude of the response decreases. In this case, the decay time is essentially determined by the L,R,C, values of the vertical plates circuit; a value of 2.1 ± 0.1 ns is found, not dependent on the pulse length. The true values

[3]) C. N. Winningstad, Rev. Sci. Instr. **29** (1958) 578.

of the pulse length, reported in fig. 2, were determined by the cable length of the discharge-line.

The calibration of the time axis was accomplished by means of a 100 Mc/s sine-wave oscillator.

divider suggested by Ashkin *et al.*[4]). The H.V. dividers are redrawn in fig. 3.

In order to give some interpretations to the results reported below, it is useful to consider the photomultiplier as an electron-optical device consisting of two main parts: the structure from

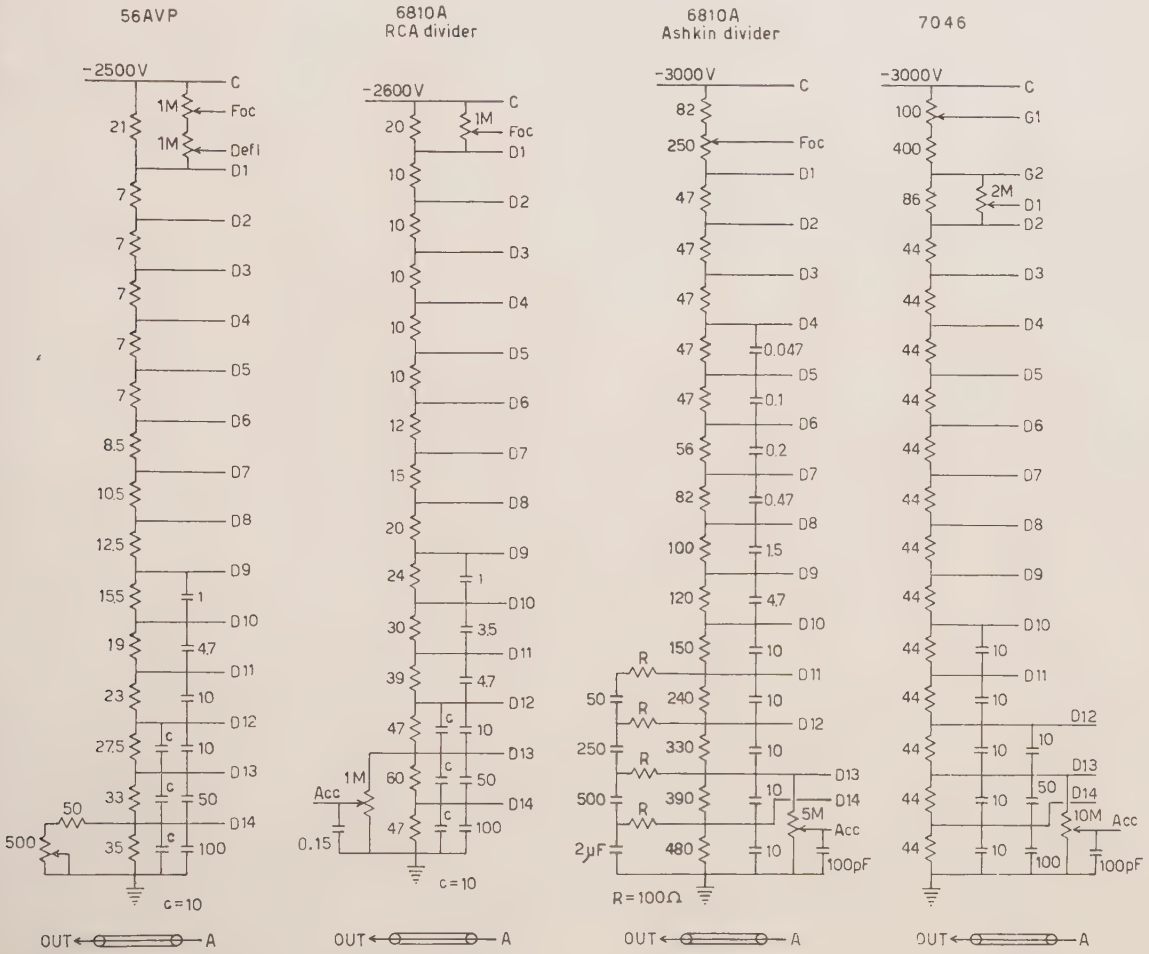

Units KΩ; 10^{-9}F

Fig. 3. High-voltage dividers used for the photomultipliers. (The adjustable voltages were kept to values corresponding to the maximum peak amplitude output without reducing the sensitive photocathode area.)

3. Experimental Results

We tested, more or less extensively, the following photomultipliers: 6810–A, 7264 and 7046 of RCA, and the 56–AVP of Philips.

The high-voltage dividers were chosen as suggested by the respective manufacturers; in addition the 6810–A was also tested with the H.V.

the photocathode to the first dynode and the electron-multiplier structure. In the first structure the transit time of the photoelectrons is mainly determined by the position of their starting point and by the focalization properties

[4]) J. Ashkin, T. Fazzini, G. Fidecaro, A. W. Merrison, H. Paul and A. V. Tollestrup, Nuovo Cimento **13** (1959) 1240.

of the structure itself. In the second structure the transit time of the electrons is affected by the focalization properties of the last multiplying stages under high space-charge density conditions.

The performance of the first structure determines the response at different distribution in space of the incoming photons; the performance of the second structure is mainly responsible for the response at different light flux input and different distribution in time of multiplied electrons.

In order to distinguish, as far as possible, the

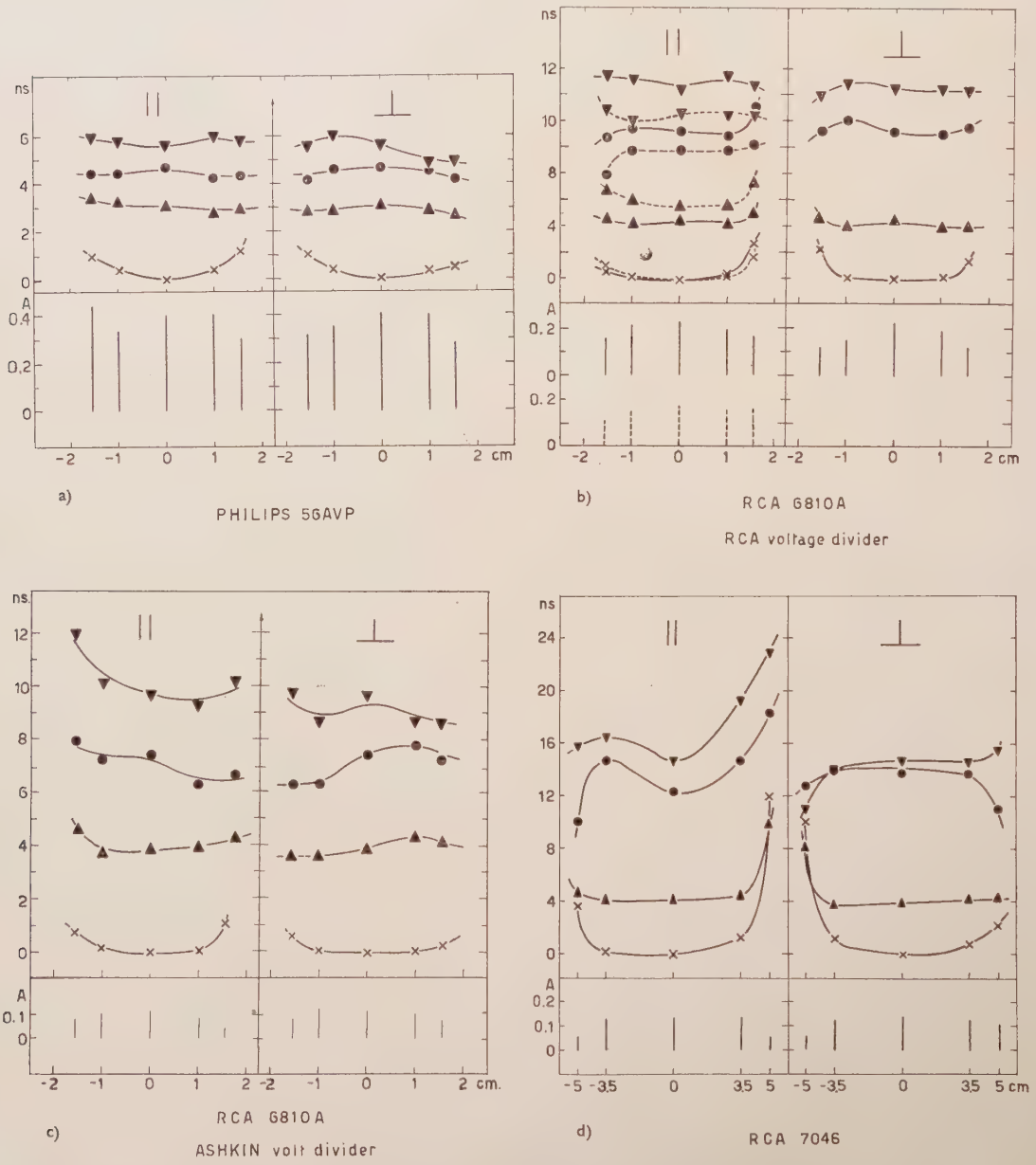

Fig. 4. Variations, for a diameteral exploration of the photocathode, with "pointlike" illumination from hydrogen lamp

▲ Risetime (from 10 % to 90 % of amplitude).
▼ Decay-time (from 90 % to 10 % of amplitude).
● Width at half amplitude.
× Time displacement of the 90 % amplitude point.

A — Peak current (A) at constant light input. (In fig. 4b, dashed lines refer to a different value of the focalization electrode voltage.)

effects on the output pulse of the two structures, we performed first the study of the variations due to the displacement of the point of illumination on the photocathode at constant light flux; then the light flux was increased at a fixed point of illumination (the center of the photocathode area).

When spread light is hitting the photocathode area, the effects of the two structures combine together.

In this case it is interesting to compare the responses when the incoming photons are bunched in a very small interval, as with Čerenkov light, to the responses with photoelectrons having a certain distribution in time of the order of 2–3 ns, as with the hydrogen lamp flashes, or 6–8 ns, as with the light from plastic scintillators.

The variations of the responses at different points of illumination on the photocathode are reported in fig. 4 based on figs. 10a, 11, 14a e.g. The resulting variations are of two kinds; a time displacement of the whole pulse and a change of the pulse shape.

For the 56–AVP the time displacement never exceeds the value of 2 ns and the change in shape is very small. The axial symmetry is also fairly good.

The behaviour of the 6810–A is quite different using the RCA H.V. divider or the Ashkin H.V. divider. The Ashkin divider shows a general improvement, apart from a small enhancement of the axial asymmetry. The main characteristic of this divider is to put the focalization electrode voltage at the maximum possible value with respect to the photocathode. This fact contributes to reduce the time displacement of the pulses.

Using the RCA H.V. divider the time displacement is greater and the shape of the pulse is dependent on the value of the focalization electrode voltage. Furthermore, with the RCA divider, the 6810–A exhibits a peculiar property (see fig. 13) that is, in a small region close to the edge of the sensitive area (1.5 cm from the center and also axially dependent) a double pulse appears; the smallest pulse is anticipated, by about 10 ns, with respect to the normal pulse.

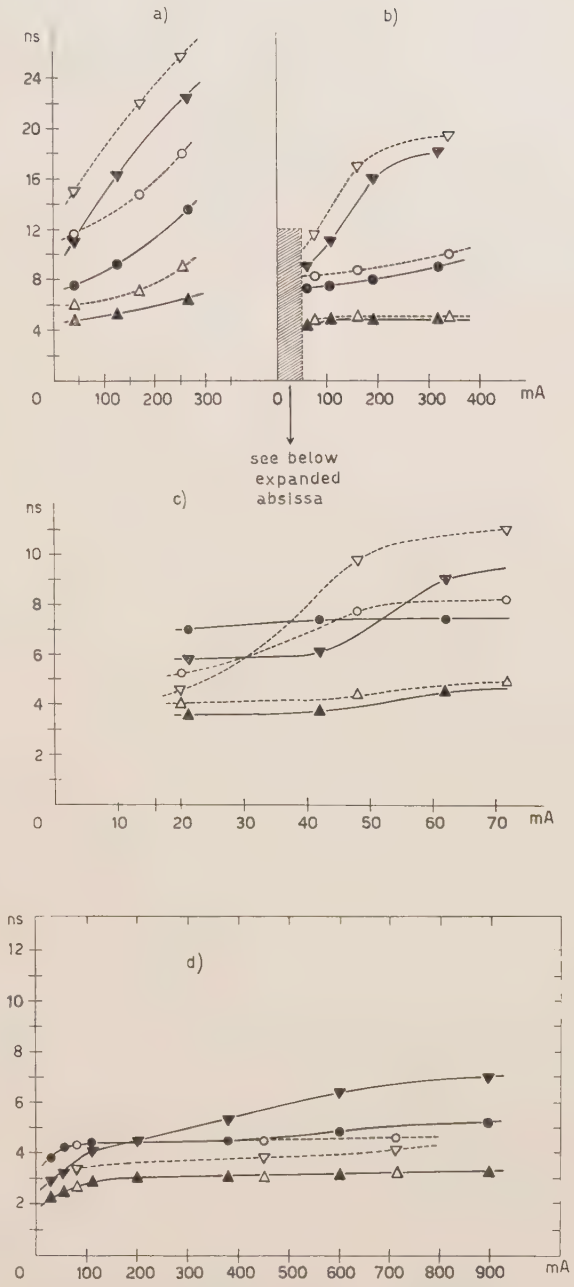

Fig. 5. Variations, with increasing light input, of:

Fig. a) for the 6810-A with RCA H.V. divider. b) for the 6810-A with the Ashkin H.V. divider. d) for the 56-AVP. (All the data in fig. 5 are corresponding to hydrogen lamp flashes.)

This effect could be explained by assuming that part of the incident light is hitting some internal electrode from which photoelectrons are extracted and successively multiplied with a total transit time definitely shorter than the mean transit time. When the whole photocathode area is strongly illuminated, this effect contributes to worsen the rise time of the pulse (see fig. 12b).

The presence of the spurious pulse is strongly dependent on the focalization electrode voltage and disappears using the Ashkin divider, in

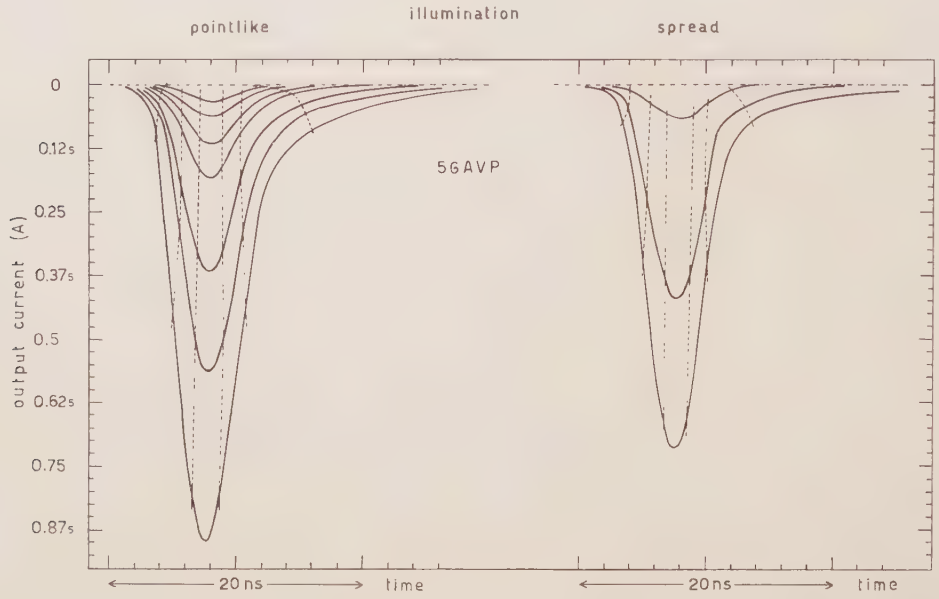

Fig. 6a. Redrawing of the output pulses from which the curves of fig. 5d were plotted.

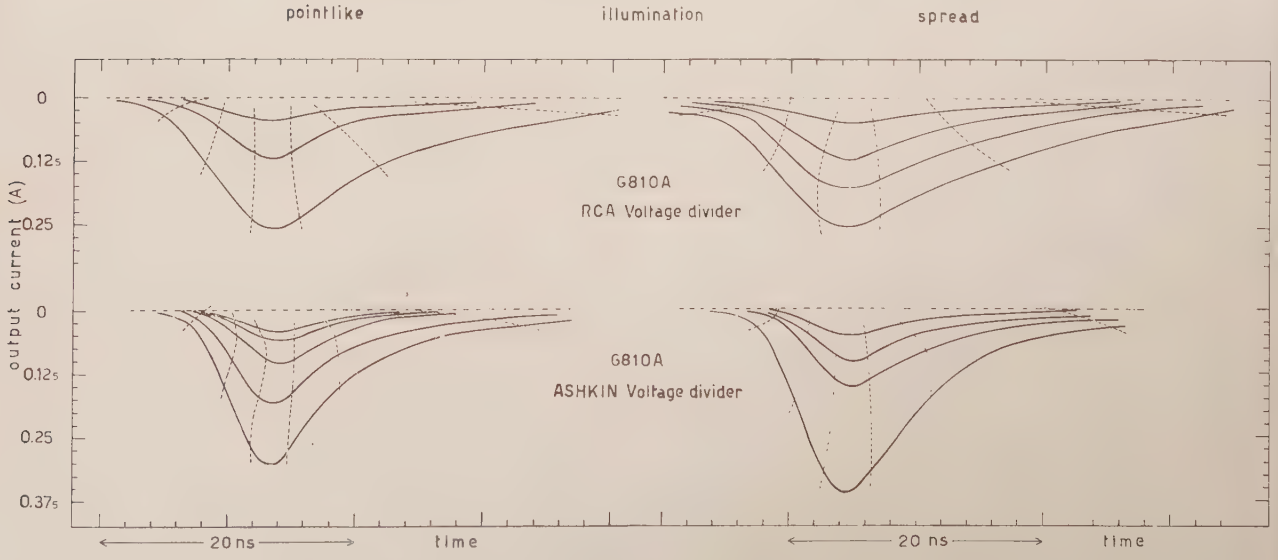

Fig. 6b. Redrawing of the output pulses from which the curves of figs. 5a, b, c, d, were plotted.

which case the focalization voltage is high enough to prevent the spurious photoelectrons to enter into the dynode multiplying chain.

In the 5 inches 7046 RCA photomultiplier, as it is to be expected, greater axial asymmetries are present and the pulse shape is strongly affected near the edge of the sensitive area (fig. 14a). This fact can produce undesirable consequences with directional light as Čerenkov radiation.

The results for the 7264 (not reported in diagrams) show a good improvement as far as time displacement is considered; it is reduced to a maximum value of 2 ns with the RCA divider. Also the spurious pulse is never present, but still the pulse shape is dependent on the point of illumination on the photocathode area. We expect that the use of the Ashkin divider could improve the performance of this photomultiplier.

The better performance of the 56–AVP with respect to the other photomultipliers considered is to be attributed to a more carefully designed electron optics in the first structure and to the presence of the deflector electrode which pushes the photoelectrons always to the same point of impact on the first dynode.

The changes of the pulse shapes at increasing light flux, are reported in diagrams of fig. 5 for the hydrogen lamp flash and in tables 2 and 3 for the Čerenkov and plastic scintillator light. Only the results of the 56–AVP and the 6810–A are reported, the other RCA tubes exhibiting similar properties to that of the 6810–A.

The output pulses taken with the hydrogen lamp are redrawn in figs. 6 a,b.

By inspection of these figures, it is seen that the 6810–A has more asymmetry in shape than the 56–AVP and this asymmetry increases strongly at increasing output current.

By comparison of the pulses given by the 56–AVP under Čerenkov light, which are symmetric in shape, it can be concluded that the asymmetry in the response of this photomultiplier to the hydrogen lamp flash, is due to the shape of the flash itself.

Furthermore, the asymmetry exhibited by the 6810–A, becomes greater using diffuse light. For this reason, we conclude that the peculiar behaviour of the 6810–A is mainly due to the insufficient compensation of the space-charge effects on the spread of the electron transit time, especially in the last stages of the multiplying chain, and that a small contribution to the asymmetry comes out also from the photocathode to the first dynode structure. Again the use of Ashkin divider improves the 6810–A, in this sense, and we expect that a more careful design of the voltage divider for the relative potential differences in the last stages of the multiplier chain, could give even better performance.

More difficult to explain is the property of the 56–AVP which gives broader signals at concentrated light than at diffuse light. This happens only at output currents larger than 400 mA. Probably this is due to the semiconductive properties of the photocathode layer which could produce, at large concentrated emission of photoelectrons, local electrostatic fields spreading the initial velocities of the photoelectrons, giving so broader output signals.

From fig. 6 and table 1, the capability of the photomultipliers as time reference at different pulse amplitudes, can be established, by taking some criteria of timing.

In table 1 the results are reported with the following criteria for timing:

1. the abscissa of the interception, with the time axis, of the tangent at the flexus point, in the rise of the pulse;

2. the abscissa of the point corresponding to the half amplitude in the rise of the pulse;

3. the abscissas of the points corresponding to the 90% of the amplitude, in the rise and decay respectively, of the pulse.

Again the excellent behaviour of the 56–AVP is to be compared to that of the 6810–A.

By examination of the single pulses taken with Čerenkov light, light from plastic scintillators and noise pulses due to single electrons, the tables 2 and 3 were written down; the reported values are corresponding to oscilloscopic data.

In the case of the 56–AVP, single electron and Čerenkov light pulses coincide in shape; by comparison of the results taken with the S.K.L.

TABLE 1

	Pulse ampl. (mA)	Time shifts (ns): tangent intersec. (ns)	50 % (rise)	90 % (rise)	90 % (decay)
6810-A RCA H.V. divider	0.05	0	0	0	0
	0.17	— 0.1	— 0.7	— 1.0	+ 0.2
	0.25	— 1.5	— 1.4	— 1.2	+ 0.2
6810-A Ashkin H.V. divider	0.05	0	0	0	0
	0.10	— 0.3	— 0.1	+ 0.2	+ 0.1
	0.15	— 0.7	— 0.2	+ 0.3	+ 0.3
	0.35	— 1.5	— 1.0	— 0.6	+ 0.3
	0.55	— 2.5	— 2.0	— 1.2	+ 0.3
56-AVP	0.07	0	0	0	0
	0.45	~ 0.1	— 0.1	— 0.1	~ 0.1
	0.73	~ 0.2	— 0.2	— 0.2	~ 0.1

The time shifts are evaluated with respect to the minimum amplitude pulse considered for each photomultiplier.

TABLE 2
Characteristic features of oscilloscopic responses from 56-AVP

	Pulse ampl. range (mA)	Rise time (ns)	Width at half ampl. (ns)	Decay time (ns)
Single electron	10 — 100	2.2 ± 0.1	3.2 ± 0.1	2.2 ± 0.1
Čerenkov light	100 — 600	2.2 ± 0.1	3.2 ± 0.1	2.2 ± 0.1
Plastic scintillator light	200 — 600	2.8 ± 0.1	5.8 ± 0.2	6.1 ± 0.3

TABLE 3
Characteristic features of oscilloscopic responses from 6810-A

	Pulse ampl. range (mA)	Rise time (ns)	Width at half ampl. (ns)	Decay time (ns)
Single electron	25 — 50	2.6 ± 0.4	4.0 ± 0.8	$2.6\ ^{-0.4}_{+3.0}$
Čerenkov light	40 — 100	2.8 — 7.0	4.0 — 7.5	4.8 — 12.0
	110 — 200	2.8 — 6.4	4.0 — 10.0	8.4 — 19.2
	200 — 500	4.0 — 4.4	12 — 13	16 — 22
Plastic scintillator	130 — 250	3.5 ± 0.4	10.8 ± 2.0	14.4 ± 2.5

pulse generator, an intrinsic width at half amplitude of the order of 2.7 ns, rise and decay time less than 2 ns, can be attributed to them. Due to the longer decay time of plastic scintillator light, the intrinsic values of width at half amplitude and decay time, should not differ very much from values in table 2.

For the 6810–A the situation with Čerenkov light pulses looks entirely different; they do not coincidence in shape with single electron pulses, which are almost symmetric. Not only there is the typical broadening at increased output current but there are big fluctuations of width at half amplitude and of the decay time of pulses of

equal amplitude. This is explained by considering that the very short duration of Čerenkov light enhances the insufficient compensation for space-charge effects, because the electrons are very bunched in time at the anode region. In fact, these fluctuations are greatly reduced with plastic scintillator and hydrogen lamp light (see table 3).

The amplitude of the response against increasing light flux, for pointlike illumination, is reported in fig. 7, showing the degree of linearity of the photomultipliers. No appreciable differences were found for spread illumination. The curve (not reported), obtained by plotting the total area of the pulse instead of the amplitude, shows a more linear behaviour in the high current region.

The resolution curves for double pulses, taken without clipping lines, are given in fig. 8. Some examples of the responses are reported in fig. 17. The amplitude of the response decreases to the

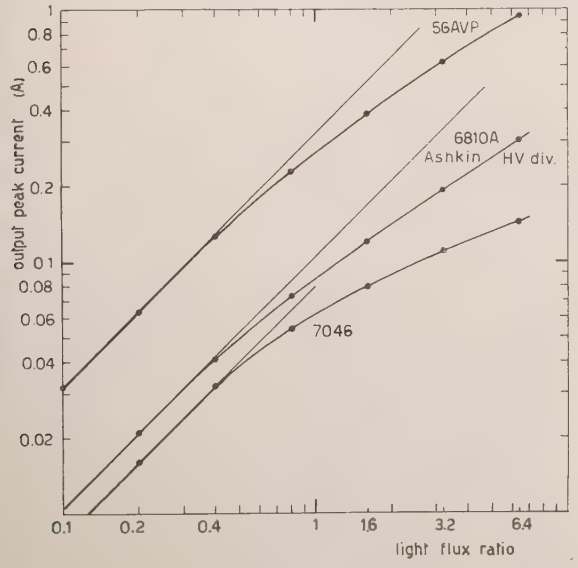

Fig. 7. Degree of linearity of the response at increasing light flux. (The points are corresponding to the maximum amplitude of the pulse.)

half value, between single and double pulse level, for time interval of 2.5 ns for the 56–AVP and 5 ns for the 6810–A. The resolution curves can be obviously improved by using clipping lines or exponential clipping lines, as can be seen from the pictures. The nonlinear behaviour of the 6810–A, at the light level used, keeps the coincident pulse amplitude of this photomultiplier, to a value less than two. It is to be expected that the resolution power for double pulse of the 6810–A can be improved by taking lower output signals.

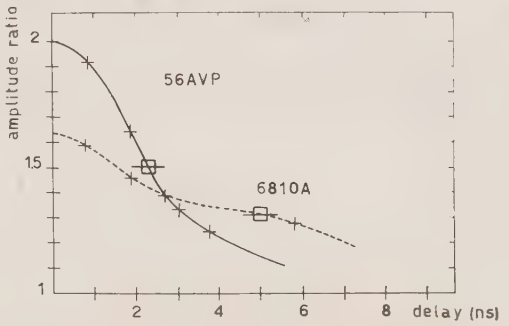

Fig. 8. Amplitude ratio of the response to double light pulses against separation in time of the pulses.

By considering the characteristic of the response of the 56–AVP to Čerenkov light, the intrinsic duration at half amplitude of the hydrogen lamp flash should be of the order of 2.5 ns, i.e. the same value given by the resolution curve of the 56–AVP. For this reason, probably the resolving power of the photomultipliers should be better than the above reported values.

Nevertheless, from these results, the approximate limits of the frequency response of the photomultipliers can be estimated. The 56–AVP could give 100% of modulation up to 100 Mc/s with peak current of the order of 100 mA, while for the 6810–A and similar RCA tubes, the limits should be 80 Mc/s at 40 mA, using the Ashkin H.V. divider. The limits for the 6810–A, with the RCA H.V. divider, was already determined[1]) to be 50 Mc/s at 20 mA.

4. Conclusions

From the results given in this paper, it can be deduced that the so called "spread of transit time" of the electrons, which determines the shape of the output pulse, is affected not only by the distribution, in space and time, of the incoming photons but also by the light flux input level. The total transit time has a statistical meaning; its mean value can be displaced in time

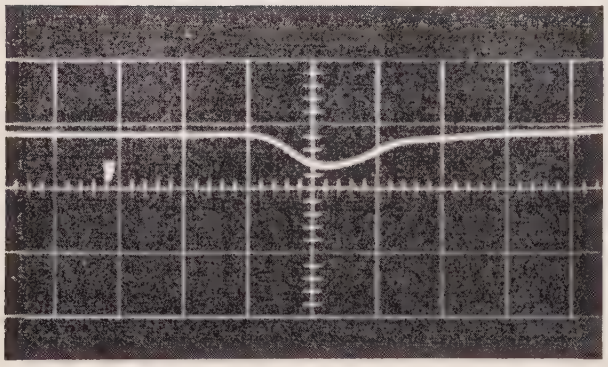

Fig. 9. Trigger stability control: the response of the 1P21 auxiliary photomultiplier to hydrogen lamp flashes; oscilloscope time axis triggered by another 1P21; time axis speed, 4.5 ns/cm.

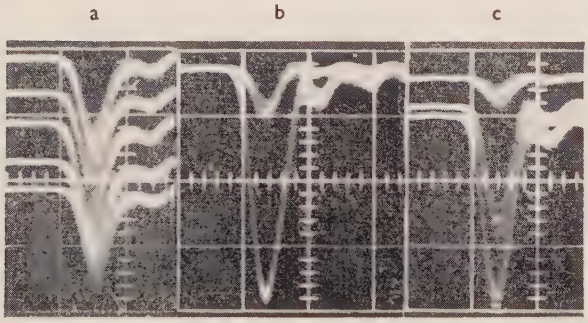

Fig. 10a. 56–AVP. Cathode exploration parallel to the dynode structure (cm.–1.6/–1/0/1/1.6 from the center). b. Response to increasing light flux, for pointlike illumination. c. Idem, for diffuse illumination. Time axis speed; 10 ns/cm, vertical sensitivity: 250 mA/cm.

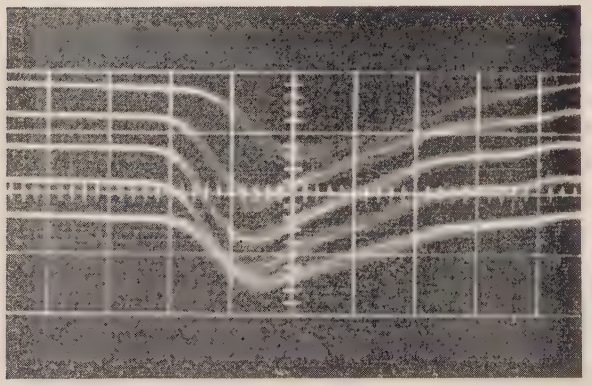

Fig. 11. Cathode exploration, parallel to the dynode structure, of the 6810-A. (RCA-H.V. divider; time axis speed: 4.5 ns/cm, vertical sensitivity: 125 mA/cm, foc. electr. voltage = 2500 V.) The illuminated point was at cm.–1.6/–1/0/1/1.6, respectively, from the center.

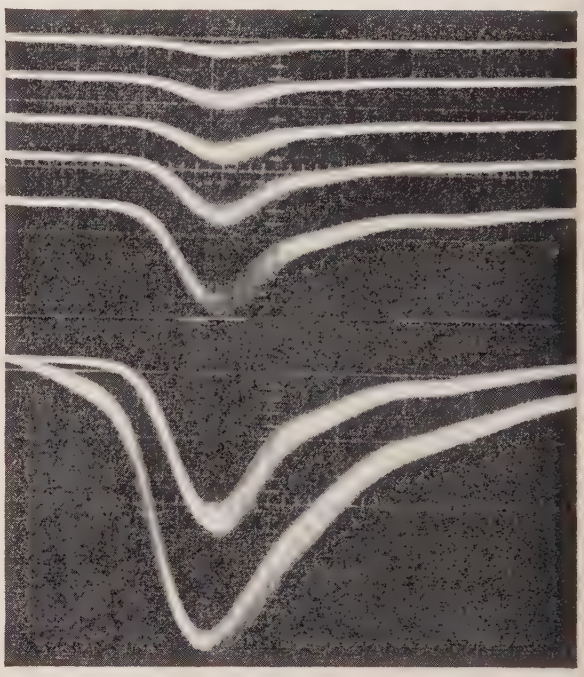

Fig. 12a. 6810-A response, at increasing light flux, for pointlike illumination. (Ashkin H.V. divider, time axis speed: 4.5 ns/cm, vertical sensitivity: 125 mA/cm.). b. Comparison between concentrated illumination (smaller pulse) and diffuse intense illumination (bigger pulse). To be noted the effect of the spurious pulse (see fig. 13) on the rise of the pulse. For the first six pulses the light flux is doubled each step.

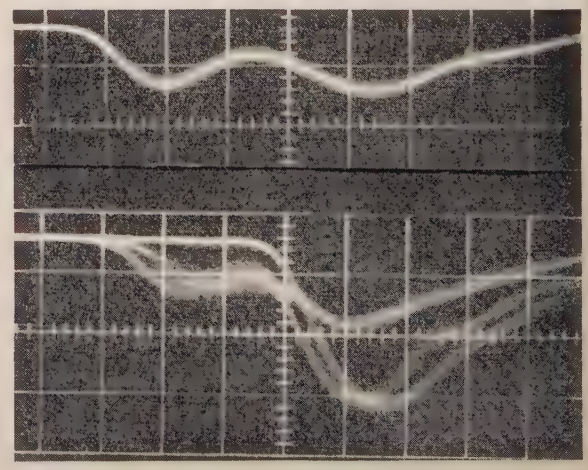

Fig. 13a. Pointlike illumination, close to the edge of the photocathode area, of the 6810-A, RCA H.V. divider, (time axis speed: 4.5 ns/cm, vertical sensitivity: 125 mA/cm, focalization electrode voltage: 2450 V). b. Effect of changing the focalization electrode voltage to about 2500 V.

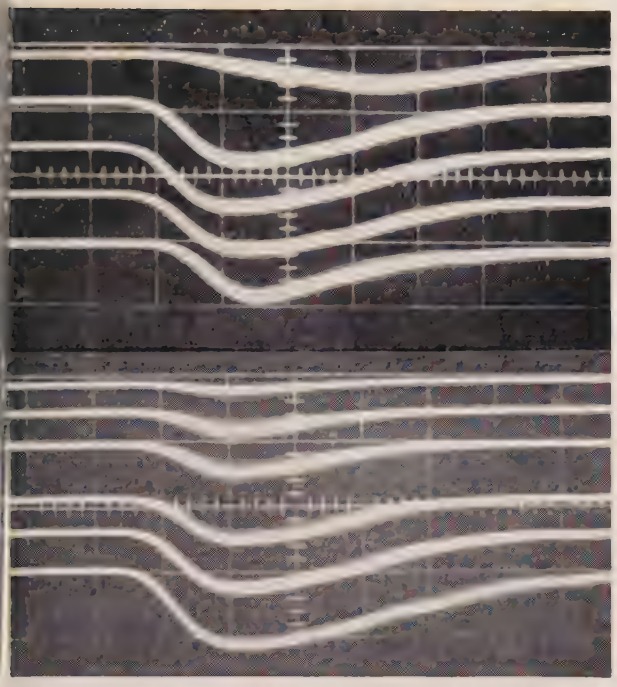

Fig. 14. 7046. a. Cathode exploration parallel to the dynode structure (cm.–5/–3.5/0/3.5/5 from the center). b. Response for pointlike illumination to light flux increasing in a geometric progression.

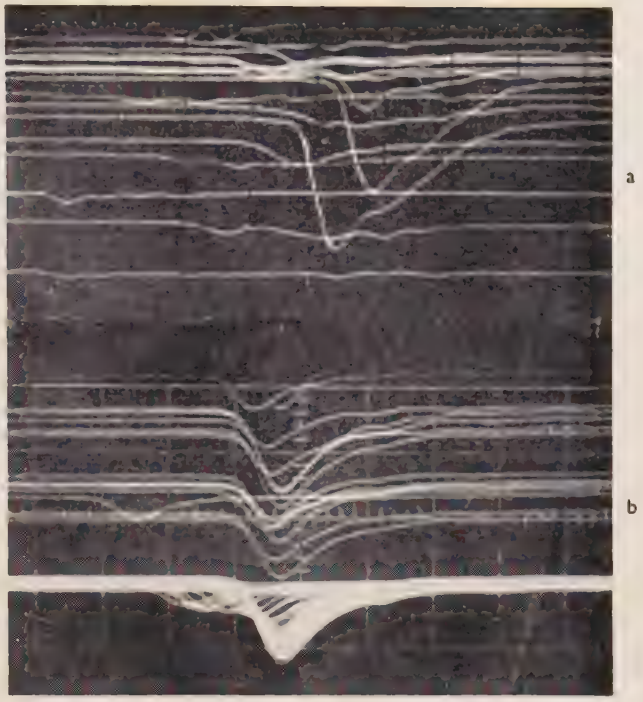

Fig. 16a. Single pulses of the 6810-A by Čerenkov light. b. Pulses by plastic scintillator light. The Ashkin H.V. divider was used for these pictures; time axis speed and vertical sensitivity as in fig. 15.

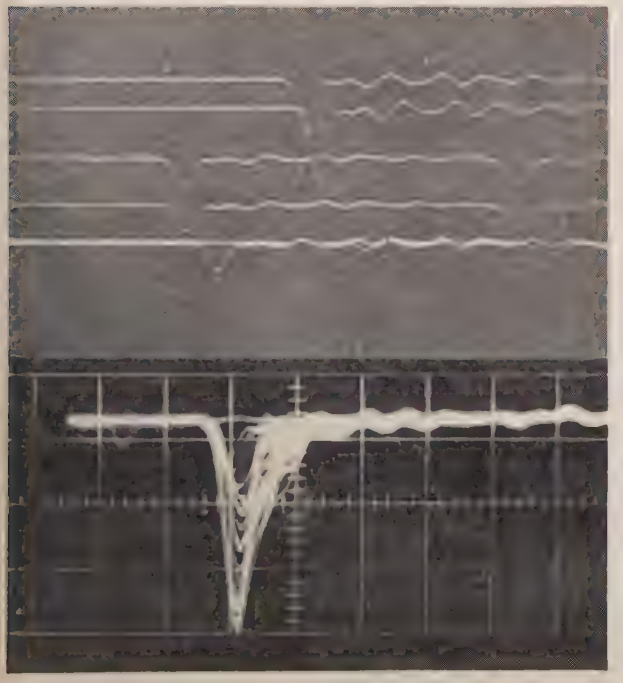

Fig. 15a. Single pulses of the 56-AVP by Čerenkov light. b. Accumulated pulses by plastic scintillator light; no clipping line. Time axis speed: 10 ns/cm; vertical sensitivity 250 mA/cm.

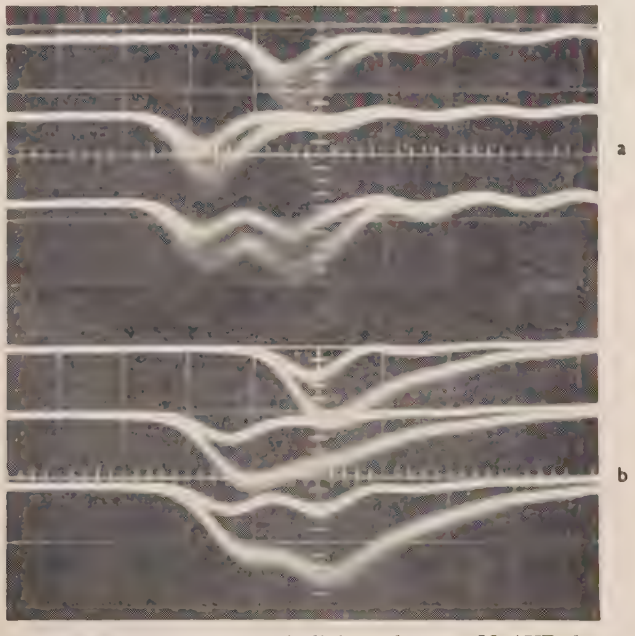

Fig. 17. Response to double light pulses. a. 56–AVP. b. 6810–A (Ashkin H.V. divider). In each line the oscilloscopic response with and without clipping line is reported. First and second lines: single pulses; third lines; added pulses. Time distance of the pulses: 6 ns, time axis speed: 4.5 ns/cm, vertical sensitivity: 125 mA/cm.

or its variance can be changed under different illumination conditions. Generally the two effects are simultaneously present.

The displacement of the mean value of the transit times is due to the photocathode to first dynode structure focalization failure; the effect is greatly reduced in the photomultipliers above mentioned with respect to older types.

The change of the variance is affected by the whole photomultiplier structure; it is minimized in the 56–AVP but is present in the RCA tubes. The better performance of the 56–AVP, in this sense, is probably due to the presence of the interelectrodes between the dynodes in the multiplying structure.

More attention should be paid to the choice of suitable H.V. dividers, even when one is working at low repetition rates.

The results agree with those obtained by the high-frequency modulated light method and the predictions given above will be tested in a successive work.

From the practical point of view of the use of photomultipliers, it comes out the possibility of having resolving times, for double coincidences, of less than 1 ns, as was already demonstrated[5,6]) with a dead time of the order of 4 ns.

Note added in proof: While this paper was in press, similar measurements have been made on the photomultiplier Philips 58 AVP. The results will be published in "Acta Electronica".

[5]) J. C. Brisson, G. Vallades et R. van Zurk, L'Electronique Nucléaire **1** (1959) 233.

[6]) R. Meunier, L'Electronique Nucléaire **1** (1959) 263.

NUCLEAR INSTRUMENTS AND METHODS 9 (1960) 315–327; NORTH-HOLLAND PUBLISHING CO.

COMPUTATIONAL METHODS FOR ANALYSIS OF RESONANCE TRANSMISSION DATA FOR S-WAVE NEUTRONS

J. E. LYNN

Nuclear Physics Division, U.K.A.E.A. Research Group, Atomic Energy Research Establishment, Harwell

Received 21 August 1960

This paper describes computational methods that may be used for the analysis of neutron transmission data in terms of neutron resonance parameters. These methods include a self-consistent scheme for correcting the experimental data to obtain a transmission dip "area" and simultaneously comparing it with the theoretical area function to obtain a relationship between a pair of resonance parameters. Several such functional relationships (from measurement of neutron transmission through different sample thicknesses) serve to find the "best values" of the parameters by least squares fitting. The paper includes diagrams of several families of curves describing the theoretical transmission dip area function (with and without Doppler broadening of the effective resonance cross section). An example of the use of these methods on actual experimental data is given. It is the 66.14 eV resonance in the cross section of U^{238}; the neutron width is found to be 25.1 ± 1.2 meV and the total radiation width is 25.1 ± 1.4 meV.

1. Introduction

A considerable amount of experimental effort is devoted to the measurement of the transmission of neutrons as a function of energy in the resonance region. The object of these measurements is to determine the parameters, in particular the total angular momentum and partial decay widths, associated with the resonances observed in the neutron cross section. The analysis of the transmission data commonly employs the area method. This depends on the fact that the area above a resonance dip in a curve of neutron transmission plotted against energy is independent of experimental resolution (provided that the bounding energy limits are far from the resonance energy). The value of this area may be compared with calculations of the same quantity for the sample thickness (nuclei per unit area) employed and possible ranges of the resonance parameters. The condition of equality of the measured and calculated areas defines a functional relationship between the resonance parameters (which can often be limited to two for this purpose). Many calculations of the transmission dip area have been made as a function of suitable resonance parameters[1,2,3]). Usually it is assumed that the energy limits bounding the area are set at infinity. This, of course, eliminates an extra parameter (the area limits) from these calculations but it also means that a direct comparison between the experimental and calculated areas cannot be made. It is essential to have the former quantity evaluated between limits not too far from the resonance energy in order that statistical errors may be reduced and because neighbouring resonances automatically prevent wide limits. Often the amount of area that is "missed" by setting these limits is quite small and it is usually the practice to calculate "wing corrections" to take account of the missing area. Initially, this is done by using approximate values of the resonance parameters. In more careful work the correction is improved by using the parameters subsequently calculated and so setting up a successive approximation calculation.

It is found that this method breaks down when very "thick" samples are employed for the

[1]) E. Melkonian, W. W. Havens, Jr. and J. Rainwater Phys. Rev. **92** (1953) 702.
[2]) D. J. Hughes, J. Nuclear Energy **1** (1955) 237.
[3]) J. E. Lynn, Nuclear Physics **7** (1958) 599.

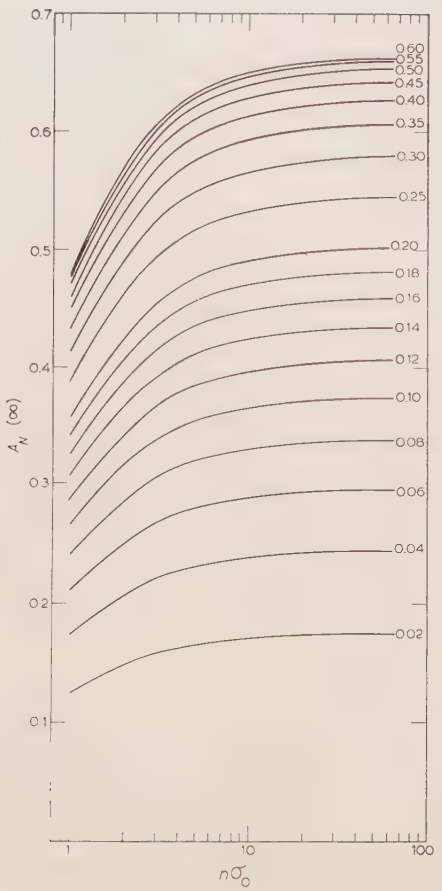

Fig. 1.

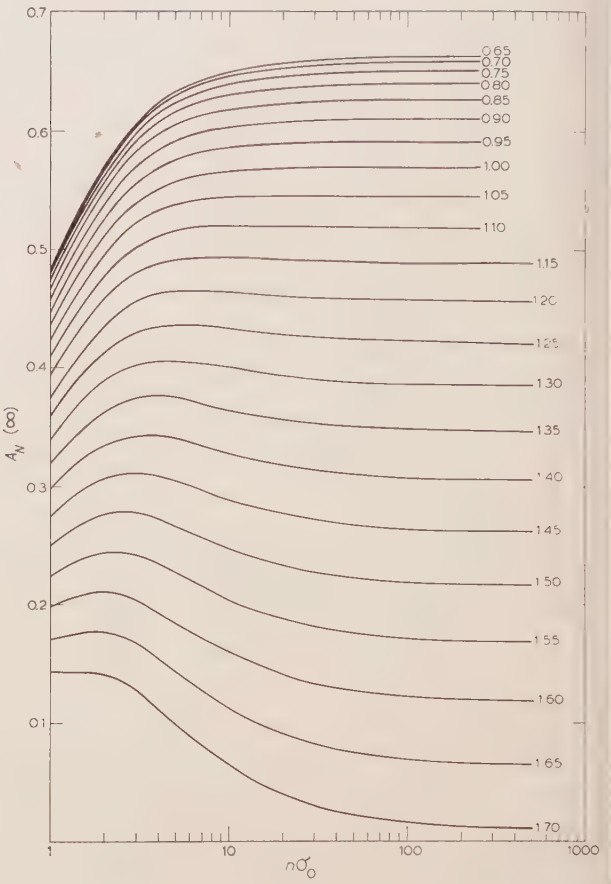

Fig. 2.

transmission measurements. The advantage in principle of using thick samples has been described previously[3]). When thick samples are used the interference term in the single-level Breit-Wigner formula for the resonance cross section of s-wave neutrons has a striking effect on the behaviour of the area as a function of sample thickness. This behaviour allows accurate determinations of the resonance parameters. With thick samples, however, the wing corrections tend to be appreciable compared with the area enclosed by the energy limits. In addition, the transmission curve over the resonance region is strongly asymmetric, implying that a knowledge of the resonance energy is needed in order to calculate the wing corrections properly, and that the resonance energy itself must be calculated from certain features of the transmission curve. Since this last calculation is also dependent on the resonance parameters it is obvious that determination of the wing correction using successive approximations is very tedious.

For these reasons we have set up a scheme of resonance transmission analysis which depends on the use of an electronic computer for reasonable rapidity and uses graphical methods to achieve "self-consistency" between experimental and calculated areas. It has been necessary to compute detailed tables of the area function to take into account both the interference effect and Doppler broadening of the resonance. These tables have been published in detail in two Harwell reports[4,5]). Some graphs based on these tables are presented here.

[4]) J. E. Lynn, Harwell Report AERE-R3353. [5]) J. E. Lynn, Harwell Report AERE-R3354.

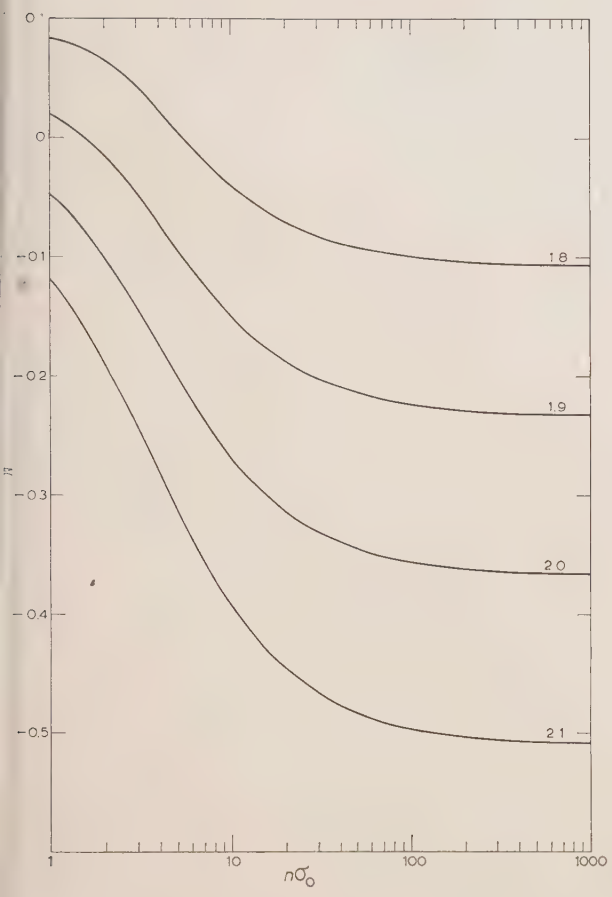

Fig. 3.

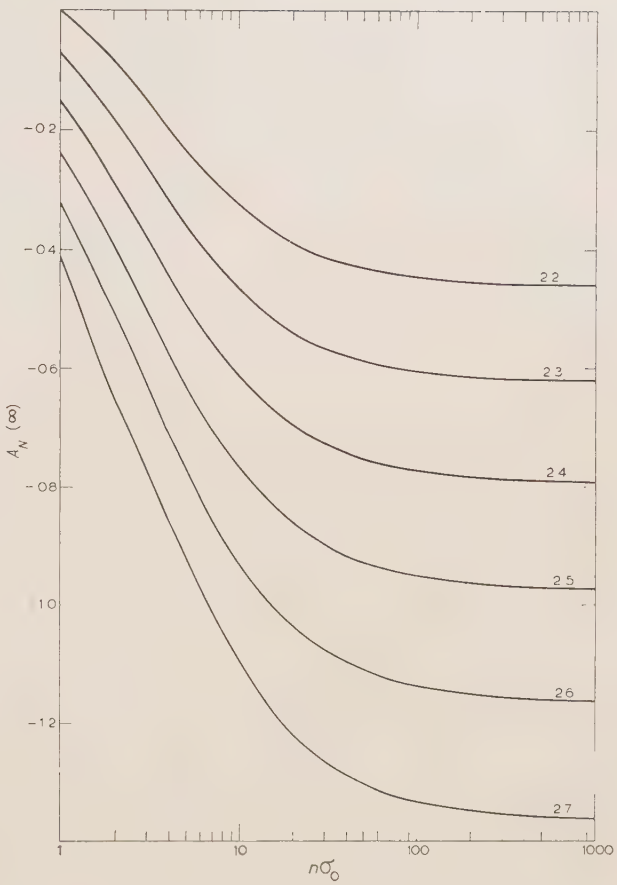

Fig. 4.

2. The Area Function

The area function which is the basis for the analysis of experimental data is derived from the single-level Breit-Wigner formula and is defined as follows:

$$A_E(\varepsilon) = \int_{-\varepsilon}^{\varepsilon} [1 - T(E)/T_p]\, d(E - E_R)\,. \tag{1}$$

Here T_p is the transmission due to the effective potential scattering, σ_p [$T_p = \exp(-n\sigma_p)$, where n is the number of atoms per unit area of the sample normal to the beam direction], $T(E) = \exp[-n\sigma(E)]$ is the transmission at neutron energy E, and E_R is the resonance energy. For low energy s-wave neutrons

$$\sigma(E) = \frac{\sigma_0}{1 + x^2} + \frac{\sigma_0 x (2a/\lambda\!\!\!^{-})}{1 + x^2} + \sigma_p \tag{2}$$

where $x = (E - E_R)/\frac{1}{2}\Gamma$, Γ is the total width of the resonance, $\sigma_0 = 4\pi\lambda\!\!\!^{-2}\, g_J \Gamma_n/\Gamma$ is the peak cross section, $2\pi\lambda\!\!\!^{-}$ is the de Broglie wavelength of the neutron (in the centre of mass system), Γ_n is the neutron width, $g_J = (2J + 1)/2(2I + 1)$ where $J\hbar$ is the total angular momentum of the excited-compound nucleus state and a is the effective potential scattering length. It may be shown[3]) that

$$A_E(\infty) = \tfrac{1}{2}\pi n\sigma_0 \Gamma e^{-n\sigma_0/2} [I_0(n\sigma_0/2) + I_1(n\sigma_0/2) - \sum_{m=1}^{\infty} \frac{(2m-3)!!}{(2m)!} \left(\frac{2n\sigma_0 a^2}{\lambda\!\!\!^{-2}}\right)^m [I_{m-1}(n\sigma_0/2) + I_m(n\sigma_0/2)] \tag{3}$$

where I_m is the Bessel function of imaginary argument of order m. A small table of the function $A_x(\infty) = (\Gamma/2)^{-1} A_E(\infty)$ has been published elsewhere[3]). It is to be stressed however that equation (2) is valid only for low energy neutrons (i.e. $a/\lambda\!\!\!^{-} \ll 1$). In part of the table given in[3]) this condition is violated and hence is not of physical interest. When $a/\lambda\!\!\!^{-} \gtrsim 1$ the single-level Breit-Wigner formula for $\sigma(E)$ is

$$\sigma(E) = \frac{\sigma_0}{1 + x^2} + \frac{\sigma_0 x \tan 2a/\lambda\!\!\!^{-}}{1 + x^2} + \sigma_p \qquad (4),$$

where now $\sigma_0 = 4\pi\lambda\!\!\!^{-2} g_J (\Gamma_n/\Gamma) \cos 2a/\lambda\!\!\!^{-}$. The function $A_E(\infty)$ is simply obtained from equation (3) by replacing $2a/\lambda\!\!\!^{-}$ in (3) by $\tan 2a/\lambda\!\!\!^{-}$. Thus

$$A_E(\infty) = \tfrac{1}{2}\pi n\sigma_0\Gamma e^{-n\sigma_0/2}\,[I_0(n\sigma_0/2) + I_1(n\sigma_0/2) - \sum_{m=1}^{\infty} \frac{(2m-3)!!}{(2m)!}\left(\frac{n\sigma_0 \tan^2 2a/\lambda\!\!\!^{-}}{2}\right)^m [I_{m-1}(n\sigma_0/2) + I_m(n\sigma_0/2)]\,. \qquad (5)$$

Correspondingly, the table of reference[3]) is everywhere useful if the parameter $2n\sigma_0 a^2/\lambda\!\!\!^{-2}$ is replaced by $\frac{1}{2}n\sigma_0 \tan^2 2a/\lambda\!\!\!^{-}$. Henceforth we shall adopt (4) and (5) as our basic equations.

It is now apparent that the area function $A_E(\infty)$ depends on three parameters which may be taken to be $n\sigma_0$, Γ and $\tan 2a/\lambda\!\!\!^{-}$. For thick samples such that $n\sigma_0 \ll 1$ a simplification results. It was shown in[3]) that

$$\lim_{n\sigma_0\to\infty} A_E(\infty) = \Gamma\sqrt{\pi n\sigma_0}\left\{1 - \sum_{m=1}^{\infty} \frac{(2m-3)!!}{(2m)!}\left(\frac{n\sigma_0 \tan^2 2a/\lambda\!\!\!^{-}}{2}\right)^m\right\} \qquad (6)$$

which may be rewritten

$$\lim_{n\sigma_0\to\infty} A_E(\infty) = \frac{\Gamma}{\tan 2a/\lambda\!\!\!^{-}}\sqrt{(\pi n\sigma_0 \tan^2 2a/\lambda\!\!\!^{-})}\left\{1 - \sum_{m=1}^{\infty} \frac{(2m-3)!!}{(2m)!}\left(\frac{n\sigma_0 \tan^2 2a/\lambda\!\!\!^{-}}{2}\right)^m\right\}. \qquad (7)$$

Thus when $n\sigma_0$ is large $A_E(\infty)$ depends only on two parameters effectively, $n\sigma_0 \tan^2 2a/\lambda\!\!\!^{-}$ and $\Gamma/\tan(2a/\lambda\!\!\!^{-})$. Since Γ enters the area function only as a multiplicative factor it is simplest to tabulate the area function divided by Γ. In view of equation (7) we consider it useful to work with the function

$$A_N(\infty) = \frac{A_E(\infty) \tan 2a/\lambda\!\!\!^{-}}{2\Gamma}.$$

This has been computed using the Ferranti Mercury computer at Harwell for values of the parameter $\frac{1}{2}n\sigma_0 \tan^2 2a/\lambda\!\!\!^{-}$ in the ranges 0.02 (0.02) 0.20 (0.05) 1.7 (0.1) 2.7 and values of $n\sigma_0$ from 1 by factors of 2 to 1024. These results have been tabulated[4]). Graphs of $A_N(\infty)$ as a function of $n\sigma_0$ for different values of $\frac{1}{2}n\sigma_0 \tan^2 2a/\lambda\!\!\!^{-}$ are presented in figs. 1, 2, 3 and 4.

3. Resonance Parameter Relationships from Experimental Data

The experimental data on the resonance dip in the transmission curve of a given thickness of material now have to be compared with the theoretical behaviour of the area function in order to obtain a relationship between the resonance parameters. A crude idea of the resonance parameters will be known when a detailed analysis of this kind is begun. It is therefore possible to decide approximately the ranges of parameters over which a relationship is desired.

It is then necessary to evaluate from the data an experimental area $A_E^{\exp}(\infty)$. To do this the following features of the transmission curve (see fig. 5) are needed. The energy limits between which the area of the transmission dip is taken are E_1 and E_2. An energy ε' is defined by $2\varepsilon' = E_2 - E_1$ and an energy E_R' by $E_R' = E_1 + \varepsilon'$. The data for determining the potential transmission T_p are contained in two observed transmissions $T(-\varepsilon'')$ and $T(+\varepsilon'')$ suitably located on either side of the dip at energies E_3 and E_4 respectively. Other energies are defined by

$$2\varepsilon'' = E_4 - E_3\,, \quad E_R'' = E_3 + \varepsilon''\,, \quad \delta\varepsilon' = E_R' - E_R\,, \quad \delta\varepsilon'' = E_R'' - E_R\,.$$

E_1, E_2, E_3 and E_4 are chosen so that E_R' and E_R'' are close to the expected position of E_R. E_1 and E_2 should be exactly half way between two experimental determinations of the transmission. The value of the transmission curve approximately half way between the lowest and highest points on the low energy side of the transmission curve $T_{\frac{1}{2}}$, is also needed. It may be obtained by interpolation. The energy to which it corresponds is called $E_{\frac{1}{2}}$.

Associated with each experimental point, i, on the transmission curve between E_1 and E_2 is the width of the energy channel, ΔE_i, over which the transmission in the neighbourhood of E_i has effectively been averaged (usually with some weighting owing to the non-rectangularity of the instrumental resolution function) to give an observed value T_i. From these data the quantities $\Sigma_{E_1}^{E_2} \Delta E_i = 2\varepsilon'$ (in the usual time-of-flight measurements) and $\Sigma_{E_1}^{E_2} T_i \Delta E_i$ must be calculated.

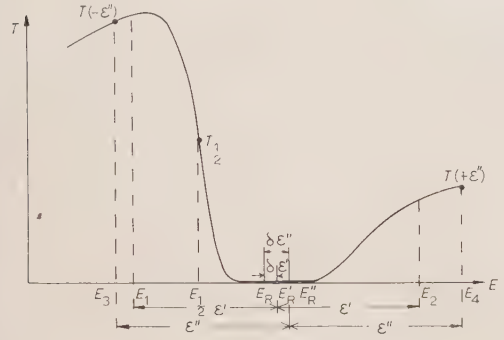

Fig. 5.

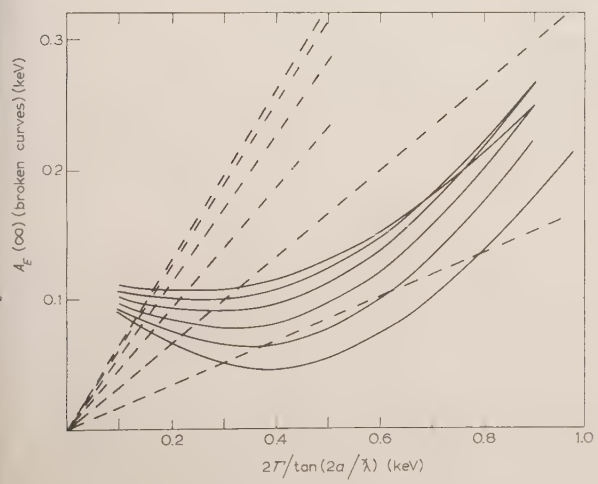

Fig. 6.

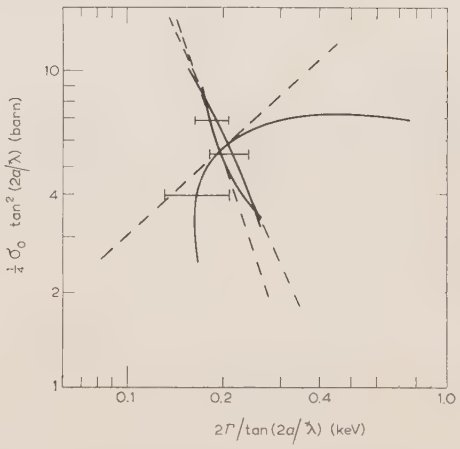

Fig. 7. Plot of self-consistent resonance parameter data for 15.5 keV resonance in Bi^{209} + n. A least squares analysis gives $\sigma_0 \tan^2 2a/\lambda\!\!\!^{-} = 22.9 \pm 3.4$ b, $\Gamma/\tan(2a/\lambda\!\!\!^{-}) = 0.103 \pm 0.028$ keV, covar $(\sigma_0 \tan^2 2a/\lambda\!\!\!^{-}, \Gamma/\tan(2a/\lambda\!\!\!^{-}))/(\sigma_0 \Gamma \tan 2a/\lambda\!\!\!^{-}) = 2.31 \times 10^{-3}$.

It is first necessary to calculate the potential transmission, T_p. It has been pointed out[3]) that the product of $T(\varepsilon'')T(-\varepsilon'')$ is approximately T_p if ε'' is sufficiently large that the effect of the resonance term in (4) is small. In general however a small correction is necessary for the resonance term and also for the fact that in this treatment $E_R'' \neq E_R$. It is easily shown that, to second order

$$T_p = \sqrt{T(\varepsilon'')T(-\varepsilon'')} \cdot \exp\left\{ \frac{n\sigma_0\Gamma^2}{4\varepsilon''^2}\left[1 + 3\frac{\delta\varepsilon''}{\varepsilon''}\right]^2 - \frac{1}{4\varepsilon''} n\sigma_0 \tan^2(2a/\lambda\!\!\!^{-}) \cdot \frac{2\Gamma}{\tan(2a/\lambda\!\!\!^{-})} \cdot \frac{\delta\varepsilon''}{\varepsilon''} \right\}. \quad (9)$$

The fact that this formula contains $\delta\varepsilon''$ draws attention to the necessity of evaluating E_R. It has been shown[6]) that this can be determined from $E_{\frac{1}{2}}$ and $T_{\frac{1}{2}}$:

[6]) J. E. Lynn, M. C. Moxon and F. W. K. Firk, Nuclear Physics 7 (1958) 613.

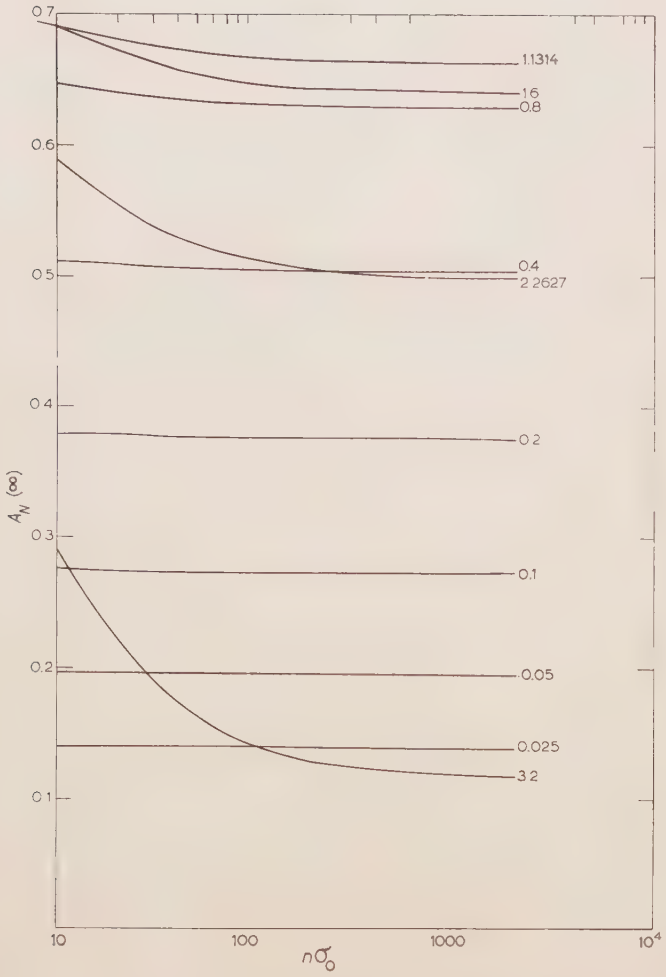

Fig. 8. $A_N(\infty)$ v. $n\sigma_0$ for $\beta = 1$ and specified values of $n\sigma_0 \tan^2 2a/\tilde{\lambda}$.

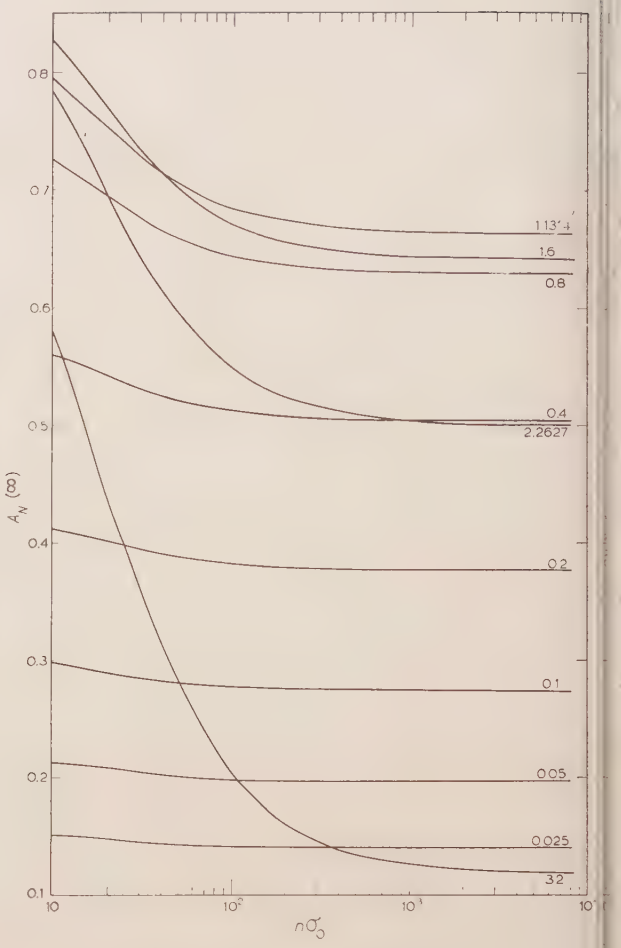

Fig. 9. $A_N(\infty)$ v. $n\sigma_0$ for $\beta = 2$.

$$E_{\frac{1}{2}} - E_R = \frac{-\frac{1}{2}n\sigma_0 \tan^2 2a/\tilde{\lambda} + \sqrt{(\frac{1}{2}n\sigma_0 \tan^2 2a/\tilde{\lambda})^2 - yn\sigma_0 \tan^2 2a/\tilde{\lambda} - (\frac{1}{2}y \tan^2 2a/\tilde{\lambda})^2}}{2y} \cdot \frac{\Gamma}{\tan 2a/\tilde{\lambda}} \tag{10}$$

where $y = \ln (T_{\frac{1}{2}}/T_p)$. The equations for T_p and E_R must be solved simultaneously. This can be carried out approximately by writing $y = z + \zeta$ where

$$y = \ln T_{\frac{1}{2}} - \tfrac{1}{2} \ln T(\varepsilon'')T(-\varepsilon'') - n\sigma_0\Gamma^2/4\varepsilon''^2$$

and

$$\zeta = -\frac{3n\sigma_0\Gamma^2}{4\varepsilon''^2} \cdot \left(\frac{\delta\varepsilon''}{\varepsilon''}\right)^2 + \frac{1}{2}\frac{n\sigma_0\Gamma}{\varepsilon''} \tan \frac{2a}{\tilde{\lambda}} \cdot \frac{\delta\varepsilon''}{\varepsilon''}.$$

The terms involving ζ in the square root term of equation (10) are small compared with the remainder of the radicand and a binomial expansion of the square root is possible. Retaining the zero and first order terms of this expansion, we can now solve equations (9) and (10) simultaneously for $\delta\varepsilon''$. The expressions are somewhat cumbersome however and will not be given here.

We may now define a quantity $A_E^{\exp}(\varepsilon')$ by

$$A_E^{\exp}(\varepsilon') = \sum_{E_1}^{E_2} \Delta E_i - \sum_{E_1}^{E_2} \frac{T_i \Delta E_i}{T_p}. \tag{11}$$

To obtain $A_E^{\exp}(\infty)$ it is necessary to add "wing corrections" to $A_E^{\exp}(\varepsilon')$. If $E_R' = E_R$ then

$$A_E^{\exp}(\infty) = A_E^{\exp}(\varepsilon') + \Delta A_E(\varepsilon')$$

where
$$\Delta A_E(\varepsilon') = \frac{n\sigma_0\Gamma^2}{2\varepsilon'}\left\{\left[1 - \frac{1}{2}n\sigma_0\tan^2\frac{2a}{\lambda\!\!\!^{-}}\right] - \frac{n\sigma_0\Gamma^2}{24\varepsilon'^2}\left[1 - n\sigma_0\tan^2\frac{2a}{\lambda\!\!\!^{-}} + \frac{1}{12}\left(n\sigma_0\tan^2\frac{2a}{\lambda\!\!\!^{-}}\right)^2\right]\right\} \quad (12)$$

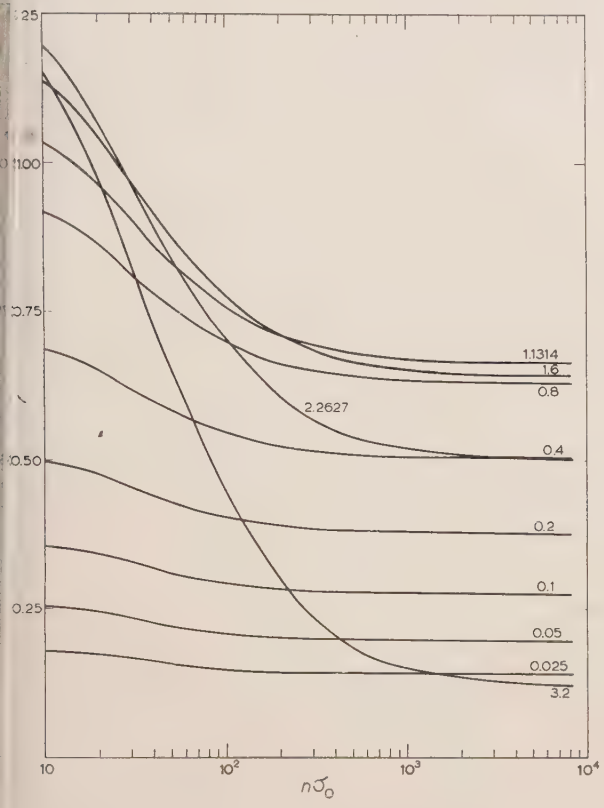

Fig. 10. $A_N(\infty)$ v. $n\sigma_0$ for $\beta = 4$.

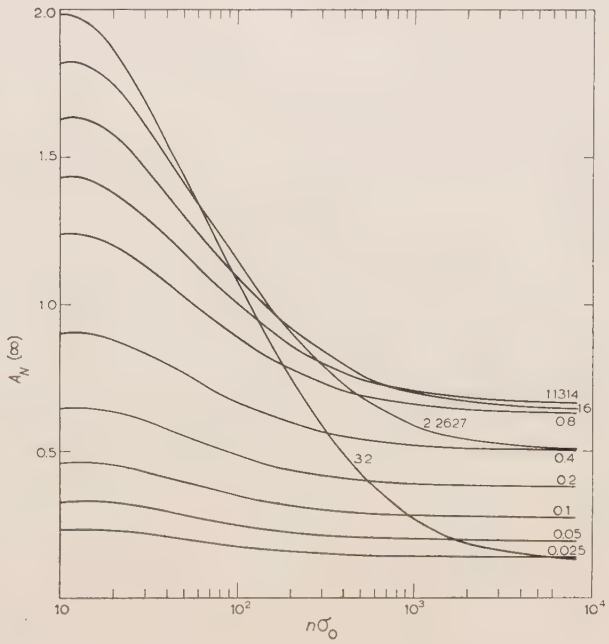

Fig. 11. $A_N(\infty)$ v. $n\sigma_0$ for $\beta = 8$.

to second order. If $\delta\varepsilon'$ is not zero then

$$A_E^{\exp}(\infty) = A_E^{\exp}(\varepsilon') + \Delta A_E(\varepsilon') - \delta A_E(\varepsilon') \quad (13)$$

where

$$\delta A_E(\varepsilon') = n\sigma_0\,\Gamma\tan(2a/\lambda\!\!\!^{-})\left\{1 - \frac{1}{2\varepsilon'}\frac{n\sigma_0\Gamma^2}{2\varepsilon'}\left(1 - \frac{1}{6}n\sigma_0\tan^2\frac{2a}{\lambda\!\!\!^{-}}\right)\right\}\frac{\delta\varepsilon'}{\varepsilon'} - \frac{n\sigma_0\Gamma^2}{2\varepsilon'}\left(1 - \frac{1}{2}n\sigma_0\tan^2\frac{2a}{\lambda\!\!\!^{-}}\right)\left(\frac{\delta\varepsilon'}{\varepsilon'}\right)^2. \quad (14)$$

It is obvious that the above terms for treatment of the experimental data are all expressible in terms of two resonance parameters, $n\sigma_0\tan^2 2a/\lambda\!\!\!^{-}$ and $\Gamma/\tan(2a/\lambda\!\!\!^{-})$, apart from a term of only second order importance, $(y\tan 2a/\lambda\!\!\!^{-})^2$, in the expression for $E_{\frac{1}{2}} - E_R$. These are the two parameters on which the area function $A_E(\infty)$ is primarily dependent and hence we take them as the two unknown variables to be experimentally determined. A set of values (say 5) of both $n\sigma_0\tan^2 2a/\lambda\!\!\!^{-}$ and $\Gamma/\tan(2a/\lambda\!\!\!^{-})$ are assumed, covering the ranges of interest. For ease of manipulation values of $n\sigma\tan^2 2a/\lambda\!\!\!^{-}$ are taken for which graphs are available in fig. 1, 2, 3 or 4. Pseudo-corrected areas $A_E^{\exp,P}(\infty)$ are then calculated from the experimental data using equations (9), (10), (11), (12), (13) and (14) and the possible pairs of parameters $n\sigma_0\tan^2 2a/\lambda\!\!\!^{-}$ and $\Gamma/\tan(2a/\lambda\!\!\!^{-})$. In our scheme this is done by means of the Mercury computer at Harwell. The programme for this calculation employs the approximate simultaneous solution of equations (9) and (10) but improves the answer by successive approximations.

The areas $A_E^{\exp,P}(\infty)$ appropriate to given pairs of resonance parameters are now compared with $A_E(\infty)$ for the same sets of parameters in order to determine a relationship between $n\sigma \tan^2 2a/\lambda\!\!\!^{-}$ and $\Gamma/\tan(2a/\lambda\!\!\!^{-})$ for which $A_E^{\exp,P}(\infty) = A_E(\infty)$ i.e. for which there is self-consistency between the parameters assumed in obtaining $A_E^{\exp,P}(\infty)$ and the parameters derived from this quantity. This process may be carried out graphically e.g. $A_E^{\exp,P}(\infty)$ may be plotted against $\Gamma/\tan(2a/\lambda\!\!\!^{-})$ [or against $n\sigma_0 \tan^2 2a/\lambda\!\!\!^{-}$] for different values of $n\sigma_0 \tan^2 2a/\lambda\!\!\!^{-}$ [or $\Gamma/\tan(2a/\lambda\!\!\!^{-})$]. $A_E(\infty)$ is plotted similarly and the points of intersection of corresponding curves give the self-consistent relation between the parameters. Standard deviations of $\Gamma/\tan 2a/\lambda\!\!\!^{-}$ [for $n\sigma_0 \tan^2 2a/\lambda\!\!\!^{-}$] for a fixed value of $n\sigma_0 \tan^2 2a/\lambda\!\!\!^{-}$ [or $\Gamma/\tan(2a/\lambda\!\!\!^{-})$] may be obtained at the same time. The variance of $A_E^{\exp,P}(\infty)$ is given approximately by

$$\operatorname{var} A_E^{\exp} = \sum_{E_1}^{E_2} \Delta T_i^2 \Delta E_i^2 / T_p^2 + \Delta T_p^2 \Big(\sum_{E_1}^{E_2} T_i \Delta E_i\Big)^2 / T_p^4$$

where ΔT_i and ΔT_p are the standard deviations of T_i and T_p respectively. The difference between the intersections of $A_E^{\exp,P}(\infty) + \sqrt{(\operatorname{var} A_E^{\exp})}$ and $A_E^{\exp,P}(\infty) - \sqrt{(\operatorname{var} A_E^{\exp})}$ with the corresponding $A_E(\infty)$ curves is twice the standard deviation of $\Gamma/\tan(2a/\lambda\!\!\!^{-})$ for fixed $n\sigma_0 \tan^2 2a/\lambda\!\!\!^{-}$ (or vice versa).

TABLE 1

Pseudo-corrected areas $A_E^{\exp,P}(\infty)$ for the 15.5 keV resonance in the cross section of Bi^{209}, the transmitting sample containing 0.115×10^{24} atoms cm^{-2}.

$2\Gamma/\tan 2a/\lambda\!\!\!^{-}$ \ $\frac{1}{4}n\sigma_0 \tan^2 2a/\lambda\!\!\!^{-}$	0.3	0.4	0.5	0.6	0.7	0.8
0.1	0.1122	0.1078	0.1032	0.0984	0.0934	0.0882
0.3	0.1082	0.0998	0.0897	0.0780	0.0646	0.0495
0.5	0.1307	0.1247	0.1142	0.0990	0.0792	0.0547
0.7	0.1788	0.1809	0.1741	0.1584	0.1337	0.1000
0.9	0.2507	0.2658	0.2661	0.2517	0.2226	0.1790

As an example of this method we treat the case of the 15.5 keV resonance in the cross section of Bi^{209}. The transmissions of three samples were measured as a function of energy. Sample thickness were 0.00903, 0.0580 and 0.115×10^{24} atoms cm^{-2}. The pseudo-corrected areas obtained for the thickest sample are shown in table 1. The data in this table were plotted as a family of six curves

TABLE 2

Points on the self-consistent curve from the analysis of the data in table 1

$\frac{1}{4}n\sigma_0 \tan^2(2a/\lambda\!\!\!^{-})$	$\frac{1}{4}\sigma_0 \tan^2(2a/\lambda\!\!\!^{-})$	$2\Gamma \tan(2a/\lambda\!\!\!^{-})$
0.3	2.51	0.170
0.4	3.48	0.167
0.5	4.35	0.170
0.6	5.22	0.190
0.7	6.10	0.220
0.8	6.97	0.195

(fig. 6) of $A_E^{\exp,P}(\infty)$ against $2\Gamma/\tan(2a/\lambda\!\!\!^{-})$ [full curves]. The six broken lines are the values of $A_E(\infty)$ for the corresponding values of $n\sigma_0 \tan^2 2a/\lambda\!\!\!^{-}$. Since this resonance is broad enough to be an almost pure elastic scattering resonance and $g_J \approx \frac{1}{2}$ for $J = I \pm \frac{1}{2}$ $(I = \frac{9}{2})$, $n\sigma \approx 8$ and this value

was used in reading $A_E(\infty)$ from fig. 2. The values of $\sigma_0 \tan^2 2a/\lambda$ obtained from the intersections of the two sets of curve are shown in table 2, together with the standard deviation of the latter quantity. The same procedure was carried out for the other two samples, with the result that we have the three curves of $\sigma_0 \tan^2 (2a/\lambda)$ as a function of $\Gamma/\tan (2a/\lambda)$ shown in fig. 7. The plot here employs logarithmic scales. The tangents to the three curves *on this diagram* at points in the region of intersection were used in the least squares analysis to obtain the best values of the parameters, their variances and covariance. Further discussion of these quantities is deferred to Section 6.

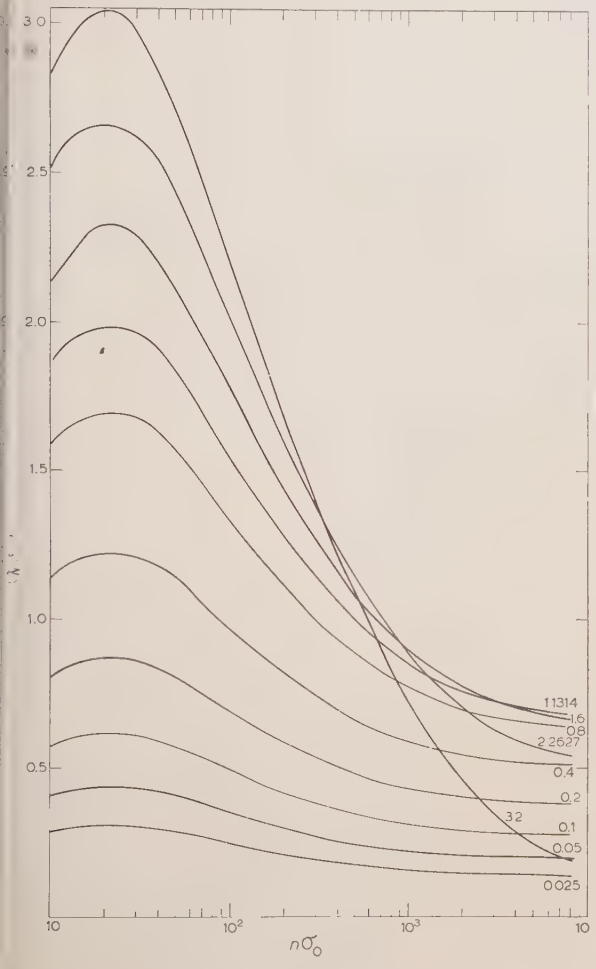

Fig. 12. $A_N(\infty)$ v. $n\sigma_0$ for $\beta = 16$.

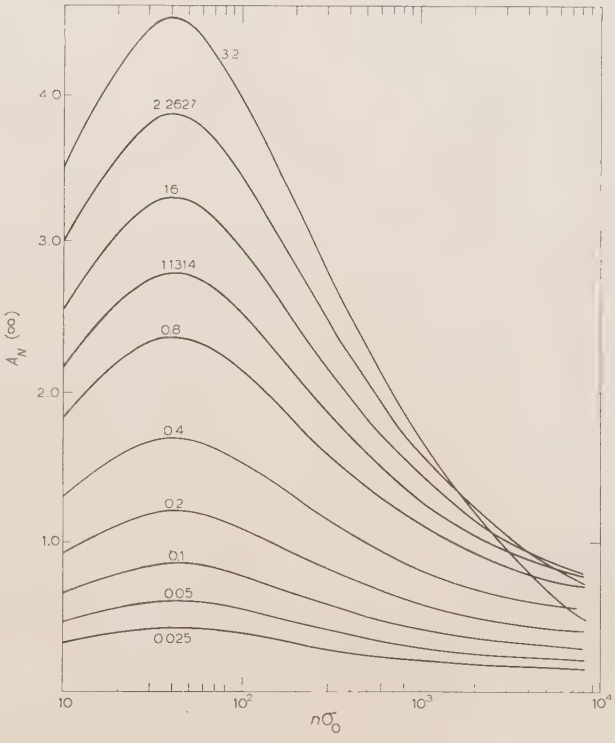

Fig. 13. $A_N(\infty)$ v. $n\sigma_0$ for $\beta = 32$.

4. The Area Function for Doppler-broadened Resonance Cross-section

Because of thermal motion of the atoms in a sample the energy of relative motion between a nucleus and neutron may vary appreciably compared with the width of the resonance line for a neutron of definite laboratory energy. For this reason we must consider the neutron transmission for effective "Doppler-broadened" cross sections[7,8]. The terms $1/(1 + x^2)$ in the resonance term and $x/(1 + x^2)$ in the interference term of equation (4) for the cross section $\sigma(E)$ are now replaced by $\Psi(\beta,x)$ and $\Phi(\beta,x)$ respectively where

$$\Psi(\beta,x) = \frac{1}{\beta\sqrt{\pi}} \int_{-\infty}^{\infty} \frac{1}{1 + y^2} \exp\left\{ -\frac{(x - y)^2}{\beta^2} \right\} dy \qquad (16)$$

[7]) H. A. Bethe, Rev. Mod. Phys. **9** (1937) 140. [8]) W. E. Lamb, Phys. Rev. **55** (1939) 190.

$$\Phi(\beta,x) = \frac{1}{\beta\sqrt{\pi}} \int_{-\infty}^{\infty} \frac{y}{1+y^2} \exp\left\{-\frac{(x-y)^2}{\beta^2}\right\} dy \tag{17}$$

$$\beta = 2\Delta/\Gamma$$

$$\Delta = (4E_R k\theta/A)^{\frac{1}{2}}.$$

k is Boltzmann's constant and θ is the effective temperature of the sample[8]). If the modified cross section formula is now used for the transmission the definition of the area function remains unchanged.

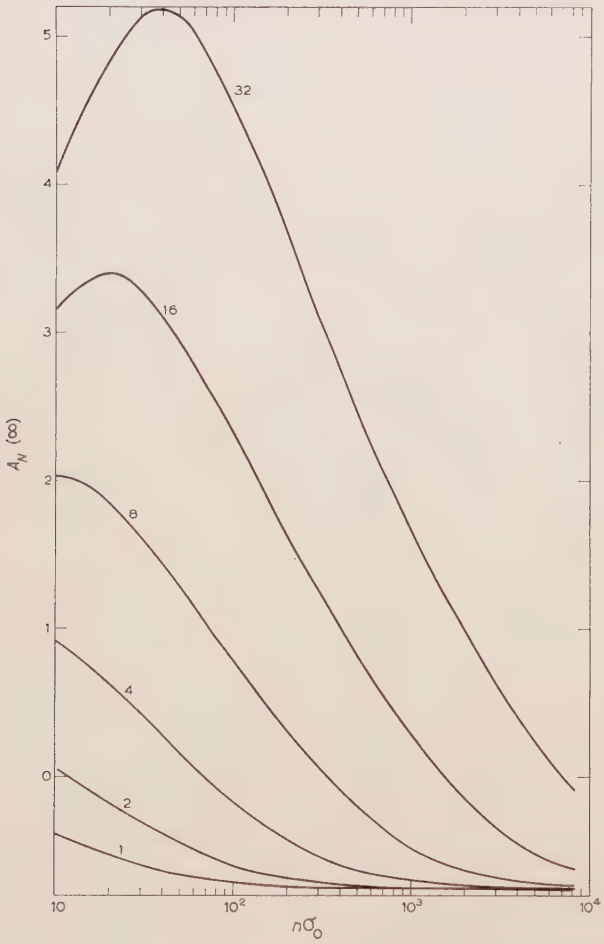

Fig. 14. $A_N(\infty)$ v. $n\sigma_0$ for $n\sigma_0 \tan^2 2a/\tilde{\lambda} = 4.525$ and specified values of β.

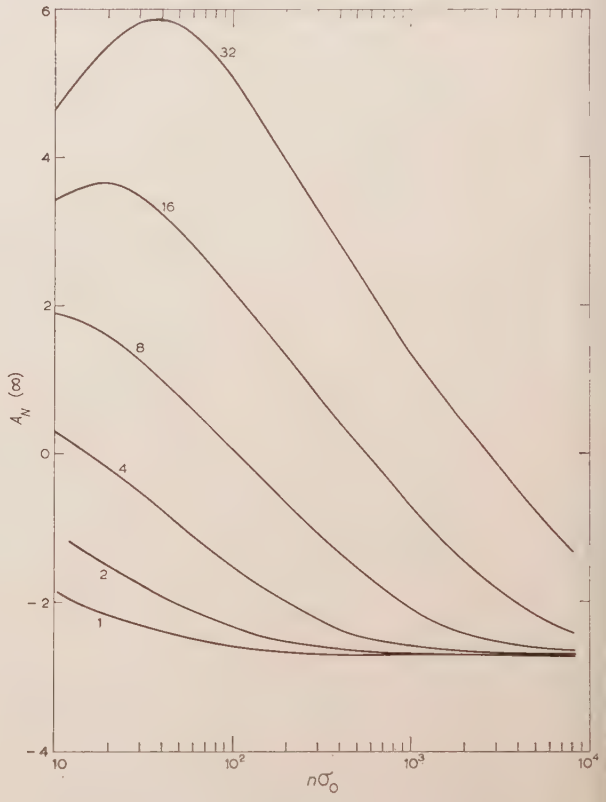

Fig. 15. $A_N(\infty)$ v. $n\sigma_0$ for $n\sigma_0 \tan^2 2a/\tilde{\lambda} = 6.4$.

The function $A_x(\infty)$ for $\beta \neq 0$ was calculated by straightforward numerical integration methods using the Mercury computer at Harwell. The function was expanded in the form

$$A_x(\infty) = \int_{-\infty}^{\infty} \{\, 1 - \exp\left[-n\sigma_0\, \Psi(\beta,x)\right] \} \, dx - \sum_{m=1}^{\infty} \frac{(n\sigma_0 \tan 2a/\tilde{\lambda})^{2m}}{(2m)!} \int_{-\infty}^{\infty} \Phi^{2m}(\beta,x) \exp\left[-n\sigma_0\, \Psi(\beta,x)\right] dx \tag{18}$$

and in the sum terms up to $m = 6$ were included in the computation. In order to calculate Ψ and Φ we start from the fact that

$$\Psi(\beta,0) = \frac{\pi^{\frac{1}{2}}}{\beta} e^{1/\beta^2} \left[1 - \operatorname{erf}(1/\beta)\right]. \tag{19}$$

For $\beta > 0.5$, to which values the computation was confined, this expression may be calculated by using the series expansion for the error function

$$\operatorname{erf} x = \frac{2}{\sqrt{\pi}}\left(x - \frac{x^3}{1!3} + \frac{x^5}{2!5} - \frac{x^7}{3!7} + \cdots\right).$$

For values of $x > 0$ (Ψ is an even and Φ an odd function of x) Ψ and Φ were calculated by step-numerical integration of the differential equations

$$\frac{\mathrm{d}^2\Psi}{\mathrm{d}x^2} = \frac{4}{\beta^4} - \frac{4x}{\beta^2}\frac{\mathrm{d}\Psi}{\mathrm{d}x} - \frac{2}{\beta^2}\left[1 - \frac{2}{\beta^2}(1 - x^2)\right]\Psi \tag{20}$$

and the use of

$$\Phi = \frac{\beta^2}{2}\frac{\mathrm{d}\Psi}{\mathrm{d}x} + x\Psi \,. \tag{21}$$

The initial condition for $\mathrm{d}\Psi/\mathrm{d}x$ is

$$\left[\frac{\mathrm{d}\Psi}{\mathrm{d}x}\right]_{x=0} = 0 \,.$$

For $x > 5\beta$ it is sufficiently accurate to employ the asymptotic series

$$\Psi(\beta,x) = y\,[1 + a_1 y + a_2 y^2 + \cdots] \tag{22}$$

$$\Phi(\beta,x) = xy\,[1 + b_1 y + b_2 y^2 + \cdots] \tag{23}$$

where

$$y = 1/(1 + x^2)\,,\quad a_1 = 1.5\beta^2\,,\quad a_2 = \beta^2(3.75\beta^2 - 2)\,,$$
$$a_3 = 7.5\beta^4(1.75\beta^2 - 2),\ a_4 = 3\beta^4(19.6875\beta^4 - 35\beta^2 + 4)$$
$$b_1 = a_1 - \beta^2\,,\ b_2 = a_2 - 2\beta^2 a_1\,,\ B_n = a_n - n^2\beta a_{n-1}\,.$$

Tables of the function $A_N = 0.25 \tan(2a/\lambda\!\!\!^{-})\, A_x(\infty)$ thus computed have been published elsewhere[5]). Values of β range from 0.5 to 64 by increasing factors of $2^{\frac{1}{2}}$, values of $n\sigma_0$ increase from 8 to 8192 by factors of 2 and values of $n\sigma_0 \tan^2 2a/\lambda\!\!\!^{-}$ increase from 0.014865 to 6.4 by factors of $2^{\frac{1}{4}}$. Some graphs illustrating the behaviour of these functions are shown in figs. 8 to 15.

5. Treatment of the Experimental Data-Doppler Broadening Case

Treatment of the experimental data is very similar to the description given in Section 3 but there is some modification of the various correction formulae. Most of the modified formulae are based on the asymptotic expansions, equations (22) and (23), using only the zero and first order terms. Thus

$$\Psi(\beta,x) \approx \frac{1}{1 + x^2}\left[1 + \frac{3\beta^2}{2x^2}\right] = \frac{1}{1 + x^2}\left[1 + \frac{3}{2}\frac{\Delta^2}{(E - E_\mathrm{R})^2}\right]$$

$$\Phi(\beta,x) \approx \frac{x}{1 + x^2}\left[1 + \frac{\beta^2}{2x^2}\right] = \frac{x}{1 + x^2}\left[1 + \frac{\Delta^2}{2(E - E_\mathrm{R})^2}\right]$$

and it is fortunate that the modifications introduced into the formulae for the no-Doppler broadening case are dependent on approximately known quantities. The asymptotic formulae in general cannot be used however for the derivation of the resonance energy which is based on the equation

$$-\ln T_{\frac{1}{2}}/T_\mathrm{p} = n\sigma_0\Psi(\beta,x_{\frac{1}{2}}) + n\sigma_0 \tan(2a/\lambda\!\!\!^{-})\cdot\Phi(\beta,x_{\frac{1}{2}}) \,. \tag{24}$$

The computer programme we employ assumes increasing values of E_R, starting from $E_{\frac{1}{2}}$ and calculates T_p from equation (24), and also from the equation

$$T_\mathrm{p} = \sqrt{T(\varepsilon'')T(-\varepsilon'')}\,\exp\left\{\frac{n\sigma_0\Gamma^2}{4\varepsilon''^2}\left(1 + \frac{3\Delta^2}{2\varepsilon''^2}\right)\left(1 + 3\frac{\delta\varepsilon''}{\varepsilon''}\right)^2 - \frac{1}{4\varepsilon''}\tan^2\frac{2a}{\lambda\!\!\!^{-}}\cdot\frac{2\Gamma}{\tan 2a/\lambda\!\!\!^{-}}\cdot\frac{\delta\varepsilon''}{\varepsilon''}\left(1 + \frac{\Delta^2}{2\varepsilon''^2}\right)\right\}. \tag{25}$$

When agreement between the two values of T_p is reached, the corresponding value of E_R is accepted as the true resonance energy. Of course in calculating equation (25) a value of Γ must be assumed. This is derived from the value of $\Gamma/\tan(2a/\lambda\!\!\!^{-})$ employed in the calculation of the pseudo-corrected areas by assuming $\tan 2a/\lambda\!\!\!^{-}$. The calculation is insensitive to any resulting error in Γ. The wing correction terms are:

$$\Delta A_E(\varepsilon') = [\Delta A_E(\varepsilon')]_{\beta=0} + \frac{n\sigma_0\Gamma^2}{2\varepsilon'}\left\{\left(0.5 - \tfrac{1}{6}\, n\sigma_0 \tan^2\frac{2a}{\lambda\!\!\!^{-}}\right)\frac{\Delta^2}{\varepsilon'^2}\right\} \tag{26}$$

$$\delta A_E(\varepsilon') = n\sigma_0\Gamma \tan 2a/\lambda\!\!\!^{-}\,\frac{\delta\varepsilon'}{\varepsilon'}\left\{1 - \frac{1}{2\varepsilon'}\frac{n\sigma_0\Gamma^2}{2\varepsilon'}\left(1 - \frac{n\sigma_0}{6}\tan^2\frac{2a}{\lambda\!\!\!^{-}}\right) + \frac{\Delta^2}{2\varepsilon'^2}\right\} - \frac{n\sigma_0\Gamma^2}{2\varepsilon'}\left(1 - \tfrac{1}{2}\, n\sigma_0 \tan^2\frac{2a}{\lambda\!\!\!^{-}}\right)\left(\frac{\delta\varepsilon'}{\varepsilon'}\right)^2. \tag{27}$$

An example of analysis of the transmission due to a Doppler-broadened resonance is provided by the 66eV resonance in the cross section of U^{238}. The transmissions were measured for samples of thickness 0.0149, 0.0850, 0.120 and 0.1295×10^{24} atoms cm^{-2}. The pseudo-corrected areas $A_E^{\exp,P}(\infty)$ for the thickest sample are shown in table 3 and the derivation of the self-consistent curves in fig. 16. The self-consistent curves themselves are plotted in fig. 17, with the resulting best values and variances of $\sigma_0 \tan^2 2a/\lambda\!\!\!^{-}$ and $\Gamma/\tan(2a/\lambda)$.

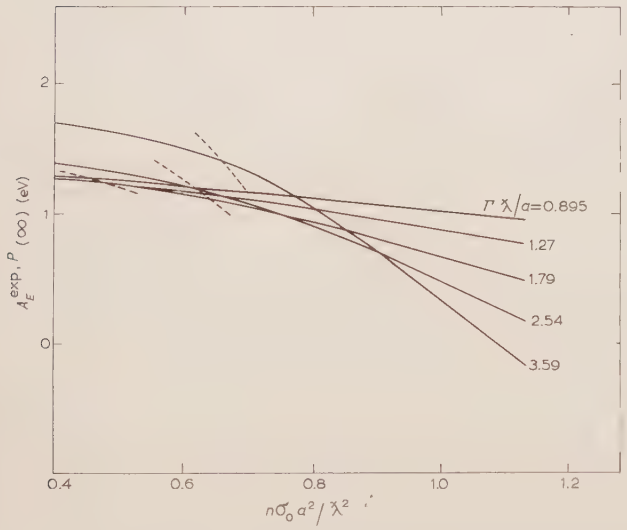

Fig. 16. Comparison of $A_E^{\exp}(\infty)$ (full curves) with theoretical behaviour of $A_E(\infty)$ for the 66 eV resonance of U^{238} + n.

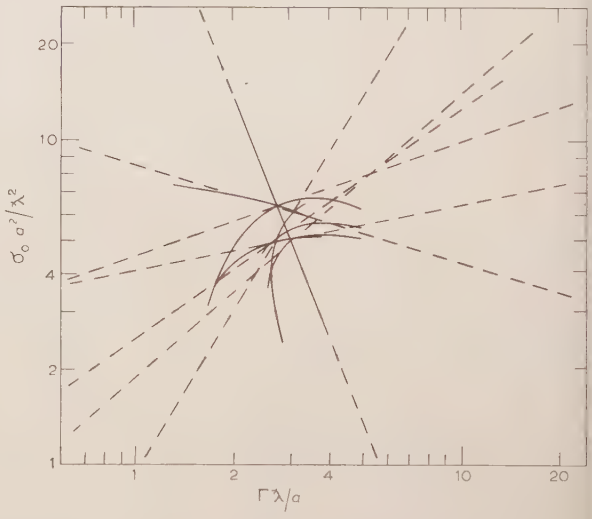

Fig. 17. Plot of self-consistent resonance parameter data for 66 eV resonance of U^{238} + n. A least-squares analysis gives $\sigma_0 a^2/\lambda\!\!\!^{-2} = 5.62 \pm 0.23$ b, $\Gamma\lambda\!\!\!^{-}/a = 2.97 \pm 0.08$ eV, covar $(\sigma_0 a^2/\lambda\!\!\!^{-2}, \Gamma\lambda\!\!\!^{-}/a)/(\sigma_0\Gamma\, a/\lambda\!\!\!^{-}) = -3.36 \times 10^{-4}$.

TABLE 3

Pseudo-corrected areas $A_E^{\exp,P}(\infty)$ for the 66 eV resonance in the cross section of U^{238}, the transmitting sample containing 0.1295×10^{24} atoms cm^{-2}

$2\Gamma/\tan 2a/\lambda\!\!\!^{-}$ \ $\frac{1}{4}n\sigma_0 \tan^2(2a/\lambda\!\!\!^{-})$	0.4	0.5657	0.8	1.1314	1.6
0.897	1.2798	1.2228	1.1251	0.9518	0.6316
1.269	1.2645	1.1828	1.0328	0.7510	0.2108
1.794	1.2814	1.1681	0.9401	0.4793	−0.4551
2.537	1.3932	1.2506	0.9153	0.1696	−1.4428
3.588	1.7033	1.5414	1.0521	−0.1647	−2.9642

6. Further Interpretation of the Resonance Parameters

6.1. THE 15 keV RESONANCE IN THE NEUTRON CROSS SECTION OF Bi^{209}

It may safely be assumed that there is negligible radiative capture or any other reaction in the cross section across this resonance. Consequently $\sigma_0 \tan^2 2a/\lambda\!\!\!^{-}$ may be written

$$4\pi^2 \frac{\lambda\!\!\!^{-2}}{a^2} \cos 2a/\lambda\!\!\!^{-} \tan^2 2a/\lambda\!\!\!^{-} \cdot g_J$$

where $J\hbar$ is the total angular momentum associated with the resonance and J may be 4 or 5 in this case. From the value of this expression we may obtain a value of $a/\lambda\!\!\!^{-}$ and hence of Γ (from $\Gamma/\tan 2a/\lambda\!\!\!^{-}$). We find that, assuming $J = 4$, $a/\lambda\!\!\!^{-} = 0.27 \pm 0.02$, $a = (9.8 \pm 0.7) \times 10^{-13}$ cm, $\Gamma = 61 \pm 7$ eV. Assuming $J = 5$, $a/\lambda\!\!\!^{-} = 0.24 \pm 0.02$, $a = (8.9 \pm 0.7) \times 10^{-13}$ cm, $\Gamma = 55 \pm 6$ eV.

6.2. THE 66 eV RESONANCE IN THE NEUTRON CROSS SECTION OF U^{238}

In this case it is necessary to derive the value of the effective potential scattering length at the resonance energy from the transmission measurements. The effective potential transmission is calculated in the course of the compution of the pseudo-corrected areas and may be printed out. If it is determined on making the corrections in this computation with the best values of the resonance parameters, we obtain the potential scattering length. At the same time the resonance energy is determined. From all the data we arrive at the following resonance parameters:

$$E_R = 66.14 \text{ eV}$$

σ_p (effective) $= (11.2 \pm 0.3)$ barn

a (effective) $= (9.45 \pm 0.12) < 10^{-13}$ cm.

$a/\lambda\!\!\!^{-} = 0.0169 \pm 0.0002$

$\Gamma\lambda\!\!\!^{-}/a = 2.970 \pm 0.083$ eV

$\Gamma = 50.2 \pm 1.5$ meV

$\sigma_0 a^2/\lambda\!\!\!^{-2} = 5.62 \pm 0.23$ barn

$\sigma_0 = 19660 \pm 900$ barn

$\Gamma_n/\Gamma = 0.500 \pm 0.023$

$\Gamma_n = 25.1 \pm 1.2$ meV

$\Gamma_\gamma = 25.1 \pm 1.4$ meV

$\sigma_0 \Gamma a/\lambda\!\!\!^{-} = 16.7 \pm 0.8$ barn eV

$\sigma_0 \Gamma^2 = 49.6 \pm 3.2$ barn eV^2

NUCLEAR INSTRUMENTS AND METHODS 9 (1960) 328–340; NORTH-HOLLAND PUBLISHING CO.

LA STABILISATION DU CHAMP MAGNETIQUE PAR UN MASER A RESONANCE MAGNETIQUE NUCLEAIRE (II) †

P. GRIVET et H. HAHN

Laboratoire d'Electronique et de Radioélectricité de la Faculté des Sciences de l'Université de Paris, B.P. no. 9, Fontenay-aux-Roses, Seine

Reçu le 18 mai 1960

In this second part we describe the various parts of the regulator build around the maser oscillator discussed in part I. Here we find a quartz frequency standard, the frequency modulation detector and the feed back loop. A long term stability $\pm 6 \times 10^{-7}$ is obtained with a laboratory electromagnet of poor spatial uniformity and could be improved with a better magnet.

3. Le Fréquencemètre

3.1. LE SCHEMA DE PRINCIPE

La mesure du champ magnétique est ramenée, grâce au maser, à une mesure de fréquence qui est située dans la gamme:

$$29.625 — 29.635 \text{ MHz} .$$

Nous nous sommes donc proposés de réaliser un fréquencemètre, qui permettait de déterminer la valeur absolue, mais surtout les variations de cette fréquence. La mesure se fait par comparaison de la fréquence inconnue avec une fréquence de référence à l'aide d'un système discriminateur; le principe du fonctionnement est représenté par le schéma de principe sur la fig. 7.

† (I): Nucl. Instr. and Meth. 9 (1960) 233.

a. Le système discriminateur

La fréquence inconnue f_x est hétérodynée au voisinage de $f_0 = 455$ kHz avec une fréquence de référence f_R et ce battement passe dans un amplificateur MF très sélectif accordé sur 455 kHz. Le discriminateur choisi reste sensible à la modulation d'amplitude et, pour cette raison est précédé d'un étage limiteur. Il délivre à sa sortie une tension continue pour tout écart de fréquence f_x par rapport à $f_R + 455$ kHz. Cette tension de sortie est filtrée de toutes ses ondulations parasites et attaque un cathode follower, qui fonctionne en changeur d'impédance. La tension de sortie est susceptible d'être enregistrée pour la mesure ou d'être prise comme signal d'erreur dans une chaîne de régulation.

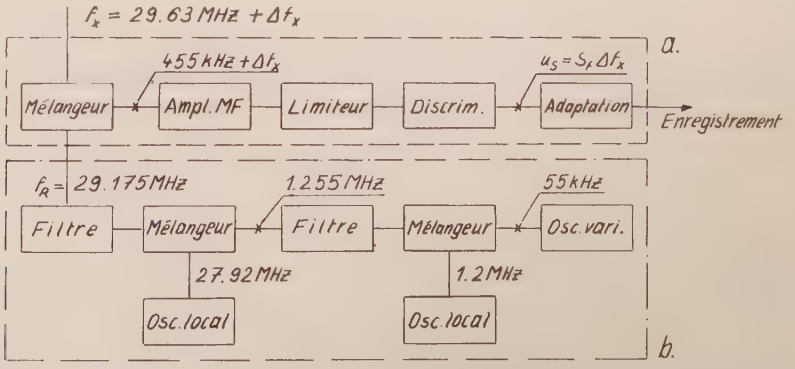

Fig. 7. Schéma de principe du fréquencemètre: a. Système discriminateur; b. Fréquence de référence.

b. La fréquence de référence

La plage de fonctionnement du discriminateur n'est que de 300 Hz et comme il peut y avoir initialement dans la connaissance de la fréquence f_x une incertitude supérieure à cet écart, il est nécessaire de disposer d'une fréquence de référence ajustable. L'expérience nous a montré qu'il était suffisant de pouvoir faire varier f_R de $\pm$ 5 kHz. Nous avons obtenu la fréquence de référence par synthése de fréquence.

La précision de la mesure relative est limitée:
– par la dérive de la fréquence de référence,
– par la dérive de la fréquence de zéro du discriminateur,
– par la dérive du zéro du cathode follower.

La sensibilité de l'appareil, c'est-à-dire la plus petite variation de f_x qui soit encore discernable, est limitée par le bruit à la sortie du système discriminateur.

3.2. LA FREQUENCE DE REFERENCE

Pour obtenir une fréquence ajustable aussi stable que possible, nous avons procédé par double changement de fréquence; la fréquence de référence est la somme de trois fréquences composantes de différents ordres de grandeur. Le choix des fréquences se fait en considérant:
– Le problème de filtrage. Les battements indésirables peuvent être plus facilement filtrés, si le rapport des deux fréquences est < 25. L'expérience nous a montré qu'il suffit alors de faire ce filtrage avec de simples circuits oscillants, d'autant plus que l'amplificateur MF est très sélectif et supprime tous les battements parasites.
– La dérive totale, qui elle aussi, est la somme de trois dérives individuelles. L'oscillateur variable ne peut pas être stabilisé par un quartz et sera par conséquent un générateur BF. C'est l'oscillateur de fréquence la plus élevée qui nous demandera le plus de soin.

Finalement nous avons choisi pour les oscillateurs locaux les fréquences 27.92 MHz et 1.2 MHz et pour l'oscillateur variable 55 $\pm$ 5 kHz.

[22]) F. D. Lewis, Proc. IRE (sept. 1955) 1046.
[23]) E. P. Felch et J. O. Israel, Proc. IRE (mai 1955) 596.

3.2.1. *L'oscillateur local à 27.92 MHz*

Un étalon de fréquence[22]) dans cette gamme utilise toujours un quartz comme élément de contrôle à cause de son grand facteur de surtension, sa constance dans le temps et son petit coefficient de température. C'est seulement avec un circuit électrique approprié que l'on en peut tirer le plus grand profit. Nous avons utilisé la résonance série du cristal et, pour cela, réalisé un circuit Clapp-Gouriet avec contrôle automatique de volume (CAV)[23]).

Nous avons réalisé un autre oscillateur à la fréquence 29.63 MHz d'aprés les mêmes principes et avons mesuré sa stabilité de fréquence par comparaison avec une horloge à quartz et à l'aide d'un compteur. Après 1 heure de chauffage, sa dérive horaire est restée inférieure à 15 Hz, soit une stabilité de 5×10^{-7}. Nous avons renoncé à des enceintes chauffantes qui sont indispensables si l'on veut pousser la stabilité de l'oscillateur au delà de cette limite.

3.2.2. *L'oscillateur local à 1.2 MHz*

Cet oscillateur ne requiert pas les mêmes soins, puisque sa fréquence est beaucoup plus basse. Nous avons adopté un montage à quartz du type Butler modifié[24]).

3.2.3. *L'oscillateur BF à fréquence variable*

La dérive de cet oscillateur variable doit être compatible, en valeur absolue, avec la stabilité de l'oscillateur HF. Nous avons opté pour un circuit LC du type Clapp-Vackar[25]), que nous avons amélioré par un contrôle automatique de volume.

Son analyse sommaire est basée sur le schéma de la fig. 8:

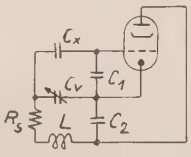

Fig. 8. Schéma de principe de l'oscillateur BF.

[24]) J. P. Buchanan, WADC Techn. rep. 56/156 (octobre 1956).
[25]) K. Henney, Radio eng. handbook (McGraw Hill, éd., New-York, 1959) ch. 16.

La pente minimum est presque indépendante de la fréquence, comme le montre la formule[25]):

$$S_m = \frac{R_s}{L}\frac{C_B C_2}{C_A}$$

avec

$$C_A = C_x\left(1 + \frac{C_v}{C_x}\right) \quad \text{pour} \quad C_v, C_x \ll C_1, C_2$$

$$C_B = C_1\left(1 + \frac{C_v}{C_x}\right)$$

d'où

$$S_m = \frac{R_s}{L}\frac{C_1 C_2}{C_x} = \frac{1}{Q}\sqrt{\frac{C_x}{L}}\frac{C_1 C_2}{C_x^2}.$$

Q = facteur de surtension du circuit oscillant pour $C_v = 0$.

En pratique, c'est la self qui détermine le Q qui atteint 500 grâce à un bobinage en fil de litz sur un pot fermé 36/22 en ferroxcube FXC-3B2. La valeur de la capacité C_x se détermine par la gamme de fréquence:

$$\frac{C_x + C_v}{C_x} = \left(\frac{60\text{kHz}}{50\text{kHz}}\right)^2 = 1.44 \left\{\begin{array}{l} C_v = 500\text{ pF} \\ C_x \cong 1\text{ nF}. \end{array}\right.$$

La dérive horaire de cet oscillateur, dont le circuit complet est indiqué sur la fig. 9, a été trouvé égale à 5 Hz, ce qui représente une stabilité de 10^{-4}/heure.

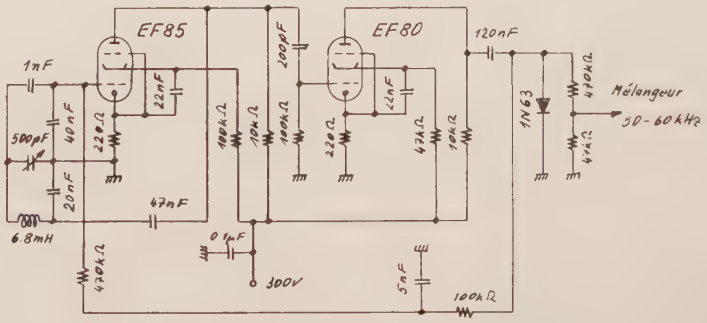

Fig. 9. Oscillateur BF à fréquence variable.

3.3. CHANGEMENT DE FREQUENCE

Après comparaison des différentes solutions qui s'offrent pour le changement de fréquence, nous avons adopté un changement de fréquence avec pentagrilles 6BE6 en excitation séparée (pentagrid mixer). Ce montage a l'avantage d'être très simple, d'offrir le meilleur découplage des deux fréquences et d'avoir une grande pente de conversion. Les heptodes ont un grand bruit de fond ($R_{eq} = 200\,k\Omega$), qui est pourtant ici sans effet, puisque les signaux sont tous très grands. Les trois étages mélangeurs sont suivis par un cathode follower, permettant la transmission du signal à l'aide d'un câble coaxial.

3.4. L'ETAGE LIMITEUR

La tension de sortie du discriminateur de fréquence dépend des variations
– de la fréquence d'excitation, qui représente l'information et
– de l'amplitude de l'excitation, correspondant à une perturbation.

Les variations de l'amplitude proviennent directement du maser ou de la variation du gain de l'amplification précédente en fonction de la fréquence. On les supprime parfaitement par deux limiteurs.

Etant donné que le limiteur a un seuil de fonctionnement, il sera précédé d'un amplificateur MF qui garantit une tension suffisante même pour les signaux les plus faibles. L'amplificateur est à contrôle automatique de volume, augmentant ainsi l'effet limiteur.

Nous adoptons dans l'étage limiteur un circuit qui est courant en transmission par modulation de fréquence[26]). Cet étage est composé de deux limiteurs en cascade. La tension de sortie est à cause des circuits oscillants sinusoidale, malgré le fonctionnement nonlinéaire de l'étage.

[26]) F. Langford-Smith, Radio designer's handbook (Iliffe & Sons éd., Londres, 1957) ch. 29.

Nous avons choisi pour les constantes de temps du

1er limiteur	0.2 msec.
2ème limiteur	40 μsec
CAV	50 msec .

Ce choix permet la suppression efficace des variations rapides et lentes de l'amplitude et surtout d'un bruit de 50 Hz, qui se manifeste habituellement comme une variation d'amplitude.

Pour une variation de 20 μV à 2V de la tension d'entrée, la tension de sortie ne varie que de 1%. L'amplification maximum pour une tension d'entrée de 20 μV est de 10^6, soit 120 dB. La tension efficace de sortie est de 23.3 V, valeur bien adaptée à l'excitation du discriminateur de fréquence.

3.5. LE DISCRIMINATEUR DE FREQUENCE

Le discriminateur de fréquence joue un rôle essentiel pour le fonctionnement de l'ensemble; c'est pourquoi nous nous sommes proposés de donner sa description détaillée. Le but du discriminateur est la conversion d'une variation de fréquence en une variation de tension continue. Sa qualité est caractérisée par:

– la pente de conversion S_f, définie par l'équation

$$u_s = S_f (f_a - f_0) = S_f \Delta f_x .$$

– la stabilité du zéro, c'est-à-dire de la fréquence de repos, pour laquelle la tension de sortie est zéro.

Le même problème s'est déjà posé pour la transmission en modulation de fréquence et le contrôle automatique de fréquence des oscillateurs locaux. Dans la plupart des cas on a adopté un "discriminateur de phase" ou un "ratio-détecteur", qui ne demande pas de limiteur préalable. Mais nous avons jugé leurs sensibilités insuffisantes pour nos besoins. La sensibilité d'un discriminateur à basse fréquence est beaucoup plus grande, mais les problèmes de filtrage deviennent critiques.

Finalement nous avons opté pour un discriminateur de fréquence à quartz[27]), qui donne une sensibilité élevée et une plage de fonctionnement suffisante pour une fréquence de repos très stable de 455 kHz. Le circuit du discriminateur est représenté sur la fig. 10; nous signalons, toutefois, que le filtre encadré représente un réseau correcteur pour le fonctionnement en régulateur.

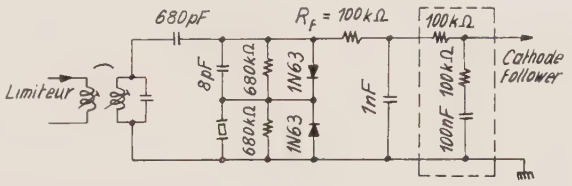

Fig. 10. Discriminateur de fréquence à quartz.

3.5.1. *Le principe de fonctionnement*

Le fonctionnement du discriminateur s'explique à l'aide de la fig. 11.

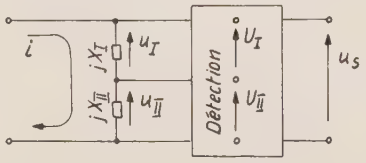

Fig. 11. Principe du discriminateur.

Un courant alternatif i, purement sinusoidal de fréquence f_a, produit, en parcourant deux réactances jX_I et jX_{II}, deux tensions alternatives u_I et u_{II}. Aprés détection individuelle des deux tensions, on prend leur différence comme tension de sortie

$$u_s = U_{II} - U_I .$$

La réactance X_I est une capacité C_I, et X_{II} représente le quartz. Les variations qualitatives des tensions en fonction de la fréquence sont indiquées sur la fig. 12.

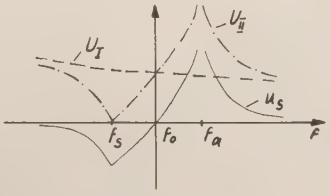

Fig. 12. Tensions du discriminateur.

[27]) P. Vigoureux et G. F. Booth, Quartz vibrators and their applications (H. M. Stationary Office, ed., Londres, 1950) p. 239.

La courbe réelle $u_s = u_s(f)$ est de la même forme que la courbe théorique de la fig. 12; mais les pics et la pente sont atténués par les résistances inévitables. La plage de fonctionnement est pratiquement limitée par la différence Δf_0 entre la résonance série f_s et la résonance parallèle f_a du quartz. Une grande pente et une large plage de fonctionnement sont des conditions incompatibles. La fréquence de repos peut être légèrement modifiée par la capacité C_I. On obtient une bonne symétrie de la courbe de discrimination par réglage des deux bobines du transformateur MF du dernier étage limiteur.

3.5.2. *L'analyse stationnaire*

L'analyse du discriminateur se fait en considérant le comportement des réactances au voisinage de la fréquence de repos f_0, ce qui donne la pente maximum définie par l'équation

$$S_{f_0} = \left(\frac{du_s}{df}\right)_0 .$$

L'analyse est dite stationnaire, parce que l'on suppose la fréquence constante en fonction du temps.

3.5.2.1. En négligeant les résistances on trouve:
– la réactance de la capacité $C_I = C_0$

$$jX_I = -jX_0 \cong \text{const.} \qquad X_0 = \frac{1}{\omega_0 C_0}$$

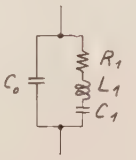

Fig. 13. Circuit équivalent du quartz.

– la réactance du quartz (fig. 13):

$$jX_{II} \cong -jX_0 \frac{\omega_0 \{ \omega^2 - (1-\delta)\omega_0^2 \}}{\omega \{ \omega^2 - (1+\delta)\omega_0^2 \}}$$

avec

$$\delta = \frac{f_a - f_s}{f_0} = \frac{\Delta f_0}{f_0} = \frac{C_1}{2C_0} \leqq 4 \times 10^{-3}$$

$$f_0 = \tfrac{1}{2}(f_a + f_s) .$$

On voit que le quartz forme pour f_0 avec la capacité C_I un circuit oscillant en série. Si l'on suppose une détection idéale, la tension de sortie devient:

$$u_s = X_{II} I - X_I I .$$

La pente maximum approximée est donnée par:

$$S_{f_0}^* = \left(\frac{dX_{II}}{df}\right)_0 I = 4 \frac{X_0}{\Delta f_0} \frac{U_0}{R_i} .$$

U_0 = tension à vide
R_i = résistance interne du dernier étage limiteur.

3.5.2.2. Corrections dues aux résistances. Le circuit équivalent du discriminateur de la fig. 14 est valable dans sa plage de fonctionnement.

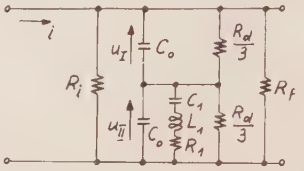

Fig. 14. Circuit équivalent du discriminateur.

La résistance interne R_i du circuit oscillant du limiteur est supposée constante et réelle, puisque sa bande passante est beaucoup plus large que

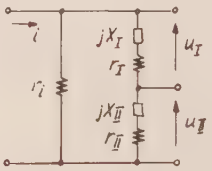

Fig. 15. Circuit équivalent approché du discriminateur.

celle du discriminateur. La résistance équivalente à une résistance R_d, shuntée par une diode de détection, est égale à $\frac{1}{3}R_d$. La résistance d'entrée du filtre est en parallèle avec R_i et pratiquement égale à R_f. Au voisinage immédiat de la fréquence de repos on trouve le circuit équivalent de la fig. 15 avec les résistances équivalentes

$$r_i = R_i \frac{1}{1 + \frac{R_i}{R_f}}$$

$$r_I = 3 \frac{X_0^2}{R_d}$$

$$r_{II} = 4R_i \left(1 + \frac{3}{4} \frac{X_0^2}{R_i R_d}\right) .$$

Les réactances ne sont que peu changées. Les tensions sont alors:

$$u_{\mathrm{I}} = \frac{[r_{\mathrm{I}} - jX_0]\, r_{\mathrm{i}}\, i}{r_{\mathrm{i}} + r_{\mathrm{I}} + r_{\mathrm{II}} + j\,\dfrac{S_{f_0}^*}{I}\,\Delta f_x}$$

$$u_{\mathrm{II}} = \frac{\left[r_{\mathrm{II}} + j\left(X_0 + \dfrac{S_{f_0}^*}{I}\,\Delta f_x\right)\right] r_{\mathrm{i}}\, i}{r_{\mathrm{i}} + r_{\mathrm{I}} + r_{\mathrm{II}} + j\,\dfrac{S_{f_0}^*}{I}\,\Delta f_x}.$$

On voit que la fréquence est légèrement décalée, sauf dans le cas $r_{\mathrm{I}} = r_{\mathrm{II}}$.

La pente de conversion, en tenant compte de l'atténuation des résistances, est alors:

$$S_{f_0} = S_{f_0}^* \frac{1}{1 + \dfrac{r_{\mathrm{I}}}{r_{\mathrm{i}}} + \dfrac{r_{\mathrm{II}}}{r_{\mathrm{i}}} \sqrt{1 + \left(\dfrac{r_{\mathrm{II}}}{X_0}\right)^2}}.$$

Le calcul numérique donne les résultats suivants qui correspondent bien aux valeurs mesurées:

$U_0 = \sqrt{2} \times 23.3$ V

$R_{\mathrm{i}} = 150\ \mathrm{k}\Omega$ $\qquad S_{f_0}^* = 130$ mV/Hz

$C_0 = 8$ pF

$f_0 = 300$ Hz $\qquad S_{f_0} = 55$ mV/Hz

$R_{\mathrm{I}} = 7.5\ \mathrm{k}\Omega$ $\qquad$ Valeur mesurée

$R_{\mathrm{d}} = 680\ \mathrm{k}\Omega$ $\qquad S_f = 53$ mV/Hz

$R_{\mathrm{f}} = 100\ \mathrm{k}\Omega$

3.6 LE CATHODE FOLLOWER

Le discriminateur est suivi par un cathode-follower à courant continu qui fonctionne en changeur d'impédance et supprime toute réaction de la sortie sur le discriminateur. Nous avons adopté un circuit symétrique, qui réduit la dérive et qui ne change pas le niveau du signal.

Entre le cathode-follower et l'enregistreur, dont la fréquence de coupure est de 1Hz, on intercale un filtre à pont en double T, accordé sur 50 Hz, qui réduit le bruit sur cette fréquence d'un facteur ~ 30. Nous avons adopté des valeurs pour R et C telles que l'atténuation à la fréquence zéro reste négligeable. Sa fonction de transfert est[28]):

$$F = \frac{1 + (Tp)^2}{1 + 4Tp + (Tp)^2} \qquad \begin{aligned} T &= RC \\ R &= 5\ \mathrm{k}\Omega \\ C &= 0.6\ \mu\mathrm{F}. \end{aligned}$$

3.7. RESULTATS

Nous avons construit la courbe de conversion statique (fig. 16). Sa pente maximum est de 53 mV/Hz, ce qui correspond bien à sa valeur calculée. La plage de fonctionnement est de

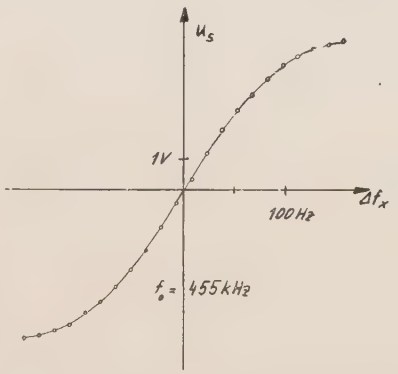

Fig. 16. Courbe de discrimination statique.

300 Hz, ce qui limite la bande passante du discriminateur. Nous avons essayé l'ensemble de cet appareillage en l'excitant par un oscillateur très stable à la fréquence 29.63 MHz; sa dérive horaire étant inférieure à 5×10^{-7}. La tension

[28]) J. E. Gibson et F. B. Tuteur, Control system components (McGraw Hill, éd., New York, 1959).

Fig. 17. Stabilité du fréquencemètre pendant 1 heure.

continue de sortie enregistrée (fig. 17) par un potentiomètre électronique montre, qu'aprés 1 heure de chauffage la dérive est inférieure à $\pm$ 6 Hz, soit une stabilité de 2×10^{-7} relative à l'oscillateur excitant. Ainsi la stabilité absolue est dans l'hypothèse la plus défavorable de 7×10^{-7}, en remarquant toutefois qu'aucun des oscillateurs à quartz employés ici ne comporte de stabilisation en température. Le niveau de bruit est de 10mV à la sortie du cathode follower et est facilement filtrable pour l'enregistrement, ce qui correspond à une sensibilité de 0.2 Hz ou 0.7×10^{-8}.

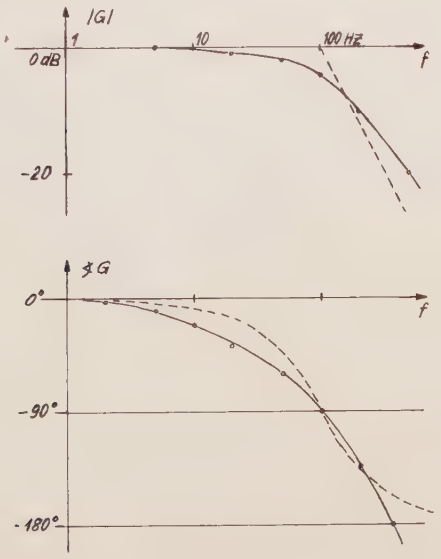

Fig. 18. Fonction de transfert du fréquencemètre.
-•-• Courbe mesurée. ––– Approximation asymptotique.

Nous avons déterminé la fonction de transfert F_d du fréquencemètre à l'aide d'un oscillateur à modulation de fréquence décrit au chapitre 2.1. La transmission reste pratiquement linéaire jusqu'à un écart de $\pm$ 100 Hz. La fonction de transfert, donnée par la courbe d'amplitude (dB) et celle de phase, est représentée en coordonnées semi-logarithmiques—le diagramme de Bode —sur la fig. 18. En cherchant l'approximation asymptotique, on peut trouver la fonction de transfert, qui est de la forme:

$$F_d = \frac{S_f}{1 + \sqrt{2}\, T_d p + (T_d p)^2} .$$

On obtient la constante de temps T_d, qui est surtout donnée par le système discriminateur, en cherchant la fréquence pour laquelle la phase retarde de 90°. Nous trouvons ainsi la valeur $T_d = 1.6$ msec.

4. La Stabilisation d'un Champ Magnétique

4.1. LE SYSTEME STABILISATEUR

Nous nous sommes proposés de stabiliser le champ magnétique d'un électro-aimant[10]) en utilisant le même dispositif que nous avons employé pour le mesurer. Comme nous l'avons montré dans les chapitres précédents, la mesure du champ fournit une tension continue; sa valeur est donnée par la grandeur et le signe d'un écart entre la fréquence du maser f_m et une fréquence de référence $f_R = 29.63$ MHz. Si nous négligeons pour l'instant l'erreur due à l'entraînement, la tension continue est de même proportionnelle à l'écart du champ magnétique B_0 par rapport à une valeur de référence $B_R = 0.6958$ Ts $= 6.958$ kG donnée par la relation $B_R = (2\pi/\gamma) f_R$.

Le problème de toute stabilisation est de réduire cet écart le plus possible, en introduisant une réaction négative. Notre système de régulation, décrit en détail dans ce qui suit, est capable d'assurer avec une préstabilisation du courant d'excitation une bonne stabilité à long terme et de supprimer les fluctuations rapides du champ. La dérive résiduelle n'est limitée que par la stabilité de la fréquence de référence, elle-même stabilisée par un quartz. L'incertitude sur la valeur du champ, produite par l'entraînement et par la mesure de la fréquence, n'est pourtant pas négligeable.

La mise en marche de la régulation requiert quelques précautions, étant donné que la plage de fonctionnement du discriminateur n'est que de 300 Hz et que les variations initiales de la fréquence f_m sont nettement plus grandes, de l'ordre de 1 kHz. Il suffit, cependant, que la fréquence reste quelques secondes dans cette plage pour faire marcher la régulation avec un gain d'abord très faible qui augmentera ensuite.

Notre dispositif de régulation fut employé à stabiliser le champ d'un ancien électroaimant Beaudouin, dont l'entrefer est de 4.7 cm et dont les pièces polaires ont un diamètre de 19.5 cm.

Il est excité par l'alimentation de Sauzade[29]) stabilisée à transistors, qui donne 15 A, sous une tension de 65 V, pour le champ de 0.6958 Ts.

4.2. L'ORGANE DE REACTION

L'organe de réaction (fig. 19) est constitué par une bobine de 2 × 8500 spires, disposée symétriquement par rapport à l'entrefer.

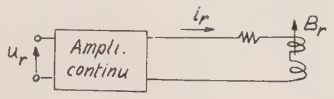

Fig. 19. Organe de réaction.

Elle est attaquée par un amplificateur à courant continu industriel qui a une résistance d'entrée de 1 MΩ, celle de sortie est de 300Ω. Cet amplificateur produit, dans son état normal de fonctionnement et en régime statique, pour 1V à l'entrée un courant de 0.5 mA dans la bobine, dont la résistance ohmique est de 6.5 kΩ. Ce courant excitateur est capable de produire un champ magnétique correcteur B_r, superposé bien entendu au champ principal et très petit par rapport à lui, et qui se calcule facilement à partir des relations fondamentales valables pour le circuit magnétique. On trouve en première approximation pour le régime statique:

$$B_r = \mu_0 \frac{N}{l_E + \frac{1}{\mu_r} l_F} i_r = \left(0.4 \frac{\text{Ts}}{\text{A}}\right) i_r$$

N = nombre total des spires (= 17 000)
l_E = largeur de l'entrefer (= 4.7 cm)
l_F = longueur moyenne du fer (≅ 2 m)
μ_r = perméabilité reversible estimée à 300.

Nous l'avons mesuré dans des conditions normales de fonctionnement et l'avons trouvé, en bon accord avec la relation calculée, en régime statique:

$$B_r = \left(0.42 \frac{\text{Ts}}{\text{A}}\right) i_r .$$

Nous avons étudié la réponse transitoire du magnétique B_r à une variation en échelon-unité du courant i_r et donc de l'excitation magnétique H_r. Le champ magnétique était mesuré dans ce but par intégration d'un signal induit dans des bobines détectrices installées sur l'électro-aimant. Le champ magnétique met un temps assez long pour répondre à une variation de l'excitation. Le temps de réponse, défini comme temps au bout duquel le système a atteint son régime définitif à 5% près[30]), est de 4 sec. Nous attribuons surtout ce temps de réponse aux courants de Foucault, parce que la culasse de l'aimant n'est pas laminée, mais il peut y avoir encore d'autres causes[31]).

Nous utiliserons dans la suite une description phénoménologique au moyen d'une fonction de transfert (F.T.), méthode courante pour l'analyse des systèmes asservis. A cet effet, l'amplificateur et la bobine de correction seront pris comme une unité fonctionnelle, appelée l'organe de réaction. Nous traçons les diagrammes de Bode de la F.T. mesurée (fig. 20). L'amplitude de l'excitation est suffisamment petite, pour que la non-linéarité due à l'hystéresis du fer soit négligeable.

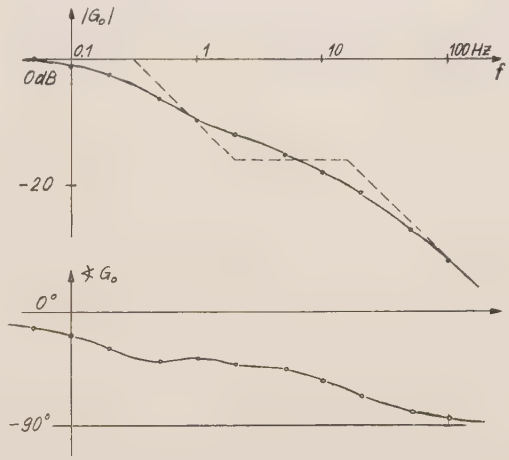

Fig. 20. Fonction de transfert de l'organe de réaction.
–•–• Courbe mesurée. ––– Approximation asymptotique.

En cherchant l'approximation asymptotique pour la réponse en amplitude, nous obtenons facilement et avec une précision suffisante la représentation mathématique de la F.T. Ce

[29]) M. Sauzade, CR Acad. Sci. Paris, **248** (1959) 205.
[30]) J. C. Gille, P. Decaulne, et M. Pellegrin, Théorie et calcul des asservissements (Dunod, éd., Paris, 1958).
[31]) R. M. Bozorth, Ferromagnetism (Van Nostrand, éd., New York, 1951).

procédé[32]) vient de ce que la FT d'un système de transmission est de la forme générale:

$$\frac{\text{sortie}}{\text{entrée}} = F = KG = K\,\frac{1 + a_1 p + \cdots + a_m p^m}{1 + b_1 p + \cdots + b_n p^n}.$$

Le facteur K est appelé gain du système et caractérise son régime statique ($p = 0$). Le facteur G est la réponse en fréquence et caractérise son comportement dynamique. Dans les cas les plus simples, les polynomes en p n'ont pas de zéros complexes, ce qui permet d'écrire:

$$G(p) = \frac{\prod_{\mu=1}^{m} (1 + T_{a\mu} p)}{\prod_{\nu=1}^{n} (1 + T_{b\nu} p)}$$

avec les constantes de temps $T_{a\mu}$ et $T_{b\nu}$ réelles.

Si celles-ci sont suffisamment différentes, on peut faire une approximation par des droites asymptotiques pour la courbe d'amplitude tracée en coordonnées de Bode. La courbe d'amplitude approchée est donc composée de segments de droites, dont la pente est un multiple entier de 6 dB/octave; celle-ci ne peut changer que pour les fréquences de cassure définies par les constantes de temps:

$$2\pi f_{a\mu} = \frac{1}{T_{a\mu}}, \qquad 2\pi f_{b\nu} = \frac{1}{T_{b\nu}}.$$

La courbe de phase ne contient aucune information nouvelle sur la FT, à condition que nous soyons sûrs d'avoir un système à déphasage minimal, ce qui est bien le cas pour notre organe de réaction.

En employant cette méthode, nous trouvons sa fonction de transfert:

$$\frac{B_r}{u_r} = F_r = \alpha K_r \frac{1 + T_{a1} p}{(1 + T_{b_1} p)\,(1 + T_{b_2} p)}$$

avec

$$K_r = 2.1 \times 10^{-4}\,\frac{\text{Ts}}{\text{V}} \qquad T_{a_1} = 0.08 \text{ sec}.$$

$$T_{b_1} = 0.5 \text{ sec} \qquad T_{b_2} = 0.01 \text{ sec}.$$

α est un facteur caractérisant l'amplification; $\alpha = 1$ pour un fonctionnement normal.

[32]) H. M. James, N. B. Nichols et R. S. Phillips, Theory of servomecanisms (Mc Graw Hill, éd., New York, 1947).

4.3. L'ANALYSE DU SYSTEME REGULATEUR

L'analyse du système est basée sur le bloc-diagramme de la fig. 21. Nous utilisons exclusivement les FT obtenues et discutées dans les chapitres précédents. Toutes les grandeurs représentent des petites variations, et en particulier la fréquence de réference est constante et nulle.

La FT du maser est

– pour le champ magnétique:

$$F_{mb} = \frac{Q_n}{Q_n + Q}\,\frac{\gamma'}{2\pi} = 0.875\,\frac{\gamma'}{2\pi}$$

– pour la fréquence de résonance du circuit oscillant:

$$F_{mf} = \frac{Q}{Q_n + Q} = \frac{1}{8}.$$

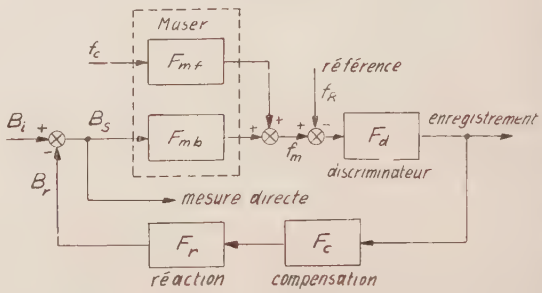

Fig. 21. Schéma de principe du système régulateur.

La FT du discriminateur est:

$$F_d = \left(53\,\frac{\text{mV}}{\text{Hz}}\right)\frac{1}{1 + p\ 2.26\,\text{ms} + (p\ 1.6\,\text{ms})^2}.$$

La FT de l'organe de réaction est:

$$F_r = \alpha\left(2.1 \times 10^{-4}\,\frac{\text{Ts}}{\text{V}}\right)\frac{1 + p\ 80\ \text{ms}}{(1 + p\ 0.5\,\text{s})\,(1 + p\ 10\,\text{ms})}.$$

La FT du réseau correcteur F_c sera donnée par la suite, quand nous discuterons de son influence.

La grandeur intéressante est représentée par le champ B_s dans l'entrefer. Sa variation, due à la présence des perturbations – les plus importantes sont une fluctuation ou une dérive du champ non regulé B_i et de la fréquence du circuit oscillant du maser f_c – est donnée par la formule:

$$B_s = \frac{1}{1 + F_0} B_i + \frac{F_{mf}}{F_{mb}}\,\frac{F_0}{1 + F_0} f_c$$

avec la FT en boucle ouverte

$$F_0 = F_{mb} F_d F_c F_r = K_0 G_0\,(p).$$

Nous examinons d'abord le système régulateur pour un $f_c = 0$.

Les performances d'une régulation sont caractérisées par:

– le facteur de régulation ρ en régime statique: $\rho = 1 + K_0 \cong K_0$.

– le facteur de régulation $\rho(\omega)$ en régime periodique. Il donne l'erreur due à une perturbation sinusoidale,

$$\rho(\omega) = | 1 + K_0 G_0 (j\omega) | \cong K_0 | G_0 (j\omega) |$$

– la fréquence de coupure, qui donne la bande de fréquence pour laquelle la régulation est efficace. Elle est définie par:

$$| 1 + K_0 G_0 (j\omega_\rho) | = 1$$

– la réponse transitoire à une perturbation en échelon-unité.

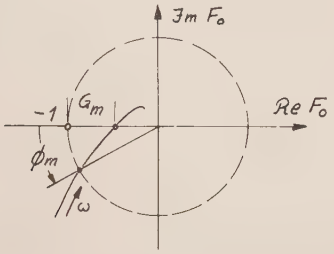

Fig. 22. Marge de phase et marge de gain dans le diagramme de Nyquist.

En pratique, nous regardons une régulation comme suffisante, lorsque toutes les perturbations possibles en fonctionnement normal sont réduites à un taux négligeable.

La régulation est d'autant plus efficace, que le gain en boucle ouverte K_0 est plus grand. Il existe, cependant, pour le gain une limite, puisque la stabilité du système en boucle fermée doit toujours être assurée. Il existe plusieurs conditions rigoureuses de stabilité, basées sur la FT en boucle ouverte. Nous allons employer au contraire une condition de stabilité approchée qui assure, dans un cas simple comme le nôtre, la stabilité et de bonnes performances du système[30,32]). Elle s'exprime sous les formes (fig. 22):

$\phi_m \geqslant 30°$; ϕ_m étant la marge de phase

$G_m \geqslant 10\text{dB}$; G_m étant la marge de gain .

Les performances du système de régulation peuvent être nettement améliorées par utilisation de réseaux de compensation.

4.3.1. *Le système sans compensation*

Les performances du système régulateur sans compensation seraient complètement insuffisantes. Sa FT en boucle ouverte est tracée sur la fig. 23. Si nous tolérons une marge de phase

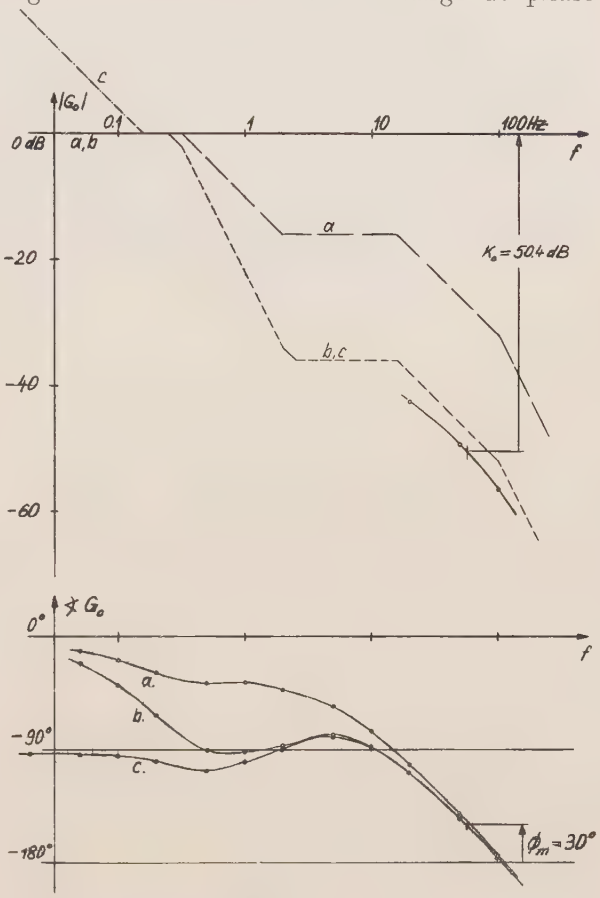

Fig. 23. Fonctions de transfert en boucle ouverte du système régulateur: a. Sans compensation; b. Avec réseau de compensation passif; c. Avec amplificateur operationnel.
–•–•– Courbes mesurées.
– – – – Approximation asymptotique.

$\phi_m = 30°$, le gain K_0 correspondant devient alors ~ 31.2dB. Le facteur d'amplification α n'est donc que de ~ 0.1. Si nous augmentons le gain au delà de cette limite, le système a tendance à osciller sur la fréquence de pompage $f_p \cong 100$ Hz, donnée par la relation

$$\measuredangle\, G_0(jf_p) = 180° .$$

Cette fréquence reste d'ailleurs inchangée dans le cas d'une compensation, puisque nous n'employons pas de réseau correcteur à contrôle dérivé. Etant donné que la fréquence de coupure

et la fréquence de pompage sont très voisines, une augmentation de celle-ci élargit la bande passante et en même temps le bruit de fond.

4.3.2. *Le système avec compensation par un réseau passif intégral*

L'utilisation d'un réseau passif à contrôle intégral permet d'augmenter le gain en boucle ouverte et donc le facteur de régulation. L'examen de la courbe de transfert de la fig. 23 nous montre qu'il serait souhaitable de pouvoir disposer d'un réseau ayant la FT

$$F_c = \frac{1 + T_c p}{1 + A T_c p}$$

avec

$$T_c = 10\,\text{m sec}\,, \qquad A = 10\,.$$

Le réseau correcteur est intercalé entre le discriminateur, dont la résistance interne R_g est de 600 kΩ, et le cathode follower, dont la résistance d'entrée est infinie.

Comme ce réseau assure également le filtrage de la porteuse (chapitre 3.5), nous nous proposons de réaliser un filtre en RC avec la FT:

$$F_c = \frac{1 + T_c p}{(1 + A T_c p)\,(1 + T_f p)}\,.$$

La constante de temps T_f est suffisamment petite pour qu'elle ne perturbe pas la régulation; ainsi nous avons choisi un $T_f = 0.16$ msec. Nous employons un procédé approché[28]) pour la synthèse d'un réseau qui produit la FT désirée. Les valeurs des éléments du filtre seront déterminées à partir des conditions suivantes (fig. 24):

$$\begin{aligned} &T_c = R_3 C_3 \\ &A T_c = (R_g + R_1 + R_2 + R_3) C_3 \\ &T_f = \frac{(R_g + R_1)\,(R_2 + R_3)}{R_g + R_1 + R_2 + R_3}\, C_1 \end{aligned} \qquad \begin{cases} R_1 = R_2 = R_3 = \\ \qquad = 100\,\text{k}\Omega \\ C_1 = 1\,\text{nF} \\ C_3 = 0.1\,\mu\text{F}\,. \end{cases}$$

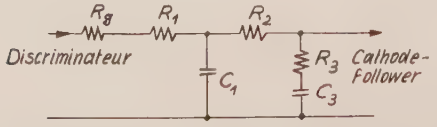

Fig. 24. Réseau de compensation passif.

Les FT du système compensé sont représentées sur la fig. 23. Nous en déduisons un gain maximum K_0 de 50.4 dB pour une marge de phase de 30°. Le calcul direct de

$$K_0 = K_{mb} K_d K_c K_r\,,$$

pour le fonctionnement normal avec $\alpha = 1$, donne 52.4 dB, ce qui correspond assez bien avec la valeur précédente.

Nous avons donné à l'excitation magnétique une variation brutale qui provoquerait sans régulation une perturbation statique de $B_i = 5 \times 10^{-4}$ Ts et nous avons enregistré la réponse de la fréquence du maser f_m à partir de laquelle nous avons pu calculer l'erreur statique $B_s = 11 \times 10^{-7}$ Ts. Nous avons donc un facteur de régulation de:

$$\rho = 455 \cong 53.2\ \text{dB}\,.$$

Pour nous résumer, nous dirons que nous avons amélioré la stabilisation d'un facteur 10 par le réseau correcteur.

L'enregistrement fig. 25 de la fréquence f_m et donc du champ magnétique montre qu'il subsiste une dérive de celle-ci par rapport à la fréquence de référence de l'ordre de 20 Hz par demi heure. Elle est surtout due à la dérive du courant d'excitation.

4.3.3. *Le système avec compensation par amplificateur opérationnel*

L'erreur statique disparaît complètement si la FT a un pôle pour $p = 0$, c'est-à-dire quand il y a un intégrateur dans la boucle de réaction. Mais son retard de phase augmente la tendance d'instabilité. Nous éviterons cet inconvénient en prenant un élément ayant la FT

$$F_c = \frac{1 + T_1 p}{T_1 p} \qquad \text{avec } T_1 = 1\,\text{sec}\,.$$

Une FT de cette forme peut être réalisée[33]) par un amplificateur à courant continu, dont l'amplification est très grande ($A_1 > 100000$), et qui est monté comme l'indique la fig. 26:
Sa FT est:

$$F = \frac{A_1(1 + pRC)}{(1 - A_1)pRC + (1 + pRC)} \cong -\frac{1 + pRC}{pRC}$$

avec $\qquad R = 1\,\text{M}\Omega \qquad C = 1\,\mu\text{F}\,.$

[33]) G. A. Korn et T. M. Korn, Electronic analog computers (McGraw Hill, éd., New York, 1956).

Les FT du système compensé sont représentées sur la fig. 23. Nous voyons que la forme de la FT de ce dernier au voisinage de la fréquence de coupure reste inchangée, ce qui nous permet de travailler avec la même amplification qu'auparavant ($\alpha = 1$). L'intégration est imparfaite pour les basses fréquences et par conséquent le facteur de régulation est fini et de l'ordre de 150 dB.

Fig. 25. Stabilité du champ magnétique pour une régulation proportionnelle.

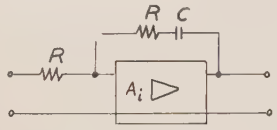

Fig. 26. Amplificateur opérationnel.

L'enregistrement de la fig. 27 montre que la fréquence du maser est pratiquement asservie à la fréquence de référence. La seule différence appréciable que l'on voit sur l'enregistrement est due à une perturbation importante, que nous avons provoquée pour étudier la réponse transitoire.

Nous calculons la réponse transitoire d'après une méthode approchée[34]). On peut négliger les pôles de la FT, dont la partie réelle est six fois plus grande que celle du pôle le plus proche de l'axe imaginaire. En appliquant cette règle nous obtenons la FT en boucle fermée:

$$B_s(p) = \frac{1}{1 + K_0 \dfrac{1 + T_i p}{T_i p}} B_i(p) \cong \frac{1}{K_0} \frac{T_i p}{1 + T_i p} B_i(p) .$$

Nous voyons clairement, que nous avons réalisé une régulation proportionnelle-intégrale. La réponse transitoire à un échelon-unité du champ est donc:

$$\frac{B_s(t)}{B_i(\infty)} = \frac{1}{K_0} e^{-t/T_i} .$$

Remarque:

Ce calcul est valable parce que le temps de réponse du champ magnétique est toujours suffisamment grand (Chap. 4.2) et par conséquent son spectre ne contient pratiquement pas de fréquences plus élevées que 1 Hz.

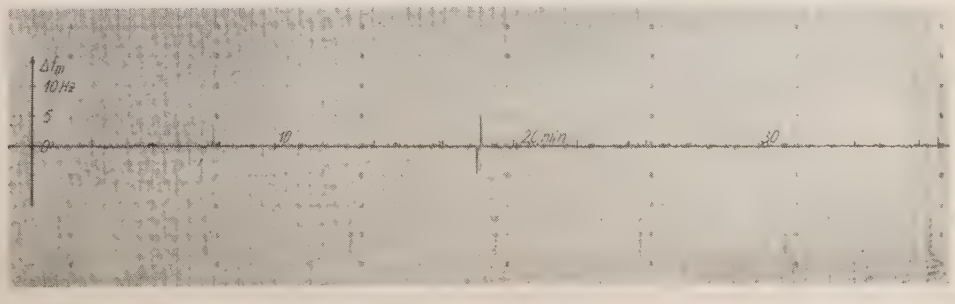

Fig. 27. Stabilité du champ magnétique pour une régulation proportionnelle-intégrale.

4.4. LES LIMITES DU SYSTEME STABILISATEUR

Les expériences nous ont prouvé qu'il est possible d'asservir parfaitement la fréquence du maser à la fréquence de référence stabilisée par

[34]) J. G. Truxal, Automatic feedback control system synthesis (McGraw Hill, éd., New York, 1955).

un quartz. Pour évaluer la stabilité du champ magnétique lui-même, il faut pourtant tenir compte des répercussions de l'entraînement, ce qui s'exprime par la formule:

$$f_m = 0 = F_{mb} B_s + F_{mf} f_c$$

ou

$$\frac{\gamma'}{2\pi} B_s = -\frac{Q}{Q_n} f_c .$$

Nous avons indiqué dans le chapitre 2.5.4 que l'on doit compter sur un f_c de $\pm$ 120 Hz, ce qui donne une stabilité relative du champ à long terme égale à $\pm$ 5.8 $\times$ 10^{-7}.

Cela équivaut à une stabilité absolue à long terme de $\pm$ 10 $\times$ 10^{-7}.

Nous avons effectué une mesure directe du champ par intégration d'une tension induite et avons trouvé une fluctuation à court terme de $\pm$ 3 $\times$ 10^{-7}.

Nous signalons ici une méthode simple pour la mesure de l'entraînement dans des conditions qui correspondent au fonctionnement normal du maser. Il suffit de mesurer la variation du champ pour une variation connue de la fréquence de résonance du circuit oscillant, la fréquence du maser f_m restant constante. Nous avons trouvé le facteur: $Q/Q_n = \frac{1}{7}$.

NUCLEAR INSTRUMENTS AND METHODS 9 (1960) 341–346; NORTH-HOLLAND PUBLISHING CO.

THE OPTICAL PROPERTIES OF SLOW CHOPPER AND TIME-OF-FLIGHT DEVICE

E. MALISZEWSKI

Polish Academy of Sciences, Institute of Nuclear Research, Warszawa

Received 20 July 1960

The transmission and resolution of a slow chopper and time-of-flight device has been determined experimentally and compared with theoretical curves. The shape of the neutron pulse was also measured.

1. Introduction

A slow chopper is an instrument designed for chopping neutron beams into short pulses in a range of energies below 0.3 eV. Employing the slow chopper device placed in the beam of neutrons and the time-of-flight technique one can measure a required spectral distribution of neutrons in experiments.

The neutron detector is placed several meters from the chopper, and the distribution of the times-of-flight of the scattered neutrons from the chopper to detector is measured.

The first use of the neutron selector in the beam of neutrons from nuclear reactor was by Fermi and Marshall[1]) and subsequently there have been many developments of their device.

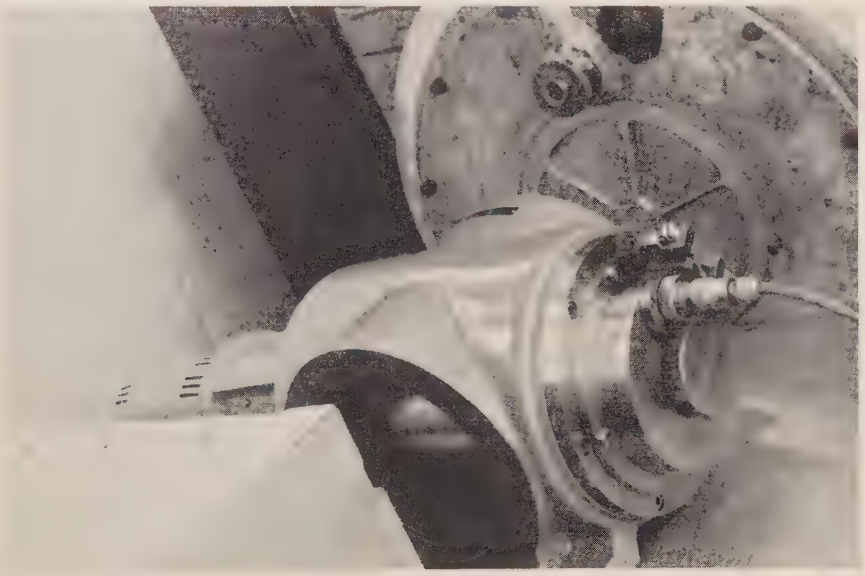

Fig. 1. Chopper photograph.

The aim of this paper is to discuss the behavior of the slow chopper device in operation at the Warsaw reactor, EWA. Fig. 1 represents a photograph of this chopper and beryllium filter. An experimental study has been done as a check on its performance. The experiments are evidently of great importance for further accurate work, and are worth discussing in some detail.

[1]) E. Fermi and J. Marshall, Phys. Rev. **72** (1947) 193.

2. Description of the Chopper Time-of-flight Apparatus

The principal features of the apparatus as were used in the determination of the beryllium filtered neutron spectrum are shown in fig. 2. A beam of neutrons emerging from the thermal column of EWA reactor is incident on the beryllium filter mounted in front of the experimental horizontal hole. A beryllium filter consists of a beryllium block 16 × 16 × 28 cm³ formed from cubes 4 × 4 × 4 cm³ of this metal surrounded by a cooling vessel and all enclosed in a vacuum container. This filter is intended to produce a beam of cold neutrons since wavelengths of neutrons passed through a filter of this sort are too long for Bragg reflexion ($\lambda_{\text{cut-off}} = 3.95$ Å).

In many of the experiments on the inelastic scattering by substances carried out up to the present time the whole spectrum of filtered neutrons has been used. The design of the slow chopper is illustrated in fig. 3. The outer diameter of the rotor is 12.5 cm. This chopper has 1.5 mm wide curved slits between 0.4 mm cadmium-plated steel plates, the effective radius of curvature of the slits $R_0 = 100$ cm. The rotor is driven through elastic coupling by a 250 W motor and can be spun up to speed 12 000 r.p.m. An electromagnetic pick-up sends a synchronising pulse to the 100-channel time analyzer. The time analyzer has a delay time ranging between 20 and 17 920 μsec and channel widths of 5, 10, 20, 40, 80 μsec are available.

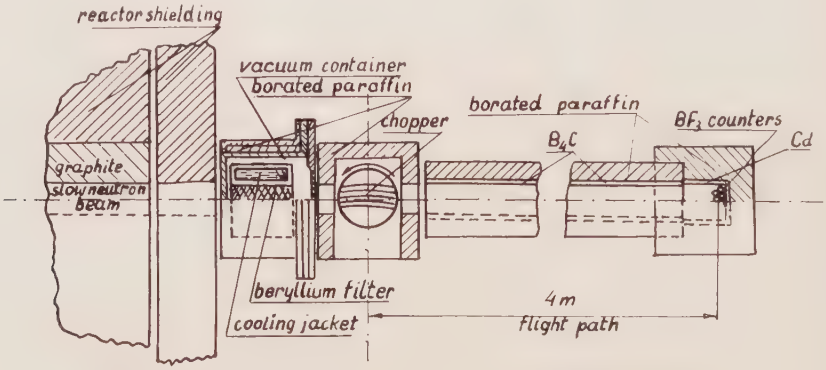

Fig. 2. Schematic drawing of chopper time-of-flight apparatus.

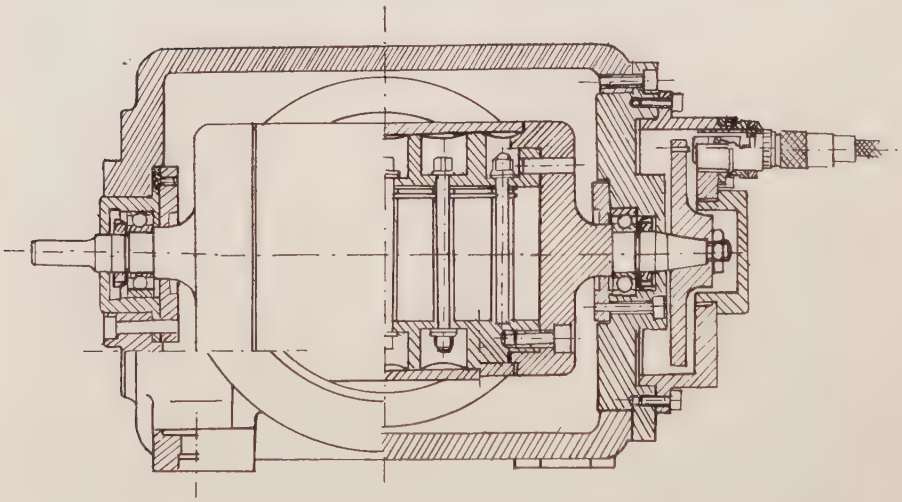

Fig. 3. Vertical section of the chopper.

The neutron detector consists of 10 BF_3 counters arranged in two layers of a 6 cm thickness.

It is important that the pulse from the pick-up starts the analyzer just when the neutrons are passing the centre of the chopper from which flight paths should be measured. A rough calibration has been made by use of the BF_3 counter as near the rotor as possible and the neutron pulse from the white neutron beam has been observed on a screen of the synchroscope with a time base triggered by the pulse from the pick-up. From a location of the neutron pulse in the synchroscope screen it might be possible to determine a time shift of the neutron pulse in comparison with the pick-up pulse. The pick-up angular positions was set by a screw adjustment. Exact calibration was afforded afterwards by the location of the Bragg cut-off in beryllium (3.95 Å) using the time analyzer. It became evident that the preliminary adjustment was almost correct.

3. Chopper Transmission and Resolution

A parallel neutron beam impinges upon a cylindrical chopper of radius r, made of neutron absorbing material and with the axis perpendicular to the neutron motion direction. The cylinder contains curved slits of width $2d$ with a radius of curvature R_0 (fig. 2). The chopper rotates around its own axis with angular velocity ω. Thus, the slits transmit neutrons during short time intervals, and in this way neutron bursts arise. The detail analysis[2–5]) of a passage of the parallel neutron beam through the rotating slit provides the following expressions for the chopper transmission curve as a function of neutron wavelength:

$$T(R) \cong \begin{cases} \dfrac{d}{r} - \dfrac{1}{6}\dfrac{r^3}{dR^2}\,; & \infty \geqslant R \geqslant \dfrac{r^2}{d} \\ \dfrac{8}{3}\sqrt{\dfrac{d}{R}} - \dfrac{2r}{R} + \dfrac{1}{6}\dfrac{r^3}{dR^2}\,; & \dfrac{r^2}{d} \geqslant R \geqslant \dfrac{r^2}{4d}. \end{cases} \quad (1)$$

[2]) K. Larsson, U. Dahlborg *et al.*, Arkiv f. Fysik **16** (1959) 199.

[3]) M. Marseguerra and G. Pauli, Nucl. Instr. **4** (1959) 140.

[4]) K. Larsson and K. Otnes, Arkiv f. Fysik **15** (1959) 49.

[5]) D. O'Connor, Unpublished work.

R is the radius of curvature of a neutron trajectory in a system connected to the chopper and is given by

$$R = \frac{h}{2m\omega\,|\,\lambda - \lambda_0\,|}$$

or

$$R = \frac{1}{2\omega\left|\dfrac{1}{v} - \dfrac{1}{v_0}\right|}\,;$$

v_0 is the neutron velocity the path of which is a straight line in this system. Maximum transmission given by d/r occurs for $v = v_0$ and v_0 is related with a radius of curvature of the chopper by $v = v_0 = 2\omega R_0$.

In the case of the upward position of the slits that means when the chopper has turned 180°, eqs. (1) are still valid, being now

$$R = \frac{1}{2\omega\left|\dfrac{1}{v} - \dfrac{1}{v_0}\right|}$$

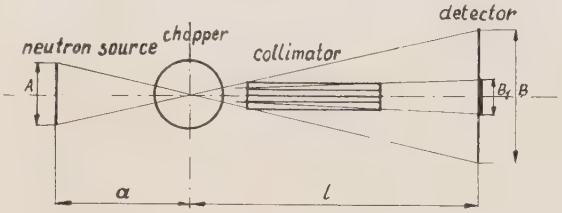

Fig. 4. Geometry of time-of-flight apparatus with and without collimator.

which corresponds to the neutrons paths turned in opposite directions.

The resolution function of the chopper time-of-flight device consists of terms which are the effects of an influence of the chopper geometry, collimation, detector thickness and channel width of the time analyzer. Fig. 4 illustrates the principle of the chopper geometry. The total resolution of the chopper apparatus for neutrons of velocity v, flight path l and time-of-flight t as given in the references[2,4]) may be written:

$$\frac{\delta t}{t} = \frac{v}{\omega l}\sqrt{\frac{f^2d^2}{r^2} + (\delta t_1)^2\omega^2} \quad \text{if} \quad \frac{2d}{r} \geqslant \frac{A}{a} \geqslant \frac{d}{r} \quad (2a)$$

and

$$\frac{2d}{r} \geqslant \frac{B}{l} \geqslant \frac{d}{r}$$

with the f value ranging between 2 and $(3 - \sqrt{3})$

$$\frac{\delta t}{t} = \frac{c}{\omega l}\sqrt{\frac{B^2}{l^2} + (\delta t_1)^2\omega^2} \quad \text{if} \quad \frac{A}{a} > \frac{B}{l} \geqslant \frac{2d}{r} \qquad (2b)$$

or

$$\frac{\delta t}{t} = \frac{c}{\omega l}\sqrt{\frac{A^2}{a^2} + (\delta t_1)^2\omega^2} \quad \text{if} \quad \frac{B}{l} > \frac{A}{a} \geqslant \frac{2d}{r} \qquad (2c)$$

where

$$\delta t_1 = \sqrt{\left(\frac{c}{v}\right)^2 + (\delta t_c)^2}\,;$$

c is an effective thickness of the detector and
δt_c is the electronic channel width.
A is the height of the neutron emitting surface,
a is its distance from the chopper,
B is the height of the detector area.

The geometry of the arrangement for measuring beryllium filtered spectrum was such, that

$$\frac{A}{a} = \frac{12}{400},$$

$$\frac{B}{l} = \frac{28}{422} \sim 0.066 \text{ (without collimator)},$$

$$\frac{B_1}{l} = \frac{7}{422} \sim 0.017 \text{ (with collimator)},$$

$$\frac{2d}{r} = 0.031.$$

4. Experimental Methods and Results

The experimental determination of the chopper transmission curve $T(\omega\lambda)$ was accomplished on the universal double crystal spectrometer[6]).

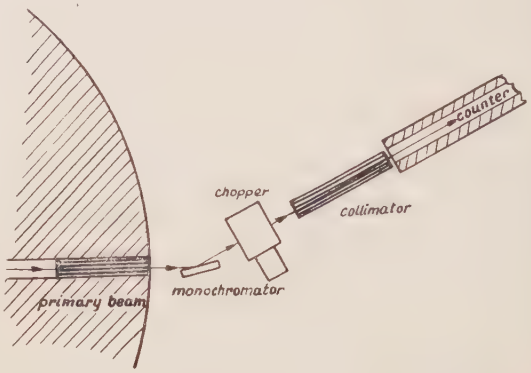

Fig. 5. Arrangement for measuring chopper transmission.

The chopper was placed on the arm of the neutron spectrometer beyond a monochromator to receive the monoenergetic neutron beam. On the protraction of the spectrometer arm at a distance 3 m from the chopper BF_3 counters were located. This arrangement is shown in fig. 5. Measure.

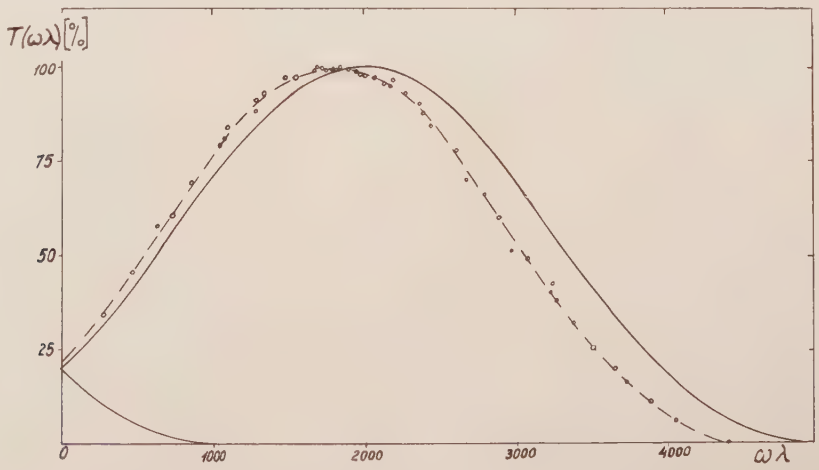

Fig. 6. Experimental and theoretical transmission curves. —— Calculated curve for $R_0 = 100$ cm and $d = 0.075$ cm. – – – Calculated curve for $R_0 = 110$ cm and $d = 0.070$ cm.

The calculations of resolution width (eq. (2a)) were done at $f = 2$ and $f = 1.3$.

The results are shown in fig. 10.

The best agreement with experimental points was obtained with effective detector thickness 6 cm for the upper curve, and 5.2 cm for the lower one.

ments were made with Cu and Fe_3O_4 single crystals as monochromators. The (111) reflecting plane of Cu was set for 1 and 1.7 Å and Fe_3O_4 for 2.5 and 3.5 Å. The intensity of reflected beam was recorded by the 100 channel time analyser

[6]) D. O'Connor and J. Šosnowski, Report No. 98/i(B), Institute of Nuclear Research, Warsaw (1959).

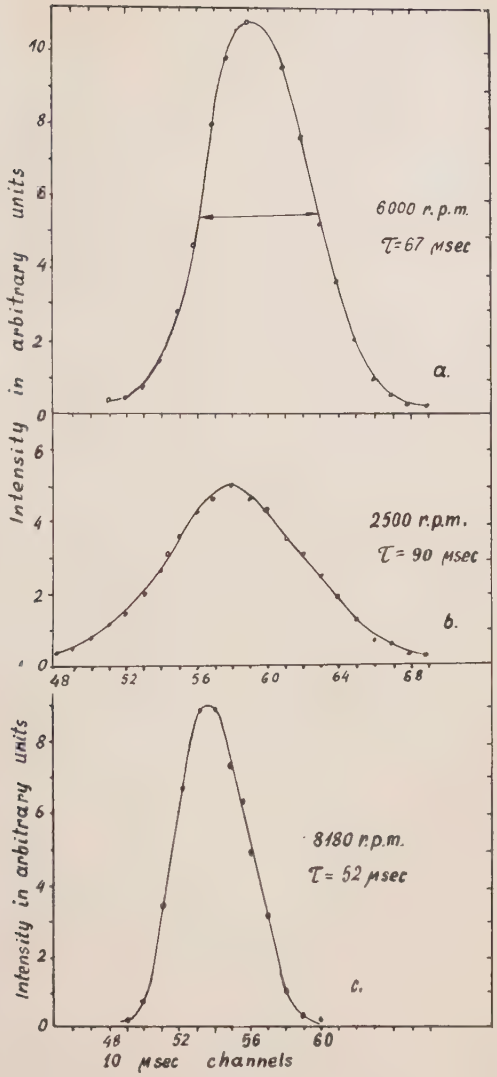

Fig. 7. Bragg reflexions after transmission through the chopper at different speeds.
Curves a and b are for Fe_3O_4(111) at $\lambda_B = 2.5$ Å;
Curve c is for Cu (111) at $\lambda_B = 1.0$ Å.

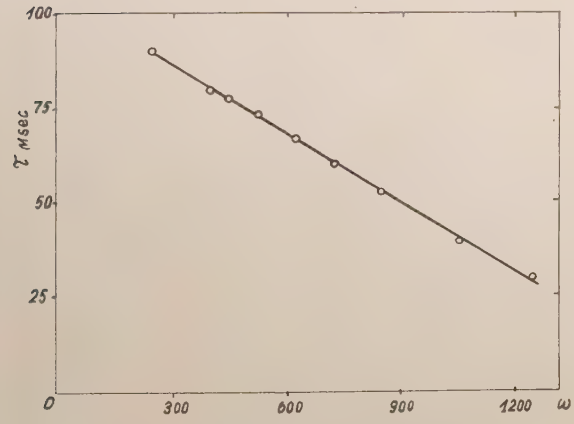

Fig. 8. Half-width τ as a function of ω.

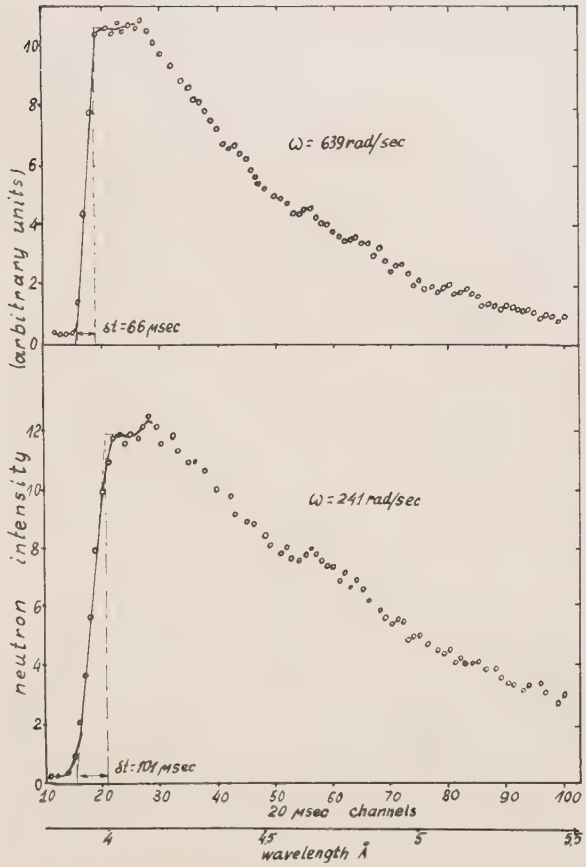

Fig. 9. Spectrum of beryllium filtered neutrons.

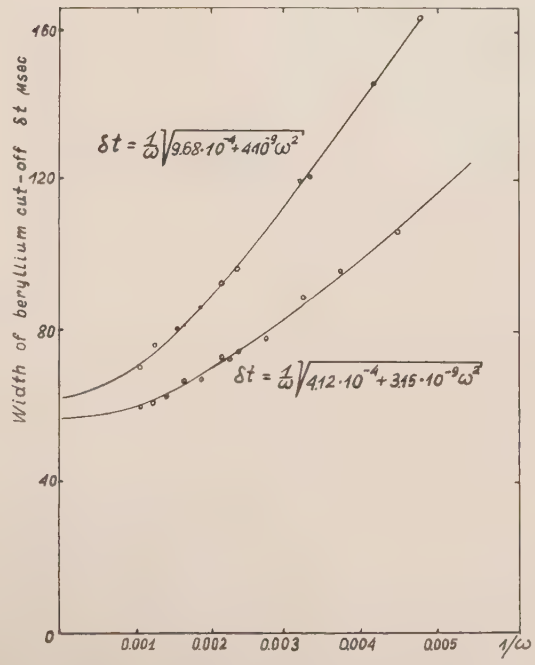

Fig. 10. Measured and calculated width of beryllium cut-off.
The upper curve is taken without collimator.

at various speeds of chopper rotation (2000–12 000 r.p.m.). Transmitted intensities for these wavelengths were used to determine the transmission curve. For each of this wavelengths the transmitted intensity was plotted versus $\omega\lambda$ yielding $T(\omega\lambda)$ shape after normalization of every curve to its maximum value. The experimental results together with the calculated $T(\omega\lambda)$ shapes, are given in fig. 6. The solid curve was calculated from (1) for the construction chopper parameters, namely $2d = 0.15$ cm, $r = 4.5$ cm and $R_0 = 100$ cm. But the dashed curve calculated for $2d = 0.14$ cm and $R_0 = 110$ cm fits the experimental data exactly. This may result immediately from the mechanical performance of chopper or form a straightening of the chopper slits at the high speeds of the rotation. The lower solid curve is the calculated transmission at the 180° position.

The same measurements of the monochromatic transmitted beam were also used to study a half-width τ of the Bragg reflexion as a function of the angular velocity ω. Some Bragg reflexions after transmission through the chopper are done in fig. 7. In fig. 8 the dependence τ upon ω can be seen.

The resolution width of the instrument was measured from the sharpness of the beryllium break[4,2] in the transmission. Beryllium has a very well defined maximum total cross section at the wavelength 3.95 Å $= 2d$ and the beryllium filtered reactor spectrum is suitable for determination of the half-width of the resolution function. The position of the beryllium break was also used as a check on the calculation of neutron velocity and thus for adjusting the electromagnetic pick-up position. The transmission of the 28 cm long block of beryllium metal for two speed of chopper rotation is given in fig. 9. The experimental and theoretical resolution widths with and without a collimator are shown in fig. 10. The collimator was of nominal half-angle 20 minutes. The flight path from the chopper centre to detector was 422 cm, channel width 20 μsec and delay time 3840 μsec. It is evident from the figure that the experimental points well agree with the calculated curves and eqs. (2) are a reasonable measure of the instrument resolution.

Acknowledgements

The author wishes to thank Mgr. K. Blinowski for his advice and interest in this work, and S. Szafran for his technical assistance in the measurements.

NUCLEAR INSTRUMENTS AND METHODS 9 (1960) 347–353; NORTH-HOLLAND PUBLISHING CO.

ON THE DESIGN OF QUADRUPOLE FOCUSING SYSTEMS

W. WEIDEMANN

Nuclear Physics Division, National Physical Research Laboratory of the South African Council for Scientific and Industrial Research, Pretoria†

Received 15 June 1960

The theory necessary for the design of a quadrupole focusing system is set out, followed by a practical design example and the conclusions that can be drawn from the results.

1. Introduction

Much has already been written on the strong-focusing of particle beams by Alternating Gradient Channels††. To the author's knowledge, however, there still does not exist a guide as to the actual design-procedure to be followed to ensure a satisfactory result. This article aspires to fill this gap, and should facilitate the quick design and testing of any quadrupole channel, either magnetic or electrostatic. Although only the non-relativistic case is discussed for a magnetic system, the method can easily be adapted for relativistic use, and electrostatic systems. However, aberrations of the systems are not discussed, as they are of secondary importance if the A.G. channel is used primarily for focusing-purposes.

2. The Theory of Quadrupoles

Note: The Giorgi System of m.k.s. units is employed throughout.

2.1. BASIC EQUATION OF MOTION

From Newton's Second Law, as applied to a particle of mass m, charge e, and moving with velocity $\boldsymbol{v}$ through a magnetic field of flux-density $\boldsymbol{B}$

$$e(\boldsymbol{v} \times \boldsymbol{B}) = m \frac{\mathrm{d}\boldsymbol{v}}{\mathrm{d}t}$$

which becomes

$$\frac{\mathrm{d}^2x}{\mathrm{d}t^2} + \frac{e}{m}\frac{\mathrm{d}z}{\mathrm{d}t}\left(\frac{\partial B_y}{\partial x}\right)x - 0$$

for motion in the x–z plane, for the coordinates as shown in fig. 1, where the field is two-dimensional, and assuming that term $(\partial By/\partial x)$ is a constant (see under 2.4.).

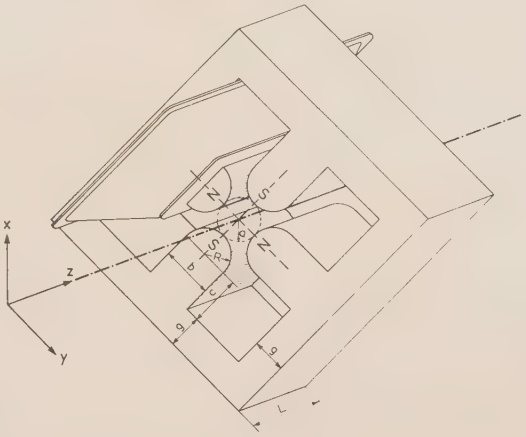

Fig. 1. A magnetic quadrupole with the symbols used.

But

$$\frac{\mathrm{d}x}{\mathrm{d}z} = \frac{\mathrm{d}x}{\mathrm{d}t}\frac{\mathrm{d}t}{\mathrm{d}z} = \frac{\mathrm{d}x}{\mathrm{d}t}\frac{1}{v}$$

and $\mathrm{d}z/\mathrm{d}t \equiv \boldsymbol{v}$ is constant for small angles between the beam and the z-axis.

$$\therefore \frac{\mathrm{d}^2x}{\mathrm{d}z^2} + \beta^2 x = 0 \qquad (1)$$

where

$$\beta^2 \equiv \frac{e}{mv}\left(\frac{\partial B_y}{\partial x}\right).$$

† From August, 1960, with the South African Atomic Energy Board, Pretoria.

†† To avoid duplication, the reader is referred to the near-complete list of pertinent literature in P. Grivet et A. Septier, Les lentilles Quadrupolaires Magnétiques. CERN 58–25 (1958); Nucl. Instr. and Meth. 6 (1960) 126, 243.

The solutions of eq. (1) are

$$\beta^2 > 0 \; ; \quad x = A \cos \beta z + B \sin \beta z \tag{2a}$$

and

$$\beta^2 < 0 \; ; \quad x = C \cosh \beta z + E \sinh \beta z \tag{2b}$$

where A, B, C, E are constants.

2.2. DETERMINATION OF CONSTANTS AND LENS EFFECT

Consider fig. 2, drawn for convergence in the x–z plane, and divergence in the y–z plane.

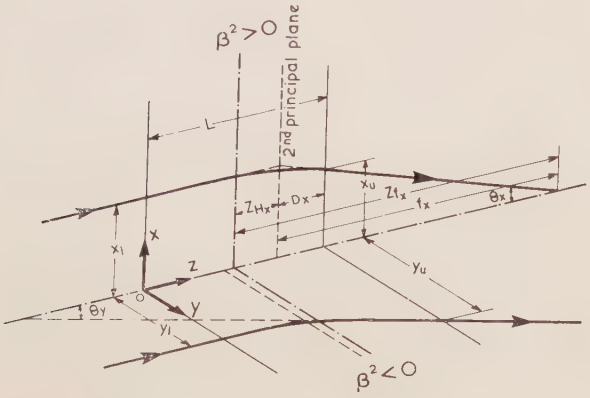

Fig. 2. Particle trajectory through a single quadrupole.

$$\left(\frac{dx}{dz}\right)_{z=0} = 0 = \beta B \qquad \text{from (2a)}$$

$$\therefore B = 0 .$$

Also

$$(x)_{z=0} \equiv x_i = A \; ,$$

$$\frac{x_i}{f_x} = \tan\theta = \left(\frac{dx}{dz}\right)_{z=L} = -\beta x_i \sin \beta L \qquad \text{from (2a)}$$

$$\therefore \frac{1}{f_x} = -\beta \sin \beta L \; . \tag{3a}$$

Again

$$(x)_{z=L} \equiv x_u = x_i \cos \beta L \qquad \text{from (2a)}$$

and

$$\frac{x_i - x_u}{D_x} - \left(\frac{dx}{dz}\right)_{z=L} = -\beta x_i \sin \beta L - \frac{x_i - x_i \cos \beta L}{D_x} .$$

$$\therefore \frac{1}{D_x} = \frac{-\beta \sin \beta L}{1 - \cos \beta L} \; . \tag{4a}$$

Note that eqs. (3a) and (4a) are not x-dependent, and thus describe the function of a monoplanar lens. It should be noted that distances with the beam are taken negative, while distances against the beam are positive, as is customary in Geometrical Optics.

It follows that

$$Z_{H_x} = -\frac{L}{2} + \frac{1 - \cos \beta L}{\beta \sin \beta L} \tag{5a}$$

and

$$Z_{f_x} = -\frac{L}{2} - \frac{\cos \beta L}{\beta \sin \beta L} \; . \tag{6a}$$

For $\beta^2 < 0$, i.e. the divergent case, the corresponding formulae are

$$\frac{1}{f_y} = \beta \sinh \beta L \tag{3b}$$

$$\frac{1}{D_y} = -\frac{\beta \sinh \beta L}{1 - \cosh \beta L} \tag{4b}$$

$$Z_{H_y} = \frac{L}{2} - \frac{1 - \cosh \beta L}{\beta \sinh \beta L} \tag{5b}$$

$$Z_{f_y} = \frac{L}{2} + \frac{\cosh \beta L}{\beta \sinh \beta L} \tag{6b}$$

2.3. COMBINATION OF LENSES

As is shown above a quadrupole field acts on moving charged particles like an astigmatic and mono-chromatic, or mono-energetic, thick lens. It is astigmatic because a focusing effect, in one plane is of necessity (div $\mathbf{B} = 0$) always accompanied by a corresponding defocusing effect in the corresponding perpendicular plane. The lens is mono-energetic in that β^2 varies with particle energy. However, for a given particle energy, and each plane, the effect of combining two quadrupoles can be calculated with the optical lens formula, and using eqs. (3) to (6), from

$$\frac{1}{F} = \frac{1}{f_1} + \frac{1}{f_2} - \frac{d}{f_1 f_2}$$

where all the distances are measured from the principal planes.

With the lengths of the two quadrupoles equal, and measuring from their centres, the focal lengths of the two planes are

$$O_2F_x = \frac{L}{2} + \left(\frac{\cosh \beta_2 L \cos \beta_1 L - \sinh \beta_2 L \sin \beta_1 L - \beta_1 (d - L) \sin \beta_1 L \cosh \beta_2 L}{\beta_2 \beta_1 (d - L) \sin \beta_1 L \sinh \beta_2 L - \beta_2 \cos \beta_1 L \sinh \beta_2 L + \beta_1 \sin \beta_1 L \cosh \beta_2 L} \right) \tag{7a}$$

where d is the separation of the two lenses (see fig. 3).

For O_2F_y the same formula applies, but with β_1 and β_2 exchanged.

If the second lens is rotated through $\frac{1}{2}\pi$ relative to the first, and if $\beta_1^2 = -\beta_2^2 \equiv \beta^2$, and $L_1 = L_2 \equiv L$, then the net focal length, measured from principal planes, is given by

$$\frac{1}{F_x} = -\beta\,[\,\sin\beta L\cosh\beta L - \sinh\beta L\cos\beta L + d\beta\sin\beta L\sinh\beta L\,]\,.$$

When this is developed in a power series

$$\frac{1}{F_x} \sim -\beta^4 L^2\,[\tfrac{2}{3}L + d] \sim \frac{1}{F_y}\,. \qquad (8)$$

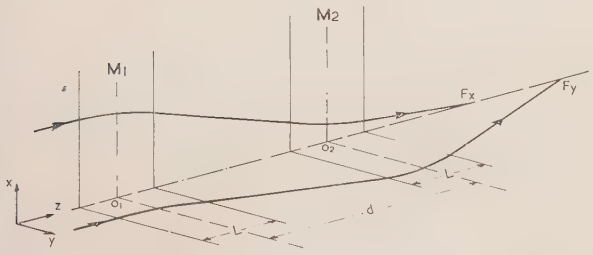

Fig. 3.
Particle trajectory through a combination of quadrupoles

This equation thus describes this combination of two quadrupoles as the equivalent of a single anastigmatic optical lens. By first analyzing a focusing problem as if it were an optical one, expressions can be obtained for the requirements of the various lenses, which can then be transformed for the quadrupoles by means of the above equation.

2.4. SHAPE OF POLES

As can be shown† the focusing requirement $\partial B_x/\partial y =$ constant (and because rot $\boldsymbol{B} = 0$, and the field is two-dimensional, it follows that $\partial B_x/\partial y = \partial B_y/\partial x$), is fulfilled by a magnetic field with a flux function of the form

$$x^2 - y^2 = \pm r^2\,. \qquad (9)$$

A flux function (9) is generated by the orthogonal magnetic scalar potential of form

$$2yx = \pm r^2\,. \qquad (10)$$

† W. C. Elmore and M. W. Garrett, Rev. Scient. Instr. **25** (1954) 480.

If poles of "infinite" permeability are presumed, they can produce this scalar potential if described by

$$2yx = \pm a^2\,.$$

Unless the poles are "infinite" hyperbolas, higher order harmonics will be introduced in the field, giving rise to aberrations. Since this condition at any rate will not be fulfilled by a practical design, and machining of hyperbolic shapes is difficult, the same magnitude of distortion can be introduced by giving the poles a circular shape, approximating the required hyperbola. The best compromise seems to be a poletip of radius R given by

$$1.125a < R < 1.15a$$

where $2a$ is the lens aperture.

2.5. CALCULATION OF THE MAGNETIC CIRCUIT

Since the air-gap is extremely large in proportion to the steel path length, it suffices to presuppose a ferromagnetic material of "infinite" permeability, and to introduce an empirical correction for leakage flux, etc., later on.

Per pole

$$\int H\cdot \mathrm{d}l = NI\,, \qquad \text{and} \qquad \boldsymbol{B} = \mu_0\boldsymbol{H}$$

$$\therefore\ \mu_0 NI = \int_0^a B_m \mathrm{d}m\,.$$

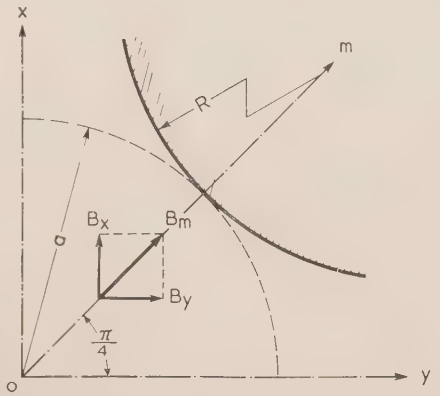

Fig. 4. Integration path of the magnetic field.

From fig. 4

$$\boldsymbol{B}_m = \boldsymbol{B}_y + \boldsymbol{B}_x$$

i.e. $$|B_m| = \frac{1}{\sqrt{2}}\left(\frac{\partial B_y}{\partial x}\right)x + \frac{1}{\sqrt{2}}\left(\frac{\partial B_x}{\partial y}\right)y$$

and for a point P of coordinates (X, Y) or $(\frac{1}{4}\pi, M)$

$$|X| = \frac{|M|}{\sqrt{2}} = |Y|.$$

Also

$$\frac{\partial B_y}{\partial x} = \frac{\partial B_x}{\partial y}$$

$$\therefore \mu_0 NI = \left(\frac{\partial B_y}{\partial x}\right) \int_0^a m \, dm = \frac{a^2}{2} \left(\frac{\partial B_y}{\partial x}\right)$$

$$\therefore \frac{\partial B_y}{\partial x} = \frac{2\mu_0 NI}{a^2}. \tag{11}$$

From definition

$$\beta^2 = \frac{e}{mc} \frac{\partial B_y}{\partial x}. \tag{12}$$

For an accelerator of potential U, equation of potential and kinetic energy gives

$$eU = \tfrac{1}{2} mv^2$$

$$\therefore v = \sqrt{\frac{2eU}{m}}. \tag{13}$$

From eqs. (11), (12), (13)

$$NI = -\frac{\beta^2 a^2}{\mu_0} \sqrt{\frac{mU}{2e}}. \tag{14}$$

3. Design Procedure

The following design sequence is suggested:

a. Decide on the aperture $2a$ of the system, i.e. the diameter of the vacuum-chamber to be used.

b. Establish a feasible optical solution of the focusing problem in the analogue, e.g. decide whether one single focusing lens is sufficient, for shorter distances, or whether it is advantageous to use two lenses, one to parallel the beam and the other then to focus it at the required point. Calculate the required focal lengths.

c. Assume a length L and a separation d (usually about $2L$) of the magnets, and with these and the focal length in eq. (8) get the required β^2.

d. Calculate the required number of ampere-turns with eq. (14).

e. Make the pole-tip a semicircle of $R = 1.15a$, on pole-pieces of width b and height $c \sim 2R$, supported on a yoke of width $g \sim 1.3R$. (Theoretically $g = 1R$ should suffice, but some rigidity is lost.)

f. Design the details of the coils.

NOTE.

(i) The optical analogue does not consider possible differences in degree of diversion of the beam in the two component planes. However, once a rough idea is formed of the requirements, more accurate calculations can be made with eqs. (7). In practice this is usually not necessary, unless severe differences of diversion are encountered.

(ii) From section 2.5 it follows that

$$B = \beta^2 \frac{mv}{e} a.$$

For linear operation, and with the usual low-impurity magnetic steels. this figure should not exceed about 0.5 Weber/m^2. This criterion immediately gives a check on the assumed L and d.

(iii) Because the field fall-off at the ends of the magnets is not a step-function, the effective magnetic length of the quadrupole is about 1.1 L. The leakage-flux between the poles, however, is also of this order, so that the effects tend to cancel. It is even suggested to add an additional 20% to the calculated number of ampere-turns, to compensate for the finite permeability of the magnet steel.

(iv) The empirical ratios of the dimensions as given above serve only as guides to the final design. It is a matter of convenience whether the yoke should be in the form of a square or a ring, although more accurate assembly is possible with a square yoke. In any case, all critical dimensions should be held within $\pm$ 0.001″.

To counteract the saturation occuring primarily at the base-corners of the pole-pieces, these should be tapered. This again tends to complicate the construction. Hence also the low suggested value of B.

(v) The ratios of dimensions suggested provide enough space even for air-cooled coils, if these have a trapezium-shaped cross-section. The usual current-density and temperature-rise limits for air-cooled transformers then apply.

4. Tests with the Quadrupoles

Usually the exact source-position is unknown, as for instance in a cyclotron. This parameter, as well as other characteristics of a quadrupole, and the behaviour of the whole system, can be determined by a number of tests.

4.1. SINGLE QUADRUPOLE

(i) Place the magnet at a distance v from the source, and obtain a line-focus on a quartz-plate at a distance u on the other side of the magnet. Let $u + v = w$.

We have $1/f = \beta \sin \beta L \sim \beta^2 L$ for small βL. Also

$$\frac{1}{u} + \frac{1}{v} = \frac{1}{f}.$$

Keep v constant, vary u, and adjust the current I, thus also β^2, each time for line-focus. If plotted as in fig. 5, we have the following:

$$OB = \frac{1}{v}.$$

$1/f$ as a function of I can be read from the graph, if line BC is taken as the base line.

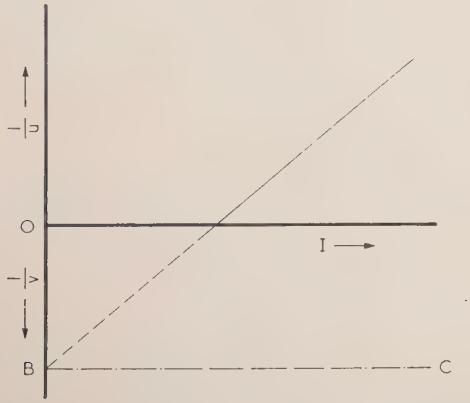

Fig. 5. Plot of inverse of image-distance versus current for line-focus.

(ii) Because

$$\frac{1}{u} + \frac{1}{w - u} = \frac{1}{f}$$

$$\therefore \frac{\partial f}{\partial u} = \frac{w - 2u}{w}, \quad \text{and} \quad \frac{\partial^2 f}{\partial u^2} = -\frac{2}{w}$$

i.e. f has a maximum value if the magnet is halfway between the source and the point of focus. Thus if w is kept constant while the magnet position is varied, the source distance is equal to the image distance at the minimum value of a I_{foc} versus u plot. This method has the advantage that it is unnecessary to vary the length of the vacuum-chamber.

4.2. TWO QUADRUPOLES

The condition of double-focus is dependent on:

(i) Object distance v,

(ii) The separation of the magnets d,

(iii) Image distance u,

(iv) The current I_1 through the first magnet,

(v) The current I_2 through the second magnet,

and

(vi) Particle momentum and charge.

With all these variables, the simplest experimental procedure to produce a double focus for a given geometry, is as follows:

Parameters v, d, and u are kept constant. While I_1 is kept constant, I_2 is varied and the image on the quartz plate observed. With increasing I_2 the image passes successively through a vertical and then a horizontal line focus, or vice versa, depending of course on the polarity of the magnets and of the charged particles of the beam. This is repeated for different values I_1, and a plot similar to fig. 6 is drawn. The intersection of the two lines at X is then the double-focusing point.

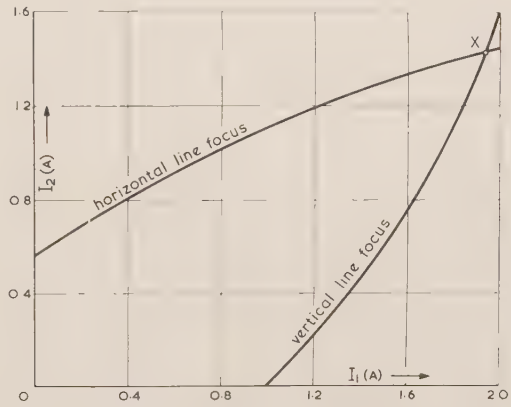

Fig. 6. Adjustment for double-focus.

4.3. TESTS WITH A WIRE-SIMULATED BEAM

A beam of momentum p can be simulated by a current, carrying "infinitely" flexible wire, under constant tension. We have

$$\frac{mv^2}{r} = e(\mathbf{v} \times \mathbf{B})$$

$$\therefore\ mv \equiv p = erB$$

or

$$\frac{\text{Weber}}{\text{meter}} = rB = \frac{mv}{e}\,\frac{v}{v} = \frac{\text{kilogram. sec. meter}^2}{\text{ampere. sec. meter. sec.}^2} = \frac{\text{Newton}}{\text{ampere}}\ .$$

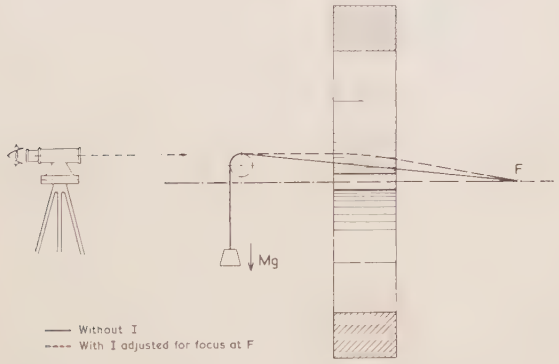

Fig. 7. Test with a wire-simulated beam.

Thus, for instance, a 16 MeV deuteron beam can be simulated by a wire, tensioned over a pulley by a 5 g weight and carrying 60 mA. For example, with a set-up as shown in fig. 7, f as a function of I can be measured. This method is practical where testing with the actual beam is inconvenient or impossible.

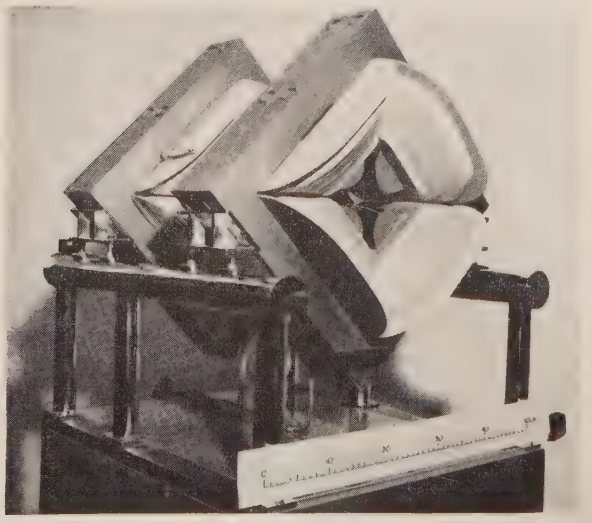

Fig. 8. The completed quadrupole system.

5. Example of a Quadrupole System

5.1. DESCRIPTION

The system as shown in fig. 8 is used to focus the external 16 MeV deuteron beam of the Pretoria Cyclotron†. The magnets, situated closely together and as near as possible to the exit-chamber to achieve maximum acceptance, focus the beam at the end of a 3000 mm long stainless steel pipe, where it will be used in experimental nuclear physics.

The details of the magnets are

Dimensions

$2a = 65$, $R = 37.5$, $b = 75$, $c = 75$, $g = 50$ and $L = 100$ mm. All critical tolerances are ± 0.02 mm.

Steel

C < 0.1%, Si < 0.27%, Mn < 0.37%, other impurities negligible.

Coils

These are air-cooled of trapezium-shaped cross-section.

2900 turns of 1.17 mm² (S.W.G. No. 18) Formex wire are wound on a 3 mm brass former, that is clad with 0.2 mm Leatheroid. The windings are coated with Glyptal Electrical Finish, and held in position by tape strips also impregnated with Glyptal.

Power supply

A main Variac feeds A.C. current stabilizers of $\pm 0.5\%$, which in turn feed two separate Variacs. The A.C. is then rectified by selenium bridge-rectifiers, one for each channel, and the D.C. outputs feed the respective magnets, with their four coils connected in series. A metering shunt for each magnet supplies the A.C. current stabilizers with the necessary signal. As the consumption under operating conditions is of the order of 600 W, this type of flexible power supply is a very cheap and reliable solution. The stabilization is sufficient for maintaining an adequate quality of focus, and adjustment of the system is straightforward.

† See also J. J. Burgerjon and W. Weidemann, The Cyclotron of the National Physical Research Laboratory, Pretoria, Second Report May, 1960 (Issued as C.S.I.R. Spec. Tech. Rep. E2); published in Nucl. Instr. and Meth. 8 (1960) 261.

5.2. PERFORMANCE

The horizontally divergent deflected beam of the cyclotron is converged while passing through the first quadrupole and vertically focused in the second quadrupole. 25% of the beam is lost between the two magnets, as a result of the vertical diversion of the beam that accompanies its horizontal focusing in the first magnet. The transmission of the system is thus 75%. The beam, which otherwise would have had the dimensions of 24 cm by 6 cm, is focused to a spot of 6 mm by 4 mm on the target. This image is caused by an object that is by no means a point source, and it is very free from aberration. Agreement between the calculated and the measured characteristics of the quadrupoles is within 5%.

Further information on the focused beam is given in the above-mentioned report on the Pretoria cyclotron.

6. Conclusion

A simple design-procedure has been set out, and its merits are demonstrated by the performance of a system that was designed in accordance with it. Although it is of little academic interest for other problems that can be solved by the use of quadrupoles, it yet should aid the designer who is faced with the problem of focusing high-energy beams.

Acknowledgements

The author wishes to thank the following: Dr. W. E. Frahn for his interest in the project; Mr. R. Lier for the accurate fabrication of the magnets; the staff of the Nuclear Physics workshop for coil construction and magnet assembly, and for helpful suggestions, and Mr. J. J. Burgerjon and the cyclotron team for help with the installing and testing of the focusing system.

NUCLEAR INSTRUMENTS AND METHODS 9 (1960) 354–356; NORTH-HOLLAND PUBLISHING CO.

A RAPID CYCLING BUBBLE CHAMBER

L. BERTANZA, P. FRANZINI, I. MANNELLI and G. V. SILVESTRINI

Istituto di Fisica dell'Universita, Pisa

Istituto Nazionale di Fisica Nucleare, Sezione di Pisa

Received 15 August 1960

The design and operation of a 1.12 liter propane-ethane gas bubble chamber, operated at room temperature with a repetition rate of 4–5 expansions per second, are described. The chamber has worked in good stability condition for several periods of 20–40 hours each.

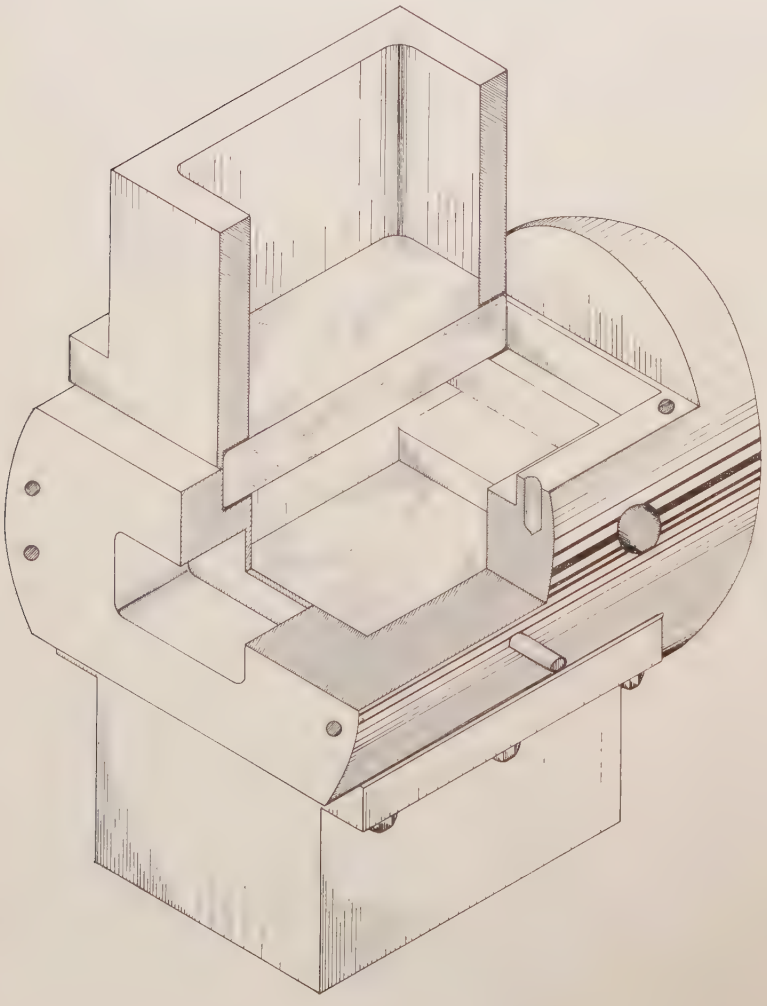

Fig. 1.

1. Introduction

A rapid cycling bubble chamber, filled with a mixture propane-ethane at 21 atm equilibrium pressure, has been used since September 1959 in an experiment in progress at the Frascati electron synchrotron. The aim of the experiment is a measurement of the polarization of the recoil proton from the reaction $\gamma + p = \pi^0 + p$, by measuring the asymmetry of magnetically selected protons in p–C scattering inside the bubble chamber.

In such an experiment, where the proton flux is less than 1 proton/pulse, a rapid cycling bubble chamber compares not unfavourably—in so far as counting rate is concerned—with the counter-techniques; in addition the bubble chamber gives generally more complete information about the reaction to be studied.

Our bubble chamber has worked up to now about 8×10^6 expansions at 4 (and sometimes 5) expansions per second, during a number of runs each consisting of 20–40 consecutive hours. (The limitation factor for the speed is at the

moment the air supply from the compressor.)

The long sensitive time (which can be regulated between 5 and 15 ms) makes this bubble chamber also convenient for cosmic rays experiments.

2. Chamber Body and Expansion System

The bubble chamber has a stainless steel body of $14 \times 10 \times 8$ cm^3 useful volume (figs. 1, 2). Two tempered glass windows 3 cm thick are clamped tight on teflon gaskets, by steel plates to the body by means of six 14 MA studs. Throughout the chamber body a number of holes allow the thermostating liquid to flow. Since the operation does not depend critically on the temperature ($\sim$ 16°C), we have used as thermostating liquid just tap-water. On one of the 10×8 cm^2 sides a 8×4 cm^2 3 mm thick window is worked; through this window the beam enters the bubble chamber.

On the opposite side the expansion system is placed, which is formed by:

1. a diaphragm made of a 0.2 mm thick mylar membrane and a 3 mm thick rubber membrane;
2. a perforated plate (holes 2 mm in diameter);
3. a 3 mm thick rubber membrane;

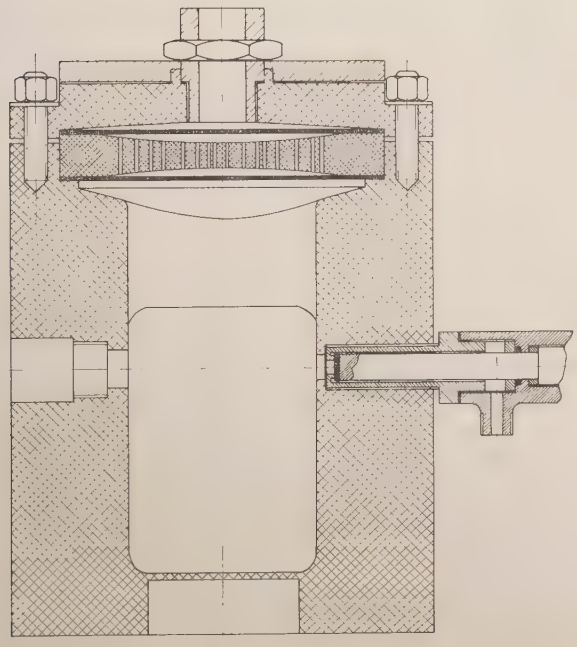

Fig. 2.

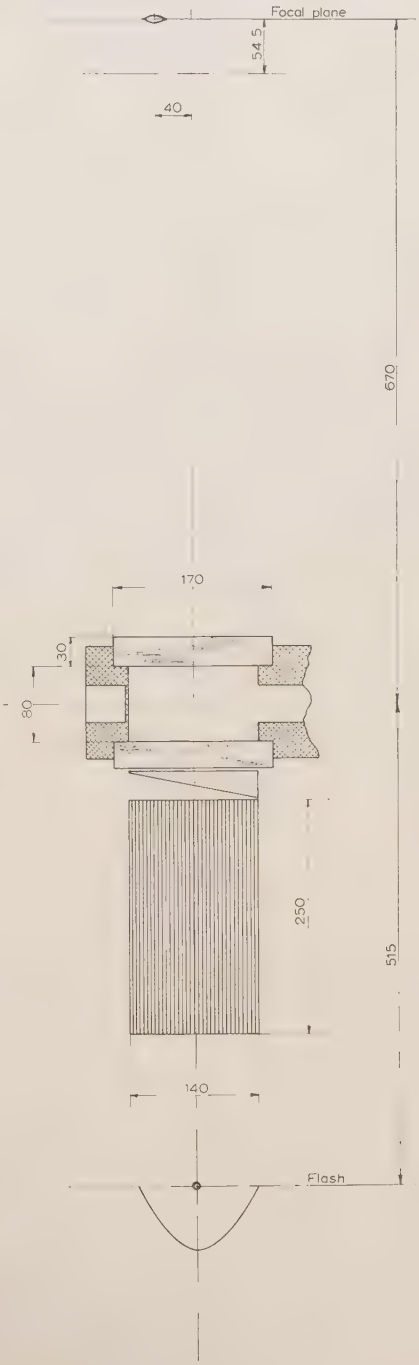

Fig. 3.

4. a stainless steel bottom connected, through a small perforated plate, to the expansion valve†.

The room between the two membranes is filled with water which, by means of a heat exchanger, is kept at tap-water temperature. The heat exchanger is necessary when the bubble chamber operates at a high rate of expansions per second for longer than 10 minutes.

An over pressure of 10 atm is used for rapid recompression of bubbles; the expansion is at atmospheric pressure. The length of the expansion is controlled by means of a capacitive pressure gauge.

The life of the membranes is of the order of 70 hours operating time ($\sim 10^6$ expansions).

3. Optics

We use a venetian blind and a perspex prism to get a dark field illumination (fig. 3). The flash (a Mullard LSD3 lamp) is triggered by the particle entering the bubble chamber, with a delay of about 2 ms. We don't see any distorsion on the tracks due to motions of the liquid. In fig. 4 a typical photo is shown. We use two-view stereophotos to get the reconstruction of the events in space. The advancing system is a Beatte Coleman commercial one, slightly modified; the maximum speed of these magazines is 3 photos/second. This is enough for our needs since we have, on the average, 1 proton every 5 seconds.

Conclusions

We have found our chamber very easy to operate. A variation of $\pm$ 1°C of the temperature does not alter considerably the sensitivity. The heat exchanger is needed not to let the temperature grow uncomfortably. In fact, without the exchanger it would increase many degrees in a few minutes. In any case it is very easy to adjust the conditions (equilibrium pressure and expansion ratio) to make our bubble chamber work at any temperature between 10 and 40 degrees.

† We use a Barksdale three ways solenoid valve.

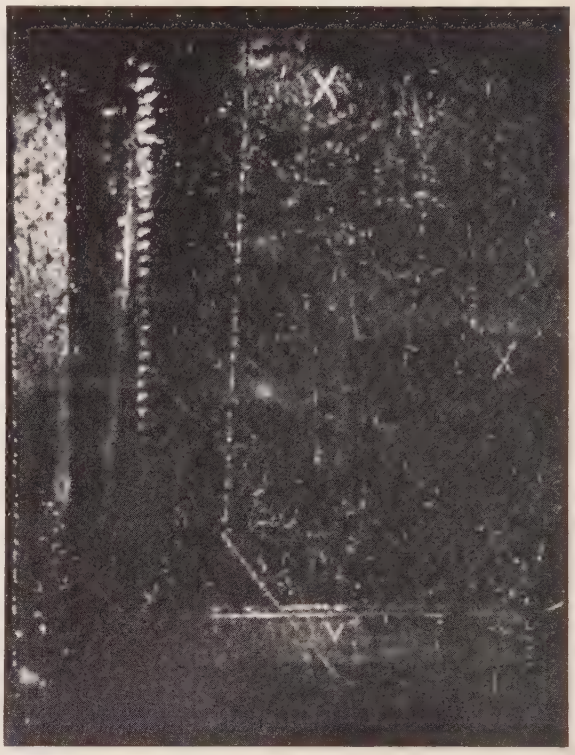

Fig. 4.

For the experiment mentioned in the introduction, we wanted to measure an asymmetry in the horizontal plane, and for this purpose we have made the chamber with horizontal windows. Although most of the bubbles are close to the upper glass when recompression begins, they disappear very rapidly. We have a slight boiling around the gaskets. But since this does not interfere with the bubble chamber operation, we did not take steps to avoid it. The operation is also insensitive to impurities in the propane or ethane.

All these advantages make a bubble chamber like ours an instrument very easy to handle, and we think it is a very convenient one to be used with rapid cycling accelerators.

Thanks are due to Prof. C. Franzinetti for helpful discussion and advice.

NUCLEAR INSTRUMENTS AND METHODS 9 (1960) 357–359; NORTH-HOLLAND PUBLISHING CO.

LETTERS TO THE EDITOR:

NOTE ON THE DETERMINATION OF TRITIUM BY MEANS OF LIQUID SCINTILLATORS AND DC-MEASUREMENTS OF PHOTOMULTIPLIER CURRENTS

TORBJÖRN WESTERMARK, BJÖRN GRAPENGIESSER, HANS LINDROTH and NADIM GHANEM†

Division of Physical Chemistry, The Royal Institute of Technology, Stockholm 70, Sweden

Received 10 September 1960

Scintillation pulse counting is today an efficient method for measuring soft beta ray emitters like tritium. This note will call attention to the possibility of simply measuring the increase in photomultiplier current when tritium used for measurements of the light emission produced upon dissolution of irradiated solids in certain liquids[1,2]). The photomultiplier current is simply read at a fixed voltage and is expected to be a linear function of the tritium concentration,

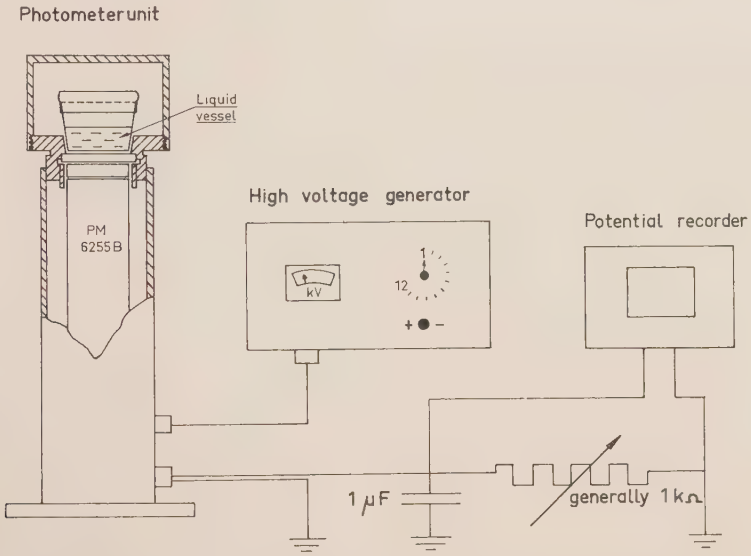

Fig. 1. Measurement of tritium samples by dissolving them in liquid scintillators in quartz glass cups placed on top of a photo-multiplier tube (in the present case EMI 6225 B—this quartz glass type is however not generally necessary) in a closed apparatus.

samples contained in conventional quartz glass cups are placed in front of the photo-cathode.

The method is of course not as sensitive as a pulse counting device but has proved very useful for sources of medium strength.

The apparatus is shown in fig. 1 and is actually the same, except for a few modifications, as that every other factor being kept constant. It is of course necessary to use a very stable voltage generator. We used a unit variable in

† On leave from The National Research Centre, El-Dokki, Cairo, U.A.R.

[1]) T. Westermark, Some points of View on Stored Energy in Irradiated Food, Risö Report No 16: Papers presented at the First Nordic Meeting on Food Preservation by Ionizing Radiations, held at Risö, April 25–26, 1960 (in print).

[2]) T. Westermark and B. Grapengiesser, Observations of the emission of light on dissolution of irradiated solids in certain liquids, Nature **188**, No. 4748 (1960) 395.

100 V steps from 700 volt to 1500 volt, the stability being better than 0.3‰ (constructed by Kuhlemans Ingenjörsbyrå, Stockholm).

We have studied both water samples and organic systems. For water samples, the pulse-counting system suggested by Kallman, Brown and Furst[3]) was found useful for the purpose. Fig. 2 (lower curve) shows the result of measuring photomultiplier output as a function of tritium concentration. The liquid volume was kept constant (5 ml) and was 90% in dioxane (the dioxane contained 1 g/l diphenyloxazole (PPO)), the rest being water. No further additives were employed. The upper curve of fig. 2 was obtained from the same samples as the lower one but with the addition of naphthalene (0.2 g in all cases). Here we got a 5.5 fold increase of sensitivity. From the upper curve and the measurement of the dark current, we infer that samples down to 3 μc of tritium water can be measured (this strength adds a current about equal to the dark current).

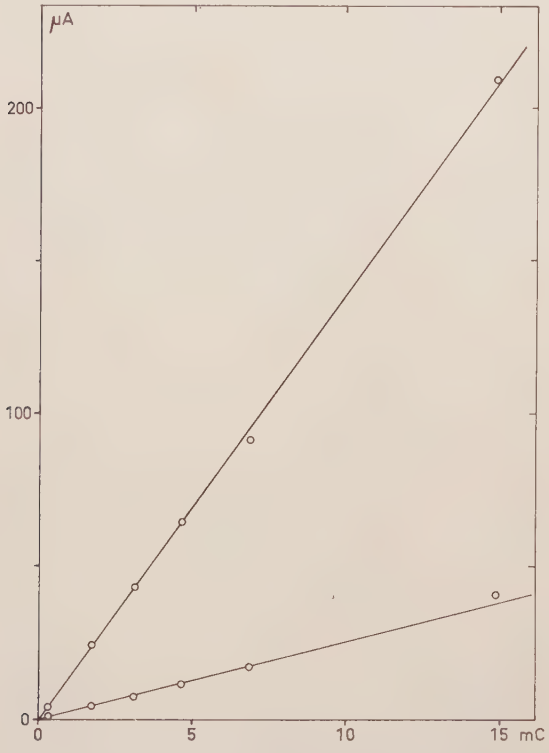

Fig. 2. Photomultiplier current (in μA, high voltage supplied 1 kV) as a function of tritium concentration using the apparatus described infig. 1. Lower curve: 0,5 ml tritium water dissolved in 4.5 ml p-dioxane with 1 g/l PPO, total volume 5 ml. Upper curve: Same as lower but with 0.2 g naphthalene added.

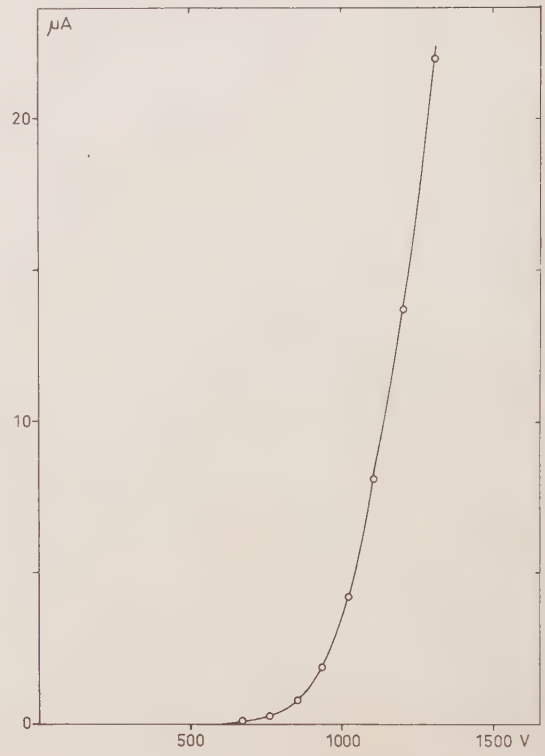

Fig. 3. Relative sensitivity of tritium determination (cf. fig. 2) at various high voltages applied to the photomultiplier tube.

An alteration in the measuring system will probably make it possible to measure weaker samples.

The accuracy obtainable is 2–5% depending on concentration. The best procedure is to standardize with a known T-concentration. The slope of the calibration line of course varies with the applied high voltage of the photomultiplier (PM). Fig. 3 shows this variation of the relative sensitivity with PM voltage. At every voltage step, straight lines were found. The particular tube used here was found to be linear up to 200 μA deflection.

[3]) H. Kallman, M. Furst and F. Brown, Nucleonics **14** (1956) 48.

[4]) T. Westermark, H. Lindroth and B. Enander, J. Appl. Rad. Isotopes **7** (1960) 331–34; N. Ghanem and T. Westermark, J. Am. Chem. Soc. **82** (1960) 4432; N. Ghanem and T. Westermark, Extensions in the techniques for the accelerated unspecific isotopic labelling of organic compounds, Paper RIC/224 read at the IAEA Conference on the Use of Radioisotopes in the Physical Sciences and Industry, Copenhagen 6–17 Sept. 1960.

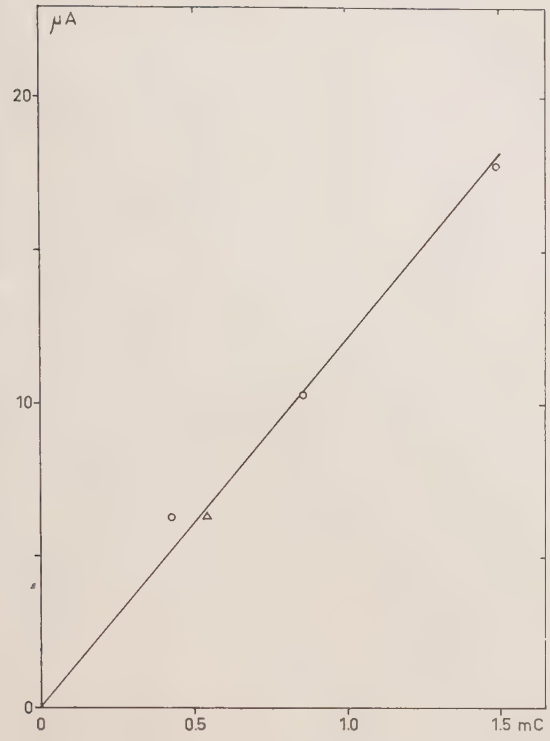

Fig. 4. Photomultiplier current as a function of tritium concentration using the apparatus described in fig. 1. Tritium-labelled polystyrene dissolved in 20 ml of Nuclear Enterprises' liquid scintillator NE 213.

Organic systems are of course more sensitive. We have found the Xylene-POPOP-system (NE 213 from Nuclear Enterprises, Canada) very practical because a lot of organic compounds can be dissolved in it. Tritium-labelled polystyrene from our micro-wave labelling project[4]) gave a response according to fig. 4. Also here 3 μc of tritium corresponds to the dark current. (Calibration of the T-polystyrene samples was kindly performed at the Isotope Techniques Laboratory, Stockholm by means of pulse-counting and comparisons with absolute standards.)

Any additive to the fluorescent solutions acting as sensitizer, wave-length shifter or quencher must, as in pulse-counting, be taken into account by means of calibration procedures. This precaution is easily taken in the arrangement described.

The system has been found to supplement the more tedious liquid scintillation pulse counting for samples strong enough to be assayed here ($\sim$ 3 μc for organic systems, $\sim$ 3 μc for water samples) provided the precision is satisfactory. An application to the determination of the tritium content in heavy water reactors operated for some time seems to be within the possibilities ($>$ 3 μc/ml)[6]. The method can obviously be extended to other radioactive substances. (When even stronger T-samples are available, say millicuries, simple bremsstrahlung measurements have proved very practical[5]).)

Tritium as water and gas was procured from The Radiochemical Centre, Amersham, England.

Mr. I. Ingefjäll is thanked for skilful laboratory assistance.

[5]) T. Westermark, L. Devell and N. Ghanem, Nucl. Instr. and Meth. **9** (1960) 141.

[6]) See e.g. I. Andersson, Ark. f. Fysik **13** (1958) 254.

NUCLEAR INSTRUMENTS AND METHODS 9 (1960) 360; NORTH-HOLLAND PUBLISHING CO.

ON THE POSSIBILITY OF A RADIATION CHEMICAL NUCLEAR TRACK CHAMBER

TORBJÖRN WESTERMARK

Division of Physical Chemistry, The Royal Institute of Technology, Stockholm 70, Sweden

Received 10 September 1960

For radiation chemistry to prove efficacious for furnishing nuclear tracks of some kind that could be used for visualizing and measurement purposes, it is necessary that the radiation chemical G value should be very high. The polymerization of organic monomers might be such a favourable case and *acrylonitrile* one of the few possible cases because the polymer formed is insoluble in its monomer. The G value is known to be very high[1]) ($\sim 10^7$). It is, however, dependent on the dose rate which might be some disadvantage for the purpose in mind.

It might be possible to see the polymer track directly in the liquid with a microscope because the density change should give a corresponding refractive index change and hence observability with phase contrast equipment. If the polymer and the monomer can be separated gently enough (evaporation, filtering), the tracks might be detected directly in the microscope. Of course it is only speculation to hope that the track will be coherent, i.e. actually picturing the nuclear track. The G value is, however, sufficiently large to support the hope that the polymer will grow together between the ionized and excited entities in the path of the nuclear particle. The growth perpendicular to the track might be sufficient for optical examination—if not, the less accessible electron-microscopical technique remains to be tested. The deciding point for this, and similar, systems seems to be the strong dose-rate dependence of the yield. The recombination of the polymerisation initiation entities (radical ions or free radicals) will reduce the dimensions of the track. It seems impossible to extrapolate the known dose-rate dependence of the G-factor to the region of the formation of a track. Hence experimental trials will have to give the answer to whether the system is successful or not.

The composition of the monomer is rather similar to that of tissue and this facilitates the radiobiological considerations. If the system can be realized, the points of merits would be the extreme simplicity of the chamber, the cheapness (despite the fact that some purification and removal of inhibitors and oxygen from the commercial chemical might be necessary) and its ability to integrate nuclear events over extended times.

If a repeated operation is wanted, the chamber would have to be replaced with a new one which should be possible because of the low price. Alpha particles would be one of the best particles for the first experiments. It might also be suggested that the polymer may get a fibrous structure which might yield textile applications.

This idea was presented at the session 4A (Design and use of strong sources) of the UNESCO Isotope Conference held in September 1957 in Paris but was, for some reason, not included in the Proceedings. The author is at present not in a position to perform any experiments of this kind—a matter which might justify this somewhat unusual way of making the suggestion.

[1]) I. A. Berstein, E. C. Farmer, W. G. Rotschild and F. F. Spalding, J. Chem. Phys. **21** (1953) 1303.

AUTHOR INDEX

Aitken, J. H., *see* Dixon

Ballini, R. et E. Pomelas, Mesures de temps dans le domaine de la nanoseconde: convertisseur de temps en amplitudes et circuits de coïncidences 29
Bell, R. E., *see* Weaver
Berlovich, E. J., *see* Bonitz
Bertanza, L., P. Franzini, I. Mannelli and G. V. Silvestrini, A rapid cycling bubble chamber . 351
Bertolini. G., F. Cappellani and A. Rota, Corrections for backscattering and energy resolution in beta spectroscopy by scintillation detectors . . 107
Bonitz, M. and E. J. Berlovich, Notes on a fast time analyzer for short lifetime measurements . . . 13
Bonner, T. W., *see* Bramblett
Bramblett, Richard L., Ronald I. Ewing and T. W. Bonner, A new type of neutron spectrometer 1

Caglioti, G., A. Paoletti and F. P. Ricci, On resolution and luminosity of a neutron diffraction spectrometer for single crystal analysis 195
Cappellani, F., *see* Bertolini
Cernigoi, C., I. Gabrielli and G. Iernetti, Behaviour of photomultipliers against short light-pulses 303

Devell, L., *see* Westermark
Dixon, W. R. and J. H. Aitken, Pulse shape discrimination and energy response of calcium tungstate crystals 229
Dmitrievsky, V. P., V. V. Kolga and B. I. Zamolodchikov, On the particle loss at a synchrocyclotron limit radius 115
Draper, J. E. and A. A. Fleischer, Apparatus and analysis for sum-coincidence (n,γ) spectrometer 67

Escarfail, J. P., *see* Preuss
Ewan, G. T., *see* Graham
Ewing, Ronald I., *see* Bramblett

Findley, R. W., R. A. Reiter and T. A. Romanowski, A precision clock for measuring time intervals 221
Fleischer, A. A., *see* Draper
Franzini, P., *see* Bertanza
Frisch, O. R. and A. J. Oxley, A semi-automatic analyser for bubble chamber photographs . . . 92

Gabrielli, I., *see* Cernigoi
Geiger, J. S., *see* Graham
Ghanem, Nadim, *see* Westermark
Glickstein, S. S. and R. G. Winter, Nuclear reactions from recoil protons in a reactor 226
Glover, Everett D., *see* Sippel
Graham, R. L., G. T. Ewan and J. S. Geiger, A one-meter-radius iron-free double-focusing $\pi\sqrt{2}$ spectrometer for β-ray spectroscopy with a precision of $1:10^5$ 245
Grapengiesser, Björn, *see* Westermark
Grivet, P. et H. Hahn, La stabilisation du champ magnétique par un maser à résonance magnétique nucléaire (I) 233
Grivet, P. et H. Hahn, La stabilisation du champ magnétique par un maser à résonance magnétique nucléaire (II) 328

Hahn, H., *see* Grivet
Heer, F. J. de, *see* Tjin A Djie
Hernandez, H. P., J. M. Peterson, B. H. Smith and C. J. Taylor, The Livermore variable-energy 90-inch cyclotron 287

Iernetti, G., *see* Cernigoi
Ikegami, H., *see* Sakai
Infante, C., Pulse height discriminator employing distributed amplification 102

Jänecke, J., *see* Jung
Jung, H., Ph. Panussi und J. Jänecke, Reversible Verstärkungsänderungen von Photomultipliern bei unterschiedlichen Zählraten 121

Kisdi-Koszó, É. and L. Turi, Phase- and vertical stability of microtrons 137
Koerts, L. A. Ch., *see* Tjin A Djie
Kolga, V. V., *see* Dmitrievsky

Lane, R. O., N. F. Morehouse, Jr., and D. L. Phillips, The correction of resonance peaks for experimental resolution 87
Lindroth, Hans, *see* Westermark
Lynn, J. E., Computational methods for analysis of resonance transmission data for S-wave neutrons 315

Maliszewski, E., The optical properties of slow chopper and time-of-flight device 341
Mannelli, I., *see* Bertanza
Morehouse, N. F., Jr., *see* Lane

Oers, W. T. H. van, A differential beam collector . 111
Orient, O. J., On the mechanism of multiple discharges in halogen-quenched G.M. counters . . 165
Orton, K. F. and K. Wilkins, Automatic live-time measurement and background subtraction for the Hutchinson-Scarrott pulse height analyzer . . . 97
Oxley, A. J., *see* Frisch

Pancholi, S. C., A new type of liquid anode gamma and beta halogen counter (Letter to the Editor) 118

Panussi, Ph., *see* Jung
Paoletti, A., *see* Caglioti
Paul, Helmut, Higher order chance coincidences in a fast-slow coincidence arrangement 131
Paulin, A., Optimale Länge des Beschleunigungsspaltes beim Mikrotron 113
Peterson, J. M., *see* Hernandez
Phillips, D. L., *see* Lane
Pomelas, E., *see* Ballini
Preuss, L. G. et J. P. Escarfail, De la décomposition des intensités spectrales en courbes de Gauss . . 212

Raboy, S. and C. C. Traul, A note on the background in NaI scintillation counters 145
Rautenbach, W. L., A high temperature sputtering ion source for a laboratory isotope separator . . 199
Reiter, R. A., *see* Findley
Ricci, F. P., *see* Caglioti
Roberts, Arthur, A new type of Čerenkov detector for the accurate measurement of particle velocity and direction 55
Romanowski, T. A., *see* Findley
Rota, A., *see* Bertolini

Sakai, M., H. Ikegami and T. Yamazaki, Sector-type double-focusing beta-ray spectrometer 154
Silvestrini, G. V., *see* Bertanza
Sippel, Robert F. and Everett D. Glover, Sedimentary rock analysis by charged particle bombardment 37
Smith, B. H., *see* Hernandez
Smith, W. I. B., Improved focussing near the cyclotron source 49

Taylor, C. J., *see* Hernandez
Thompson, L. C., A method for the measurement of gamma-ray spectra in omnidirectional gamma-ray fields 175
Tjin A Djie, H. R. E., F. J. de Heer and L. A. Ch. Koerts, Small scattering chamber for large angular region 172
Traul, C. C., *see* Raboy
Turi, L., *see* Kisdi-Koszó

Vincent, C. H., The rapid recognition of a significant increase in the rate of arrival of pulses occurring at random 181

Waaben, Sigurd, Synchrotron magnet power circuit with a distributed capacitor bank 78
Wåhlin, E., Automatic mass number determination for isotope separators and mass spectrometers . 21
Weaver, R. S. and R. E. Bell, Method of evaluating delayed coincidence experiments 149
Weidemann, W., On the design of quadrupole focusing systems 347
Westermark, T., L. Devell and N. A. Ghanem, On the use of bremsstrahlung for the determination of tritium in aqueous and organic systems . . . 141
Westermark, Torbjörn, On the possibility of a radiation chemical nuclear track chamber (Letter to the Editor) 360
Westermark, Torbjörn, Björn Grapengiesser, Hans Lindroth and Nadum Ghanem, Note on the determination of tritium by means of liquid scintillators and DC-measurements of photomultiplier currents (Letter to the Editor) . . . 357
Wilkins, K., *see* Orton
Winter, R. G., *see* Glickstein

Yamazaki, T., *see* Sakai

Zamolodchikov, B. I., *see* Dmitrievsky

BOOK REVIEWS

Francis, Gordon, Ionization phenomena in gases (Lars Högberg) 120
A series in the radiochemistry of the elements (W. C. Parker) 120
Sangren, Ward C., Digital computers and nuclear reactor calculations (Werner Schneider) . . . 242
Gruhle, Wolfgang, Elektronische Hilfsmittel des Physikers (E. Matthias) 243
Linhart, J. G., Plasma physics (Lars Högberg) . . 243

SUBJECT INDEX

Accelerators and Reactors

Improved focussing near the cyclotron source, W. I. B. Smith 49
Synchrotron magnet power circuit with a distributed capacitor bank, Sigurd Waaben 78
Optimale Länge des Beschleunigungsspaltes beim Mikrotron, A. Paulin 113
On the particle loss at a synchrocyclotron limit radius, V. P. Dmitrievsky, V. V. Kolga and B. I. Zamolodchikov 115
Phase- and vertical stability of microtrons, É. Kisdi-Koszó and L. Turi 137
A high temperature sputtering ion source for a laboratory isotope separator, W. L. Rautenbach 199
Nuclear reactions from recoil protons in a reactor, S. S. Glickstein and R. G. Winter 226
The Livermore variable-energy 90-inch cyclotron, H. P. Hernandez, J. M. Peterson, B. H. Smith and C. J. Taylor 287
On the design of quadrupole focusing systems, W. Weidemann 347

Detectors

A new type of Čerenkov detector for the accurate measurement of particle velocity and direction, Arthur Roberts 55
Corrections for backscattering and energy resolution in beta spectroscopy by scintillation detectors 107
A differential beam collector, W. T. H. van Oers 111
On the use of bremsstrahlung for the determination of tritium in aqueous and organic systems, T. Westermark, L. Devell and N. A. Ghanem 141
A note on the background in NaI scintillation counters, S. Raboy and C. C. Traul 145
On the mechanism of multiple discharges in halogen-quenched G. M. counters, O. J. Orient 165
The rapid recognition of a significant increase in the rate of arrival of pulses occurring at random, C. H. Vincent 181
Pulse shape discrimination and energy response of calcium tungstate crystals, W. R. Dixon and J. H. Aitken . . 229
A rapid cycling bubble chamber, L. Bertanza, P. Franzini, I. Mannelli and G. V. Silvestrini 354

Errata

A. F. Fischmann-Arbel and Israel Bar-David, A method of linear pulse amplifier design (Nuclear Instruments 7 (1960) p. 153) 244
G. Gianelli and L. Stanchi, Nonlinear operations on pulses by means of p — n junctions (Nuclear Instruments 8 (1960) p. 79) 244

Instruments and Methods for Nuclear Spectroscopy

A new type of neutron spectrometer, Richard L. Bramblett, Ronald I. Ewing and T. W. Bonner 1
Automatic mass number determination for isotope separators and mass spectrometers, L. Wåhlin 21
Apparatus and analysis for sum-coincidence (n,γ) spectrometer, J. E. Draper and A. A. Fleischer 67
The correction of resonance peaks for experimental resolution, R. O. Lane, N. F. Morehouse, Jr. and D. L. Phillips 87
Automatic live-time measurement and background subtraction for the Hutchinson-Scarrott pulse height analyzer, K. F. Orton and K. Wilkins 97
Higher order chance coincidences in a fast-slow coincidence arrangement, Helmut Paul 131
Method of evaluating delayed coincidence experiments, R. S. Weaver and R. E. Bell 149
Sector-type double-focusing beta-ray spectrometer, M. Sakai, H. Ikegami and T. Yamazaki 154
Small scattering chamber for large angular region, H. R. E. Tjin A Djie, F. J. de Heer and L. A. Ch. Koerts . . 172
A method for the measurement of gamma-ray spectra in omnidirectional gamma-ray fields, L. C. Thompson . . . 175
On resolution and luminosity of a neutron diffraction spectrometer for single crystal analysis, G. Caglioti, A. Paoletti and F. P. Ricci 195
De la décomposition des intensités spectrales en courbes de Gauss, L. G. Preuss et J. P. Escarfail 212
A one-meter-radius iron-free double-focusing $\pi\sqrt{2}$ spectrometer for β-ray spectroscopy with a precision of $1:10^5$, R. L. Graham, G. T. Ewan and J. S. Geiger 245
Computational methods for analysis of resonance transmission data for S-wave neutrons, J. E. Lynn 315

Instruments and Methods for High Energy Physics

A semi-automatic analyser for bubble chamber photographs, O. R. Frisch and A. J. Oxley 92

Letters to the Editor

A new type of liquid anode gamma and beta halogen counter, S. C. Pancholi 118
Note on the determination of tritium by means of liquid scintillators and DC-measurements of photomultiplier currents, Torbjörn Westermark, Björn Grapengiesser, Hans Lindroth and Nadim Ghanem 357
On the possibility of a radiation chemical nuclear track chamber, Torbjörn Westermark 360

News Items

1961 International Conference on High Magnetic Fields, Massachusetts Institute of Technology, November 1–3, 1961 243
The Third International Conference on Analog Computation, Belgrade, Yugoslavia, September 4–9, 1961 244

Nuclear Electronics

Notes on a fast time analyzer for short lifetime measurements, M. Bonitz and E. J. Berlovich. 13
Mesures de temps dans le domaine de la nanoseconde : convertisseur de temps en amplitudes et circuits de coïncidences, R. Ballini et E. Pomelas 29
Pulse height discriminator employing distributed amplification, C. Infante 102
Reversible Verstärkungsänderungen von Photomultipliern bei unterschiedlichen Zählraten, H. Jung, Ph. Panussi und J. Jänecke 121
A precision clock for measuring time intervals, R. W. Findley, R. A. Reiter and T. A. Romanowski. 221
La stabilisation du champ magnétique par un maser à résonance magnétique nucléaire (I), P. Grivet et H. Hahn 233
Behaviour of photomultipliers against short light-pulses, C. Cernigoi, I. Gabrielli and G. Iernetti 303
La stabilisation du champ magnétique par un maser à résonance magnétique nucléaire (II), P. Grivet et H. Hahn 328
The optical properties of slow chopper and time-of-flight device, E. Maliszewski 341

Miscellaneous

Sedimentary rock analysis by charged particle bombardment, Robert F. Sippel and Everett D. Glover 57

Spotlight on Industry

This section appears each month and features various happenings of interest in the nuclear industrial world and objective information on products of the nuclear manufacturers. It is offered entirely as a service and all nuclear manufacturers are cordially invited to submit clearly objective and descriptive material on their endeavours and product developments for consideration for use in this section.

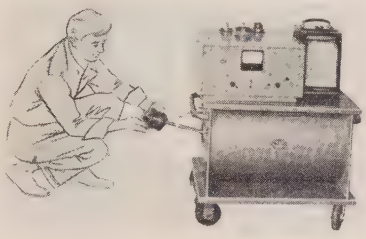

NEW SYSTEM DETECTS AND MEASURES RADIOACTIVITY IN GAS OR WATER

Nuclear Measurements Corp., 2460 N. Arlington Ave., Indianapolis 18, Ind.

Called the fluid monitoring system, this system provides the large volume required for detection at MAC (maximum acceptable concentration) levels. Used in conjunction with NMC alpha and beta-gamma air particulate monitors, it measures activity of the gaseous component of the discharge from these units. A motor blower assembly is available for completely independent operation.

The system consists of a mobile 30-liter chamber, (FMS-1) logarithmic count ratemeter (LCRM-2M) with built-in bell and alarm lights, and portable Esterline-Angus recorder. The chamber accepts standard GM (beta-gamma) counters or NaI scintillation (gamma only) counter as detectors. Use of two probes provides increased sensitivity, allows comparison of each and assures safe operation even though one should fail.

The chamber is surrounded by a lead shot shield equivalent to 2″ of solid lead. Shot may be added through a large port in the top, and removed through drain plugs in the bottom.

NEW VALVE TESTER

Electrical Instruments Ltd., Montrose avenue, Slough, England

This Valve Tester (Model 45C) is capable of testing over 5000 different types of valves, British American, and Continental. Two ranges of Mutual Conductance are provided 0–3 mA/V and 0–15 mA/V, and tests are also incorporated for Element Shorts, Cathode Leakage and Emission. A separate T.V. tube adaptor Model 445 is available (shown in illustration) which now incorporates a special base for the latest wide angle 110° tubes. A very important feature of this new instrument is the incorporation of test facilities for checking the latst 12 volt car radio valves.

Valves can be measured rapidly even by unskilled operators due to the simplicity in operation of the Valve Tester, and the accurate moving coil meter enables the valves to be "matched" or compared for push-pull circuits. The 45C incorporates 21 valve holders and is supplied complete with instruction book and valve characteristic manual. Test facilities are provided for earlier type valves as well as the very latest T.V. types etc.

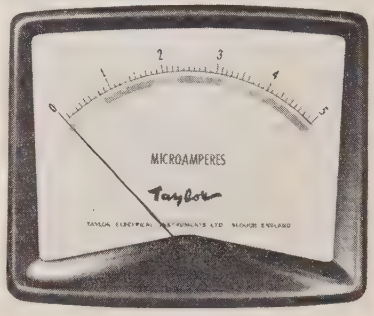

NEW "VISTA" RANGE-CONTEMPORARY STYLE PANEL METERS

Taylor, Electrical instruments Ltd. Montrose, Avenu Slough, England

A new range of contemporary style Panel Meters is announced which incorporate our well established centre pole meter movement of advanced design, with D.C. sensitivities commencing from 5 μA.

Four models are available with nominal scale lengths from $1\frac{5}{8}$″ to $4\frac{1}{2}$″. The bases of all instruments are made so that the meters can be interchanged with standard type meters of earlier design. The ranges available include moving coil D.C. or A.C. with rectifiers, thermocouple from 10 mA–F A and moving iron types from 10 mA to 50 A; voltmeters from 10 V. Mirror scales and special scales to customers' own requirements can be supplied in addition to knife edge or spade type pointers.

The new mouldings are designed to provide open scales, resulting in shadowless readings.

A NEW RANGE OF CRYSTAL-PHOTOMULTIPLIER ASSEMBLIES

Nuclear Enterprises (G.B.) Ltd., Bankhead Medway, Edinburgh 11, Scotland

The assemblies combine high quality scintillation crystals (ranging from thin NaI(T1) crystals (0.015″) up to

special large 9″ diameter crystals) with specially selected high resolution EMI photomultipliers to give optimum resolution. Other crystals are also available for alpha, beta and proton, particle detection, and typical resolution figures are: for the Cs^{137} MeV gamma ray photopeak for crystals up

to and including 3″ × 3″, 7.0 to 9.5%, and for large crystals, 8.0 to 10.0%, excluding well type crystals where the resolution averages 2% higher. Integral mounting (crystal directly mounted on to photomultiplier face) is used for assemblies of all crystals up to and including 2″ diameter, apart from the thin crystal assembly IA–HG; while demountable assemblies are used for crystals with diameters in the range 2″ to 5″ facilitate ready replacement of the photomultiplier, precluding the need to return the assembly for replacement as with the integral type. Compact cathode follower preamplifier units, including a dynode resistor chain, are available for fitting to all assemblies.

Special assemblies to cover very low level activity measurements are included in the new range. As in the case of the other Nuclear Enterprises crystal-photomultiplier assemblies, NaI(T1) crystals with a potassium content of only 1 to 3 parts per million are used in these special assemblies, and also quartz windows, stainless steel canisters and de-based photomultipliers.

For applications other than gamma ray counting, special Integral Assemblies with thin CsI(T1) crystals for alpha particle or proton detection, and anthracene crystals for beta particle detection are available. Additionally, special large crystal assemblies with NaI(T1) crystals up to 9″ diameter and arrays of three or four photomultipliers can be supplied.

GLASS WITH LOW RADIOACTIVITY

Corning Glass Works

This new glass has a radioactivity of less than 10 counts per minute per kilogram. (Most glasses in present use have a count of more than 175.)

Corning noted that its 96 per cent silica glass has a count of about 50. However, faceplate diameters are limited to three inches with this glass, whereas diameters of one to 16 inches are possible with the new glass.

Corning noted also that fused silica, an ultra-pure material, has a count of about 10. However, fused silica is difficult to form into bulbs and does not seal easily to tube bases. The new glass is easily formed and seals well to Dumet, Sylvania 4 and similar alloys. The company said thermal coefficient of expansion of the new glass is about 95×10^{-7}/°C.

NEW LOWBETA SYSTEM

Sharp Laboratories, Inc., Box 1302, La Jolla, California

This advanced, low-level beta detection system contain such features as recorded background of less than 0.25

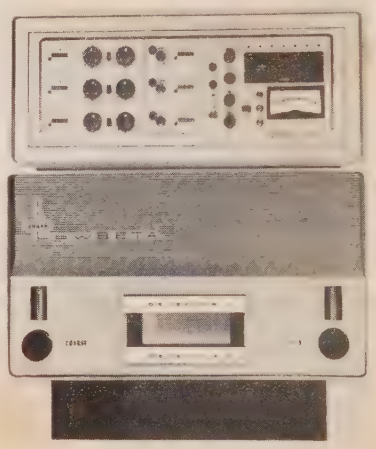

counts per minute for a 1-inch diameter detector, shield size only 18-inches square, shield weight only 1500 pounds, transistorized electronics, plug-in printed circuit cards, illuminated programming panel and electronics fit for carbon dating.

NEW PULSE GENERATOR

Radiation Instrument Co., P.O. Box 733 Silver Spring, Maryland, U.S.A.

"Nanosecond and microsecond pulses are obtainable from the Model 414 Calibration Pulser. Decay times are in 10 steps from 3 millimicroseconds to 100 microseconds. Amplitude ranges are in 11 steps from 1 millivolt full scale to 100 volts full scale. Internal standard cell calibration is included. Brochures are available. Radiation Instrument Co., P.O. Box 733, Silver Spring, Maryland, U.S.A."

DATE DUE

GAYLORD			PRINTED IN U.S.A.